Doctoral Thesis

Electronic States of the First Order Ferrimagnet $ErCo_2$ Studied by Polarization Dependent Hard X-Ray Photoemission Spectroscopy

March 2018

Doctoral Program in Integrated Sciences and Engineering
Graduate School of Sciences and Engineering
Ritsumeikan University

AMINA Abdelsamea Abozeed Farghaly

Doctoral Thesis

Reviewed by Ritsumeikan University

Electronic States of the First Order Ferrimagnet $ErCo_2$ Studied by Polarization Dependent Hard X-Ray Photoemission Spectroscopy

(偏光依存硬 X 線光電子分光による一次フェリ磁性転移を示す $ErCo_2$ の電子状態の研究)

March 2018

2018 年 3 月

Doctoral Program in Advanced Mathematics and Physics

Graduate School of Sciences and Engineering

Ritsumeikan University

立命館大学大学院理工学研究科

基礎理工学専攻博士課程後期課程

AMINA Abdelsamea Abozeed Farghaly

アミーナ アブデル - サミア アボジド ファルギリ

Supervisor: Professor IMADA Shin

研究指導教員：今田　真　教授

Table of Contents

&

Abbreviations

Table of Contents

Table of Contents ……..…… i

Abbreviations ……..…… ii

Chapter 1. Introduction ……..……..…… 1

Chapter 2. Experimental Set up and Measuring Technique ……..…….34

Chapter 3. Method of Analysis **……**…..……..……... 53

Chapter 4. Electronic Structure of the Laves Phase Compound $ErCo_2$ Studied by Polarization Dependent Hard X-Ray Photoemission Spectroscopy ……..……...……...… 70

Chapter 5. Rare-earth Fourth Order Multipole Moment in Cubic $ErCo_2$ Probed by Linear Dichroism in Core-Level Photoemission ……..……..…… 96

Chapter 6. Conclusions and Suggestions for Future Work ……..…….125

Appendices ……128

List of Publications ……..…… 152

Acknowledgement ……..……. 154

Abbreviations

Abbreviation	Description
BS	Background subtracted
CEF	Crystal electric field
C. G	Center of gravity
CPA	Coherent potential approximation
DOS	Density of state
DFT	Density function theory
E_K	Kinetic energy
EA	Easy axis
E_B	Binding energy
E_F	Fermi level
E_p	Pass energy
ESCA	Electron spectroscopy for chemical analysis
FWHM	Full wave half maximum (energy resolution)
HSA	Hemispherical photoelectron analyzer
HAXPES	Hard X-ray photoemission spectroscopy
H_{cr}	Critical field
IEM	Itinerant electron metamagnetism
KKR	Korringa, Kohn, and Rostoker
λ	Magnetostriction
LD	Linear dichroism
LSDA	Local spin density approximation
M	Magnetic moment
MCE	Magnetocaloric effect
MMT	Metamagnetic transition
M_o	Orbital moment
M_s	Spin moment
ω_s	Spontaneous volume magnetostriction
P_c	Critical pressure
PDOS	Partial densities of state

Abbreviation	**Description**
P_L	Linear polarization
p-pol	Horizontally polarized light
R	Rare earth
SIC	Self-Interaction Corrections
s-pol	Vertically polarized light
T_C	Curie temperature
T	Transition metal
TIMR	Temperature induced moment reorientation
UHV	Ultra-high vacuum
UPS	Ultraviolet photoelectron spectroscopy
XAS	X-ray absorption spectroscopy
XPS	X ray photoemission spectroscopy
Z_4^{cube}	Fourth order multipole
Z_6^{cube}	Sixth order multipole

Chapter 1

Introduction

Chapter 1

Introduction

1.1. Rare-Earth Transition-Metal Laves phase

Rare-earth (*R*: Sc, Lu, Ce, Pr, Nd, Sm, Gd, Tb, Dy, Ho, Er, and Tm) transition-metal (T: Al, Fe, Co, and Ni) Laves phase RT_2 intermetallic compounds form a wide class of magnetic materials. They combine a localized magnetism of the *R* sublattice with an itinerant magnetism of the 3*d* sublattice, the magnetic interaction between Co 3*d* and *R* 4*f* moments, as well as the crystal electric field effects (CEF) on *R* 4*f* and Co 3*d* electrons. On the other hand, the large magnetic anisotropy and magnetostriction originating from the *R* sublattice, makes such intermetallics very interesting subjects from the scientific point of view [1.1-1.4].

Although most RT_2 compounds have the same cubic C15 structure of $MgCu_2$ type (Fd3m space group) with similar lattice parameters, they exhibit different magnetic behavior. No magnetic moment has been detected on Al and Ni in these compounds. While Fe is magnetic in the RFe_2 compounds; the magnetic moment of Fe is nearly constant in all these compounds, it is about 1.4 μ_B in the case of trivalent R and arising to about 1.6 μ_B in $GdFe_2$. RFe_2 compounds are ferromagnet for light rare earth or ferrimagnet for heavy rare earth, and Curie temperature (T_C) is always high. The RFe_2 compounds have giant magnetostriction and the contribution of Fe sublattice to the total anisotropic magnetostriction is negligible compared to the *R* sublattice contribution [1.1, 1.2, 1.5]. RCo_2 is in contrast to other Laves phase, in which the *d*-electron system is either non-magnetic as RNi_2 and RAl_2 or has a stable magnetic moment as RFe_2. RCo_2 exhibits an intermediate behavior and undergoes a metamagnetic transition. The RCo_2 compounds have much lower T_C than RFe_2, except in $GdCo_2$ whose T_C exceeds room temperature. For this reason, RCo_2 compounds are not interesting for some applications, but the metamagnetism found in these compounds attracted a great attention [1.1-1.5].

In the light rare earth ($J = L - S$) the spin is opposite to the total moment and the *R* magnetic moment $M_R = g_R \mu_B J_R$ is oriented antiparallel to each other and parallel to transition metal (T) moments. While in the heavy earth ($J = L + S$) the spin is parallel to the total moment and the *R* magnetic moments is oriented parallel to each other and antiparallel to

transition metal (T) moments. Also, in all cases there is antiparallel coupling of the rare-earth and cobalt spins [1.6] as a shown in **Fig. 1.1**.

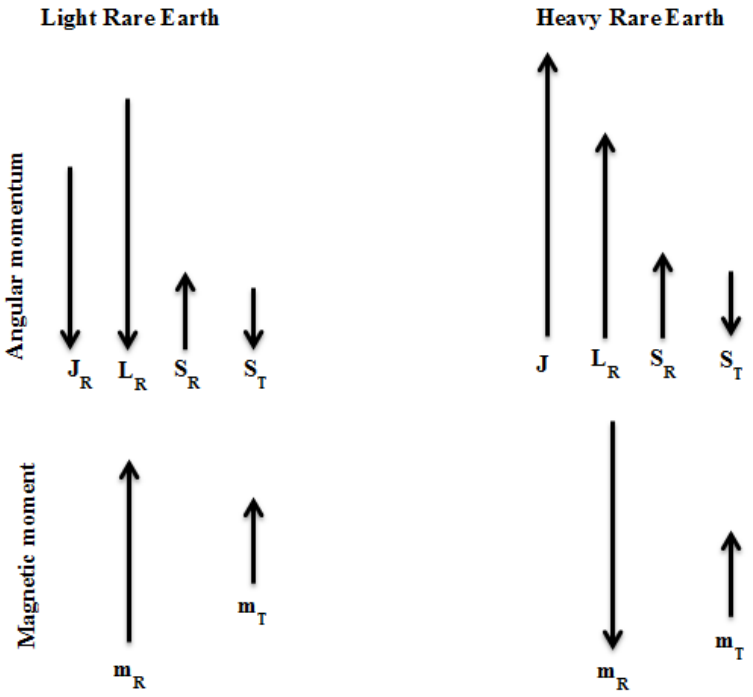

Fig. 1.1. Magnetic properties of light and heavy rare earth.

The intrinsic properties of R_nT_m compounds can be described in terms of *exchange interactions and magnetocrystalline anisotropy* [1.3]. The exchange interactions take place between all unpaired spins in the 3*d*-4*f* system and can be described by three different exchange interaction parameters: J_{TT}, J_{RT} and J_{RR}. J_{TT} is positive and leads to the ferromagnetic coupling between 3d spins. J_{RT} comes from the internal magnetic structure; its negative sign reflects an antiparallel coupling between the spins of the 4*f* and 3*d* atoms and leads to a parallel orientation between 3*d* and 4*f* moments in the case of light rare-earth and antiparallel alignment for the heavy rare earth. J_{RR} is usually the weakest one in the 3*d*-4*f* compounds, but plays an important role in RCo_2.

In the magnetic system the magnetocrystalline anisotropy is observed by the oriented magnetization along a specific crystallographic direction of single crystal samples, while the information about the magnetocrystalline anisotropy may be lost in the case of non-single crystal samples. The magnetocrystalline anisotropy energy can be written as:

$$E_a = \sum_{n=0}^{\infty} \sum_{m=0}^{n} K_n^m \, sin^n\theta cosm\varphi \qquad (1.1)$$

The angles θ and φ are the polar and azimuthal angles of the magnetization with respect to the main symmetry direction of the elementary cell respectively, K_n^m is the anisotropy constants. The 3*d*-4*f* intermetallic compounds have large magnetic anisotropy originates from the rare earth ions and is transferred by the 3*d*-4*f* exchange interactions to the 3*d* sublattice. The contribution of the rare earth to the magnetocrystalline anisotropy is dominant at low temperatures whenever the 4*f* ions have nonzero orbital moments, this contribution decreases rapidly with increasing temperatures and becomes comparable in magnitude with that of the 3d sublattice. Temperature induced moment reorientation (TIMR) phenomena can occur with increasing temperature as a result of a mutual cancellation of the anisotropy contributions from the 4*f* and 3*d* sublattices. The 3*d* contribution to anisotropy is dominant at temperatures above the moment-reorientation temperature (T_{MR}) [1.3].

1.2. *R*Co$_2$ Crystal Structure

X-ray diffraction patterns of *R*Co$_2$ measured at room temperature evidenced the presence of a cubic Laves phase crystal structure of space group Fd$\bar{3}$m symmetry [1.7]. In this structure the R and Co atoms occupy a single position, namely 8a and 16d sites, respectively as a shown in **Fig. 1.2a**, where the Er atoms form a diamond lattice and the remaining space inside the cell is occupied by the four Co tetrahedrons. For R=Sm, Tb, Er and Tm, below T_C the cubic symmetry undergoes rhombohedral distortion of space group R$\bar{3}$m symmetry due to magnetostrictive effect (magnetostriction means a change of dimensions and shape of sample due to a change of its magnetic state), the tetrahedron of cobalt atoms elongate along the easy magnetization direction which is [111] direction of the cubic structure. So, in this structure the cobalt atoms occupy two inequivalent crystallographic sites, namely 3b and 9e sites and one crystallographic site 6c for Er atoms as a shown in **Fig. 1.2b**, which illustrated the ferrimagnetic arrangement between *R* and Co magnetic moments below T_C [1.8, 1.9].

In *R*Co$_2$ compounds, the existence of crystal lattice distortion below the magnetic ordering temperature due to magnetostrictive effect is responsible for the large anisotropic magnetostriction along the magnetization direction. The nature of distortion depends on the orientation of the easy axis of the crystal. In a cubic crystal system there are three orientations: tetragonal one with the easy axis (EA) along [100] direction, rhombohedral one with EA along [111] direction and rhombic one with EA along [110] direction [1.10]. At low temperatures the easy magnetization direction follows the sign of Stevens factor B_J for the *R*

ions as a shown in **table 1.1**. For the negative sign of B_J, the easy axis orients along the cubic edge, while for the positive sign it aligns along the body diagonal [1.3].

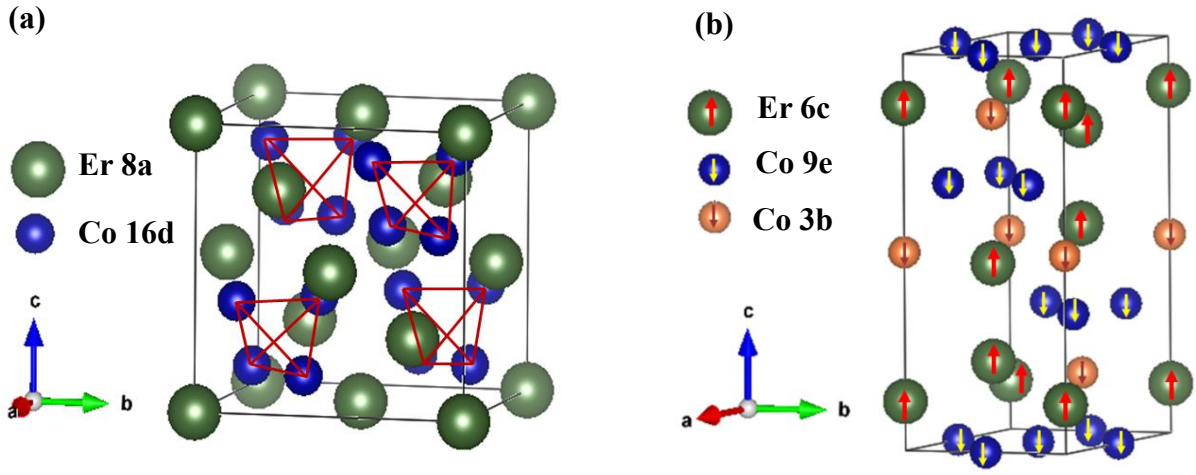

Fig. 1.2. Schematic representation of RCo_2 (a) cubic Laves phase crystal structure of space group $Fd\bar{3}m$. (b) Rhombohedral crystal structure of space group $R\bar{3}m$ (hexagonal unit cell). C axis of (b) corresponds to the [111] direction of (a).

Table 1.1. Correlation between the easy direction of magnetization and Stevens factor B_J in RCo_2 compounds at low and high temperatures [1.3].

Compound	B_J	Easy direction	
		Low T	High T
Pr	-	100	100
Nd	-	110	100
Sm	+	111	111
Gd	0	100	100
Tb	+	111	111
Dy	-	100	100
Ho	-	110	100
Er	+	111	111
Tm	+	111	111

The magnetostriction for a crystal with cubic symmetry in any direction is expressed by:

$$\lambda = 1.5\lambda_{100}\left(\sum_i \alpha_i^2\,\beta_i^2 - \frac{1}{9}\right) + 3\lambda_{111}\sum_{i<j}\alpha_i\,\alpha_j\beta_i\beta_j \qquad (1.2)$$

where λ_{100} and λ_{111} are the magnetostriction constants, while α_i and β_j are the direction cosines (i, j=1, 2, 3 for x, y, z axes respectively) of magnetization and measurement directions respectively [1.11-1.14].

In RCo_2 compounds, the existence of the magnetic ordering of the itinerant electron system would cause a large spontaneous volume magnetostriction ω_s where ω_s is defined as the difference between the unit cell volume at a given temperature $V_m(T)$ and the paramagnetic unit cell volume $V_p(T)$ and given as [1.13]:

$$\omega_s(T) = \frac{V_m(T) - V_p(T)}{V_p(T)} \tag{1.3}$$

where $V_p(T)$ is obtained by extrapolation from the paramagnetic temperature region.

1.3. Physical properties of Laves phase *R*Co_2

The cubic Laves phase *R*Co_2 (*R*: rare earth or yttrium) intermetallic compounds have been extensively studied from both experimental and theoretical points of view due to their complex electronic and magnetic structures, which give rise to a handful of interesting physical phenomena such as itinerant Co 3d electron metamagnetism (IEM), giant magnetic anisotropy and magnetocaloric effect (MCE) [1.8, 1.9, 1.14]. *R*Co_2 shows very interesting magnetic phenomena which have been discussed on the basis of (a) the combination of itinerant 3*d* band of Co and localized 4*f* electrons of *R*, (b) the magnetic interaction between Co 3*d* and *R* 4*f* moments, and (c) the crystal electric field effects (CEF) on *R* 4*f* and Co 3*d* electrons.

RCo_2 compounds are ferrimagnet below Curie temperature (T_C), *R*Co_2 compounds with light rare earth (Pr, Nd, Sm) exhibit a ferromagnetic behavior and the R and Co magnetic moments are parallel oriented, while those with heavy rare earth (Gd, Tb, Dy, Ho, Er) have an anti-parallel coupling between rare-earth and cobalt moments [1.2, 1.11]. The large internal exchange field produced by the ferromagnetically order rare-earth 4*f* moments is sufficient to induced Co magnetic moment of about one Bohr magneton oriented antiparallel to the rare earths in zero external magnetic field [1.15, 1.2, 1.11, 1.16]. In the ordered magnetic state, the magnetic behavior of *R*Co_2 is mostly dominated by the *R* sublattice, where *R* magnetic moment is much larger than that of the two Co atoms [1.2]. If *R* is nonmagnetic rare earth ($ScCo_2$, YCo_2, $LuCo_2$), these compounds are Pauli exchange enhanced paramagnet and the Co

magnetization can be induced only by applying strong external magnetic fields larger than 70 T [1.17].

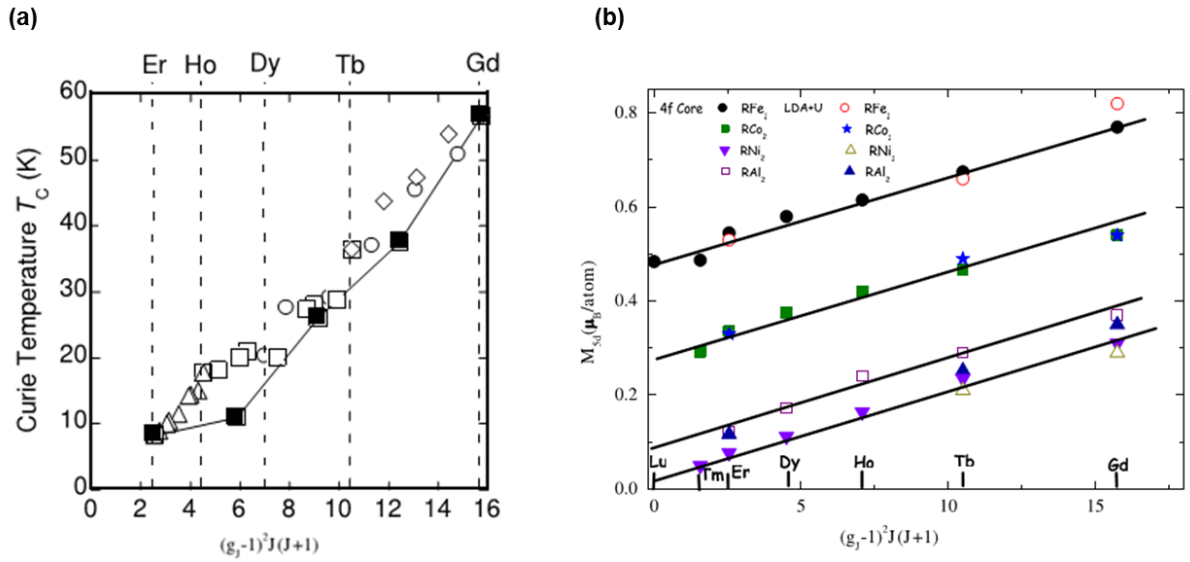

Fig. 1.3. (a) T_C of *R* [1.18]. (b) *R* 5*d* band polarization [1.19], as a function of the rare earth's de Gennes factor.

The (*R*-Co) exchange interactions are usually described by a Campbell (4*f*-5*d*-3*d*) model [1.20], where *R* 5*d* band polarization plays a dominant part [1.19]. The magnetic measurements and band structure calculations performed on RT_2 compounds showed that *R* 5d band polarization is due to the contribution of both the *R* 4*f*-5*d* local intra-atomic exchange interactions ($J_{4f-5d}, J_{4f-6s}, J_{4f-6p}$) and *R* 5*d*-T 3*d* short range exchange interactions. The *R* 4*f*-5*d* local intra-atomic exchange interactions are proportional to rare earth's de Gennes factor $G = (g_J - 1)^2 J(J+1)$ as a shown in **Fig. 1.3b** for the heavy rare earth (RT_2), a linear dependence is illustrated between *R* 5d band polarization and rare earth's de Gennes factor. Thus, **Fig. 1.3a** reveals T_C of the rare earth as a function in de Gennes factor. When the magnetic moment of the transition metal is increased the *R* 5*d* band polarization increases to higher values (M_{5d} (Fe)> M_{5d} (Co)> M_{5d} (Al)> M_{5d} (Ni)). *R* 5*d*-T 3*d* short range exchange interactions are proportional to the number of 3*d* transition metal atoms neighboring to an *R* site and their moments (magnitude and sign) [1.19, 1.21]. As will describe in the next paragraph, the IEM is induced in RCo_2 compounds due to the ferromagnetically ordered 4*f* moments of rare-earth, and the strong *R* 4*f*-Co 3*d* exchange interactions mediated by the *R* 5*d*-Co 3*d* hybridization. The magnetic properties of these compounds analyzed by Bloch *et al* [1.22] in the framework of IEM concept, which was firstly discussed by Wohlfarth and Rhodes [1.23].

Many interesting magnetic properties observed in these compounds can be explained by the shape of the density of state (DOS) curve near the Fermi level (E_F) [1.24, 1.25]. The RCo_2 electronic structure is characterized by a high instability of Co 3*d* magnetic moments due to the large DOS of Co 3*d* bands just below the E_F; this is the critical condition for the occurrence of large Co 3d moments which can be strongly changed by external factors such as magnetic field, pressure, impurities and temperature [1.26]. The assumption that the cobalt sublattice has metamagnetism is affirmed by calculations of the DOS of YCo_2, $DyCo_2$, $HoCo_2$, and $ErCo_2$ [1.8, 1.27]. The RCo_2 compounds were considered as good models for studying of basic properties of IEM; where the interactions of the localized 4*f* electrons with itinerant electrons 3*d* and the high DOS around the E_F energy play vital role in the appearance of IEM [1.28].

Another interesting profile of RCo_2 compounds is the order of magnetic transition. *R*= Dy, Ho and Er exhibit first order magnetic transition at T_C and the metamagnetic transition is observed in a narrow temperature range above T_C, whereas second order magnetic transitions are found in cases of other rare-earth elements between *R*=Pr and Tm. The R dependence of the magnetic ordering process has been explained by Bloch *et al*.[1.22] based on the model where R moment interacts with Co moment of itinerant 3*d* electrons, which shows itinerant electron metamagnetism (IEM) [1.23] in the case of YCo_2.

Moreover, in the ordered magnetic state, giant magnetocrystalline anisotropy and also magnetostriction of RCo_2 have attracted much attention [1.11, 1.29-1.31, 1.12]. Except for Gd^{3+} without orbital moment, the contribution to anisotropy from R under CEF is larger than that from Co[1.11]. This is also supported by the fact that RAl_2, in which Co is replaced by nonmagnetic Al, tends to have the same easy magnetization direction as RCo_2 [1.12, 1.32].

1.4. Physical properties of $ErCo_2$

Among the RCo_2 intermetallic compounds, $ErCo_2$ shows a first order phase transition from paramagnetic to ferrimagnetic phase [1.29] at a transition temperature $T_C \cong 35$ K (T_C value's varying in the range between 31-35 K are revealed in the literature) at zero applied magnetic field and the metamgnetic transition is observed in a narrow temperature range above T_C. So $ErCo_2$ can be considered as a good candidate to discuss the IEM concept and MCE, where the exchange interactions are moderate and the E_F lies just above a sharp peak in the DOS [1.9, 1.27, 1.28]. The existence of IEM in $ErCo_2$ can be strongly affected by external factors such as impurities, magnetic field, pressure, and temperature [1.26].

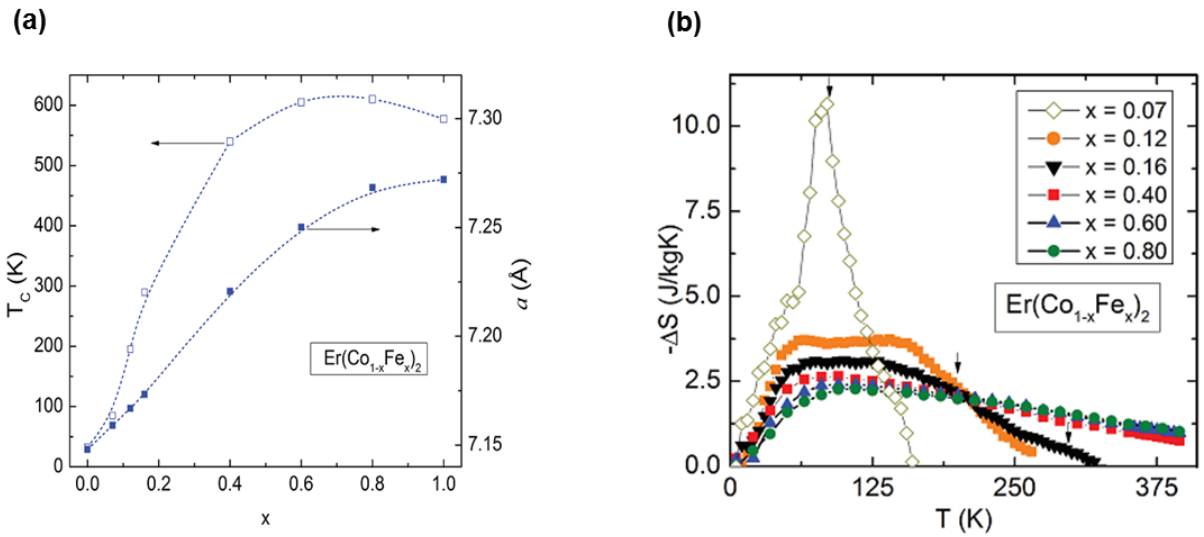

Fig. 1.4. (a) Dependences of crystal lattice parameter and T_C on Fe concentration (x). (b) Temperature dependence of magnetic entropy at different Fe concentration (x) in $Er(Co_{1-x}Fe_x)_2$ compounds [1.34].

The addition of impurity ferromagnetism of Fe ion to $ErCo_2$ originates rapidly increasing in T_C as a shown in **Fig. 1.4a** [1.34], decreasing magnetization and the change in the character of the magnetic phase transition from first order magnetic phase transition in $ErCo_2$ to second order in Er $(Co_{1-x}Fe_x)_2$ [1.11, 1.35] which is responsible for decreasing magnetocaloric effect (MCE), as a shown in **Fig. 1.4b** [1.34].

The magnetization behavior of single crystal $ErCo_2$ investigated [1.36] during transition through T_C along [100] and [111] axes is illustrated in **Fig. 1.5a**. The spontaneous magnetization M_s of this compound hardly changes up to T_C, while the magnetization curves have metamgnetic character above T_C in the temperature range between 35 K to 45 K as a shown in **Fig. 1.5a**. At specific critical field value H_{cr}, suddenly the magnetic state of $ErCo_2$ changes from paramagnetic state to ferrimagnetic state (first order phase transition). The value of H_{cr} depends on the direction of the applied field: ($H_{cr}^{[111]} < H_{cr}^{[110]} < H_{cr}^{[100]}$) as elucidated in **Fig. 1.5a**. Also, the spontaneous magnetization along [111] direction larger than that along [100] direction.

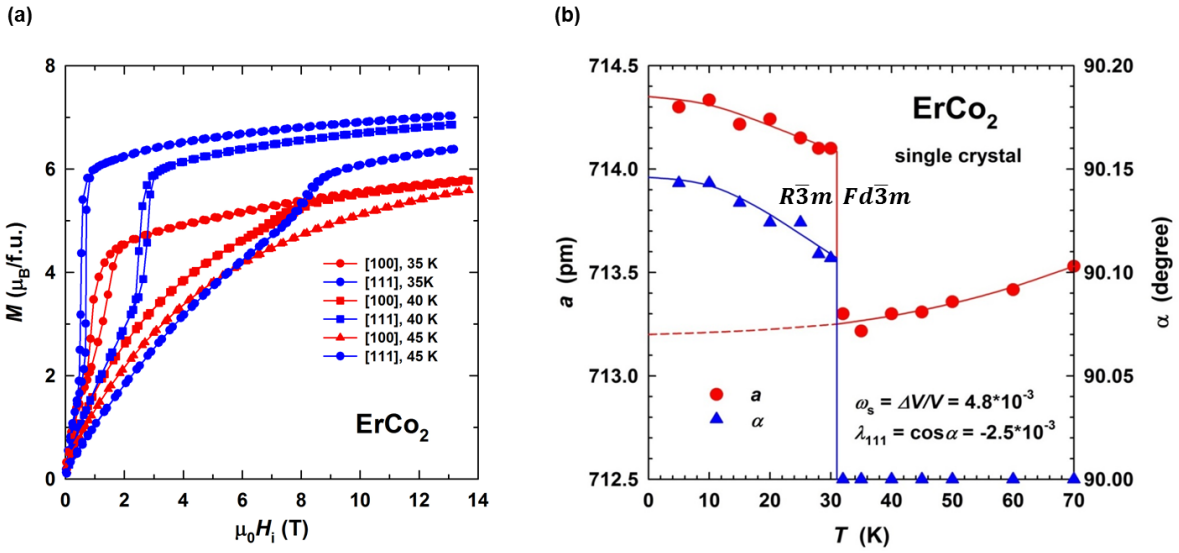

Fig. 1.5. (a) Magnetization curves of single crystal $ErCo_2$ measured along [100] and [111] axes during paramagnetic-ferrimagnetic metamgnetic transition. (b) Temperature dependence of the lattice constant and the anisotropic magnetostriction constant of $ErCo_2$. (These data supported by Prof. Andreev and his coauthors).

Fig. 1.5b shows the temperature dependence of the lattice parameters a of $ErCo_2$ above and below T_C, confirming that $ErCo_2$ exhibits first order phase transition at $T_C \cong 31$ K and the lattice constant suddenly increases at this temperature which reflects the abruptly change of the density of state in Co 3d subbands at E_F due to the splitting of the majority and minority spin sub-bands and the Co moment formation [1.37]. Also, **Fig. 1.5b** reveals α (α is the angle of a, b and c axes) in $ErCo_2$ compound, α jumps below the T_C. λ_{111} is magnetostriction constant and it is non-zero below T_C. $ErCo_2$ has large spontaneous volume magnetostriction $\omega_s = 4.8 \times 10^{-3}$.

The pressure dependent magnetic transition in RCo_2 has been subjected to several studies [1.26, 1.33, 1.38, 1.9]. **Fig. 1.6b** shows pressure dependence of T_C of $ErCo_2$ where at low pressures T_C of $ErCo_2$ decrease linearly with increasing pressure and at high pressure (above critical pressure: P_c) T_C becomes nearly pressure independent and MT vanished at P_c. At $P > P_c$ the *R*–Co–*R* exchange interaction becomes ineffective to induce the metamagnetism of Co 3d subbands, also DOS of Co 3d in the vicinity of E_F decreases [1.26,1.33, 1.38]. Furthermore, in the ordered magnetic state T_C and magnetic moment of Er sublattice is influenced little by pressure. In contrast, T_C and magnetic moment of Co sublattice decrease with increasing pressure as a shown in **Fig. 1.6a** and inset of **Fig. 1.6b** [1.9].

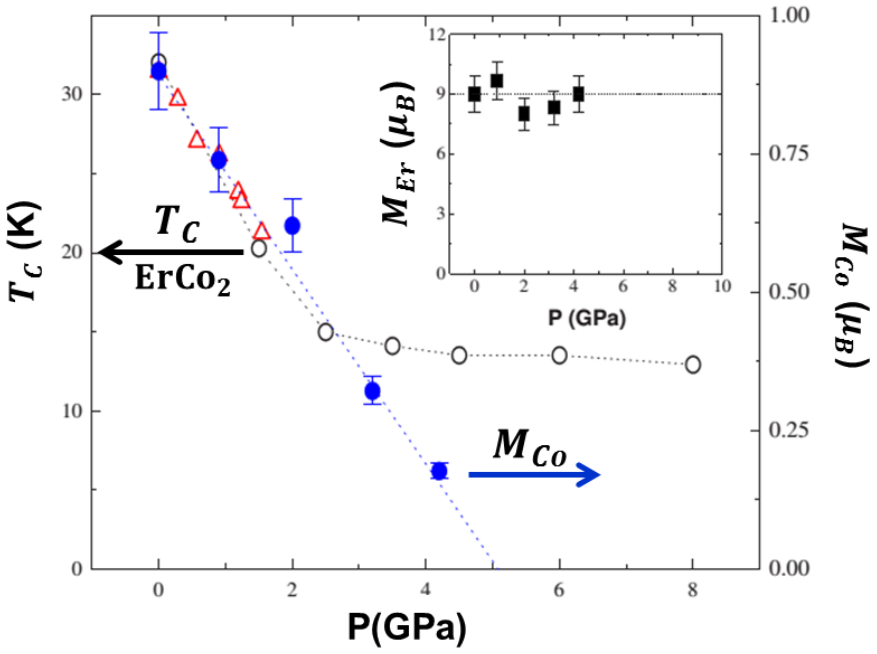

Fig. 1.6. Pressure dependence of T_C of $ErCo_2$ (black open circle and red triangle), Pressure dependences of Co magnetic moments (blue solid circle). In the inset, Pressure dependences of Er magnetic moment [1.33].

1.5. Crystal Electric Field (CEF)

Crystal field is an electrostatic field derived from neighboring atoms in the crystal. The neighboring ions, surrounding the atom with the unpaired electrons, are called the ligands [1.39]. The total Hamiltonian for 4*f* electrons is given as:

$$\mathcal{H} = \mathcal{H}_{ion} + \mathcal{H}_{CEF} + \mathcal{H}_{mag} \tag{1.4}$$

where:

$\mathcal{H}_{ion}$: describes the intra-atomic interactions in an R ion.

$\mathcal{H}_{CEF}$: denotes the CEF part representing the electrostatic field acting on the 4*f* electrons from the surrounding charge.

$\mathcal{H}_{mag}$: is the effective exchange interaction between the 4*f* and 3*d* moments.

Therefore, for 3*d*-transition metal: Crystal field > LS coupling > internal magnetic field, while for 4*f*-rare-earth: LS coupling > Crystal field > internal magnetic field.

The physical reason for this difference in behavior is the following: the 3*d*-electron-charge clouds reside more at the outside of the ions than the 4*f*-electrons-charge clouds. Consequently, the former electrons experience a much stronger influence of the crystal field

than the latter. The opposite is true for the spin-orbit interaction, the spin-orbit interaction is stronger with the larger atomic weight. Hence, it is larger for the rare earth than the 3d transition elements [1.40]. The CEF Hamiltonian acting on 4*f* electrons for the cubic symmetry in terms of Stevens operators written as [1.41, 1.42]:

$$\mathcal{H}_{CEF} = O_4 B_4 + O_6 B_6 \tag{1.5}$$

$$O_4 = [O_4^0 + 5.O_4^4] \qquad O_6 = [O_6^0 - 21.O_6^4]$$

where: O_4 and O_6 are the Stevens equivalent operators of fourth and sixth degree, respectively, and their contents depend on the quantization direction chosen. B_4 and B_6 are factors which determine the scale of the crystal field splitting. This Hamiltonian rewritten by Lea *et al.* into the form [1.43]:

$$H_{CEF} = Wx\left(\frac{O_4}{F(4)}\right) + W(1-|x|)\left(\frac{O_6}{F(6)}\right) \tag{1.6}$$

This expression is well known as Lea-Leask-Wolf (LLW) Hamiltonian [1.43]. Note that $|x| \leq 1$, W and x are crystal field parameters of Lea-Leask-Wolf notations; W is an energy scale factor, x represents the relative importance of the fourth- and sixth degree terms. The parameters W and x are related to the B_4 and B_6 coefficients by:

$$B_4 F(4) = Wx \tag{1.7}$$

$$B_6 F(6) = W(1-|x|) \tag{1.8}$$

where the quantities F(4) and F(6) are common constants and their values depend on RE element.

This CEF effect leads to giant magnetocrystalline anisotropies of the rare-earth ions. The Stevens operators in terms of angular momentum operators are written as [1.42]:

$$O_4^0 = [35J_z^4 - 30J(J+1)J_z^2 + 25J_z^2 - 6J(J+1) + 3J^2(J+1)^2] \tag{1.9}$$

$$O_4^4 = \frac{1}{2}(J_+^4 + J_-^4) \tag{1.10}$$

$$O_6^0 = [231J_z^6 - 315J(J+1)J_z^4 + 735J_z^4 + 105J^2(J+1)^2J_z^2 - 525J(J+1)J_z^2 + 294J_z^4 - 5J^3(J+1)^3 + 40J^2(J+1)^2 - 60J(J+1)] \tag{1.11}$$

$$O_6^4 = \frac{1}{4}[(11J_z^2 - J(J+1) - 38)\left(J_+^4 + J_-^4\right) + (J_+^4 + J_-^4)(11J_z^2 - J(J+1) - 38)] \quad (1.12)$$

The eigenvalues of $\boldsymbol{J^2}$ and J_z corresponding to the eigenvectors $|j,m\rangle$ are given as [1.44]:

$$\boldsymbol{J^2}\,|j,m\rangle = \hbar^2 j(j+1)|j,m\rangle \quad (1.13)$$

$$J_z\,|j,m\rangle = \hbar m\,|j,m\rangle \quad (1.14)$$

where the values of j are either integer or half integer ($j = 0, \frac{1}{2}, \frac{3}{2}, \ldots\ldots$), and $-j \le m \le j$, so for each j there are $2j+1$ values of m.

The matrices representing $\boldsymbol{J^2}$ and J_z are **diagonal** since $\boldsymbol{J^2}$ and J_z are commute and their diagonal elements are $\hbar^2 j(j+1)$ and $\hbar m$, respectively [1.44], these matrices are given by:

$$\langle j`, m`|\,\boldsymbol{J^2}|j,m\rangle = \hbar^2 j(j+1)\delta_{j`j}\delta_{m`m} \quad (1.15)$$

$$\langle j`, m`|J_z\,|j,m\rangle = \hbar m\delta_{j`j}\delta_{m`m} \quad (1.16)$$

But since the raising and lowering operators $J_\pm$ are not commute with J_z, the matrices representing $J_\pm$ are **not diagonal** [1.44] as follows:

$$\langle j`, m`|\,J_\pm\,|j,m\rangle = \hbar\sqrt{j(j+1) - m(m\pm 1)}\,\delta_{j`j}\delta_{m`,m\pm 1} \quad (1.17)$$

1.6. Multipole Moment

In f electron systems, the spin and orbital degrees of freedom are coupled through strong spin-orbit interaction to form a *J*-multiplet. The *J*-multiplet is further split into several crystalline electric field levels, where each level has its own electric and magnetic characters. In such cases, it is appropriate to describe the electronic degrees of freedom in terms of multipole moments. Multipole moment is a concept that was established in the classical electromagnetism. Among these multipoles are magnetic and electric multipole moments. A magnetic multipole breaks the spherical symmetry in the charge distribution. On the other hand, an electric multipole breaks the parity and is responsible for ferroelectricity. Multipole moment characterizes the anisotropy charge distribution. Due to the localized nature of f electrons and its large orbital angular momentum; multipoles with higher ranks become active in orbitally degenerate systems and this behavior increases in the case of high degeneracy as quartet or triplet CEF states. Furthermore, high degeneracy often permits higher multipoles

such as octupole $(l = 3)$; hexadecapole $(l = 4)$; dotriacontapole $(l = 5)$; and hexacontatetrapole $(l = 6)$ [1.45-1.48].

In quantum statistical mechanics, multipole moments should be regarded as the expectation value and it can be deduced as following:

In the case of the environment around the *R* atom has a cubic symmetry, the CEF Hamiltonian ($\mathcal{H}_{CEF}$) in terms of multipole expansion is expressed as [1.42]:

$$\mathcal{H}_{CEF} = \sum_i [\, A_4^0(35z_i^4 - 30r_i^2z_i^2 + 3r_i^4) + A_4^4(x_i^4 - 6x_i^2y_i^2 + y_i^4) + A_6^0(231z_i^6 - 315r_i^2z_i^4 + 105r_i^4z_i^2 - 5r_i^6) + A_6^4(11z_i^2 - r_i^2)(x_i^4 - 6x_i^2y_i^2 + y_i^4)] \quad (1.18)$$

where $A_4^4 = 5A_4^0$ and $A_6^4 = -21A_6^0$, this is equivalent with:

$$\mathcal{H}_{CEF} = \sum_i \left[20A_4^0 \left(x_i^4 + y_i^4 + z_i^4 - \frac{3}{5}r_i^4 \right) - 224A_6^0 \left\{ (x_i^6 + y_i^6 + z_i^6) + \frac{15}{4}(x_i^2y_i^4 + x_i^2z_i^4 + y_i^2x_i^4 + y_i^2z_i^4 + z_i^2x_i^4 + z_i^2y_i^4) - \frac{15}{14}r_i^6 \right\} \right] \quad (1.19)$$

where the first term (...) corresponds to the fourth order multipole (hexadecapole), and the second term $\{\ldots\}$ resembles to the sixth order multipole (tetrahexacontapole).

Separating multipole into radial and angular distribution parts:

$$\mathcal{H}_{CEF} = 20A_4^0\langle r^4 \rangle \sum_i \left(\frac{x_i^4 + y_i^4 + z_i^4}{r_i^4} - \frac{3}{5} \right) - 224A_6^0\langle r^6 \rangle \sum_i \left(\frac{x_i^6 + y_i^6 + z_i^6}{r_i^6} + \frac{15}{4}\frac{x_i^2y_i^4 + x_i^2z_i^4 + y_i^2x_i^4 + y_i^2z_i^4 + z_i^2x_i^4 + z_i^2y_i^4}{r_i^6} - \frac{15}{14} \right) \quad (1.20)$$

where $\langle r^n \rangle$ is the expectation value of the distance of the 4*f* electrons from the nucleus, and its assumed constant. The angular distribution part, referring to the (….) part in each term, which depends only on angles θ and ϕ of the polar coordinates and are dimensionless can be called multipoles [1.49].

The dimensionless multipole of the nth order in Racha normalization is defined as [1.50, 1.51]:

$$\int |Z(\theta,\phi)|^2 \, sin\theta d\theta d\phi = \frac{4\pi}{2n+1} \tag{1.21}$$

n is the rank of the multipole moments, which are called the monopole ($n = 0$), dipole ($n = 1$), quadrupole ($n = 2$), octupole ($n = 3$), etc.

The dimensionless fourth and sixth order multipole in Racha normalization in the cubic system is expressed as:

$$Z_4^{cube}(\theta,\phi) = \frac{5\sqrt{7}}{4\sqrt{3}}\left(\frac{x_i^4 + y_i^4 + z_i^4}{r_i^4} - \frac{3}{5}\right) \tag{1.22}$$

$$Z_6^{cube}(\theta,\phi) = -\frac{7}{\sqrt{2}}\left(\frac{x_i^6 + y_i^6 + z_i^6}{r_i^6} + \frac{15}{4}\frac{x_i^2y_i^4 + x_i^2z_i^4 + y_i^2x_i^4 + y_i^2z_i^4 + z_i^2x_i^4 + z_i^2y_i^4}{r_i^6} - \frac{15}{14}\right) \tag{1.23}$$

Using these normalized cubic multipoles, the CEF Hamiltonian can be written as:

$$H_{CEF} = \left[\frac{16\sqrt{3}}{\sqrt{7}}A_4^0\langle r^4\rangle \sum_i Z_4^{cube}(\theta_i,\phi_i) + 32\sqrt{2}A_6^0\langle r^6\rangle \sum_i Z_6^{cube}(\theta_i,\phi_i)\right] \tag{1.24}$$

The CEF parameters $A_4^0\langle r^4\rangle$ and $A_6^0\langle r^6\rangle$ do not depend strongly on *R* within the same series of compounds, in RCo$_2$ series $A_4^0\langle r^4\rangle$ is positive and $A_6^0\langle r^6\rangle$ is negative [1.52].

Stevens operators equivalent is expressed as [1.42]:

$$20\sum_i\left\{\frac{x_i^4 + y_i^4 + z_i^4}{r^4} - \frac{3}{5}\right\} \equiv \beta_J(O_4^0 + 5O_4^4) \tag{1.25}$$

and

$$-224\sum_i\left\{\frac{x_i^6 + y_i^6 + z_i^6}{r_i^6} + \frac{15}{4}\frac{x_i^2y_i^4 + x_i^2z_i^4 + y_i^2x_i^4 + y_i^2z_i^4 + z_i^2x_i^4 + z_i^2y_i^4}{r_i^6} - \frac{15}{14}\right\} \equiv \gamma_J(O_6^0 - 21O_6^4) \tag{1.26}$$

β_J and γ_J are Stevens multiplicative factors depending upon L, S and *J* of the $4f^n$ state of *R* and these factors are listed in **table 1.2** for the trivalent rare earths [1.42, 1.43].

Table 1.2 List of Steven's factors α_J, β_J, γ_J and crystal field parameters F(4) and F(6) for the trivalent rare earth ions [1.42, 1.43].

Ions	Ground term	$\alpha_J \times 10^2$	$\beta_J \times 10^4$	$\gamma_J \times 10^6$	F(4)	F(6)
Ce $^{3+}$	$4f^1$ $^2F_{5/2}$	-5.71	63.5	0	60	-
Pr $^{3+}$	$4f^2$ $^3H_4$	-2.10	-7.35	61.0	60	1260
Nd $^{3+}$	$4f^3$ $^4I_{9/2}$	-0.643	-2.91	-38.0	60	2520
Pm $^{3+}$	$4f^4$ $^5I_4$	0.771	4.08	60.8	60	1260
Sm $^{3+}$	$4f^5$ $^6H_{5/2}$	4.13	25.0	0	60	-
Tb $^{3+}$	$4f^8$ $^7F_6$	-1.01	1.22	-1.12	60	7560
Dy $^{3+}$	$4f^9$ $^6H_{15/2}$	-0.635	-0.592	1.03	60	13860
Ho $^{3+}$	$4f^{10}$ $^5J_8$	-0.222	-0.333	-1.30	60	13860
Er $^{3+}$	$4f^{11}$ $^4I_{15/2}$	0.254	0.444	2.07	60	13860
Tm $^{3+}$	$4f^{12}$ $^3H_6$	1.01	1.63	-5.60	60	7560
Yb $^{3+}$	$4f^{13}$ $^2F_{7/2}$	3.17	-17.3	148.0	60	1260

Using these equivalents, the CEF Hamiltonian **equation** (1.20) in terms of Stevens operators can be rewritten as:

$$H_{CEF} = A_4^0 \beta_J \langle r^4 \rangle (O_4^0 + 5O_4^4) + A_6^0 \gamma_J \langle r^6 \rangle (O_6^0 - 21O_6^4) \quad (1.27)$$

$$= B_4^0 (O_4^0 + 5O_4^4) + B_6^0 (O_6^0 - 21O_6^4) \quad (1.28)$$

where: $B_4^4 = 5B_4^0$, $B_6^4 = -21B_6^0$,

$A_4^0 = 8B_4^0/\beta_J$, $A_4^4 = \frac{8}{\sqrt{70}} B_4^4/\beta_J$, $A_6^0 = 16B_6^0/\gamma_J$, $A_6^4 = \frac{16}{3\sqrt{14}} B_6^4/\gamma_J$

and, $B_4 F(4) = Wx$ $B_6 F(6) = W(1 - |x|)$

then,

$$H_{CF} = Wx\left(\frac{O_4^0 + 5O_4^4}{F(4)}\right) + W(1 - |x|)\left(\frac{O_6^0 - 21O_6^4}{F(6)}\right) \quad (1.29)$$

where Wx and $W(1 - |x|)$ are proportional to $A_4^0 \langle r^4 \rangle$ and $A_6^0 \langle r^6 \rangle$ respectively. Since the proportionality coefficients strongly depend upon R element, W, x and B values depend strongly on R element even if their signs change [1.52]. $F(4)$ and $F(6)$ values are listed in **Table 1.2** for the trivalent *R* element.

By comparing **equations** (1.22) and (1.23) with **equations** (1.25) and (1.26) respectively we can obtain the expectation value of the fourth and sixth order multipole moments respectively:

$$\langle \frac{O_4^0 + 5O_4^4}{F(4)} \rangle = \frac{16\sqrt{3}}{\sqrt{7}\beta_J F(4)} \langle \sum_i Z_4^{cube}(\theta_i, \phi_i) \rangle \qquad (1.30)$$

$$\langle \frac{O_6^0 - 21O_6^4}{F(6)} \rangle = \frac{32\sqrt{2}}{\gamma_J F(6)} \langle \sum_i Z_6^{cube}(\theta_i, \phi_i) \rangle \qquad (1.31)$$

Table 1.3. Multiplicative factors of *f* splitting states in the cubic system of fourth and sixth order.

***f* splitting**	f_4^{Cube}	f_6^{Cube}
a_{2u}	$-\frac{2}{11}\sqrt{\frac{7}{3}}$	$\frac{20}{143}\sqrt{2}$
t_{1ux}	$\frac{1}{11}\sqrt{\frac{7}{3}}$	$\frac{25}{429}\sqrt{2}$
t_{2ux}	$-\frac{1}{33}\sqrt{\frac{7}{3}}$	$-\frac{15}{143}\sqrt{2}$

In the cubic system, the multiplicative factors of *f* splliting state are f_4^{Cube} and f_6^{Cube} of the fourth and sixth order respectively, these factors are listed in **Table 1.3**.

The *R* 4f energy levels are split by spin-orbit coupling and further split by a CEF in solids, through which the outer 4*f* charge distributions are deviate from spherical symmetry as a shown in **Fig.1.7**. The experimental and theoretical predictions of 4*f* ground state symmetry and the values of CEF parameters are not straightforward since it is unclear which sites act as effective ligands for *f* sites. CEF parameters of RCo$_2$ have been investigated by analyses of experimental results such as inelastic neutron scattering spectra [1.30], anisotropy in the magnetic susceptibility of single crystals [1.1, 1.2], and specific heat measurement [1.54], which were the standard experimental technique for determining 4*f* ground state symmetry.

Direct measurement of multipole moments will enable quantitative test of interpretations based on various models including CEF. For transition metal systems, estimation of multipole moments by means of X-ray resonant Raman scattering has been demonstrated [1.55]. While, there have been no reports about quantitative estimation of multipole moments of rare earth elements.

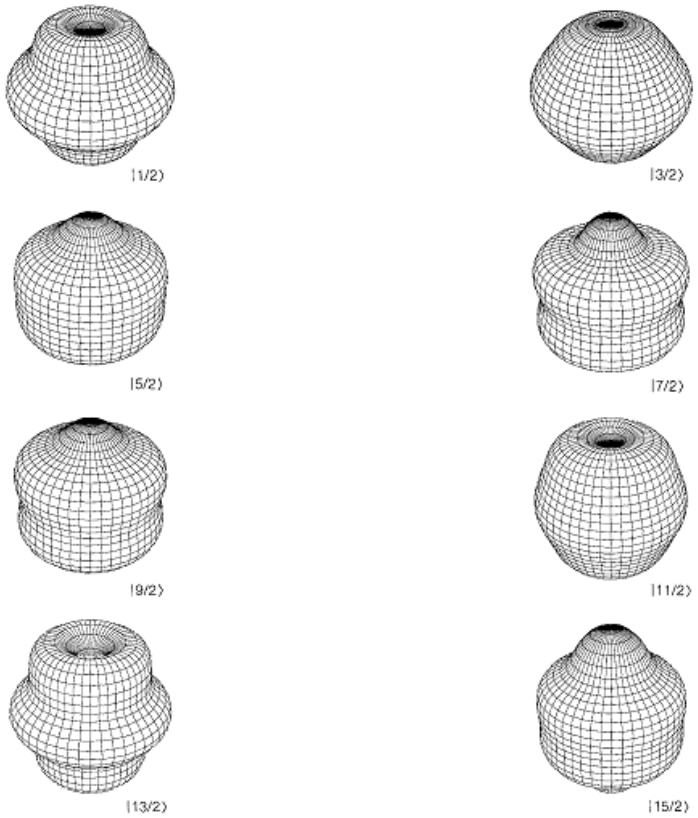

Fig.1.7. the spatial 4f-charge distribution of Er^{3+} ($J = 15/2$) as a free ion [1.53].

Linear dichroism (LD) in 3*d*-to-4*f* soft X-ray absorption spectroscopy (XAS) for single crystals is powerful technique for determining 4*f* orbital symmetry, as reported for $Ce^{3+}(4f^1)$ compounds [1.56-1.60]. However, it is difficult to apply this technique to compounds in cubic symmetry, since there is no anisotropic axis relative to the electric field of the incident light. LD in core-level hard X-ray photoemission spectroscopy (HAXPS) is a novel technique to investigate 4*f* ground state symmetry and interpret the deviation of 4*f* charge distribution from asphericity (multipole), as recently has been reported for heavy-fermion compounds [1.61-1.63]. Especially, polarization dependence LD of the spectrum has been found to be useful in the discussion of the ground state symmetry. Also, in this work we have successfully estimated CEF parameters and the fourth order multipole moment of the rare-earth atom (Er^{+3}) in the cubic crystal electric field using LD in Er $3d_{5/2}$ core-level photoemission spectra (XPS) of cubic $ErCo_2$ which has been measured by means of the bulk sensitive HAXPES.

1.7. Photoemission Spectroscopy (PES)

Since the first experiment performed by Kai Siegbahn and his co-workers in the 1950s (Noble prize in 1981) [1.64, 1.65], PES has grown to be one of the most universal and powerful technique available for investigating the electronic structures of materials [1.66, 1.67]. PES has widespread practical applications in various fields like surface chemistry or material science, and has significantly contributed to the understanding of fundamental principles in solid state physics.

A PES phenomenon is based on the photoelectric effect. The incident photon with energy $h\nu$ will collide with the electrons in solid. The energy required to remove an electron from the surface of solid is called the work function of the solid and denoted by Φ_0. If the incident photon energy is larger than Φ_0, the core or valence electron which absorbs a photon of energy $h\nu$ can be escape from the atom and emit out of the surface as photoelectrons by kinetic energy E_K. In this process, the energy conservation rule is given as:

$$E_k^V = h\nu - \Phi_0 - E_B \tag{1.32}$$

where E_k^V is the kinetic energy of the emitted electron relative to the vacuum level (E_{Vac}), and E_B is the binding energy as a shown in **Fig. 1.8**. In real experiments the kinetic energy E_K is measured from E_F and directly observed instead of E_k^V, then the energy conservation rule is written as:

$$E_K = h\nu - E_B \tag{1.33}$$

Considering the whole electron system, E_B is the energy of the hole produced by the photoemission process including the relaxation energy of the total electron system. E_B is given by the energy difference between the N electron initial state (E_i^N) and the (N-1) electron final state (E_f^{N-1}) as follows:

$$E_B = E_f^{N-1} - E_i^N \tag{1.34}$$

where the surrounding electrons tend to fill the hole to lower the total energy of the system.

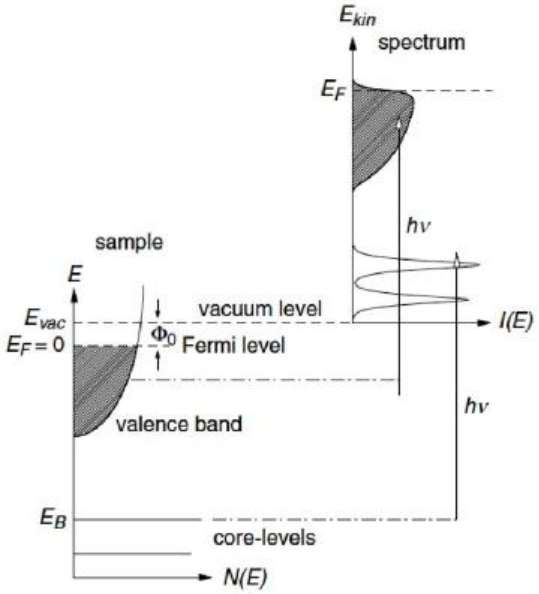

Fig. 1.8. Schematic view of the photoemission process.

At present, various types of soft light excitation sources (from ultraviolet to X-ray) are available under the laboratory conditions. Low-energy photons (20-100 eV), as in ultraviolet photoelectron spectroscopy (UPS), e.g. helium discharge lamps (He I: 21.23 eV, He II: 40.82 eV), medium-energy photons, as in X-ray photoelectron spectroscopy (XPS), e.g. aluminum Al K_α (1486.6 eV) and magnesium Mg K_α (1253.7 eV) are the most commonly X-ray sources. Unfortunately, the applications of these laboratory sources are limited for studying surfaces owing to the rather small probing depth of photoelectrons. In contrast, hard X-rays for excitation results in the emission of electrons having high kinetic energies; this leads to greater probing depths owing to the increased photoelectron mean free path [1.66].

1.8. Synchrotron radiation

Currently, using synchrotron radiation for photoelectrons excitation has become with great important as it enables some measurements that cannot be accomplished using traditional VUV or X-ray sources available in the laboratory [1.66, 1.67]. Several synchrotron facilities have been constructed in different countries such as SPring8 in Japan (Hyogo), BESSY and DORIS III in Germany (Berlin and Hamburg), the Australian Synchrotron in Melbourne, Maxlab in Sweden (Lund), the Advanced Light Source in the USA (Berkeley), the ESRF in Grenoble (France), and the NSRRC in Taiwan (Hsinchu). These are just examples of synchrotron facilities among numerous others suitable for PES experiments. In comparison to the laboratory sources, the key advantage of the synchrotron

facilities is the ease of selection of the photon-energy which can be accomplished by using a monochromator which in turn is provided from a continuous spectrum over a wide energy range. The synchrotron light has also other significant advantages such as variable polarization, high intensity and brightness, possibility of time resolution, and small photon spots. Although of all these advantages of the synchrotron light, using the relatively simple and cheap laboratory sources is still beneficial for various applications [1.66, 1.67].

1.9. Hard X-Ray Photoemission Spectroscopy (HAXPES)

The first high-resolution HAXPES experiments were performed using synchrotron radiation by Lindau *et al.* [1.68] in 1974 who used X-rays from a bending magnet at Stanford synchrotron radiation laboratory to measure the intrinsic linewidth of the Au 4*f* core levels with high energy resolution. HAXPES is a novel technique for studying the electronic structures of materials with applications in a variety of fields such as chemistry, physics, materials science, and industrial applications [1.69]. Recently, several studies using high-resolution HAXPES have been performed. The electronic structures of solids, including valence transitions in bulk systems [1.70, 1.71], multilayer systems [1.72] and the valence bands of thin films [1.73] have been reported. Very recently, 4*f* ground state symmetry has been investigated in heavy-fermion compounds by means of core-level HAXPES [1.61, 1.62], especially focusing on the polarization dependence, e.g. linear dichroism (LD), of the spectrum. In this work we have successfully studied electronic states of $ErCo_2$ using high resolution HAXPES. Moreover, we have estimated the fourth order multipole moment $< Z_4^{cube} >$ of the 4*f* electron charge distribution in the cubic $ErCo_2$ using LD in the Er $3d_{5/2}$ core level XPS.

1.10. Photoelectron Inelastic Mean Free Path

High bulk sensitivity is one of the most important characteristics of HAXPES. This high bulk sensitivity is based on the longer photoelectron mean free path owing to the longer probing depth of the photoelectrons than those at soft X-ray and/or vacuum ultraviolet (VUV) excitations, as a shown in **Fig. 1.9**. The photoelectron inelastic mean free path as a function of kinetic energy in solids exhibits a minimum value at kinetic energies of 20-100 eV [1.66, 1.74-1.76] corresponding to VUV excitations, where the sample has surface sensitivity because a possible bulk sensitivity starts after several hundred eV and then more bulk sensitive can be

observed at higher excitation energy. The longer probing depth makes the measurement insensitive to the surface contamination.

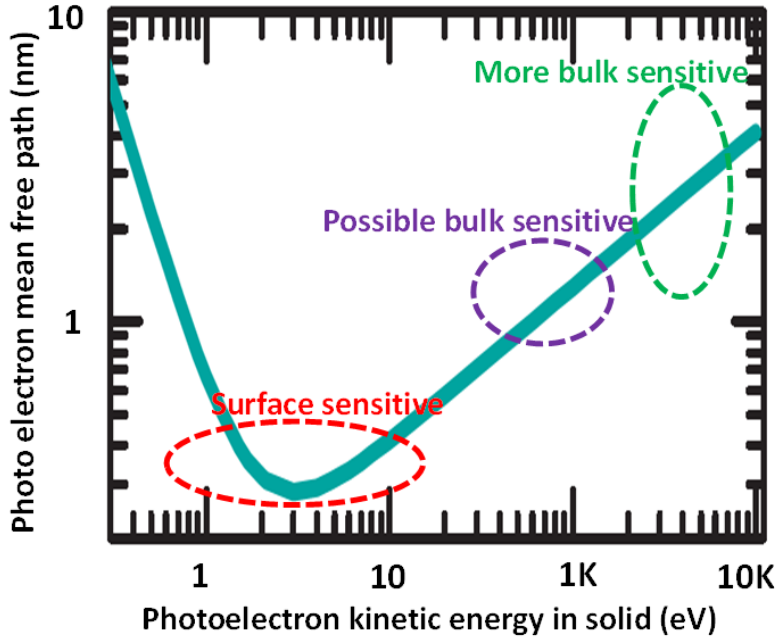

Fig. 1.9. Schematically drawn photoelectron mean free path as a function of its kinetic energy in solids, on the basis of many literatures [1.66, 1.74-1.76].

1.11. Photoionization Cross Section

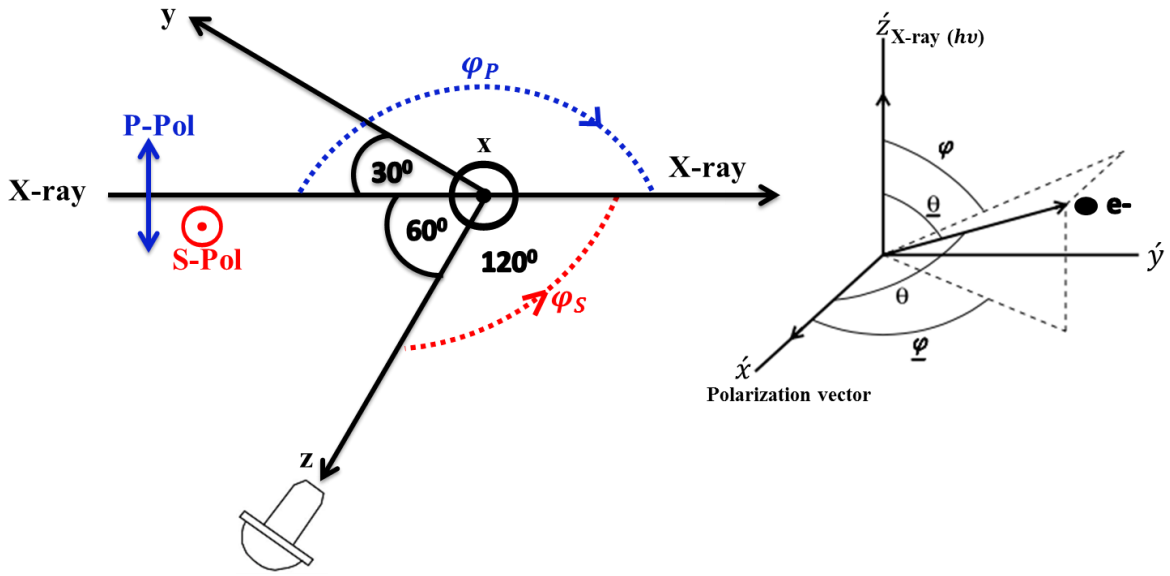

Fig. 1.10. Schematically drawn of the experimental geometry for HAXPES measurements at BL19LXU of SPring8.

Photoionization cross-section is defined as the probability of a photon of a given energy to be absorbed by an atom to excite the photoelectrons. The photoionization cross-section decays rapidly in the HAXPES regime with increasing photon energy. This decay makes strong orbital dependence more pronounced, so photoionization cross-section have been considered in HAXPES analysis. The angular dependence for the differential photoionization cross section in the case of linearly-polarized light is written as [1.77]:

$$\frac{d\sigma}{d\Omega}(\theta,\varphi) = \frac{\sigma}{4\pi}\left[1 + \left(\beta + \Delta\beta_{lp}\right)P_2(cos\theta) + (\gamma cos^2\theta + \delta)sin\theta cos\varphi + \eta P_2(cos\theta)cos2\varphi + \mu cos2\varphi + \xi(1 + cos2\varphi)P_4(cos\theta)\right] \quad (1.35)$$

where σ is the subshell photoionization cross section, P_2 is the second order Legendre polynomial, as a shown in **Fig. 1.10**, θ is the angle between the photoelectron direction (z) and the photon polarization vector (s-pol or p-pol), φ is the angle between the photon momentum vector (X-ray) and the plane passing through the direction of the photoelectron and the photon polarization vector. The first two summands in **equation** (1.35) represents a dipole angular distribution parameters, the third summand gives the non-dipolar parameters, while the last three summands show the photoelectron angular distribution effect [1.77].

Fig. 1.10 demonstrates a schematically draw of the experimental geometry for HAXPES measurements at BL19LXU of SPring8, when the HAXPES used with a linearly polarized excitation, in this case (θ =90^0 and φ =120^0) for vertical polarization configuration (s-pol) and (θ =30^0 and φ =180^0) for horizontal polarization configuration (p-pol).

The differential photoionization cross section in the case of vertical polarization is written as:

$$\left[\frac{d\sigma}{d\Omega}(\theta,\varphi)\right]^{vert} = \frac{\sigma}{4\pi}\left[1 - \frac{1}{2}\left(\beta + \Delta\beta_{lp}\right) - \frac{1}{2}\delta + \frac{1}{4}\eta - \frac{1}{2}\mu + \frac{3}{16}\xi\right] \quad (1.36)$$

and in the case of horizontal polarization is given by:

$$\left[\frac{d\sigma}{d\Omega}(\theta,\varphi)\right]^{hori} = \frac{\sigma}{4\pi}\left[1 + \frac{5}{8}\left(\beta + \Delta\beta_{lp}\right) - \frac{3}{8}\gamma - \frac{1}{2}\delta + \frac{5}{8}\eta + \mu + \frac{3}{64}\xi\right] \quad (1.37)$$

HAXPES has unique properties besides the high bulk sensitivity in contrast to the soft X-ray as following: (a) the comparison of the photoionization cross sections for the *s* and *p* electronic states per electrons with those for the *d* and *f* electronic states, and (b) strong orbital dependence of the photoelectron angular distribution with respect to the angle between the

two directions of photoelectron detection and the light polarization (electric field vector) when a linearly polarized light is used as excitation light source [1.77-1.79]. Moreover, the calculations on the basis of the photoelectron angular distribution parameters (**Fig.1.10)** predict that the photoelectron intensity for the *s* and i*p* (i>4) electronic state is strongly suppressed for the s-polarization configuration (s-pol), where the polarization vector (electric field) of the incident light is perpendicular to the plane made of the photoelectron detection direction and the incident light direction as illustrated in **Fig. 1.10** compared with the p-polarization configuration (p-pol), where the polarization vector is within the plane made of the photoelectron detection direction and the incident light direction. While the angular dependence of photoelectron intensity is relatively weak for the d and f states, and the d and f spectral weights are not suppressed very much even in the s-pol as demonstrated in **Fig 1.11**. The HAXPES with a linearly polarized excitation at p-pol configuration is rather sensitive to the *s* and i*p* electronic states, while that at s-pol configuration is highly sensitive to the *d* and *f* electronic states. Therefore, the extraction of the contributions of *s* and i*p* states as well as that for the *d* and *f* states in the bulk valence band of solids becomes feasible by the linear polarization-dependent HAXPES [1.80, 1.81] and photoionization cross-section play a vital role in the analysis of HAXPES data. Also, in this work we have successfully observed polarization dependent in $ErCo_2$ valence band HAXPES spectra and we have elucidated the crucial role of photoionization cross section to interpret the HAXPES spectra.

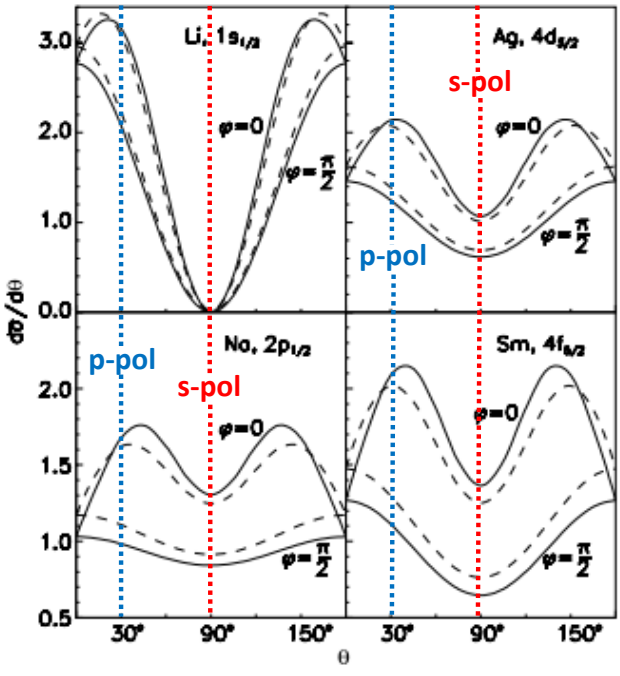

Fig. 1.11. Photoelectron angular dependence using linearly polarized light at photoelectron energy 10 keV [1.77].

1.12. Aim of the Present work

The aim of the present work is studying electronic states of first order ferrimagnetic single crystal $ErCo_2$ experimentally and theoretically; experimentally by using linear polarized hard X-ray photoemission spectroscopy (HAXPES) and theoretically by some calculating programs like Akai KKR and XTLS. Most features of $ErCo_2$ electronic structure (valence band HAXPES) was described well by studying $ErCo_2$ band structure calculation using Akai KKR. Furthermore, the theoretical analyses reproduced well the experimental temperature and the polarization dependent $ErCo_2$ valence band HAXPES. Linear dichroism (LD) in Er $3d_{5/2}$ core-level photoemission spectra (XPS) of cubic $ErCo_2$ has been investigated by means of bulk sensitive hard X-ray photoemission. Also, the theoretical calculations using XTLS program reproduced the observed LD. Moreover, the ground states and the fourth order multipole moment of Er^{3+} 4*f* electrons in the cubic crystal electric field (CEF) was quantified using LD in Er $3d_{5/2}$ XPS. Furthermore, $ErCo_2$ crystal axes were identified by the Laue XRD spectroscopy.

1.13. Thesis outlines

To achieve the above objectives, the present thesis is organized in six chapters as follows:

Chapter 1 is entitled "Introduction" and provides a brief description about several topics related with my study such as rare-earth (*R*) transition-metal (T) Laves phase RT_2 intermetallic compounds, RCo_2 crystal structure and their physical properties, the crystal electric field (CEF) Hamiltonian acting on 4*f* electrons in the cubic system, multipole moment of the rare-earth atom in the cubic crystal electric field. Also, other topics were discussed such as description of photoemission spectroscopy (PES) phenomenon, synchrotron radiation, hard X-ray photoemission spectroscopy (HAXPES) and its unique properties than soft X-ray and/or vacuum ultraviolet (VUV) excitations as high bulk sensitivity, and comparison of the photoionization cross sections for the *s* and *p* electronic states per electrons with those for the *d* and *f* electronic states and strong orbital dependence. This chapter also presents the objectives of the thesis and the contents of its chapters.

Chapter 2 with the title "Experimental Set-up and the Measuring Technique" and introduces details about the descriptions of $ErCo_2$ (sample) crystal growth, sample cutting and its preparation before photoemission experiment, beamline 19LXU setup and double crystal

phase retarder, low temperature two-axis manipulator, Co-axial monitoring system with long-working-distance microscope and hemispherical photoelectron analyzer (HSA). This chapter also describes the experimental techniques leading to the results obtained in this study.

Chapter 3 has the title "Method of Analysis" and describes the methodology of (a) band structure calculations in the disordered and ordered magnetic state using KKR-CPA-LSDA method and (b) the calculation of polarization dependent 3*d* XPS spectra and multipole moments in the ground and excited states using XTLS program.

Chapter 4 will be introduced with the title "Electronic Structure of the Laves Phase Compound $ErCo_2$ Studied by Polarization Dependent Hard X-Ray Photoemission Spectroscopy". It presents the band structure calculations in both structures of $ErCo_2$, the temperature and polarization dependent $ErCo_2$ valence band HAXPES spectra in the cubic symmetry, and the crucial role of the photoionization cross section to interpret the HAXPES spectra of $ErCo_2$.

Chapter 5 will discuss "Rare-earth Fourth Order Multipole Moment in Cubic $ErCo_2$ Probed by Linear Dichroism in Core-Level Photoemission". It explains $ErCo_2$ core levels XPS spectra, the experimental and simulated polarization dependent Er $3d_{5/2}$ XPS and their LDs in $ErCo_2$ at two different orientations, the ground state symmetry and fourth order multipole moment of Er 4*f* electrons in the cubic crystal electric field can be quantify using LD in Er $3d_{5/2}$ XPS, and the crucial role of the fourth order moment to interpret LD temperature dependent data.

Finally, **Chapter 6** is entitled "Conclusions and Suggestions for Future Work" and reports the main conclusions that can be drawn from the thesis as a whole and summarizes the proposed future research topics related to the thesis work.

1.14. References

[1.1] H. Kirchmayr and C. Poldy, Handbook on the Physics and Chemistry of Rare Earths, ed. K. A. Gschneidner, Jr. , and L. Eyring (North-Holland, Amsterdam, 1979) Vol. 2, p. 151.

[1.2] K. H. J. Buschow, in Ferromagnetic Materials, ed. E. P. Wohlfarth (North-Holland, Amsterdam, 1980) Vol. 1, p. 297.

[1.3] J. J. M. Franse and R. J. Radwanski, Handbook of Magnetic Materials, ed. K. H. J. Buschow (Elsevier, Amsterdam, 1993) Vol. 7, p. 307 .

[1.4] E. Gratz and A. S. Markosyan, Physical properties of RCo_2 Laves phase, J. Phys. Condens. Matter, Vol. 13, p. R385 (2001). DOI: 10.1088/0953-8984/13/23/202.

[1.5] M. Cyrot and M. Lavagna, Density of states and magnetic properties of the rare-earth compounds RFe_2, RCo_2 and RNi_2, Journal de Physique,Vol. 40, P. 763 (1979).

DOI: 10.1051/jphys:01979004008076300.

[1.6] R. M. Moon, W. C. Koehler and J. Farrell, Magnetic structure of rare-earth-cobalt (RCo_2) intermetallic compounds, J. Appl. Phys. 36 (1965) 978. DOI: 10.1063/1.1714286.

[1.7] A. Iandelli, A. Palenzona, H. Kirchmayr and C. Poldy, Handbook on the Physics and Chemistry of Rare Earths, ed. K. A. Gschneidner, Jr. , and L. Eyring (North-Holland, Amsterdam, 1979) Vol. 2, Ch. 13, p. 1.

[1.8] E. Gratz and A.S. Markosyan, Physical properties of RCo_2 Laves phase, J. Phys. Condens. Matter,Vol. 13, p. R385 (2001). DOI: 10.1088/0953-8984/13/23/202.

[1.9] D. P. Kozlenko, E. Burzo, P. Vlaic, S.E. Kichanov, A.V. Rutkauskas and B.N. Savenko, Sequential cobalt magnetization collapse in $ErCo_2$: beyond the limits of itinerant electron metamagnetism, Sci. Rep. nature, Vol. 5, p. 8620 (2015). DOI: 10.1038/srep08620.

[1.10] A. S. Markosyan, Distortion of the crystal structure and magnetostriction in the compounds RCo_2 (R= Y, Dy, Ho, Er), J. Sov. Phys. Solid state, Vol. 23, p.965 (1981).

[1.11] A. V. Andreev, A. V. Deryagin, S. M. Zadvorkin, V. N. Moskalev and E. V. Sintsyn, Influence of the 3d-metal on the magnetic properties of quasibinary rare-earth intermetalics $Er(Fe_{1-x}Co_x)_2$, Phys. Met. Metallogr., Vol. 59, p. 57 (1985).

[1.12] A. V. Andreev, In: Handbook of Magnetic Materials, ed. K. H. J. Buschow (Elsevier, Amsterdam, 1995) Vol. 8, Chap. 2, p. 59.

[1.13] Z. W. Ouyang, F. W. Wang, Q. Hang, W. F. Liu, G. Y. Liu, J. W. Lynn, J. K. Liang and G. H. Rao, Temperature dependent neutron powder diffraction study of the Laves phase compound $TbCo_2$, J. Alloys Compd. Vol. 390, p. 21 (2005).

DOI: 10.1016/j.jallcom.2004.08.028.

[1.14] E. Burzo, P. Vlaic, D. P. Kozlenko, S. E. Kichanov, N. T. Dang, E. V. Lukin and B. N. Savenko, Magnetic properties of $TbCo_2$ compound at high pressures, J. Alloys Compd. Vol. 551, p. 702 (2013). DOI: 10.1016/j.jallcom.2012.10.178.

[1.15] J. W. Ross and J. Crangle, Magnetization of cubic Laves phase compounds of rare earths with cobal, Phys. Rev., Vol. 133, p. A509 (1964).

[1.16] E. Burzo, A. Chelkovski and H. R. Kirchmayr, Compounds of rare-earth elements and 3d elements, Landolt Börnstein Handbook,Vol. 19d2, Springer Verlag, 1990.

[1.17] T. Goto , T. Sakakibara, K. Murata, H. Komatsu and K. Fukamichi, Itinerant electron metamagnetism in YCo_2 and $LuCo_2$, J. Magn. Magn. Mater, Vol. 90-91, p. 700 (1990). DOI: 10.1016/S0304-8853(10)80256-2.

[1.18] Y. Hirayama, T. Nakagawa and T. A. Yamamoto, Curie temperatures and modified de Gennes factors of rare earth nitrides, Solid State Commun., Vol. 151, p. 1602 (2011).

DOI: 10.1016/j.ssc.2011.07.021.

[1.19] E. Burzo, L. Chioncel, R. Tetean and O. Isnard, On the R 5d band polarization in rare-earth-transition metal compounds, J. Phys.: Condens. Matter, Vol. 23, p. 026001 (2011).

DOI: 10.1088/0953-8984/23/2/026001.

[1.20] J. Campbell, Indirect exchange for rare earths in metals, J. Phys. F: Met. Phys. Vol. 2, p. L47 (1972). DOI: 10.1088/0305-4608/2/3/004.

[1.21] M. A. Laguna-Macro, J. Chaboy , C. Piquer, H. Maruyama, N. Ishimatsu, N. Kawamura, M. Takagaki and M. Suzuki, Revealing Fe magnetism in lanthanide-iron intermetallic compounds by tuning the rare-earth $L_{2,3}$-edge x-ray absorption edges, Phys. Rev. B, Vol. 72, p. 052412 (2005) 052412. DOI: 10.1103/PhysRevB.72.052412.

[1.22] D. Bloch, D. M. Edwards, M. Shimizu and J. Voiron, First order transitions in ACo_2 compounds, J. Phys.: Metal. Phys F, Vol. 5, p. 1217 (1975).

DOI: 10.1088/0305-4608/5/6/022.

[1.23] E. P. Wohlfarth and P. Rhodes, Collective electron metamagnetism, Phil. Magn. Vol. 7, p. 1817 (1962). DOI: 10.1080/14786436208213848.

[1.24] H. Yamada, Electronic structure and magnetic properties of the cubic laves phase transition metal compounds, Physica B, Vol. 149, p. 390 (1988).

DOI: 10.1016/0378-4363(88)90270-7.

[1.25] D. Gignoux, F. Givord and R. Lemaire, Onset of ferromagnetism and spin fluctuations in rare earth (or actinide)-3d compounds, J. Less-Common Met. Vol. 94, p. 1 (1983).

[1.26] S. Watanabe, N. Ishimatsu, H. Maruyama, H. Kobayashi, M. Itou, N. Kawamura and Y. Sakurai, Instability of Co spin moment in $ErCo_2$ probed by magnetic Compton scattering under high pressure, J. Phys. Soc. Jpn. Vol. 80, p. 093705 (2001).

DOI: 10.1143/JPSJ.80.093705.

[1.27] H. Yamada and M. Shimizu, Metamagnetic transition of YCo_2, J. Phys. F: Met. Phys. Vol. 15, p. L175 (2001).

[1.28] H. Yamada, J. Inoue and M. Shimizu, Electronic structure and magnetic properties of the cubic Laves phase compounds ACo_2 (A=Sc, Ti, Zr, Lu and Hf) and $ScNi_2$, J. Phys F: Met Phys, Vol. 15, p. 169 (1985).

[1.29] G. Petrich and R. L. Mössbauer, Phys. Lett. A, Vol. 26, p. 403 (1968).

[1.30] N. C. Koon and J. J. Rhyne, Ground state spin dynamics of $ErCo_2$, Phys. Rev. B, Vol. 23, p. 207 (1981). DOI: 10.1103/PhysRevB.23.207.

[1.31] V. V. Aleksandryan, R. Z. Levitin, A. S. Markosyan, V. V. Snegirev and A. D. Shchurova, Properties of isotropic and anisotropic magnetoelastic interactions of intermetallic RCo_2 compounds,Sov. Phys. JETP, Vol. 65, p. 502 (1987).

[1.32] H.-G. Purwins and A Leson, Adv. Phys. Vol. 39, p. 309 (1990).

[1.33] N. Ishimatsu, S. Miyamoto, H. Maruyama, J. Chaboy, M. A. Laguna-Marco and N. Kawamura, Experimental evidence of pressure-induced suppression of the cobalt magnetic moment in $ErCo_2$, Phys. Rev. B, Vol. 75, p. 180402(R)(2007).

DOI: 10.1103/PhysRevB.75.180402

[1.34] M. S. Anikin, E. N. Tarasov, N. V. Kudrevatykh, M. A. Semkin, A. S. Volegov, A. A. Inishev and A. V. Zinin, Features of magnetocaloric effect in $Er(Co\text{-}Fe)_2$ Laves phases, in IV

Sino-Russian ASRTU Symposium on Advanced Materials and Processing Technology, KnE Materials Science, Vol. 2016, p. 5 (2016). DOI: 10.18502/kms.v1i1.554.

[1.35] X. B. Liu and Z. Altounian, Magnetogaloric effect in Co-rich $Er(Co_{1-x}Fe_x)_2$ Laves phase, J. Appl. Phys. Vol. 103, p. 07B304 (2008). DOI: 10.1036/1.2829758.

[1.36] V. V. Aleksandryan, N. V. Baranov, A. I. Kozlov and A. S. Markosyan, Band metamagnetism of the d-subsystem of the $ErCo_2$ single crystal: investigation of magnetic and electrical properties, Phys. Met. Metall., Vol. 66, p. 50 (1988).

[1.37] A. Pirogov, A. Podlesnyak, T. Strässle, A. Mirmelstein, A. Teplykh, D. Morozov and A. Yermakov, Neutron-diffraction investigation of the metamagnetic transition in $ErCo_2$, Appl. Phys. A, Vol. 74, p. s598 (2002). DOI: 10.1007/s003390201617.

[1.38] O. Syshchenko, T. Fujita, V. Sechovśky, M. Diviš and H. Fujii, J. Alloys Compd., Magnetism in $HoCo_2$ and $ErCo_2$ under high pressure, Vol. 317–318, p. 438 (2001). DOI: 10.1016/S0925-8388(00)01365-7.

[1.39] H. Kirchmayr and C. Poldy, Handbook on the Physics and Chemistry of Rare Earths, ed. K. A. Gschneidner, Jr. , and L. Eyring (North-Holland, Amsterdam, 1979) Vol. 2,Chap. 17, p. 295.

[1.40] K. H. J. Buschow and K. R. De Boer, Physics of magnetism and magnetic materials, Chap. 5, 2004.

[1.41] K. W. H. Stevens, Matrix elements and operator equivalents connected with the magnetic properties of rare earth ions, Proc. Phys. Soc. Sect. A, Vol. 65, p. 209 (1952). DOI: 10.1088/0370-1298/65/3/308.

[1.42] M. T. Hutchings, Hand book of: Point-charge calculations of energy levels of magnetic ions in crystalline electric fields, Solid State Phys., ed. F.Seitz, and D.Turnbull (Academic Press, New York, 1964) Vol. 16, p. 268.

[1.43] K. R. Lea, M. J. M. Leask and W. P. Wolf, The raising of angular momentum degeneracy of f-electron terms by cubic crystal fields, J. Phys. Chem. Solids, Vol. 23, p. 1381 (1962). DOI: 10.1016/0022-3697(62)90192-0 .

[1.44] N. Zettili, Hand book of Quantum Mechanics, ed. J. Wiley and S. Ltd, (Chichester, New York, 2001), Chap. 5, p. 269.

[1.45] J. Jensen and A. Mackintosh, In: Hand book of Rare Earth Magnetism Structures and Excitations, ed. J. Birman, S. F. Edwards, C. H. Llewellyn Smith, M. Rees, (CLARENDON PRESS, OXFORD, 1991), Chap. 1, p. 39.

[1.46] H. Kusunose, Description of multipole in f-electron systems, J. Phys. Soc. Jpn., Vol. 77, p. 064710 (2008). DOI: 10.1143/JPSJ.77.064710.

[1.47] Y. Kuramoto, H. Kusunose and A. Kiss, Multipole orders and fluctuations in strongly correlated electron systems, J. Phys. Soc. Jpn. Vol. 78, p. 072001 (2009).

DOI: 10.1143/JPSJ.78.072001.

[1.48] T. Kaneko and Y. Ohta, Electric and magnetic multipoles and bond orders in excitonic insulators, Phys. Rev. B, Vol. 94, p. 125127 (2016). DOI: 10.1103/PhysRevB.94.125127.

[1.49] H. A. Bethe and Ann. Physik, Vol. 3, p. 133 (1929).

[1.50] J. Sievers, Z. Phys. B-Condensed Matter,Vol. 45, p. 289 (1982).

[1.51] H. Kusunose, J. Phys. Soc. Jpn.Vol. **77**, p. 064710 (2008).

[1.52] H. G. Purwins and A. Leson, Adv. Phys. Vol. 39, p. 309 (1990).

[1.53] U. Walter, Charge distributions of crystal field states, Z. Phys. B, Vol. 62, p. 299 (1986).

[1.54] H. Imai, H. wada, and M. Shiga, Calorimetric study on magnetism of $ErCo_2$, J. Magn. Magn. Mater, Vol. 140-144, p. 835 (1995). DOI: 10.1016/0304-8853(94)01471-X.

[1.55] G. van der Laan, G. Ghiringhelli, A. Tagliaferri, N. B. Brookes and L. Braicovich, Phys. Rev. B, Vol. 69, p. 104427 (2004).

[1.56] T. Willers, B. Fåk, N. Hollmann, P. O. Körner, Z. Hu, A. Tanaka, D. Schmitz, M. Enderle, G. Lapertot, L. H. Tjeng and A. Severing, Crystal-field ground state of the noncentrosymmetric superconductor $CePt_3Si$: A combined polarized soft x-ray absorption and polarized neutron study, Phys. Rev. B, Vol. 80, p. 115106 (2009).
DOI: 10.1103/PhysRevB.80.115106.

[1.57] P. Hansmann, A. Severing, Z. Hu, M. W. Haverkort, C. F. Chang, S. Klein, A. Tanaka, H. H. Hsieh, H.-J. Lin, C. T. Chen, B. Fåk, P. Lejay and L. H. Tjeng, Determining the crystal-

field ground state in rare earth heavy fermion materials using soft-X-ray absorption spectroscopy, Phys. Rev. Lett., Vol. 100, p. 066405 (2008).
DOI: 10.1103/PhysRevLett.100.066405.

[1.58] T. Willers, Z. Hu, N. Hollmann, P. O. Körner, J. Gergner, T. Burnus, H. Fujiwara, A. Tanaka, D. Schmitz, H. H. Hieh, H.-J. Lin, C. T. Chen, E. D. Bauer, J. L. Sarro, E. Goremychkin, M. Koza, L. H. Tjeng and A. Severing, Crystal-field and Kondo-scale investigations of $CeMIn_5$ (M=Co, Ir, and Rh): A combined X-ray absorption and inelastic neutron scattering study, Phys. Rev. B, Vol. 81, p. 195114 (2010).
DOI: 10.1103/PhysRevB.81.195114.

[1.59] T. Willers, D. T. Adroja, B. D. Rainford, Z. Hu, N. Hollmann, P. O. Körner, Y.-Y. Chin, D. Schmitz, H. H. Hieh, H.-J. Lin, C. T. Chen, E. D. Bauer, J. L. Sarro, K. J. McClellan, D. Byler, C. Geibel, F. Steglich, H. Aoki, P. Lejay, A. Tanaka, L. H. Tjeng and A. Severing, Spectroscopic determination of crystal-field levels in $CeRh_2Si_2$ and $CeRu_2Si_2$ and of the $4f^0$ contributions in CeM_2Si_2 (M=Cu, Ru, Rh, Pd, and Au), Phys. Rev. B, Vol. 85, p. 035117 (2012). DOI: 10.1103/PhysRevB.85.035117.

[1.60] K. Chen, F. Strigari, M. Sundermann, S. Agrestini, N. J. Ghimire, S.-Z. Lin, C. D. Batista, E. D. Bauer, J. D. Thompson, E. Otero, A. Tanaka and A. Severing, Exchange field effect in the crystal-field ground state of $CeMAl_4Si_2$, Phys. Rev. B, Vol. 94, p. 115111 (2016).
DOI: 10.1103/PhysRevB.94.115111.

[1.61] T. Mori , S. Kitayama, Y. Kanai, S. Naimen, H. Fujiwara, A. Higashiya, K. Tamasaku, A. Tanaka , K. Terashima, S. Imada , A. Yasui, Y. Saitoh, K. Yamagami, K. Yano, T. Matsumoto, T. Kiss, M. Yabashi, T. Ishikawa, S. Suga, Y. Ōnuki, T. Ebihara and A. Sekiyama, Probing strongly correlated 4f-orbital symmetry of the ground state in Yb compounds by linear dichroism in core-level photoemission, J. Phys. Soc. Jpn.Vol. 83, p. 123702 (2014). DOI: 10.7566/JPSJ.83.123702.

[1.62] Y. Kanai, T. Mori , S. Naimen , K. Yamagami, H. Fujiwara, A. Higashiya, T. Kadono, S. Imada, T. Kiss, A. Tanaka , K. Tamasaku, M. Yabashi, T. Ishikawa, F. Iga and A. Sekiyama, Evidence for Γ_8 ground-state symmetry of cubic YbB_{12} probed by linear dichroism in core-level photoemission, J. Phys. Soc. Jpn., Vol. 84, p. 073705 (2015).
DOI: 10.7566/JPSJ.84.073705.

[1.63] Y. Kanai, T. Mori, S. Naimen, K. Yamagami, S. Kitayama, H. Fujiwara, A. Higashiya, T. Kadono, S. Imada, T. Kiss, A. Tanaka, T. Muro, K. Tamasaku, M. Yabashi, T. Ishikawa, F. Iga, T. Ebihara, F. Honda, Y. Onuki and A. Sekiyama, Linear dichroism in 3d core-level and 4f valence-band photoemission spectra of strongly correlated rare-earth compounds, J. Electron Spectrosc. Relat. Phenom., Vol. 220, p. 61 (2017).
DOI: 10.1016/j.elspec.2016.12.012.

[1.64] K. Siegbahn, Preface to hard X-ray photo electron spectroscopy (HAXPES), Nucl. Instr. and Meth. A, Vol. 54, p. 1 (2005). DOI: 10.1016/j.nima.2005.05.007.

[1.65] K. Siegbahn, C. Nordling, A. Fahlman, R. Nordberg, S.-E. Karlsson and I. Lindgren, ESCA Atomic, Hand book on Molecular and Solid State Structure Studied by Means of Electron Spectroscopy, ed. Almqvist and Wiksells, 1967.

[1.66] M. Cardona, ed. L. Ley, Hand book on Photoemission in Solids I, Topics in Applied Physics, (Springer, Berlin, Heidelberg, New York, 1978) Vol. 26.

[1.67] S. Hufner, Photoelectron Spectroscopy. Principles and Applications, third ed., (Springer, Berlin, Heidelberg, New York, 2003).

[1.68] I. Lindau, P. Pianetta, S. Doniach and W.E. Spicer, Nature, Vol. 250, p. 214 (1974).

[1.69] K. Kobayashi, Nucl. Instr. Meth. Phys. Res. A, Hard X-ray photoemission spectroscopy, Vol. 601, P. 32 (2009). DOI: 10.1016/j.nima.2008.12.188.

[1.70] G. Panaccione, M. Sacchi, P. Torelli, F. Offid, G. Cautero, R. Sergo, A. Fondacaro, C. Henriquet, S. Huotari, G. Monacof and L. Paolasini, J. Electron Spectrosc. Relat. Phenom., Bulk electronic properties of V_2O_3 probed by hard X-ray photoelectron spectroscopy, Vol. 156-158, p. 64 (2007). DOI: 10.1016/j.elspec.2006.11.050.

[1.71] M. Ye, A. Kimura, Y. Miura, M. Shirai, Y. T. Cui, K. Shimada, H. Namatame, M. Taniguchi, S. Ueda, K. Kobayashi, R. Kainuma, T. Shishido, K. Fukushima and T. Kanomata, Phys. Rev. Lett. Vol. 104 (17), P. 176401 (2010).

[1.72] C. Dallera, L. Duo, L. Braicovich, G. Panaccione, G. Paolicelli, B. Cowie and J. Zegenhagen, Appl. Phys. Lett. Vol. 85, p. 4532 (2004).

[1.73] G. H. Fecher, B. Balke, A. Gloskowskii, S. Ouardi, C. Felser, T. Ishikawa, M. Yamamoto, Y. Yamashita, H. Yoshikawa, S. Ueda and K. Kobayashi, Appl. Phys. Lett. Vol. 92, P. 193513 (2008).

[1.74] S. Tanuma, C. J. Powell and D. R. Penn, PROPOSED FORMULA FOR ELECTRON INELASTIC MEAN FREE PATHS BASED ON CALCULATIONS FOR 31 MATERIALS, Surf. Sci., Vol. 192, p. L849 (1987).

[1.75] S. Tanuma, C. J. Powell and D. R. Penn, Surf. Interface Anal.,Vol. 43, p. 689 (2011).

[1.76] S. Suga and A. Sekiyama, Photoelectron Spectroscopy. Bulk and Surface Electronic Structures Springer-Verlag, Heidelberg (2014).

[1.77] M. B. Trzhaskovskaya, V. K. Nukulin, V. I. Nefedov and V. G. Yarzhemsky, Non-dipole second order parameters of the photoelectron angular distribution for elements Z = 1-100 in the photoelectron energy range 1-10 keV, At. Data Nucl. Data Tables, Vol. 92, p. 245 (2006). DOI:10.1016/j.adt. 2013.12.002.

[1.78] M. B. Trzhaskovskaya, V. I. Nefedov and V. G. Yarzhemsky, PHOTOELECTRON ANGULAR DISTRIBUTION PARAMETERS FOR ELEMENTS Z = 1 TO Z = 54 IN THE PHOTOELECTRON ENERGY RANGE 100-5000 eV, At. Data Nucl. Data Tables, Vol. 77, p. 97 (2001). DOI:10.1006/adnd.2000.0849.

[1.79] M. B. Trzhaskovskaya, V. I. Nefedov and V. G. Yarzhemsky, PHOTOELECTRON ANGULAR DISTRIBUTION PARAMETERS FOR ELEMENTS Z = 55 TO Z = 100 IN THE PHOTOELECTRON ENERGY RANGE 100-5000 eV, At. Data Nucl. Data Tables, Vol. 82, p. 257 (2002). DOI:10.1006/adnd.2002.0886.

[1.80] A. Sekiyama, A. Higashiya and S. Imada, Polarization-dependent hard X-ray photoemission spectroscopy of solids, J. Electron Spectrosc. Relat. Phenom., Vol. 190, p. 201 (2013). DOI: 10.1016/j.elspec.2013.08.008.

[1.81] A. Sekiyama, High-energy photoemission spectroscopy for investigating bulk electronic structures of strongly correlated systems, J. Electron Spectrosc. Relat. Phenom., Vol. 208, p. 100 (2016). DOI: 10.1016/j.elspec.2016.02.001.

Chapter 2

Experimental Set up and Measuring Technique

Chapter 2

Experimental Set up and Measuring Technique

2.1. Sample Preparation

2.1.1. $ErCo_2$ Crystal Growth and its characterizations

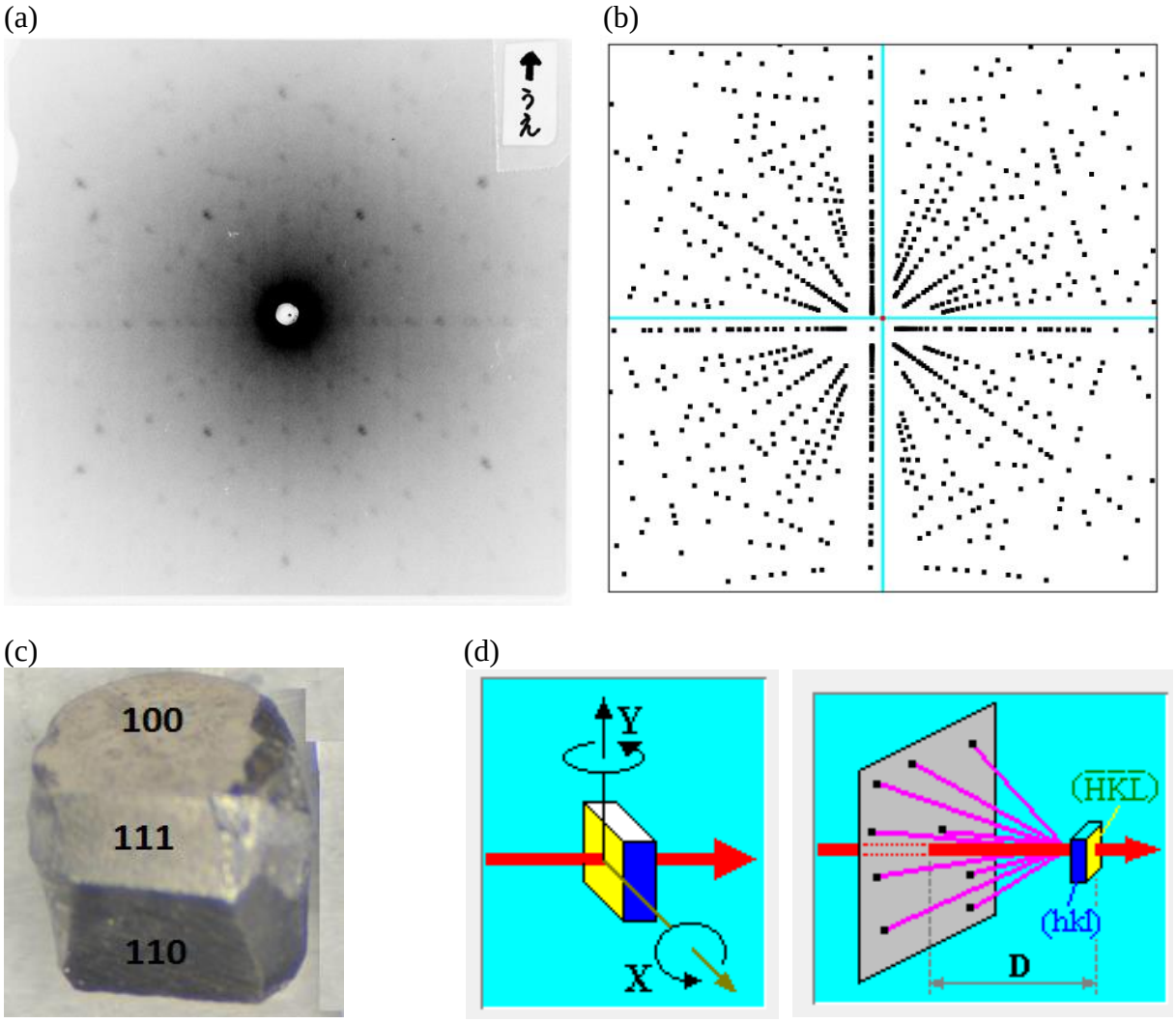

Fig. 2.1. (a) Experimental back-reflection Laue image of $ErCo_2$. (b) Simulted Laue image, ([HKL]~[110]), (and [hkl]~[001]), rotation angle alonge X=1° and alonge Y=-1°. (c) Image of $ErCo_2$ single crystal sample. (d) Refer to the rotation angle alonge X and Y axes and [HKL] and [hkl] planes.

One of the famous crystal growth methods is Czochralski method which allows obtaining single crystals of many intermetallic compounds. Czochralski invented this simple method for crystal growth during his experiments in measuring the crystallization velocity of

metals. The idea of this method was based on pulling of fibers of different metals from their melts [2.1-2.3].

Fig. 2.1c illustrates a single crystal of $ErCo_2$ was grown (by Prof. Andreev) by a modified Czochralski method [2.1-2.3] in a tri-arc furnace on copper water-cooled bottom from 7 g mixture of the pure elements (99.9% Er and 99.99% Co). The pulling of crystal was performed under argon protecting atmosphere using a tungsten rod as a seed and at pulling speed of 10 mm/h. In order to avoid the appearance of phase $ErCo_3$, the initial composition was taken as $ErCo_{1.96}$. The resulting single crystal was cylinder-shaped with a height of 20 mm and a diameter of 4 mm. Back-scattered Laue pattern confirmed the single-crystalline state of the sample (**Fig. 2.1a**). Simulated Laue patterns (**Fig. 2.1b**) performed in order to define the crystal axes. The rotation angle along X and Y axes and [HKL] and [hkl] planes are defined in **Fig. 2.1d.**

Single crystal samples were prepared in order to obtain information about the magnetization mechanism. **Fig. 2.2** shows the characteristics of single crystal $ErCo_2$. **Fig. 2.2a** reveals that although sample dependent, all samples are single crystals. The field dependences of magnetization of the single crystal $ErCo_2$ at different temperatures along [111] and [100] axes are elucidated in **Fig. 2.2b** and **2.2c** respectively. The spontaneous magnetization (M_s) in the magnetically ordered range (2 K to 35 K) hardly changes with temperature and drop rapidly at T_C, the values of M_s along [111] axis is larger than that along [100] axis. The main change in the magnetization is between 35 K and 45 K temperature range (paramagnetic-ferrimagnetic metamgnetic transition). Above T_C the magnetization curves have metamgnetic character and suddenly $ErCo_2$ compound changes from paramagnetic to ferrimagnetic state (first order phase transition) at a certain critical field (H_{cr}). The values of H_{cr} depend strongly on the direction of the applied field (H_{cr} along [111] direction is smaller than that along [100] direction). In the higher fields, the field dependence of magnetization becomes linear. These magnetic properties of the $ErCo_2$ single crystal agree with the previous studies [2.4].

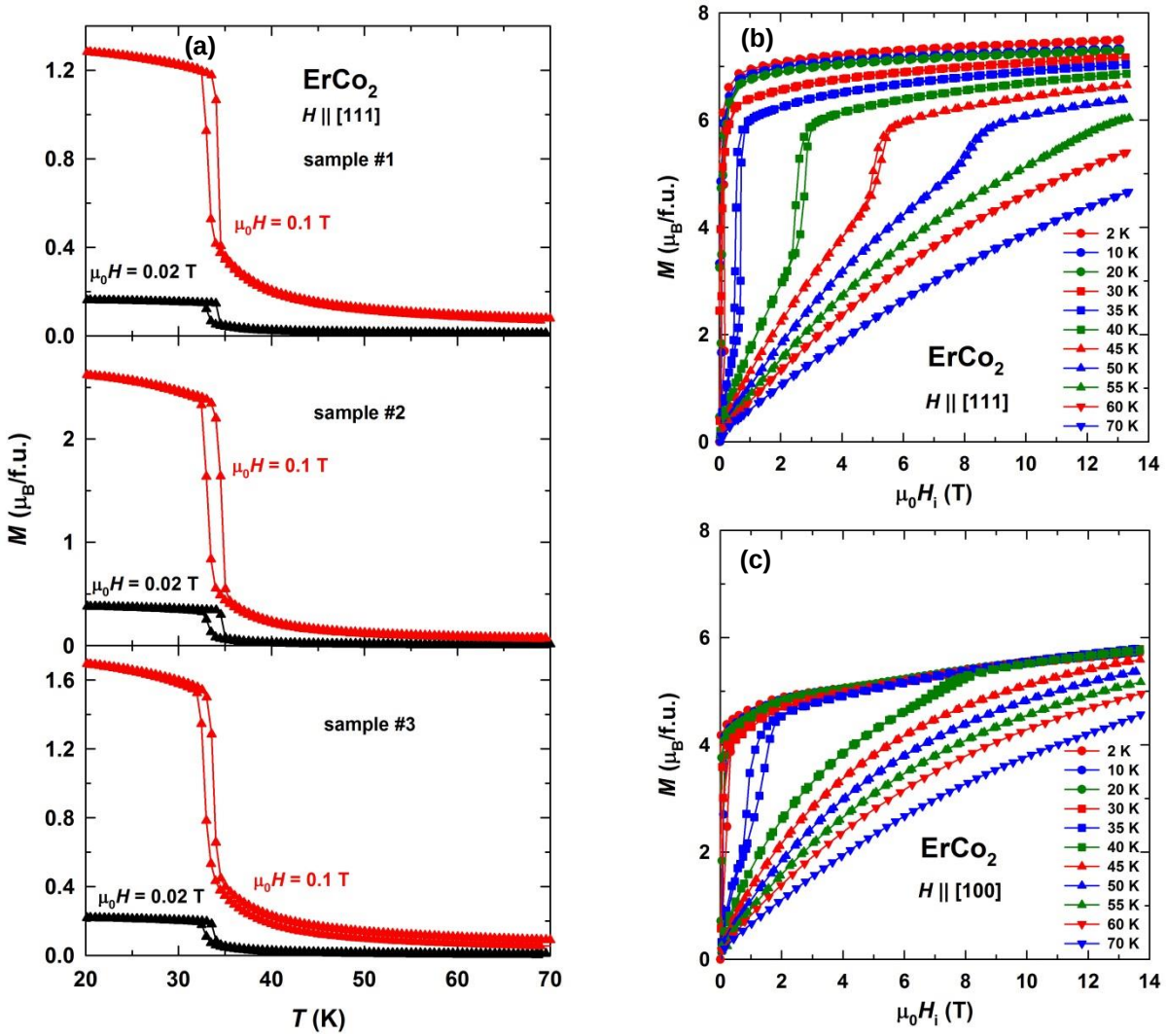

Fig. 2.2. (a) $ErCo_2$ single crystal sample dependent. Magnetization curves of single crystal $ErCo_2$ at different temperatures along (b) [111] direction and (c) [100] direction. (these results supported by Prof. Andreev and his collaborators).

2.1.2. Sample Cutting

The sample has been successfully cut to five parts by using discharge wire with radius 0.2 mm. Three of them represent [100] direction and the other two parts represent [110] direction, as a shown in **Fig. 2.3**. The sample before cutting (**Fig. 2.3a**) was fixed on holder by using insulator glue (torr seal). In order to make the sample conductor, solder is fixed around any side from the sample (**Fig. 2.3b**). The whole sample (**Fig. 2.3c**) was cut to two parts A (**Fig. 2.3d**) and B (**Fig. 2.3e**), where the sample A represents [110] direction and the sample B represents [100] direction. Furthermore, the sample A was cut into two parts A1 (**Fig. 2.3f**) and A2 (**Fig. 2.3g**). In order to obtain flat surface, a small part was cut from both sides of the two parts A1 (**Fig. 2.3h**) and A2 (**Fig. 2.3i**) where the direction of this flat surface

represent [110] direction. The other part of the sample B was also cut into other three parts as a shown in **Fig. 2.3j** and **Fig. 2.3k** and this represents [100] direction.

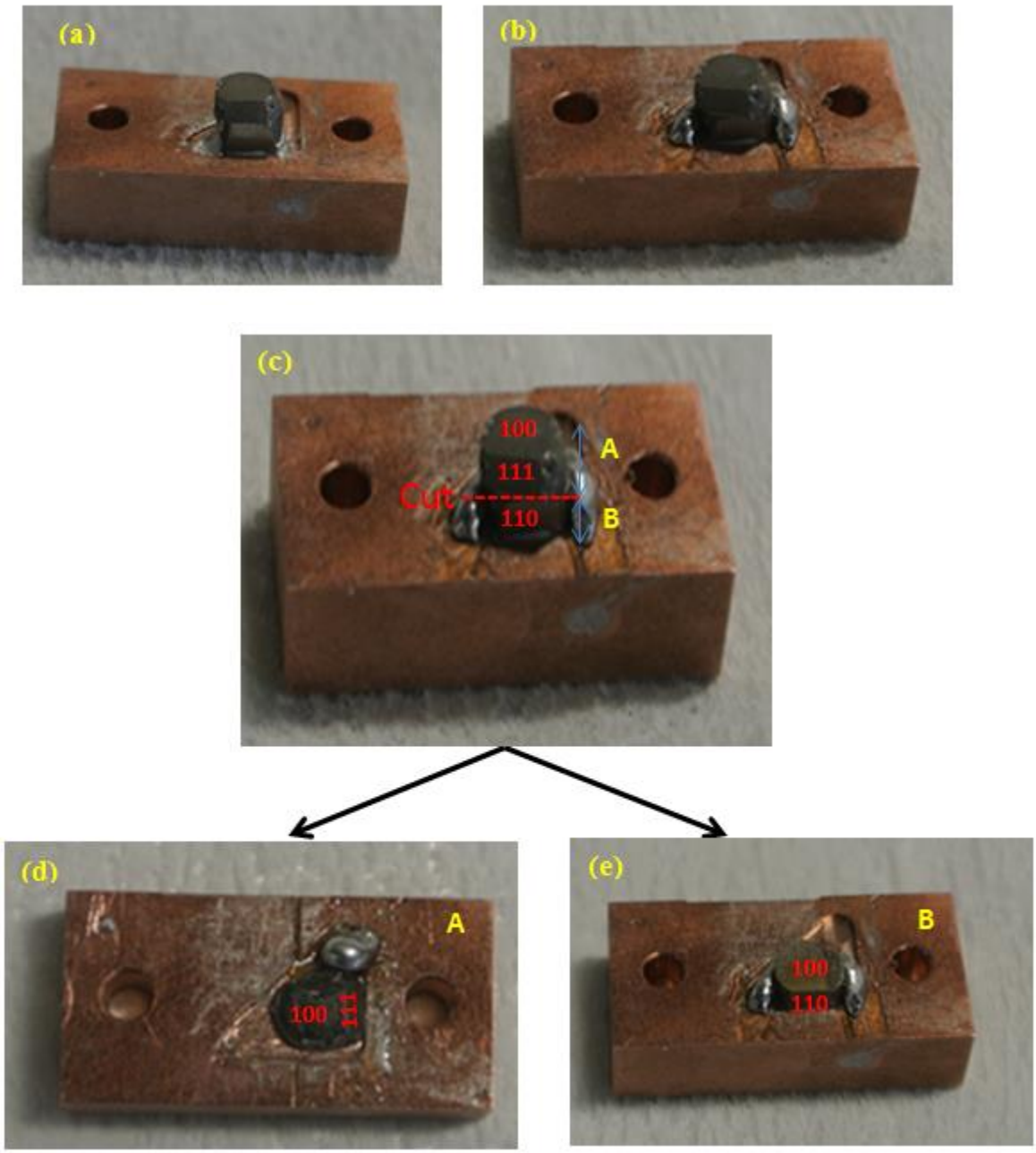

Fig. 2.3. The sample cutting steps (continued to the next page).

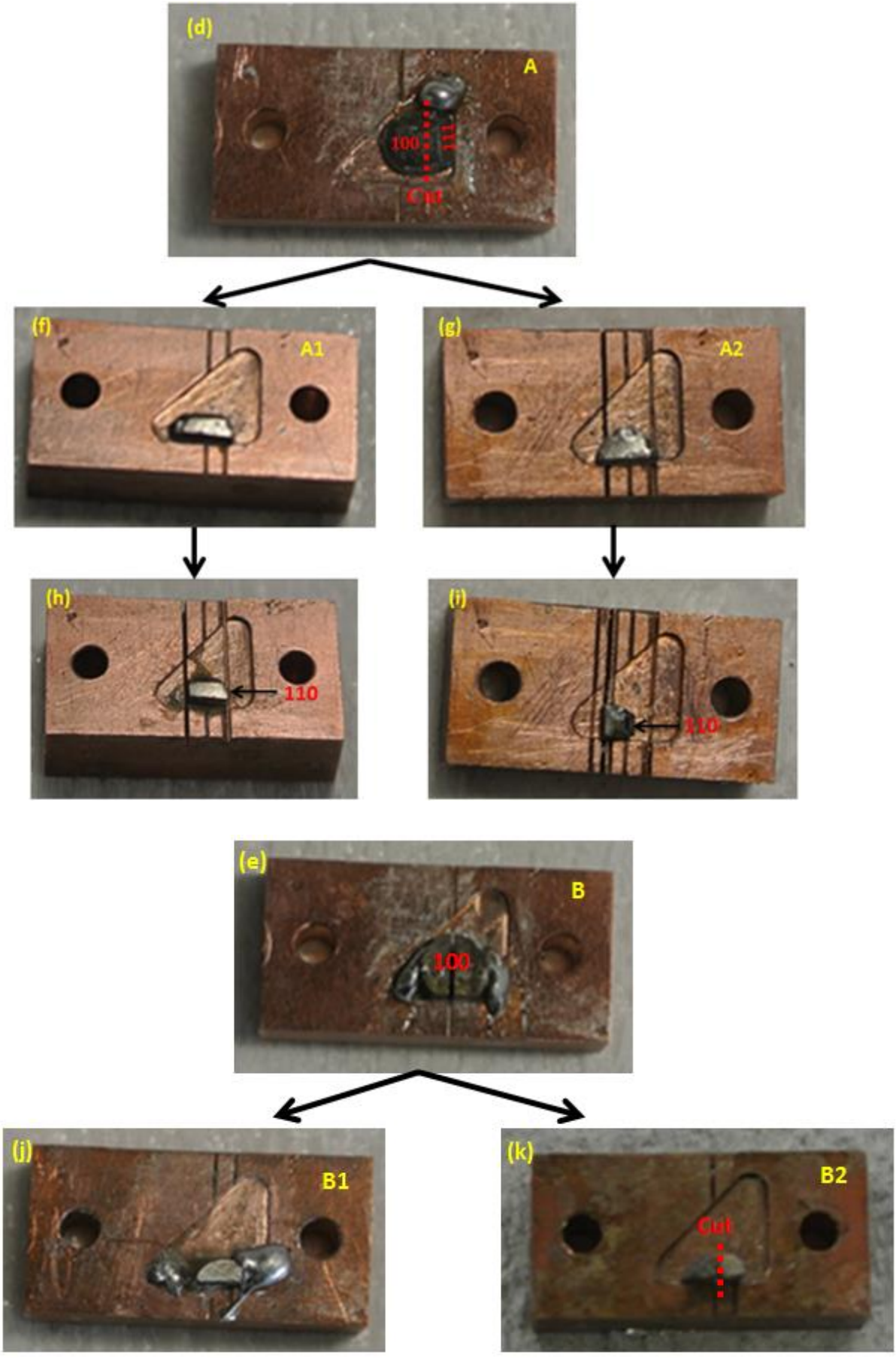

Fig. 2.3. The sample cutting steps (continued from the previous page).

2.1.3. Sample Preparation for Photoemission Experiment

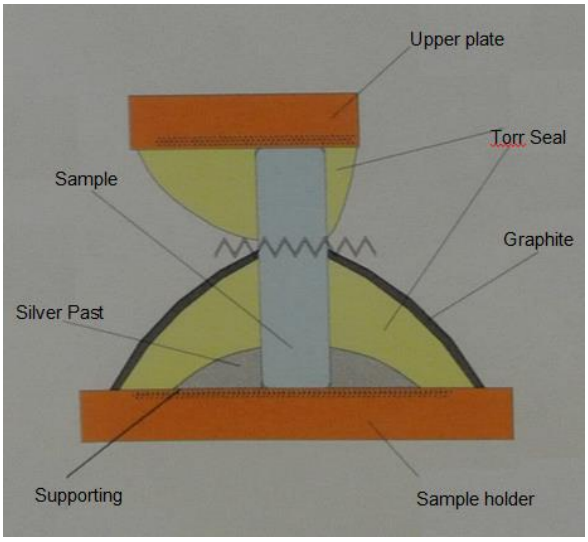

Fig. 2.4. Sample facing view after preparation.

Procedures of the sample preparation before the photoemission experiment:

1. The sample holder was cleaned by using metal polishing (Pikal),
2. A suitable small holder was cleaned and set over the sample holder,
3. Preparing conducting glue (Muromac) by mixing silver glue:liquid glue (200:7) for 10 minutes,
4. Little portion of the conducting glue was put over the small holder then the sample was set over them. All this system was put on a heater at 100 ^{o}C for 30 minute, at the same time the sample resistivity was measured. To eliminate experimental charging, a small amount of a conductive silver paste was placed on the corners of the samples to ensure a conductive path from the surface to the grounded sample holder,
5. The sample conductivity and its pastiness with sample holder were affirmed,
6. For increasing the sample pastiness, we prepared none conducting glue (torr seal) and put little of it around the sample and the holder, then put all system over the heater for 15 minute.
7. Little from graphite was put on torr seal.
8. Small plate was fixed over the sample by torr seal for sample fracture.
9. All system was put over a heater at 100 ^{o}C for 12 hours.
10. Sample resistivity was measured.

Sample facing view after the explained preparation is shown in **Fig. 2.4**.

2.2. Beamline 19LXU Setup and Double Crystal Phase Retarder

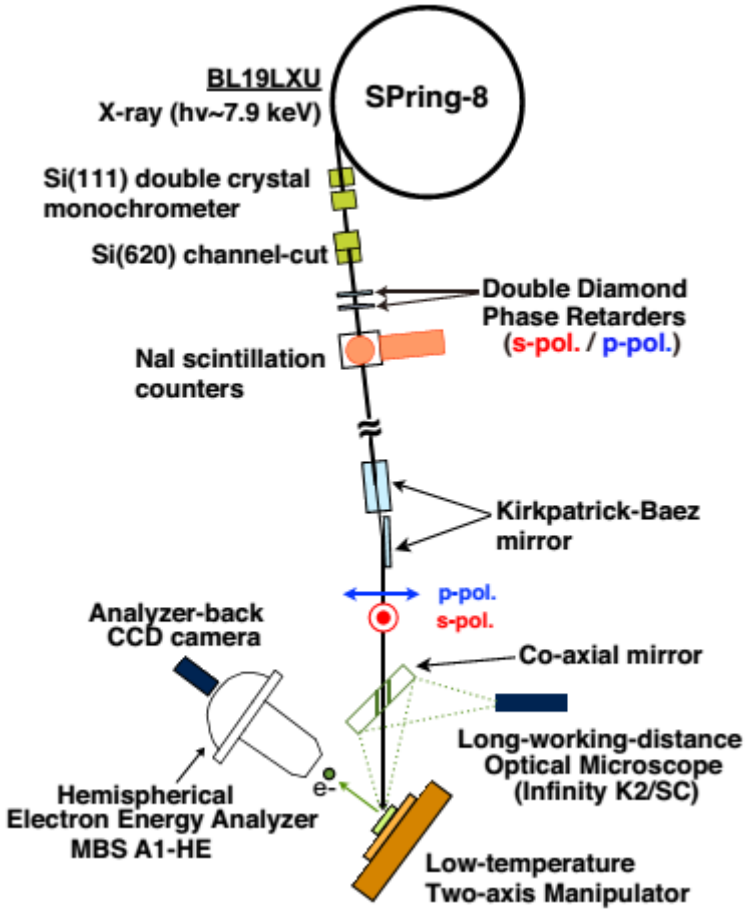

Fig. 2.5. The experimental geometry (top view) for the polarized HAXPES at BL19LXU in Spring-8 [2.9].

The polarization dependent HAXPES measurements using linearly polarized light [2.5-2.7] have been performed at BL19LXU of Spring-8 [2.8] using an MBS A1-HE hemi-spherical photoelectron spectrometer which is inclined at 60^{o} from the incident X-ray beam. **Fig. 2.5** [2.9] (correspond to **Fig. 2.12**) demonstrates a schematic diagram of the typical setting of the beamline optics for the polarized HAXPES. Linearly polarized light is transfer from an in-vacuum 27 m along 780 period undulator [2.10-2.12]. The incident X-ray was set to ≅ 7.9 keV using Si [111] double crystal monochrometer and was further monochromatized using Si [620] channel-cut crystal. Two single-crystalline [100] diamonds were used as a phase retarder placed downstream of the channel cut crystal to switch the linear polarization of the excitation light from the horizontal to the vertical direction [2.13]. The original horizontally polarized light are converted into circular polarization using the first diamond plate (**Fig. 2.6a**), and then transformed to vertical polarization by the second diamond plate (**Fig. 2.6b**).

The thickness of each diamond plate was 0.25 mm, and the transmittance of the X-ray beam after the double diamond phase retarder was about 50%. The degree of the linear polarization P_L was detected by NaI scintillation counters placed downstream of the double diamond phase retarder, and is defined as:

$$P_L = \frac{I_h - I_v}{I_h + I_v} \tag{2.1}$$

where I_h and I_v are intensities of the horizontal and vertical polarized light, respectively.

In our setup, the best P_L value of the polarization switched X-ray after the phase retarder was estimated as -0.96 as illustrated in **Fig. 2.6b**.

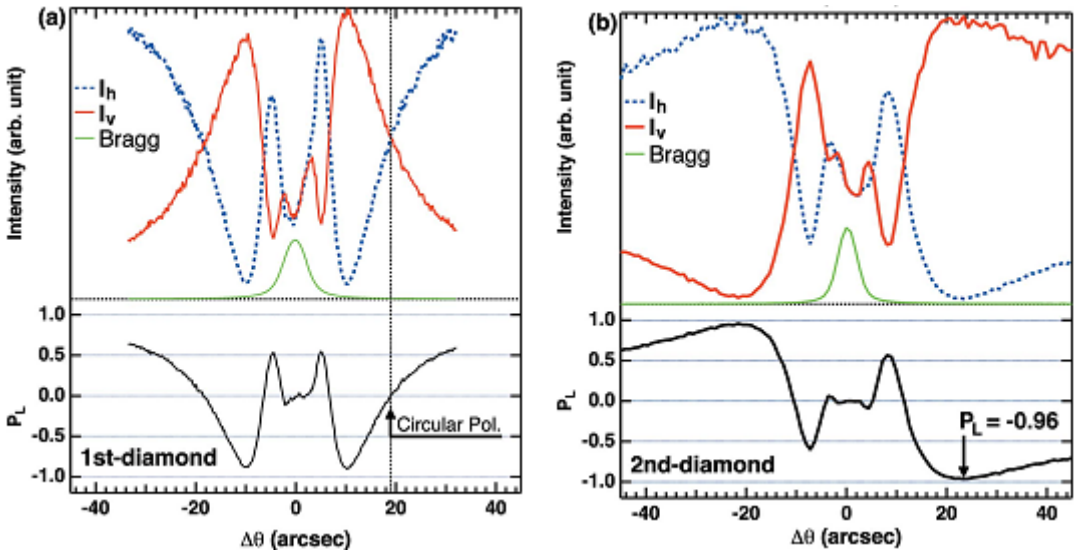

Fig. 2.6. Offset angle dependence of the photon intensities relative to the diamond (220) Bragg reflections for the first (a) and second (b) diamond. The evaluated degree of linear polarization P_L is also plotted at the bottom of (a) and (b).

The excitation light was focused onto the sample by using an ellipsoidal Kirkpatrik-Baez mirror [2.14] within 25 μm ×25 μm (FWHM) (**Fig. 2.5**). The electric field vector of the horizontally (vertically) polarized light excitation is defined as p-polarization (s-polarization). To detect LD accurately in core level and valence band photoemission spectra, the photon flux was optimized so as to set comparable photoelectron count rates between the s-polarization and p-polarization configurations.

2.3. Low Temperature Two-Axis Manipulator

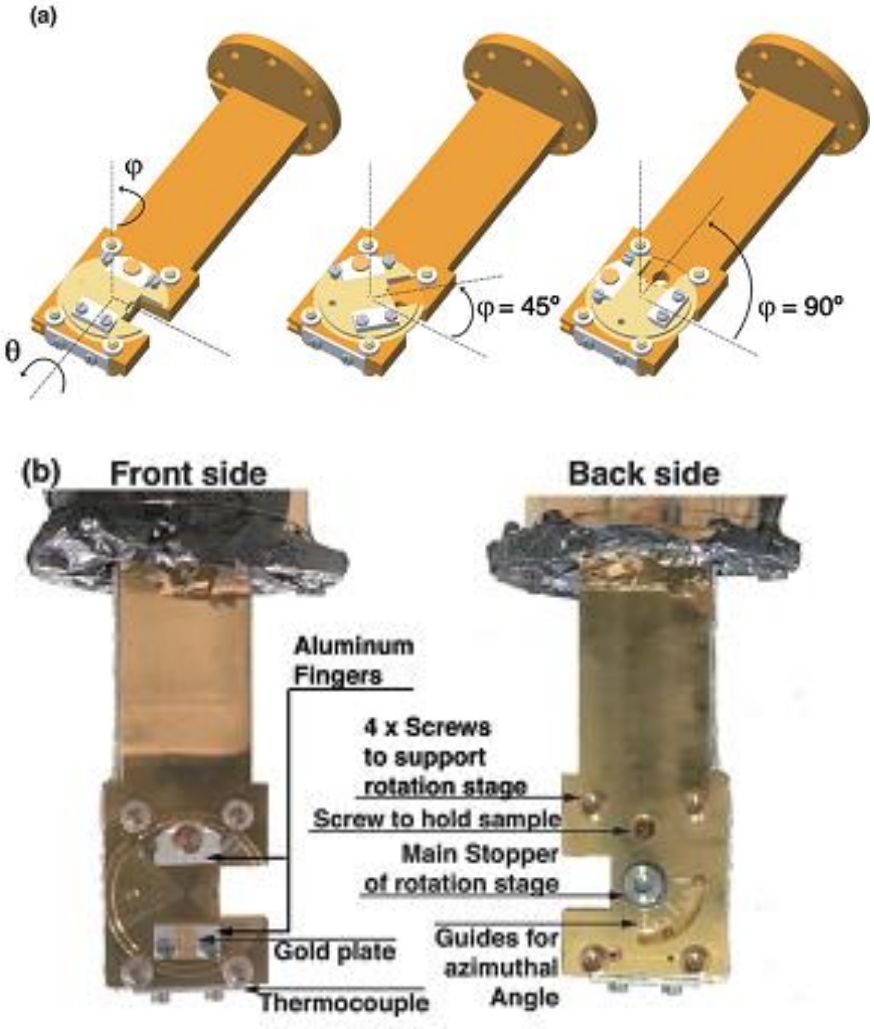

Fig. 2.7. (a) Schematic view of developed low-temperature two-axis manipulator with the definition of azimuthal angle φ and polar angle θ and simulations for the azimuthal rotation with rotation angles of 45^0 (middle) and 90^0 (right). (b) Photographs of the manipulator taken from the front (left) and back (right) [2.8].

The experimental geometry was controlled using a two-axis manipulator [2.9] to easily optimize the detection direction of photoelectrons. **Fig. 2.7a** [2.9] reveals schematic drawings of the manipulator. The body of the manipulator is made from oxygen free copper with gold plating. The rotation feedthrough provides polar rotation θ. The top of the rotation stage (manipulator) is made from Be-Cu and gives the azimuthal rotation φ over a 90^0 range. The bottom of the rotation stage has bowl-shaped to acquire thermal contact, and is tightly fixed by a non-magnetic screw from the back. This screw is loosened during the rotation, but there are four screw support the rotation stage to prevent it from falling during rotation as illustrated in **Fig. 2.7b** [2.9]. Using a closed-cycle He refrigerator (**Fig. 2.13**), enables sample cooling from 300 K to 9 K in 1.5 hour, which gives a good chance to study the electronic

structure of the ground states in many rare earth compounds. While during the azimuthal rotation stage the thermal contact is lost, one can immediately cool down the sample using adjustable sample temperature system (**Fig. 2.18**) after re-tighting the rotation stage. Through the rotation stage, the sample is fixed between two aluminum fingers with a crew to hold the sample using a hexagonal wrench from the back. Also, the same wrench can be used for the manipulator rotation stage. To guide the rotation angle, there are seven indication marks every 15^{o}. A charge coupling device (CCD) camera is mounted on the back of the hemispherical analyzed, in order to monitor the sample and fix the rotation angle with more precisely. The camera image is captured then shown on the computer screen by a program with a function to calculate the rotation angle with accuracy of $\pm 1^{o}$. **Fig. 2.8** reveals the rotation process of the two axis manipulator recorded by CCD camera with magnification of ~3 achieved using a varifocal lens (Tamron: 13VM20100AS). **Fig. 2.8** illustrates the azimuthal rotation of 45^{o} (the middle panel), and the last panel shows further polar rotation at 55^{o}. Recently, the polarized HAXPES for various rare-earth compounds been have studied by selecting the photoelectron detection direction with the two axis manipulator [2.15-2.17].

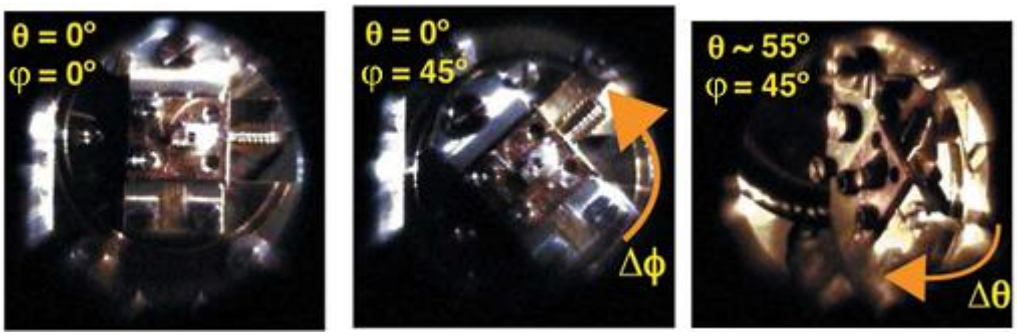

Fig. 2.8. CCD camera image of the manipulator (top).

2.4. Co-Axial Monitoring System with Long-Working-Distance Microscope

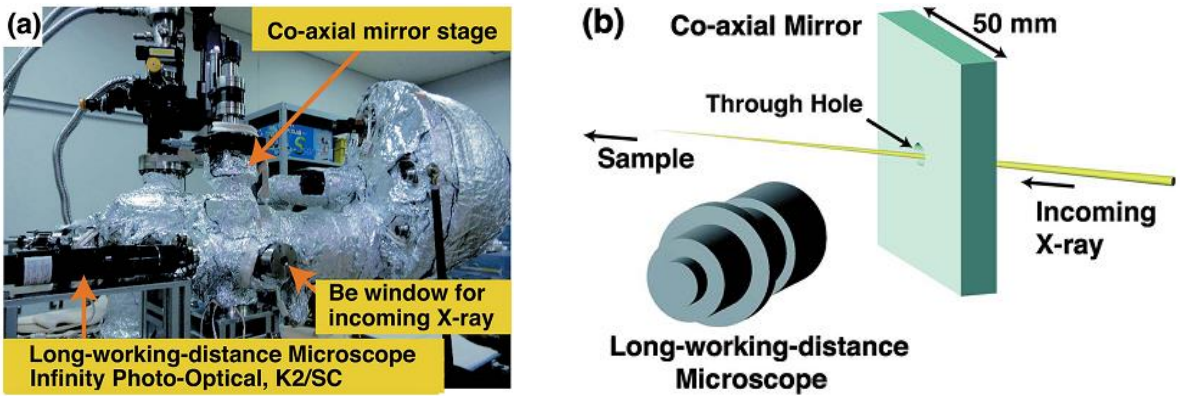

Fig. 2.9. (a) Photograph of the co-axial sample monitoring system combining the long-working-distance microscope with co-axial mirror; (b) schematic view.

Although, the two-axis rotation system is very powerful for optimizing the photoelectrons detection direction, it is difficult sometimes to normalize spectra recorded at different angles. This might be due the surface roughness: the excitation area of X-ray on a rough surface is often not exactly the same when the sample surface is not flat, yielding a variation of the photoemission intensity. So it is better to record the photoemission signal from the same region on the sample surface in the case of a very weak dichroic signal, for the comparison of the spectra before and after any rotation. In order to minimize this problem, a co-axial sample monitoring system (**Fig. 2.9**) combining a long working distance optical microscope (Infinity photo-optical, K2/SC) and an aluminum mirror (50 mm square) having a 5 mm-diameter through-hole for the X-ray beam have been installed as a shown in **Fig. 2.9b**.

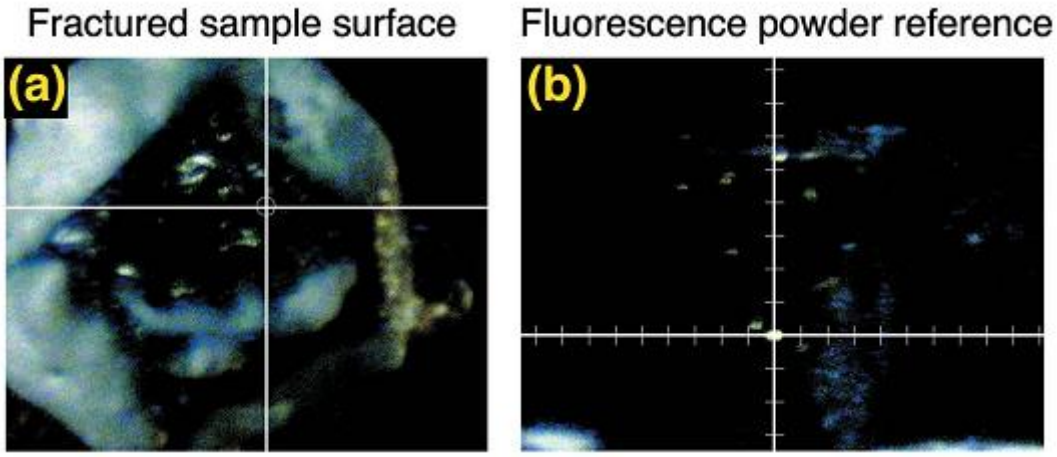

Fig. 2.10. Co-axial microscope image of (a) the fractured surface of YbB_{12} and (b) the fluorescence-powder reference on the gold reference on the manipulator.

A micro-positioning technique with similar monitoring systems [2.18, 2.19] is used to select the sample position as a shown in **Fig. 2.10a**. The intersection between the incident X-ray beam and the photoelectron analyzer axis is marked in advance onto the microscope monitor using a fluorescent substrate, which is positioned to maximize the counts of the detected photoelectrons by the photoelectron analyzer. In order to adjust a specific region on the sample surface to this intersection, first the target region was set to the mark on the microscope monitor then the sample position was scanned along the beam axis while keeping the target region on the mark until detecting the maximum counts of photoelectrons to avoid the ambiguity of the focal depth of the microscope. Moreover, to mark the beam spot at any time as in **Fig. 2.10b** there is a gold reference with a small amount of phosphor powder was put on the aluminum fingers (**Fig. 2.7a**). There is no problem caused by the phosphor powder

on the gold surface for optimizing the count rate according to the high photoelectron kinetic energy and long probing depth at HAXPES.

Fig.2.12 to **Fig. 2.18** shows some photo about the experimental equipment at SPring-8 BL19LXU.

2.5. Electrostatic hemi-spherical photoelectron spectrometer

Hemispherical photoelectron analyzer (HSA) was used to analysis the energy of the emitted photoelectrons. HSA consists of two concentric hemispheres of radii R1 and R2, as shown in **Fig. 2.11**. The photoelectrons were focused into the analyzer entrance slit by an electrostatic lens system. The photoelectrons were dispersed inside the analyzer depending on their kinetic energies. The energy-dispersed electrons were detected at the exit slit of the HSA at 180° with respect to the entrance slit. A negative potential was applied outside the hemispherical ($V_2/2$) while a positive potential was applied inside the hemispherical ($V_1/2$). Only electrons having certain kinetic energy can pass to the exit slit, at this time, the potential difference between the two hemispherical is V_p, and the kinetic energy of electrons passing from the entrance slit to exit slit follow a circular path with constant radius R=(R1+R2)/2, the pass energy (E_p) can be defined as:

$$E_p = \frac{eV_p}{\frac{R2}{R1} - \frac{R1}{R2}} \tag{2.2}$$

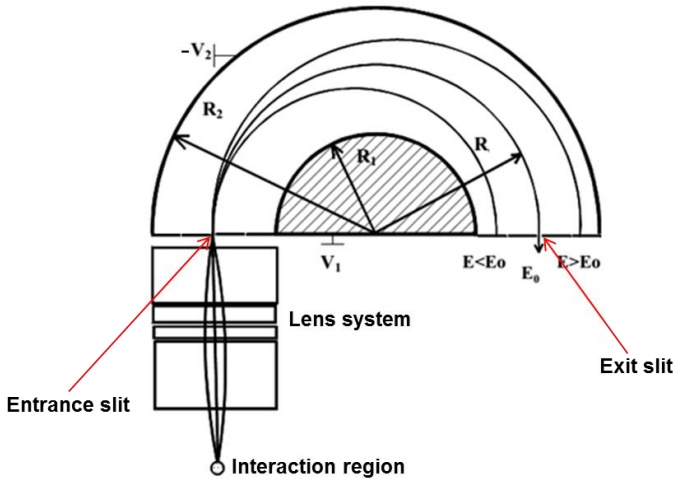

Fig. 2.11. Schematic representation of the electrostatic hemi-spherical photoelectron spectrometer.

The factors influence the energy resolution (ΔE) achieved within a spectrum are the radius of the analyzer (R), the pass energy (E_p), the slit width (w), the maximum emission angle in the dispersive direction (α) and the maximum emission angle in the nondispersive direction β. The relation between these influencing factors can be given by the relation [2.20]:

$$\frac{\Delta E}{E_p} = \frac{w}{2R} + 1(\frac{\alpha}{2})^2 + 0(\beta^2) \qquad (2.3)$$

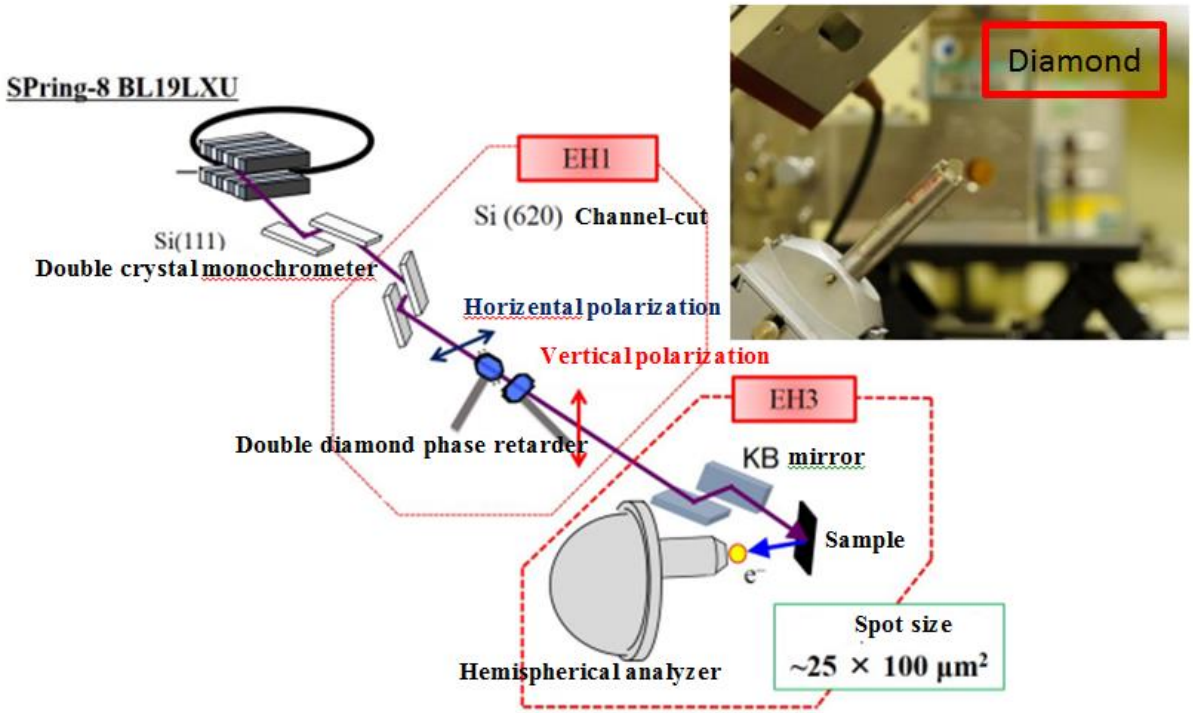

Fig. 2.12. The experimental place of BL19LXU in Spring8 for the polarized HAXPES.

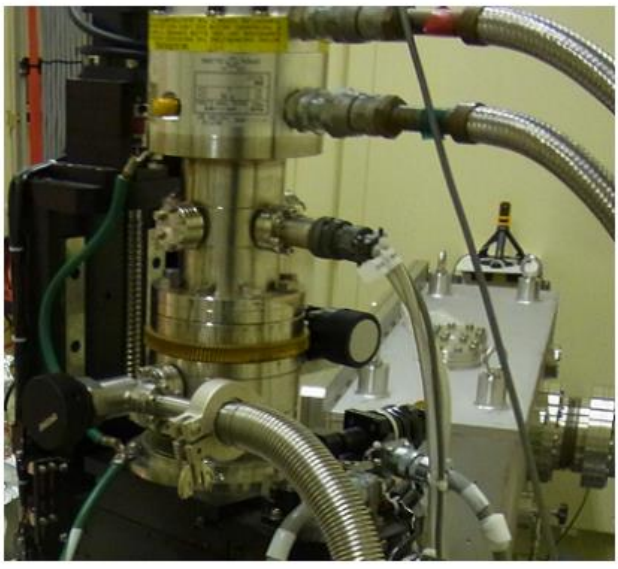

Fig. 2.13. BL19LXU ultra high vacuum He refrigerator.

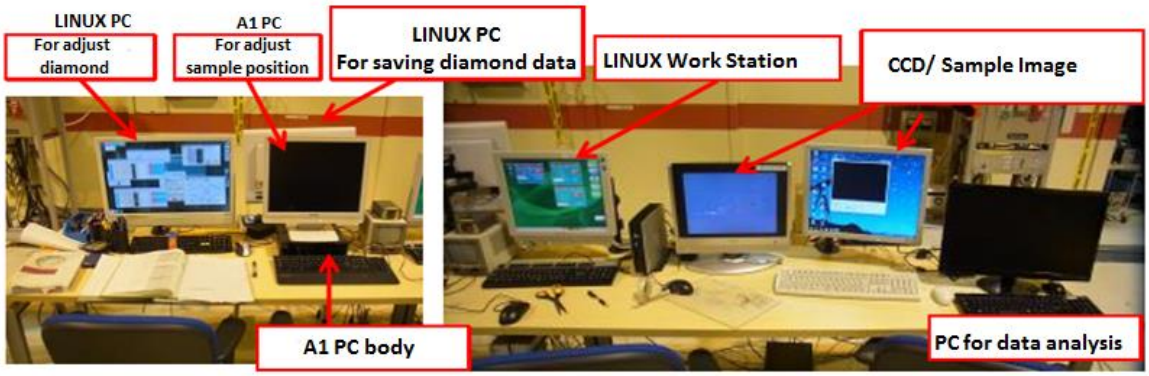

Fig. 2.14. PCs at BL19LXU.

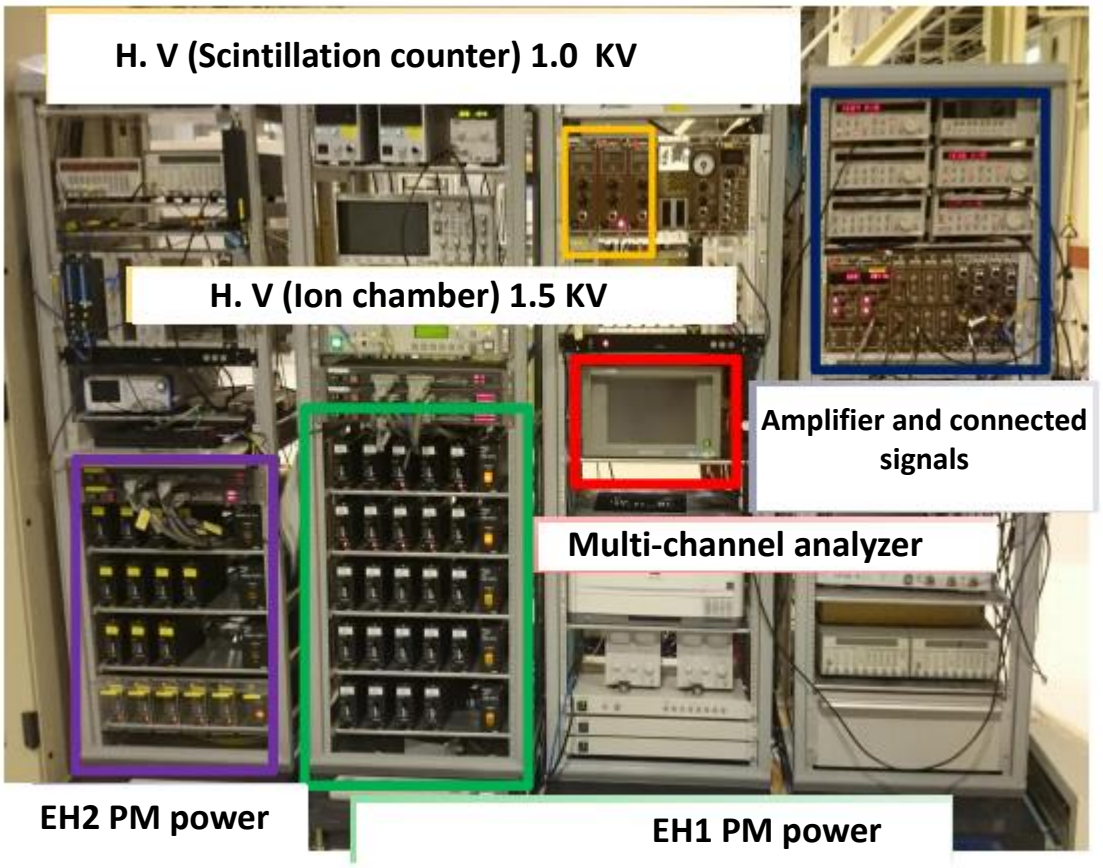

Fig. 2.15. BL19LXU high voltage devices.

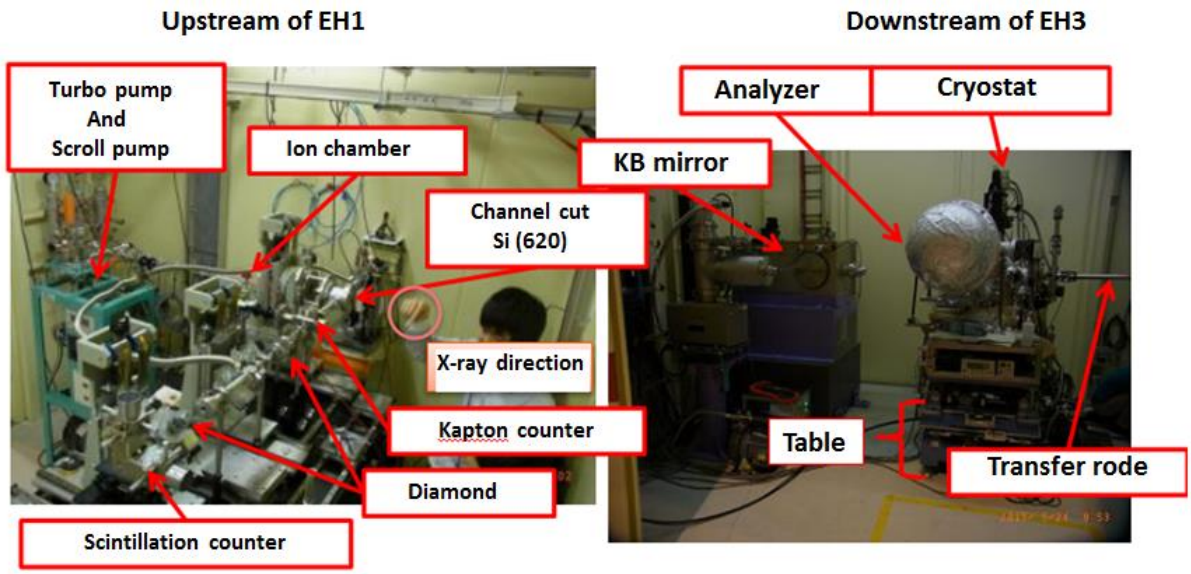

Fig. 2.16. Setting up the profile in EH1 and EH3.

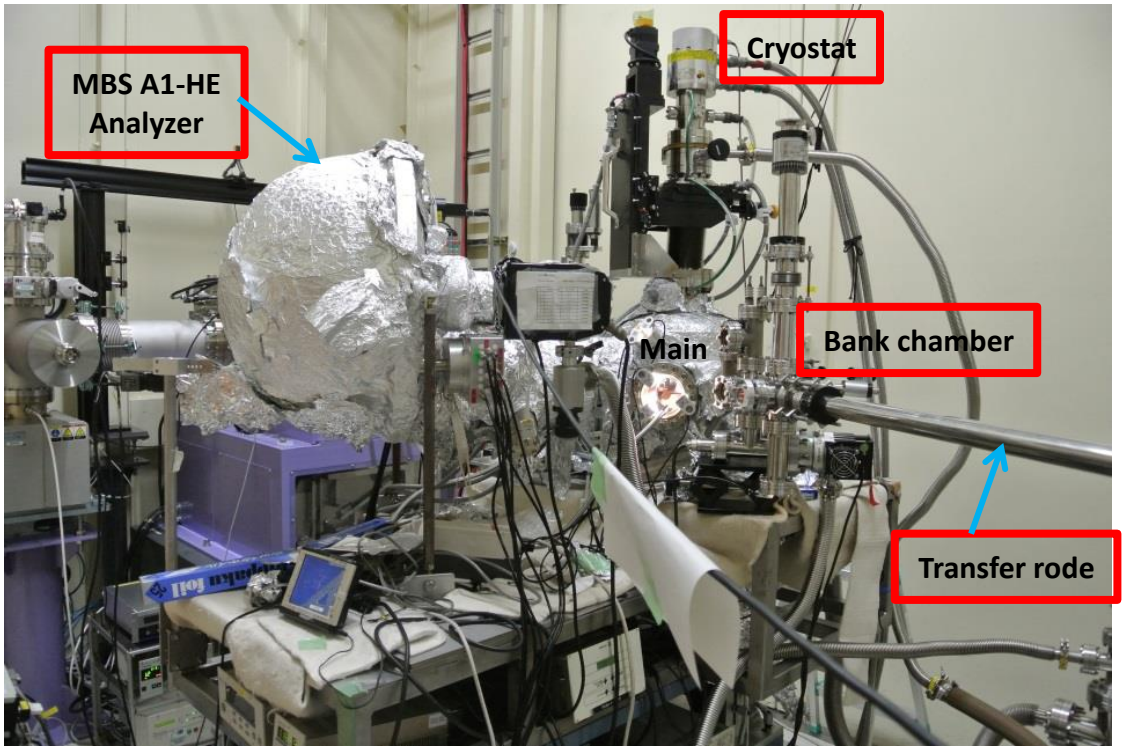

Fig. 2.17. HAXPES experimental apparatus.

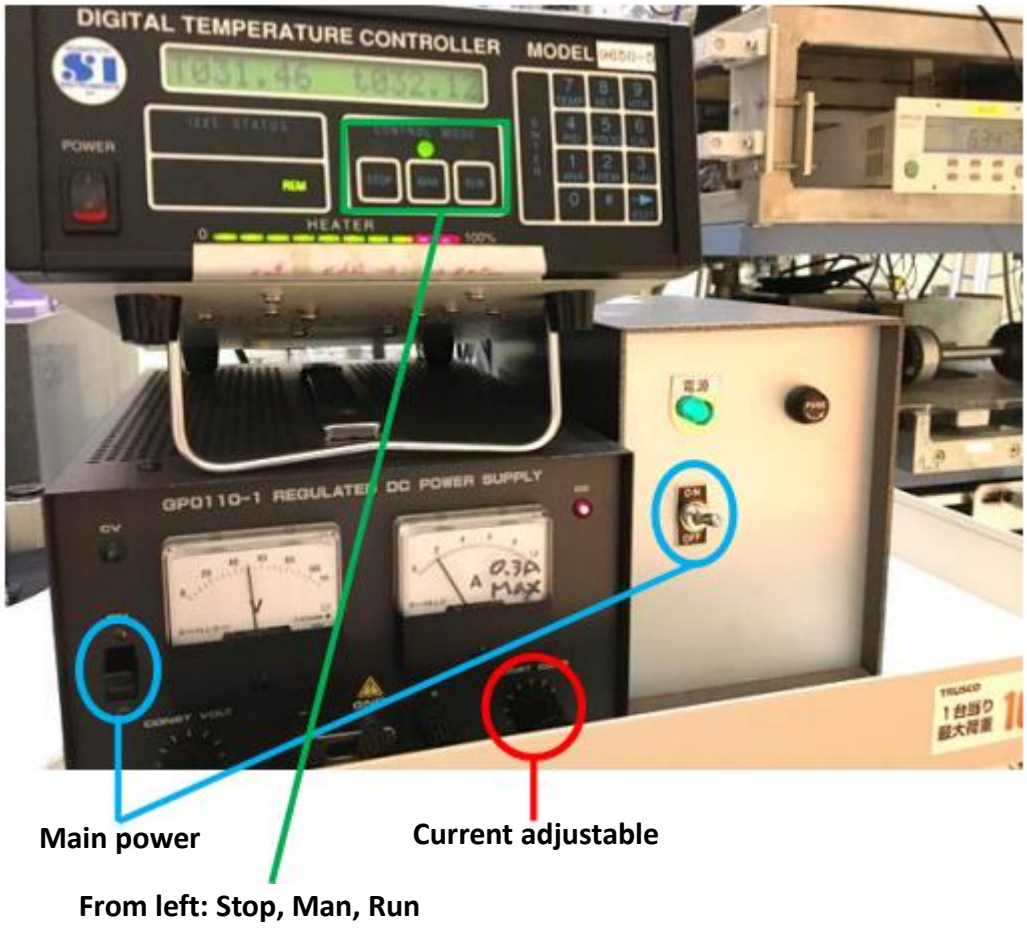

Fig. 2.18. Adjustable sample temperature system.

2.7. References

[2.1] J. Czochralski, Z. Phys. Chem. Vol. 92, p. 219 (1918).

[2.2] E. Talik and M. Oboz, Czochralski Method for Crystal Growth of Reactive Intermetallics, Acta Phys. Pol. A, Vol. 124, p. 340 (2013).

DOI: 10.12693/APhysPolA.124.340.

[2.3] A. Menovsky and J. J. M. Franse, Crystal growth of some rare earth and uranium intermetallics from the melt, J. Cryst. Growth, Vol. 65, p. 286 (1983).

DOI: 10.1016/0022-0248(83)90062-3.

[2.4] V. V. Aleksandryan, N. V. Baranov, A. I. Kozlov and A. S. Markosyan, Band metamagnetism of the d-subsystem of the $ErCo_2$ single crystal: investigation of magnetic and electrical properties, Phys. Met. Metall. Vol. 66, p. 50 (1988).

[2.5] A. Sekiyama, J. Yamaguchi, A. Higashiya, M. Obara, H. Sugiyama, M. Y. Kimura, S. Suga, S. Imada, I. A. Nekrasov, M. Yabashi, K. Tamasaku and T. Ishikawa, The prominent 5d-orbital contribution to the conduction electrons in gold, New J. Phys., Vol. 12, p. 043045 (2010). DOI: 10.1088/1367-2630/12/4/043045.

[2.6] A. Sekiyama, A. Higashiya and S. Imada, Polarization-dependent hard X-ray photoemission spectroscopy of solids, J. Electron Spectrosc. Relat. Phenom., Vol. 190, p. 201 (2013). DOI: 10.1016/j.elspec.2013.08.008.

[2.7] C. Weiland, A. K. Rumaiz, P. Pianetta and J. C. Woicik, Recent applications of hard x-ray photoelectron spectroscopy, J. Vac. Sci. Technol. A, Vol. 34, p. 030801 (2016).

DOI: 10.1116/1.4946046.

[2.8] M. Yabashi, K. Tamasaku and T. Ishikawa, Characterization of the transverse coherence of hard synchrotron radiation by intensity interferometry, Phys. Rev. Lett., Vol. 87, p. 140801 (2001). DOI: 10.1103/PhysRevLett.87.140801.

[2.9] H. Kitamura, T. Bizen, T. Hara, X. M. Maréchal, T. Seike and T. Tanaka, Recent developments of insertion devices at SPring-8, Nucl. Instrum., Methods Phys. Res. A, Vol. 467–468, p. 110 (2001). DOI: 10.1016/S0168-9002(01)00242-X.

[2.10] M. Yabashi, T. Mochizuki, H. Yamazaki, S. Goto, H. Ohashi, K. Takeshita, T. Ohata, T. Matsushita, K. Tamasaku, Y. Tanaka and T. Ishikawa, Design of a beamline for the SPring-8 long undulator source 1, Nucl. Instrum. Methods Phys. Res. A, Vol. 467–468, p. 678–681 (2001). DOI: 10.1016/S0168-9002(01)00444-2.

[2.11] M. Yabashi, K. Tamasaku and T. Ishikawa, Characterization of the Transverse Coherence of Hard Synchrotron Radiation by Intensity Interferometry, Phys. Rev. Lett. Vol. 87, p. 140801 (2001). DOI: 10.1103/PhysRevLett.87.140801.

[2.12] K. Okitsu, Y. Ueji, K. Sato and Y. Amemiya, X-ray double phase retarders to compensate for off-axis aberration, J. Synchrotron Rad., Vol. 8, p. 33 (2001).

DOI: 10.1107/S0909049500019567.

[2.13] S. Matsuyama and H. Yumoto, Textbook for hard X-ray focusing with Kirkpatrick-Baez optics, (2009).

[2.14] H. Fujiwara, S. Naimen, A. Higashiya, Y. Kanai, H. Yomosa, K. Yamagami, T. Kiss, T. Kadono, S. Imada, A. Yamasaki, K. Takase, S. Otsuka, T. Shimizu, S. Shingubara, S. Suga, M. Yabashi, K. Tamasaku, T. Ishikawa and A. Sekiyama, Polarized hard X-ray photoemission system with micro-positioning technique for probing ground-state symmetry of strongly correlated materials, J. Synchrotron Rad., Vol. 23, p. 735 (2016).

DOI: 10.1107/S1600577516003003.

[2.15] T. Mori , S. Kitayama, Y. Kanai, S. Naimen, H. Fujiwara, A. Higashiya, K. Tamasaku, A. Tanaka , K. Terashima, S. Imada , A. Yasui, Y. Saitoh, K. Yamagami, K. Yano, T. Matsumoto, T. Kiss, M. Yabashi, T. Ishikawa, S. Suga, Y. Ōnuki, T. Ebihara and A. Sekiyama, Probing strongly correlated 4f-orbital symmetry of the ground state in Yb compounds by linear dichroism in core-level photoemission, J. Phys. Soc. Jpn., Vol. 83, p. 123702 (2014). DOI: 10.7566/JPSJ.83.123702.

[2.16] Y. Kanai, T. Mori , S. Naimen , K. Yamagami, H. Fujiwara, A. Higashiya, T. Kadono, S. Imada, T. Kiss, A. Tanaka , K. Tamasaku, M. Yabashi, T. Ishikawa, F. Iga and A. Sekiyama, Evidence for Γ_8 ground-state symmetry of cubic YbB_{12} probed by linear dichroism in core-level photoemission, J. Phys. Soc. Jpn. Vol., 84, p. 073705 (2015).

DOI: 10.7566/JPSJ.84.073705.

[2.17] Y. Kanai, T. Mori, S. Naimen, K. Yamagami, S. Kitayama, H. Fujiwara, A. Higashiya, T. Kadono, S. Imada, T. Kiss, A. Tanaka, T. Muro, K. Tamasaku, M. Yabashi, T. Ishikawa, F. Iga, T. Ebihara, F. Honda, Y. Onuki and A. Sekiyama, Linear dichroism in 3d core-level and 4f valence-band photoemission spectra of strongly correlated rare-earth compounds, J. Electron Spectrosc. Relat. Phenom., Vol. 220, p. 61 (2017).

DOI: 10.1016/j.elspec.2016.12.012.

[2.18] T. Muro, Y. Kato, T. Matsushita, T. Kinoshita, Y. Watanabe, A. Sekiyama, H. Sugiyama, M. Kimura, S. Komori, S. Suga, H. Okazaki and T. Yokoya, In situ positioning of a few hundred micrometer-sized cleaved surfaces for soft-x-ray angle-resolved photoemission spectroscopy by use of an optical microscope, Rev. Sci. Instrum., Vol. 80, p. 053901 (2009).

DOI: 10.1063/1.3124145.

[2.19] H. Fujiwara, T. Kiss, Y. K. Wakabayashi, Y. Nishitani, T. Mori, Y. Nakata, S. Kitayama, K. Fukushima, S. Ikeda, H. Fuchimoto, Y. Minowa, S. K. Mo, J. D. Denlinger, J. W. Allen, P. Metcalf, M. Imai, K. Yoshimura, S. Suga, T. Muro, and A. Sekiyama, Soft X-ray angle-resolved photoemission with micro-positioning techniques for metallic V_2O_3, J. Synchrotron Rad., Vol. 22, p. 776 (2015). DOI: 10.1107/S1600577515003707.

[2.20] MBS A-1 instrument manual Ver. 1.1

Chapter 3

Method of Analysis

Chapter 3

Method of Analysis

3.1. Band structure calculation using KKR-Green's function method

The KKR-CPA-LSDA method is one of the methods of electronic structure calculation and is also called Green's function method. KKR refers to the initials of Korringa, Kohn, and Rostoker, who invented this method. LSDA means Local spin density approximation. CPA is the coherent potential approximation which can describe the disorder systems [3.1]. The density function theory depends on two fundamental mathematical theorems proved by Hohenberg and Kohn and the derivation of a set of equations by Kohn and Sham in mid of 1960s [3.2].

3.1.1. Hohenberg- Kohn Theorem

The Hohenberg- Kohn theorem [3.2, 3.3] is based on the ground state energy from Schrodinger's equation is a unique function of the electron density. So the ground state energy E can be expressed as E[n(r)], where n(r) is the electron density. The second Hohenberg-Kohn Theorem is the electron density that minimizes the energy of the overall functional is the true electron density corresponding to the full solution of the Schrodinger's equation. Consider a system of N- electrons under an external potential $v(r)$ is described by the following Hamiltonian H.

$$H = T + V + U \tag{3.1}$$

where T is the kinematic energy, V is the potential energy and U is the Coulomb energy between electrons, i.e.:

$$T = \sum_i -\nabla_i^2 \tag{3.2}$$

$$V = \sum_i v(r_i) \tag{3.3}$$

$$U = \sum_{i<j} \frac{2}{|r_i - r_j|} \tag{3.4}$$

where the atomic unit ($\hbar^2 = 1$, $e^2 = 1$, $m_e = 0.5$) is used.

The electron density $n(r)$ in the ground state Ψ at a particular position in space r is given by:

$$n(r) = \sum_{i=1}^{N} |\Psi_i(r)|^2 \tag{3.5}$$

where N is the number of electrons.

Reduction ad absurdum proved $v(r)$ is a unique function of $n(r)$. If another potential $\grave{v}(r)$ with ground state $\grave{\Psi}$ gives rise to the same density $n(r)$, we get the different wave functions Ψ and $\grave{\Psi}$. If the ground state energies and the Hamiltonian associated with Ψ , $\grave{\Psi}$ by E , È, and H , Ĥ, by using the minimum property of the ground state:

$$\text{È} = \langle \grave{\Psi} | \grave{\text{H}} | \grave{\Psi} \rangle < \langle \Psi | \grave{\text{H}} | \Psi \rangle = \langle \Psi | H - V + \grave{V} | \Psi \rangle$$

$$\text{È} < E + \int (\grave{v}(r) - v(r))\, n(r) dr \tag{3.6}$$

By exchanging primed and unprimed quantities, we found by the same way that:

$$E < \text{È} + \int (v(r) - \grave{v}(r))\, n(r) dr \tag{3.7}$$

The sum of these two inequalities **equations (3.6)** and **(3.7)** leads to the inconsistent result:

$$E + \text{È} < \text{È} + E \tag{3.8}$$

Therefore, v(r) is a unique function of $n(r)$. In turn, the N-electron ground state wave function Ψ and all ground state properties are functions of $n(r)$.

The variation principle for $E_v[n]$ is derived, the energy function for a given potential $v(r)$ is define as:

$$E_v[n] \equiv \int v(r) n(r) dr + F[n] \tag{3.9}$$

$$F[n(r)] \equiv T[n] + U[n] \tag{3.10}$$

where $E_v[n]$ equals the ground state energy E for the correct $n(r)$, $F[n]$ is a universal function valid for any number of particles and any external potential, it is independent of $v(r)$. The expression $E_v[n] \equiv \int v(r) n(r) dr + F[n]$ has its minimum values, the correct ground state energy associated with $v(r)$. If $F[n]$ was known, the ground state properties of any system can be determined.

3.1.2. Kohn-Sham equations

From Hohenberg and Kohn theory [3.1, 3.2, 3.4], approximation methods for treating an inhomogeneous electron system are developed by Kohn and Sham. Where they showed that the correct electron density can be expressed in a way that involves solving a set of equations in which each equation involves only a single electron. The ground state energy E_v of an inhomogeneous electron system for a given external potential $v(r)$ can be written as:

$$E_v[n] = \int v(r)n(r)dr + \frac{1}{2}\iint \frac{n(r)n(\grave{r})}{|r-\grave{r}|}drd\grave{r} + G[n] \tag{3.11}$$

$$G[n] \equiv T_s[n] + E_{XC}[n] \tag{3.12}$$

Where $G[n]$ is the universal function of the density, $T_s[n]$ is the kinetic energy of a non-interacting system of electrons, and $E_{XC}[n]$ is the exchange and correlation energy of an interacting system of electrons.

From the stationary property of **equation (3.11)** we obtained the condition:

$$\frac{\delta E_v[n]}{\delta n(r)} = 0 \tag{3.13}$$

By applying the condition in **equation (3.13)** on equation **(3.11)**:

$$\int \delta n(r)\left\{\phi(r) + \frac{\delta T_s[n]}{\delta n(r)} + V_{XC}(n(r))\right\}dr = 0 \tag{3.14}$$

where:

$$\phi(r) = v(r) + \int \frac{n(\grave{r})}{|r-\grave{r}|}d\grave{r} \tag{3.15}$$

$$V_{XC}(n) = \frac{dnE_{XC}(n)}{dn} \tag{3.16}$$

$$n(r) = \sum_{i=1}^{N} |\Psi_i(r)|^2 \tag{3.17}$$

where $V_{XC}(n)$ is the exchange correlation potential.

Then the Kohn and Sham equations have the form:

$$-\frac{1}{2}\nabla^2 + \left[\phi(r) + V_{XC}\big(n(r)\big)\right]\Psi_i(r) = \epsilon_i\Psi_i(r) \tag{3.18}$$

3.1.3. Local spin density approximation (LSDA)

In the band structure calculation, LDA [3.1, 3.2, 3.5] is the most widely used due to its simplicity and its success in describing the ground state and equilibrium properties of many different types of materials. LDA works very well for metals but there are problems with calculations of the electronic structure of semiconductors and insulators, especially the band gap in semiconductors and insulators is too small when compared with the experiment.

The exchange-correlation energy for a homogeneous electron gas is calculated as following:

$$E_{XC}[n]/N = \varepsilon_{XC}(n(r)) \tag{3.19}$$

By making the exchange potential as local, in the local density approximation (LDA) we can regard an inhomogeneous electron system as a system locally homogeneous, i.e.:

$$E_{XC}[n] = \int n(r)\varepsilon_{XC}\big(n(r)\big)dv \tag{3.20}$$

$$E_{XC}[n] = E_X[n] + \int n(r)\varepsilon_C\big(n(r)\big)dr \tag{3.21}$$

where $E_X[n]$ is the exchange energy of a Hartree-Fock system of density $n(r)$ and $\varepsilon_C(n)$ is the correlation energy per particle of a homogenous electron gas. Therefore, the exchange-correlation potential is given by:

$$V_{XC}(r) = \varepsilon_{XC}\big(n(r)\big) + n(r)\frac{d\varepsilon_{XC}\big(n(r)\big)}{n(r)} \tag{3.22}$$

In the spin polarized case [3.6], the exchange correlation energy is written as:

$$E_{XC}[n] = \int n(r)\varepsilon_{xC}(n\uparrow(r), n\downarrow(r))dr \tag{3.23}$$

and the exchange correlation potential is written as:

$$V_\alpha^{XC}(r) = \left[\frac{\partial}{\partial n_\alpha}\{n\varepsilon_{xC}\big(n\uparrow(r), n\downarrow(r)\big)\}\right]_{\substack{n\uparrow=n\uparrow(r)\\ n\downarrow=n\downarrow(r)}} \tag{3.24}$$

where $\alpha = \uparrow$ or $\downarrow$.

3.1.4. Self-Interaction Corrections (SIC)

Perdew and Zunger presented the SIC method [3.5, 3.7] as an attempt to exceed LSDA underestimate. SIC methods require itinerant and localized electrons. Benefits of applying self-interaction correction to the LSDA in electronic structure calculations are: improvement the total energy values, separating the exchange and correlation energies from it, obtaining accurate binding energies, enhancing the description of the density of state and treatment the LSDA underestimate of the band gaps in insulators where SIC has been successfully applied in a number of electronic structures calculation of wide-gap insulators, giving very reasonable results of the band gap.

(Magic number)×(SIC) is subtracted from the total energy, which is to be minimized. Here, SIC is defined as:

SIC=$\frac{1}{2}$ (Hartree potential) + (exchange-correlation energy), where contribution from local valence electron as R 4f is taken.

3.1.5. Electron Density distribution

Electronic density of state (DOS) [3.2] is one of the primary quantities used to describe the electronic state of a material. From the Green's function of the system, we obtained the electron density distribution directly. It is shown from the eigen function expansion of the Green's function. The eigen function ϕ_n of the Schrodinger equation $H\phi = E\phi$ which associated with the eigen value E_n and the Green's function of the system satisfies:

$$\mathcal{H}\phi_n = E_n\phi_n \tag{3.25}$$

$$[E - \mathcal{H}]G(r, \grave{r}) = \delta(r - \grave{r}) \tag{3.26}$$

Expanding $G(r, \grave{r})$ into ϕ_n is with the expansion coefficient $G_n(\grave{r})$:

$$G(r, \grave{r}) = \sum_n G_n(\grave{r})\phi_n(r) \tag{3.27}$$

By multiplying it by $[E - \mathcal{H}]$ from the left hand side, we get:

$$[E - \mathcal{H}]G(r, \grave{r}) = \sum_n G_n(\grave{r})[E - \mathcal{H}]\phi_n(r) = \delta(r - \grave{r}) \tag{3.28}$$

By multiplying **equation (3.28)** by $\phi_n^*(\grave{r})$, we obtain:

$$G_n(\grave{r}) = \phi_n^*(\grave{r})/(E - E_n) \tag{3.29}$$

where:

$$G(r, \grave{r}) = \sum_n \frac{\phi_n^*(\grave{r})\phi_n(r)}{(E - E_n)} \tag{3.30}$$

$G(r, \grave{r})$ can be obtained from the definition:

$$\frac{1}{x+i\epsilon} = p.\frac{1}{x} - i\pi\delta(x) \tag{3.31}$$

$$G(r, \grave{r}) = \sum_n \frac{\phi_n^*(\grave{r})\phi_n(r)}{(E - E_n + i\epsilon)} = p.\sum_n \frac{\phi_n^*(\grave{r})\phi_n(r)}{(E - E_n)} - i\pi \sum_n \delta(E - E_n)\, \phi_n^*(\grave{r})\phi_n(r) \tag{3.32}$$

In **equation (3.32)** the electron density distribution expression $n(r, E)$ is:

$$n(r, E) = \sum_n \delta(E - E_n)\, \phi_n^*(r)\phi_n(r) = -\frac{1}{\pi} ImG(r, r) \tag{3.33}$$

Therefore, the electron density distribution is directly obtained if we know the Green's function of the crystal. If we integrated $n(r, E)$ over the unit cell, DOS can be obtained.

3.1.6. KKR-Coherent potential approximation (KKR-CPA)

CPA [3.8-3.10] gives sufficient good description of the electronic states in random systems (paramagnetic state). Let the disordered alloy system be A_c, B_{1-c} (c is the concentration). The first assumption of the KKR-CPA is that the occupation of a site either by A or B atoms is independent of the occupancy of the surrounding sites. This means that short range order is neglected for the purposes of the electronic structure calculation is approximated by a random substitutional alloy. The second assumption is inverting the order of solving the Kohn-Sham equations and taking the configuration averaging. Consequently, we can find a set of Kohn-Sham equations that describe an 'average' medium. Supposing that either A or B atoms at the origin in the effective medium, Green's function which starts from the origin and comes back to the origin can be given by:

$$G_{LL'}^{(A or\ B)} = \sum_{L''} \tilde{G}_{LL''} \left[1 - (t_{(A\ or\ B)} - \tilde{t})\tilde{G}\right]^{-1}_{L''L'} \tag{3.34}$$

where $\tilde{G}_{LL'}$ and $\tilde{t}$ are Green's function and coherent t matrix of the effective medium respectively. The CPA description determining $\tilde{t}$ (self-consistent equation) is:

$$(c)G^{A}_{LL'} + (1-c)G^{b}_{LL'} = \tilde{G}_{LL'} \tag{3.35}$$

This equation means that we determine the Green's function of the medium by taking weighted average of the Green's function where the component atom is placed at the origin in the effective medium.

Subroutines

The KKR package consists of more than 100 subroutines. A brief flowchart is given in **Fig. 3.1**. A comment on each subroutine is also given in **Table 1**. **Tables 2** and **3** reveal the parameters used in the input file and specx file respectively. **Fig.3.2** shows the input file and specx file.

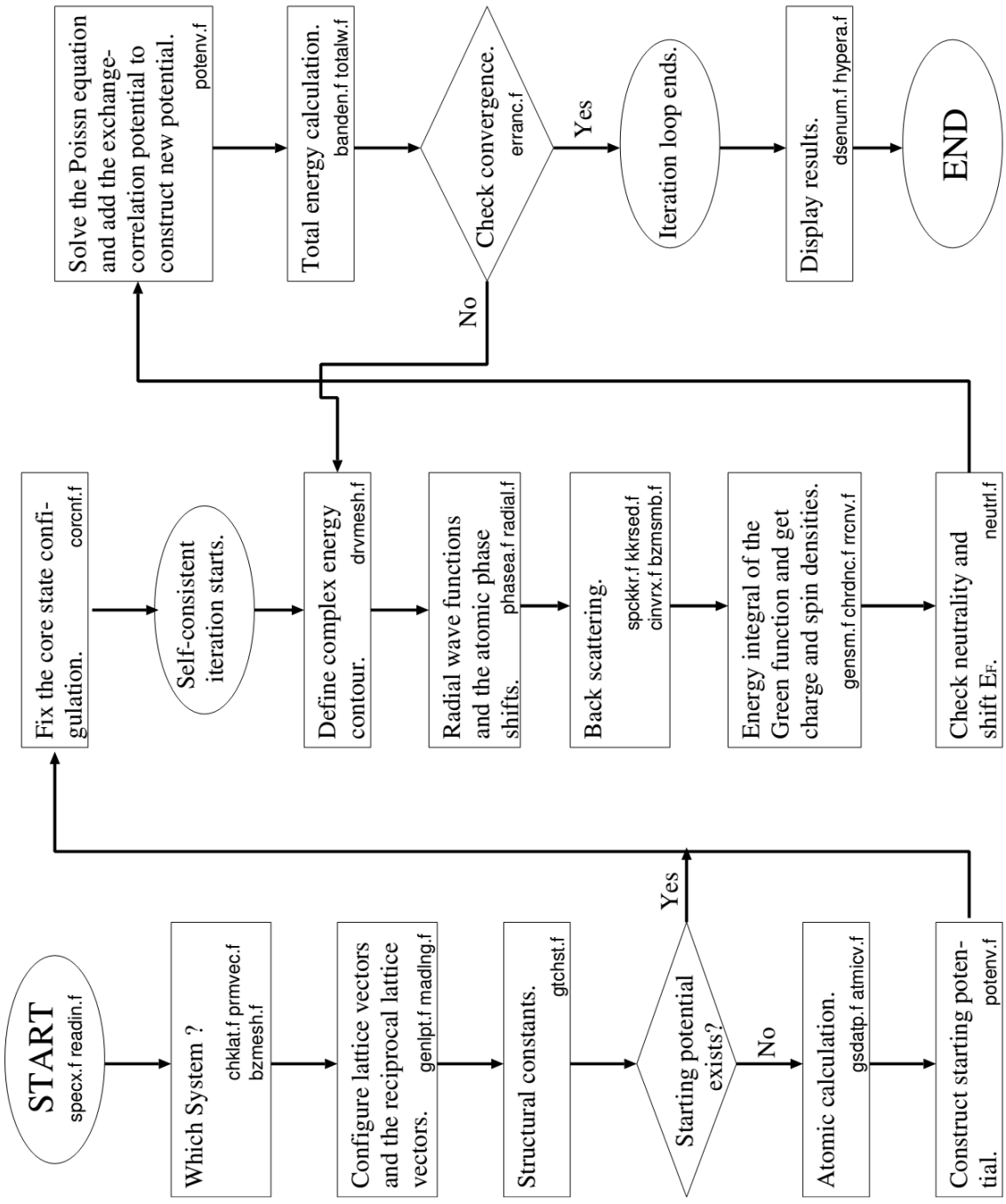

Fig. 3.1. The flow chart of the band structure calculation.

Table 3.1. Subroutines in the KKR package.

Subroutine	Comment
specx.f	Some parameters and arrays are defined and spmain is called.
readin.f	A given input file is read in.
spmain.f.	Main routine of the KKR
chklat.f	Check muffin tin radii and modify them if they conflict.
prmvec.f	The primitive lattice vector and the reciprocal lattice vector are generated.
bzmesh.f	k-points in the Brillouin zone are set up.
genlpt.f	Lattice points in the real and reciprocal space are generated.
madlng.f	The madelung constants are calculated.
gtchst.f	The KKR structure constants are calculated.
gsdatp.f	Initial potentials are constructed from the atomic calculations.
atmicv.f	The atomic calculation is performed.
corcnf.f	The configuration of the core states is confirmed.
drvmsh.f.	The energy contour is defined
phasea.f	The atomic *t*-matrix is calculated.
radial.f	The radial Schrodinger equation is solved.
fczero.f	Single site Green's function.
cstate.f	The radial Schrodinger equation is solved for the core states.
spckkr.f	The crystal Green's function is constructed.
kkrsed.f	The structure constant are interpolated for each energy point.
cinvrx.f	$(1 - gt)^{-1}$ is calculated.
bzmsmb.f	Integration in k-space.
chrdnc.f	The charge density distribution is calculated.
neutrl.f.	The charge neutrality is calculated and ε_f is shifted
potenv.f	The Poisson equation is solved. The exchange-correlation potential is calculated.
banden.f	The energy eigenvalues are summed up.
totalw.f	The total energy of the system is calculated.
erranc.f	The convergence is checked, and new input potential is constructed.
dsenum.f	The results are printed out.
hypera.f	The hyperfine field is calculated.

Table 3.2. Parameters used in input file.

Field	Value	Meaning
go	go	perform a band structure calculation.
	dos	calculate a density of states.
	dsp	display a previous result.
	spc	calculate Bloch spectral function (dispersion relation).
file	*file name*	file name in which a potential data is written.
brvtyp		which type of the Bravais lattices.
	fcc	face centered cubic
	bcc	body centered cubic
	hcp(hex)	hexagonal close packed
	sc	simple cubic
	bct	body centered tetragonal
	st	simple tetragonal
	fco	face centered orthorhombic
	bco	body centered orthorhombic
	bso	base centered orthorhombic
	so	simple orthorhombic
	bsm	base centered monoclinic
	sm	simple monoclinic
	trc	triclinic
	rhb(trg)	rhombohedral (trigonal)
	fct	face centered tetragonal
a		lattice constant in atomic unit.
c/a		c/a ratios of lattice constants.
b/a		b/a ratios of lattice constants.
alpha		α in degrees.
beta		β in degrees.
gamma		γ in degrees.
edelt	$\sim$0.001	Imaginary part at the Fermi level in Ry (see Fig. 1).
ewidth	—	Width of the energy contour in Ry (see Fig. 1).
reltyp	nrl	no relativistic treatment.
	sra	scaler relativistic approximation.
sdftyp	mjw, vbh, vwn	which exchange correlation potential is used.
magtyp	mag	magnetic.
	nmag	non-magnetic.
	-mag(rvrs)	change the sign of the magnetization.
	kick	transfer to the magnetic state artificially.
record	init	initially start a calculation.
	2nd	continues the last calculation.
	1st	continues the second last calculation.
outtyp	update	potential data is updated.
	quit	potential data is not updated.
bzqlty	0, 1, 2,...	The bigger, the finer mesh in the Brillouin zone.
	t, s, m, l, h, u	see nfqlty.f
maxitr		the maximum number of the iteration loop.
pmix	0.01-0.03	a parameter used in mixing V^{in} and V^{out}.
ntyp		how many types of atom exist in a unit cell.
type	*type name*	names of the respective types of site.
ncmp		how many components exist in the site.
rmt		muffin tin radius in a.
field		external magnetic field at each site in Ry.
l_max		the maximum angular momentum taken into account.
anclr		atomic number.
conc		concentration of the components at the site.
natm		number of atoms in a unit cell.
atmicx	*coordinates*	where each atom is (in a).
atmtyp	*type name*	which type of the site at the lattice point.

Table 3.3. Parameters used in specx.

Parameter	Meaning
natmmx	maximum number of atoms in a unit cell.
ncnpmx	maximum number of types of atoms in a unit cell.
msizemx	maximum size of the KKR matrix. $\geq \sum_{i=1}^{natm}(l_{max,i}+1)^2$
mxlmx	$l \geq$mxlmx are truncated.
nk1mx,nk3mx	nk1mx+nk3mx is maximum number of k-points in the Brillouin zone.
msex	mesh points on the energy contour for go=dos, spc.
ngmx	The chebyshev expansion is performed up to ngmx-th order.
nrpmx	maximum number of lattice points used in the Ewalt's sum.
ngpmx	maximum number of reciprocal lattice points used in the Ewalt's sum.
msr	radial mesh points.
mse0	(data) mesh points on the energy contour for go=go.
tol	(data) tolerance of convergence

(a)

```
c--------------------ErCo2-----------------------------------------
   go   data/ErCo2_45_0.32_1
c-------------------------------------------------------------------
c  brvtyp     a        c/a   b/a   alpha   beta   gamma
    fcc      13.479,          ,     ,      ,      ,      ,
c-------------------------------------------------------------------
c  edelt    ewidth    reltyp   sdftyp   magtyp   record
   0.001     0.9       SRALS     mju      mag      2nd
c-------------------------------------------------------------------
c  outtyp   bzqlty   maxitr   pmix
   update     4      1000     0.01
c-------------------------------------------------------------------
c   ntyp
    2
c-------------------------------------------------------------------
c  type   ncmp    rmt    field   mxl  anclr  sic   mn     conc
     Er     1     0.0    0.025     3    68    f    0.32   100
     Co     1     0.0    0.0       2    27    n           100
c-------------------------------------------------------------------
c  natm
   6
c-------------------------------------------------------------------
c  atmicx                          atmtyp
c  x         y         z
   0         0         0         Er
   0.75      0.25      0.75      Er
   0.625     0.625     0.625     Co
   0.375     0.875     0.125     Co
   0.875     0.125     0.375     Co
   0.125     0.375     0.875     Co
c-------------------------------------------------------------------
```

(b)

```
                        program specx
c-------------------------------------------------------------------
c     ------------------------------
c     --- KKR-CPA + spin-orbit version ---
c     ------------------------------
c      KKR-CPA band structure calculation
c      originaly coded by H.Akai and M.Akai, 1980, on ACOS
c           adapted to NEC sx1&2, Aug. 1986 at Osaka
c           adapted to CRAY xmp, Aug. 1986 at Juelich
c           adapted to HITAC s820, Nov. 1989 at ISSP
c           adapted to HP 730, July. 1992
c                latest version on 11 Feb. 1996
c      CPA is implemented by H.Akai, 7 Sep. 1996, Osaka
c      Adapted to spin-orbit included version, 18 April, 1997, Osaka
c      Fixed spin moment procedure implemented, 8 Aug. 1999, Duisburg
c-------------------------------------------------------------------
      implicit real*8 (a-h,o-z)
      parameter
     & (natmmx=6, ncmpmx=2, msizmx=96, mxlmx=4, nk1x=1500, nk3x=1,
     & msex=2001, ngmx=21, nrpmx=650, ngpmx=650, npmx=650, msr=400,
     & nfmx=40)
c
c--- the following part is used for all cases.
"specx.f" 251L, 9918C                          19,6          Top
```

Fig. 3.2. (a) Input file. (b) specx file. In Akai KKR program.

3.2. XTLS (Polarization Dependent)

XTLS [3.11] program used for the analysis of high energy spectra as (XAS, HAXPES, etc…). The ionic calculations including the full multiplet theory [3.12] performed using XTLS program in order to calculate not only 3*d* and 4*f* XPS spectra but also the energy levels and multipole moments of the ground and excited states. Atomic parameters, namely F and G parameters, for Coulomb interaction and ζ parameters for spin-orbit interaction were obtained from the result of Cowan's code calculation [3.13] based on Hartree-Fock method. For the linear polarized HAXPES at BL19LXU of SPring8, there are some basic concepts should be taken in account in the analysis of the spectra as follows:

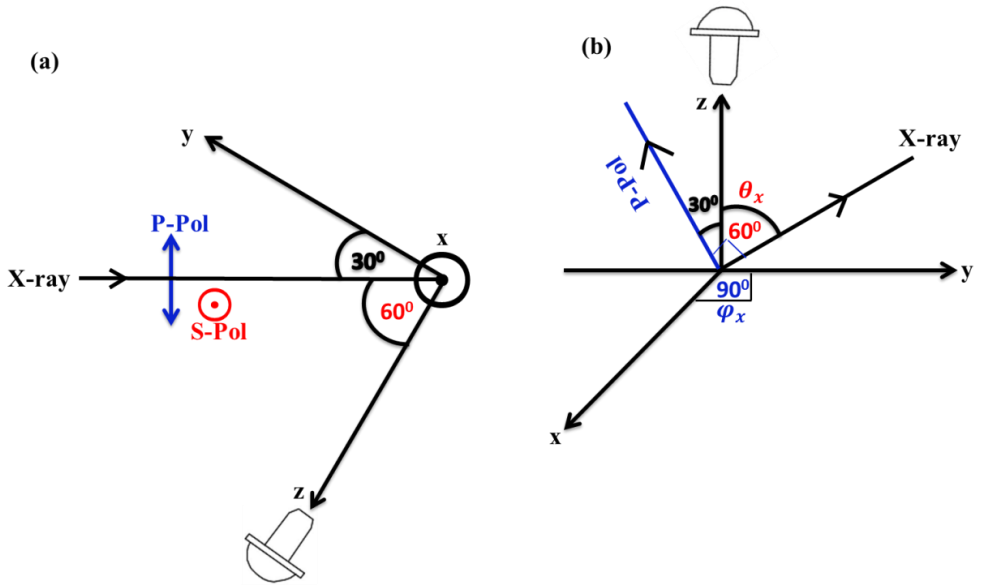

Fig. 3.3. Schematically drawn of experimental geometry for HAXPES measurements at BL19LXU of SPring8.

3.2.1. Vector of Emitted Photoelectron (Eang)

Since the emitted photoelectron detection direction "e¯" is along z-axis and both x and y axes are perpendicular on z axis as a shown in **Fig. 3.3a**, the component of the emitted photoelectron detection direction can be written as:

$$\text{Eang} = (0, 0, 1) \tag{3.36}$$

3.2.2. Polarization Vector (Electric Field)

In the case of linear polarized light (BL19LXU), as illustrated in **Fig. 3.3a**, the electric field vector of the vertical polarized light (s-pol) ($\boldsymbol{E_{vert}}$) is a long x-axis and perpendicular on X-ray direction, photoelectron detection direction and y axis, so $\boldsymbol{E_{vert}}$ component is:

$$\boldsymbol{E_{vert}} = E(1, 0, 0) \tag{3.37}$$

While the electric field vector of the horizontal polarized light (p-pol) ($\boldsymbol{E_{hori}}$) is along y-z plane and perpendicular on X-ray direction and s-pol direction, so $\boldsymbol{E_{hori}}$ component is:

$$\boldsymbol{E_{hori}} = E\left(0, -\frac{1}{2}, \frac{\sqrt{3}}{2}\right) \tag{3.38}$$

3.2.3. Photoexcitation Operator ($E.r$) in Terms of Spherical Harmonic

Photoexcitation operator in terms of Cartesian coordinate is given as:

$$\boldsymbol{E}.\boldsymbol{r} = E_x x + E_y y + E_z z \tag{3.39}$$

$$x = r\sqrt{\frac{4\pi}{3}}\,\frac{-Y_{11}(\theta,\varphi) + Y_{1-1}(\theta,\varphi)}{\sqrt{2}} \tag{3.40}$$

$$y = r\sqrt{\frac{4\pi}{3}}\,\frac{i[Y_{11}(\theta,\varphi) + Y_{1-1}(\theta,\varphi)]}{\sqrt{2}} \tag{3.41}$$

$$z = r\sqrt{\frac{4\pi}{3}}\,Y_{10}(\theta,\varphi) \tag{3.42}$$

$$\boldsymbol{E}.\boldsymbol{r} = r\sqrt{\frac{4\pi}{3}}\left[\frac{-E_x + iE_y}{\sqrt{2}}Y_{11}(\theta,\varphi) + E_z Y_{10}(\theta,\varphi) + \frac{E_x + iE_y}{\sqrt{2}}Y_{1-1}(\theta,\varphi)\right] \tag{3.43}$$

where θ and φ are defined in **Fig. 3.3b**.

By comparing **equation (3.37)** and **equation (3.38)** with **equation (3.43)**, we get the photoexcitation operator for s-pol as:

$$\boldsymbol{E}.\boldsymbol{r} \propto \left[-\frac{E}{\sqrt{2}}Y_{11}(\theta,\varphi) + 0.Y_{10}(\theta,\varphi) + \frac{E}{\sqrt{2}}Y_{1-1}(\theta,\varphi)\right] \tag{3.44}$$

Photoexcitation operator for p-pol:

$$\boldsymbol{E}.\boldsymbol{r} \propto \left[-\frac{iE\cos\theta}{\sqrt{2}}Y_{11}(\theta,\varphi) + E\sin\theta\, Y_{10}(\theta,\varphi) + \frac{-iE\cos\theta}{\sqrt{2}}Y_{1-1}(\theta,\varphi)\right] \tag{3.45}$$

The corresponding commands in XTLS program are:

```
CAk_s(th,ph,R)=(
 rt2=sqrt(2d0);
    {1, 1, -R/rt2*sin(ph), R/rt2*cos(ph), 1, 0, 0d0 , 0d0 , 1, -1, R/rt2*sin(ph), R/rt2*cos(ph) });
CAk_p(th, ph, R)=(
 rt2=sqrt(2d0);
    {1, 1, R/rt2*cos(th)*cos(ph), R/rt2*( -cos(th)*sin(ph) ), 1, 0, R*sin(th), 0d0
```

, 1, -1, -R/rt2*cos(th)*cos(ph), R/rt2*(-cos(th)*sin(ph))});

where R represent electric field vector (E)

In 3d XPS, there are two different probability of excitation are between (d and f) or (d and p) electrons, the corresponding commands in XTLS are (R1df=) or (R1dp=) respectively. The rotation angles (α, β and γ) determined based on Euler angles. The xcard file for such polarization conditions in order to obtain 3d XPS spectra using XTLS program written as:

```
XCARD:
 //XCARD for ErCo2 3dXPS
(
Emin=-40.0;
Emax=40.0;
step=0.025;
DeltaRec=step*2;
Ndat=(Emax-Emin)/step;
mag=0.0;
w=-0.00001235;
x=-0.24;
F4=60.0;
F6=13860.0;
a=sqrt(70.0)/8.0;
b=3.0*sqrt(14.0)/16.0;
gamma=2.0699E-6;
beta=0.444E-4;
B40=(w*x)/F4;
B44=5.0*B40;
B60=w*(1.0-abs(x))/F6;
B64=-21.0*B60;
A40=B40*(8.0/beta);
A44=B44/(a*beta);
A60=B60*(16.0/gamma);
A64=B64/(b*gamma);
```

```
crystal={4.0,0,A40,4.0,4.0,A44,4.0,-4.0,A44,6.0,0,A60,6.0,4.0,A64,6.0,-4.0,A64};
   R1df=1d0;
   R1dp=0d0;
   Pi=4d0*atan(1d0);
   phiX  =  90.0*(Pi/180d0); //90 deg
   thetaX=  60.0*(Pi/180d0); //60 deg
   alpha=-90.0*(Pi/180d0);    //-90 deg
   beta=-9.5*(Pi/180d0);      //-9.5 deg
   gamma=135.0*(Pi/180d0);   //135 deg
   CAk_p(th,ph,R)=(
    rt2=sqrt(2d0);
   { 1, 1, R/rt2*cos(th)*cos(ph), R/rt2*( -cos(th)*sin(ph) ), 1, 0, R    *sin(th), 0d0 , 1,-1,-R/rt2*cos(th)*cos(ph),
R/rt2*( -cos(th)*sin(ph) )
    }
    );
   CAk_s(th,ph,R)=(
    rt2=sqrt(2d0);
    { 1, 1, R/rt2*sin(ph),R/rt2*cos(ph), 1, 0, 0d0 , 0d0, 1,-1,-R/rt2*sin(ph),R/rt2*cos(ph)
    }
    );
)
CNFG:
       3d   4f
 #i1  10  11
 #f1   9  11
PARA:
Red=1.0;
EXEC:
  Mode =XPS;
  Dichro={P,S,L,K,R};
 Eang={0,0,1};
 Ninit=17;
 Range={Ndat, Emin, Emax, DeltaRec};
```

```
 Mag={4f};
OPRT://No.1 initial
  Rk (#i1 4f 4f)={12.87, 9.47, 7.03};//(F4f4f2,F4f4f4,F4f4f6);
  Zeta(#i1 4f)=0.30;
  rAk(#i1,4f)={alpha, beta, gamma, crystal};
OPRT://No.2 final
  Rk (#f1 3d 4f )={9.85, 4.68, 6.83, 4.01, 2.77};//(F3d4f2, F3d4f4, G3d4f1,G3d4f3,G3d4f5)
 Rk (#f1 4f 4f )={16.68, 10.52, 7.58};//(F4f4f2,F4f4f4,F4f4f6);
  Zeta(#f1 3d)=16.77;
  Zeta(#f1 4f)=0.36;
  rAk(#f1,4f)={alpha, beta, gamma, crystal};
 OPRT://No.3
  CAk^P(#i1 #f1 3d ef)=CAk_p(thetaX,phiX,R1df);
  CAk^P(#i1 #f1 3d ep)=CAk_p(thetaX,phiX,R1dp);
  CAk^S(#i1 #f1 3d ef)=CAk_s(thetaX,phiX,R1df);
  CAk^S(#i1 #f1 3d ep)=CAk_s(thetaX,phiX,R1dp);
  rAk^L(#i1 #f1 3d ef)={phiX+Pi, Pi-thetaX, 0.0, 1, 1, R1df};
  rAk^L(#i1 #f1 3d ep)={phiX+Pi, Pi-thetaX, 0.0, 1, 1, R1dp};
  rAk^K(#i1 #f1 3d ef)={phiX+Pi, Pi-thetaX, 0.0, 1, 0, R1df};
  rAk^K(#i1 #f1 3d ep)={phiX+Pi, Pi-thetaX, 0.0, 1, 0, R1dp};
  rAk^R(#i1 #f1 3d ef)={phiX+Pi, Pi-thetaX, 0.0, 1,-1, R1df};
  rAk^R(#i1 #f1 3d ep)={phiX+Pi, Pi-thetaX, 0.0, 1,-1, R1dp};
 XEND:
```

The multipole moment calculations using XTLS program can be performed using the previous xcard file after cancelling out the crystal rotation.

3.3. References

[3.1] J. B. Staunton, S. S. A. Razee, M. F. Ling, D. D. Johnson and F. J. Pinski, Magnetic alloys, their electronic structure and micromagnetic and microstructural models, Review article, J. Phys. D: Appl. Phys., Vol. 31, p. 2355 (1998).

[3.2] D. S. Sholl and J. A. Steckel, Handbook in Density function theory, Ch. 1, (2009).

[3.3] P. Hohenberg, W. Kohn, inhomogeneous electron gas, Phys. Rev., Vol. 136, p. B 864 (1964).

[3.4] W. Kohn and L. J. Sham, self-consistent including exchange and correlation effects,Phys. Rev., Vol. 140, p. A1133 (1965).

[3.5] I. N. Yakovkin and P. A. Dowben, The problem of the band gap in LDA calculations, Surface Rev. and Letters, Vol. 14, p. 481 (2007).

[3.6] J. Kubler, Handbook in Theory of Itinerant Electron Magnetism, Oxford, P. 53, 2000.

[3.7] J. P. Perdew and Alex Zunger, Self-interaction correction to density-functional approximations for many-electron systems, Phys. Rev. B, Vol. 23, p. 5048 (1981).

[3.8] J. Staunton, P. Weinberger and B. L. Gyorffy, On the electronic structure of paramagnetic Ni_cPt_{1-c} alloys: a relativistic calculation, J. Phys. F: Met. Phys., Vol. 13, p. 779 (1983).

[3.9] P. Soven, Coherent-Potential Model of Substitutional Disordered Alloys, Phys. Rev., Vol. 156, p. 809 (1967).

[3.10] G. M. Stocks, W. M. Temmerman and B. L. Gyorffy, Complete Solution of the Korringa-Kohn-Rostoker Coherent-Potential Approximation Equations: Cu-Ni Alloys, Phys. Rev. Letter, Vol. 41, p. 339 (1978).

[3.11] A. Tanaka and T. Jo, J. Phys. Soc. Jpn., Vol. 63, p. 2788 (1994).

[3.12] B. T. Thole, G. van der Laan, J. C. Fuggle, G. A. Sawatzky, R. C. Karnatak and J.-M. Esteva, 3d X-ray-absorption lines and the $3d^9\,4f^{n+1}$ multiplets of the lanthanides Phys. Rev. B, Vol. 32, p. 5107 (1985).

[3.13] R. D. Cowan, The Theory of Atomic Structure and Spectra (University of California Press, Berkeley, 1981).

Chapter 4

Electronic Structure of the Laves Phase Compound $ErCo_2$ Studied by Polarization Dependent Hard X-Ray Photoemission Spectroscopy

Chapter 4

Electronic Structure of the Laves Phase Compound $ErCo_2$ Studied by Polarization Dependent Hard X-Ray Photoemission Spectroscopy

Abstract

$ErCo_2$ band structure calculations for the cubic and rhombohedral structures have been performed. The calculations affirmed the presence of the ferrimagnetic coupling between Er 4*f* and Co 3*d* in the magnetically ordered phase. In the rhombohedral phase, although Co atoms are located in two different atomic sites 9e and 3b, the densities of states and moments of Co 9e and Co 3b are almost similar. Band structure calculations revealed that the contribution of itinerant electrons Co 3*d* to the density of state (DOS) is dominant around Fermi level (E_F) which is the reason in appearance of metamagnetic transition (MMT). The calculated $ErCo_2$ magnetic moment is $\cong 6.6802\mu_B$. In the paramagnetic phase, the majority and minority spins densities of states are almost similar except Er 4*f* band. The Partial densities of states (PDOSs) of Er 4*f* band in both $ErCo_2$ structures have no essential differences and were unaffected by the magnetic phase transition due to highly localized nature of Er 4*f* state. The valence band electronic structures of $ErCo_2$ have been investigated by linear polarized hard X-ray photoemission spectroscopy (HAXPES) in the paramagnetic and ferrimagnetic phases. These experimental data are well described by band structure calculations. Furthermore, the polarization dependent $ErCo_2$ valence band HAXPES spectra in the cubic symmetry have been successfully observed and the experimental results were found to be in a good agreement with the theoretical ones. Moreover, the crucial role of the photoionization cross section to interpret the HAXPES spectra of $ErCo_2$ will be clarified in this work.

4.1. Introduction

The cubic Laves phase RCo_2 (*R*: rare earth or yttrium) intermetallic compounds have been extensively studied from both experimental and theoretical point of view due to their complex electronic and magnetic structures, which give rise to a handful of interesting physical phenomena such as itinerant Co 3*d* electron metamagnetism (IEM), giant magnetoresistance and magnetocaloric effect [4.1-4.8]. The magnetic properties of these

compounds analyzed by Bloch et al [4.9] in the framework of IEM concept, which was first discussed by Wohlfarth and Rhodes [4.1]. RCo$_2$ compounds are ferrimagnet below Curie temperature (T_C) and crystalize in the cubic Laves phase (MgCu2-typ, C15) structure of space group $Fd\bar{3}m$ symmetry above T_C. In the ordered magnetic state, the cubic symmetry undergoes rhombohedral distortion (so-called Laves phase) of space group $R\bar{3}m$ symmetry due to the magnetostrictive effects [4.10, 4.11]. RCo$_2$ compounds with light rare earth (Pr, Nd, Sm) exhibit a ferromagnetic behavior and the R and Co magnetic moments are parallely oriented, while those with heavy rare earth (Gd, Tb, Dy, Ho, Er) an anti-parallel coupling of rare-earth and cobalt moments is evidenced. The large internal exchange field produced by the ferromagnetically order rare-earth 4f moments is sufficient to induced Co magnetic moment of approximately $M_{Co} = 1.00 \pm 0.15\ \mu_B$ oriented antiparallel to the rare earths in zero external magnetic field [4.10-4.12]. If R is nonmagnetic rare earth (ScCo$_2$, YCo$_2$, LuCo$_2$), these compounds are Pauli exchange enhanced paramagnet and the Co magnetization can be induced only by applying strong external magnetic fields larger than 70 T [4.13]. The exchange interactions (R-Co) are usually described by a Campbell (4f-5d-3d) model, where R 5d band polarization plays a dominant part [4.14].

The magnetic measurements and band structure calculations performed on RT$_2$ (R: heavy rare earth, T: Fe, Co, Ni) compounds showed that R 5d band polarization is due to the contribution of both the R 4f-5d local intra-atomic exchange interactions and R 5d-T 3d short range exchange interactions. The R 4f-5d local intra-atomic exchange interactions are proportional to rare earth's de Gennes factor $G = (g_J - 1)^2 J(J+1)$, while R 5d-T 3d short range exchange interactions are proportional to the number of 3d transition metal atoms neighboring to an R site and their moments (magnitude and sign) [4.15-4.16]. The IEM is induced in RCo$_2$ compounds due to the ferromagnetically ordered 4f moments of rare-earth, and the strong R 4f–Co 3d exchange interactions mediated by the R 5d–Co 3d hybridization. Many interesting magnetic properties observed in these compounds can be explained by the shape of the DOS curve near the E_F [4.17]. The RCo$_2$ electronic structure is characterized by a high instability of Co 3d magnetic moments due to the large DOS of Co 3d bands just below the E_F; this is the critical condition for the occurrence of large Co 3d moments which can be strongly changed by external factors such as magnetic field, pressure, impurities and temperature [4.18].The assumption that the cobalt sublattice has metamagnetism is affirmed by calculations of the DOS of YCo$_2$, and DyCo$_2$, HoCo$_2$, and ErCo$_2$ [4.3, 4.19]. The RCo$_2$ compounds were considered as good models for studying of basic properties of IEM; where

the interactions of the localized 4*f* electrons with itinerant electrons 3*d* and the high DOS around the E_F energy play vital role in appearance of IEM [4.20].

Among the RCo_2 intermetallic compounds, $ErCo_2$ shows a first order phase transition from paramagnetic to ferrimagnetic phase at a transition temperature $T_C \cong 35K$ (T_C value's varying in the range between 31-35 K are revealed in the literature) at zero applied magnetic field. So $ErCo_2$ can be considered as a good candidate to discuss the IEM concept, where the exchange interactions are moderate and the E_F lies just above a sharp peak in the DOS [4.8, 4.19-4.22].

Hard X-ray photoemission spectroscopy (HAXPES) is a novel technique to study the electronic structures of solid, so HAXPES studies have attracted much attention [4.23-4.27]. HAXPES has unique characteristics besides the high bulk sensitivity in contrast to the soft X-ray as following: (a) the comparison of the photoionization cross sections for the *s* and *p* electronic states per electrons with those for the *d* and *f* electronic states, so photoionization cross-section have to considered in HAXPES analysis, and (b) strong orbital dependence of the photoelectron angular distribution with respect to the angle between the photoelectron detection direction and the polarization direction (electric field direction) when a linearly polarized light is used as excitation light source [4.28, 4.29]. The calculations on the basis of the photoelectron angular distribution parameters predict that the photoelectron intensity for the *s* and i*p* (i>4) electronic state is strongly suppressed for vertical polarization configuration (s-pol), where the polarization vector (electric field vector) of the incident light is perpendicular to the plane made of the photoelectron detection direction and the incident light direction compared with the horizontal polarization configuration (p-pol), where the polarization vector is within the plane made of the photoelectron detection direction and the incident light direction. Therefore, the extraction of the contributions of *s* and *p* states as well as that for the *d* and *f* states in the bulk valence band of solids becomes feasible by the linear polarized HAXPES, since p-pol configuration is rather sensitive to the *s* and *p* electronic states, while s-pol configuration is highly sensitive to the *d* and *f* electronic states [4.25, 4.26].

In this chapter, band structure calculations have been performed in both $ErCo_2$ structure (Cubic and rhombohedral). $ErCo_2$ valence band spectrum in the disordered and ordered magnetic phases has been measured using HAXPES. Polarization dependent $ErCo_2$ valence band HAXPES spectra in the paramagnetic phase have been successfully observed.

Furthermore, the experimental data are well analyzed by the results of band structure calculations and imply the photoionization cross section.

4.2. Experimental and Computing Method

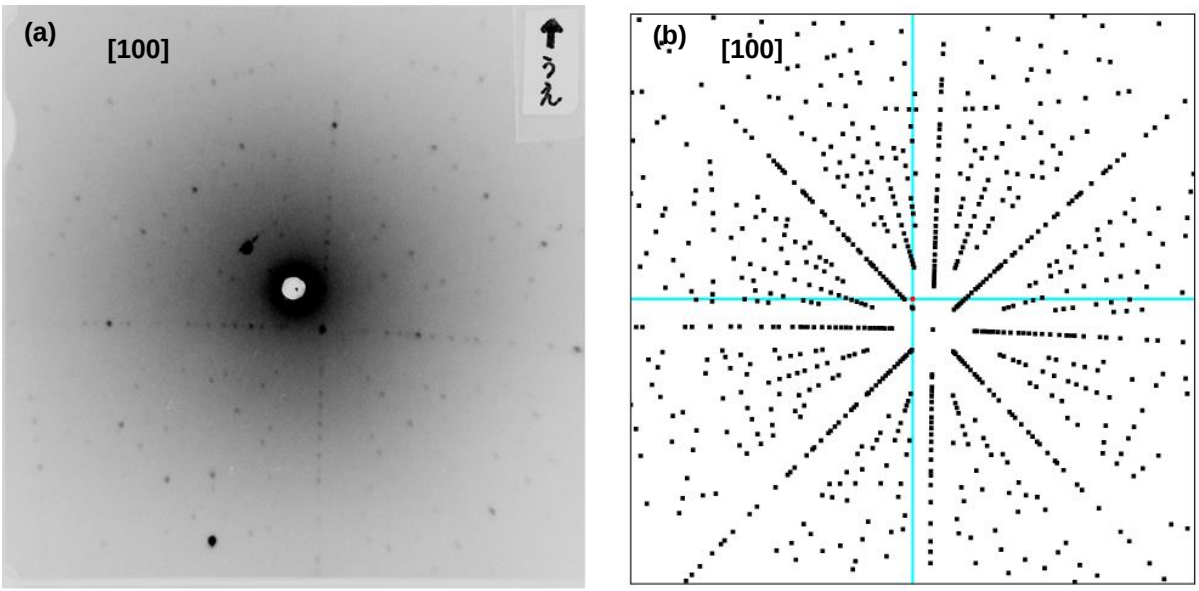

Fig. 4.1. (a) Experimental X-ray back-reflection Laue pattern of $ErCo_2$ along [100] direction, (b) simulated Laue pattern ([HKL]=[001], [hkl]=[0.95 1 0], rotate along X= 3° and rotate along Y= 2°).

A single crystal of $ErCo_2$ was grown by a modified Czochralski method [4.30-4.32] in a tri-arc furnace on copper water-cooled bottom from 7 g mixture of the pure elements (99.9% Er, 99.99% Co). The pulling of crystal was performed under argon protecting atmosphere, a tungsten rod was used as a seed, at pulling speed 10 mm/h. In order to avoid appearance of phase $ErCo_3$, the initial composition was taken as $ErCo_{1.96}$. The resulting single crystal was cylinder-shaped with a height of 20 mm and a diameter of 4 mm. Back-scattered Laue patterns confirmed the single-crystalline state of the sample. **Fig. 4.1** iIllustrates X-ray back-scattered Laue pattern of $ErCo_2$ along [100] direction and its simulation. Laue X-ray spectroscopy was employed to identify the crystal axes.

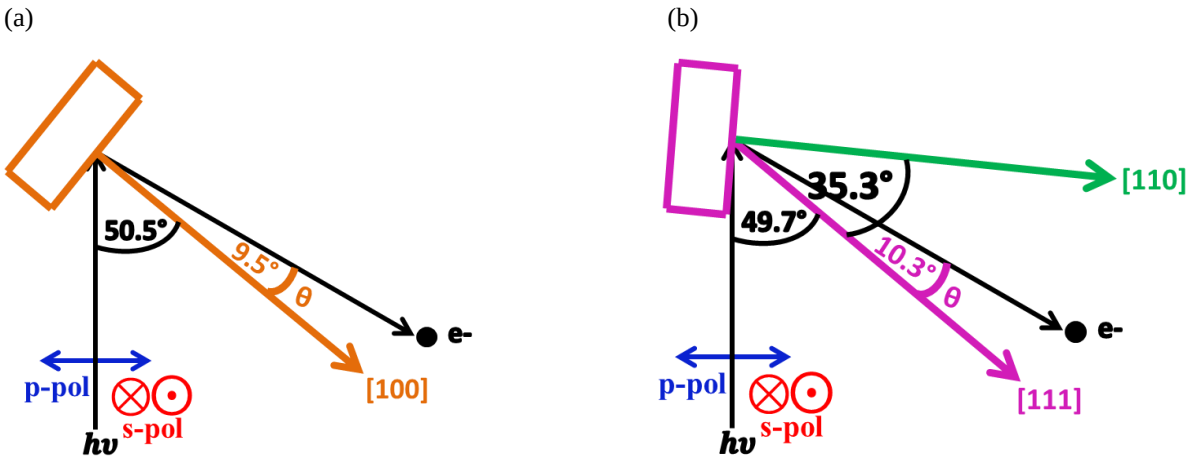

Fig. 4.2. Experimental geometry for HAXPES measurements. Rectangles represent the sample. The angle (θ) between photoelectron detection direction and crystal axis (a) [100] is 9.5° and (b) [111] is 10.3°.

The temperature and polarization dependent measurements of single crystal $ErCo_2$ valence band HAXPES spectra [4.26, 4.33] have been performed at BL19LXU of Spring-8 [4.34] using an MBS A1-HE hemi-spherical photoelectron spectrometer. The photon energy is set to ≅ 7.9 KeV by Si [111] double crystal monochrometer selected linearly polarized radiation along the horizontal direction and further monochromatized by Si [620] channel-cut crystal. Two single-crystalline [100] diamonds were used as a phase retarder located downstream of the channel cut crystal in order to switch the linear polarization of X-ray beam from the horizontal to the vertical direction [4.35]. The thickness of each diamond plate is 0.25 mm, and the transmittance of the X-ray beam after the double diamond phase retarder is ≅47.2%. Degree of the linear polarization P_L detected by NaI scintillation counters placed downstream of the double diamond phase retarder. P_L of the polarization switched X-ray after the phase retarder was estimated as ≅ -0.85. Since the detection direction of photoelectrons was set in the plane with an angle to the incident photons of 60°, as shown in **Fig. 4.2**, the experimental configuration at the horizontally (vertically) polarized light excitation corresponds to the p-polarization (s-polarization). The excitation light was focused onto the sample by using an ellipsoidal Kirkpatrik- Baez mirror. To precisely detect polarization dependent photoemission spectra, the photon flux was optimized so as to set comparable photoelectron count rates between the s-polarization and p-polarization configurations.

The sample was fractured under ultra-high vacuum ≅ 1.2×10^{-7} Pa along the [100] plane in *situ*. The experimental geometry was controlled using a newly developed two-axis manipulator [4.27], where the normal emission direction parallel to the [100] direction in **Fig.**

4.2. The qualities of the sample and surface were checked on the basis of the absence of any core level spectral weight caused by the impurities as a shown in ESCA (electron spectroscopy for chemical analysis), O 1s and C 1s of sample (**Fig. 4.3a, b** and **c** respectively). $ErCo_2$ valence band temperature dependent measurements have been performed along [100] direction above ($T \cong 45\ K$) and below ($T \cong 25\ K$) T_C which is $34\ K$, while $ErCo_2$ valence band polarization dependent measurements have been recorded at $T \cong 45$ K along [100]. Measurement have been performed at 200 eV pass energy under energy resolution (FWHM) ≅ 220 meV as a shown in **Fig.4.3d**. Also, at $T \cong 45$ K $ErCo_2$ valence band polarization dependent measurements have been performed along [111] direction at 200 eV pass energy and energy resolution (FWHM) ≅ 375.5 meV.

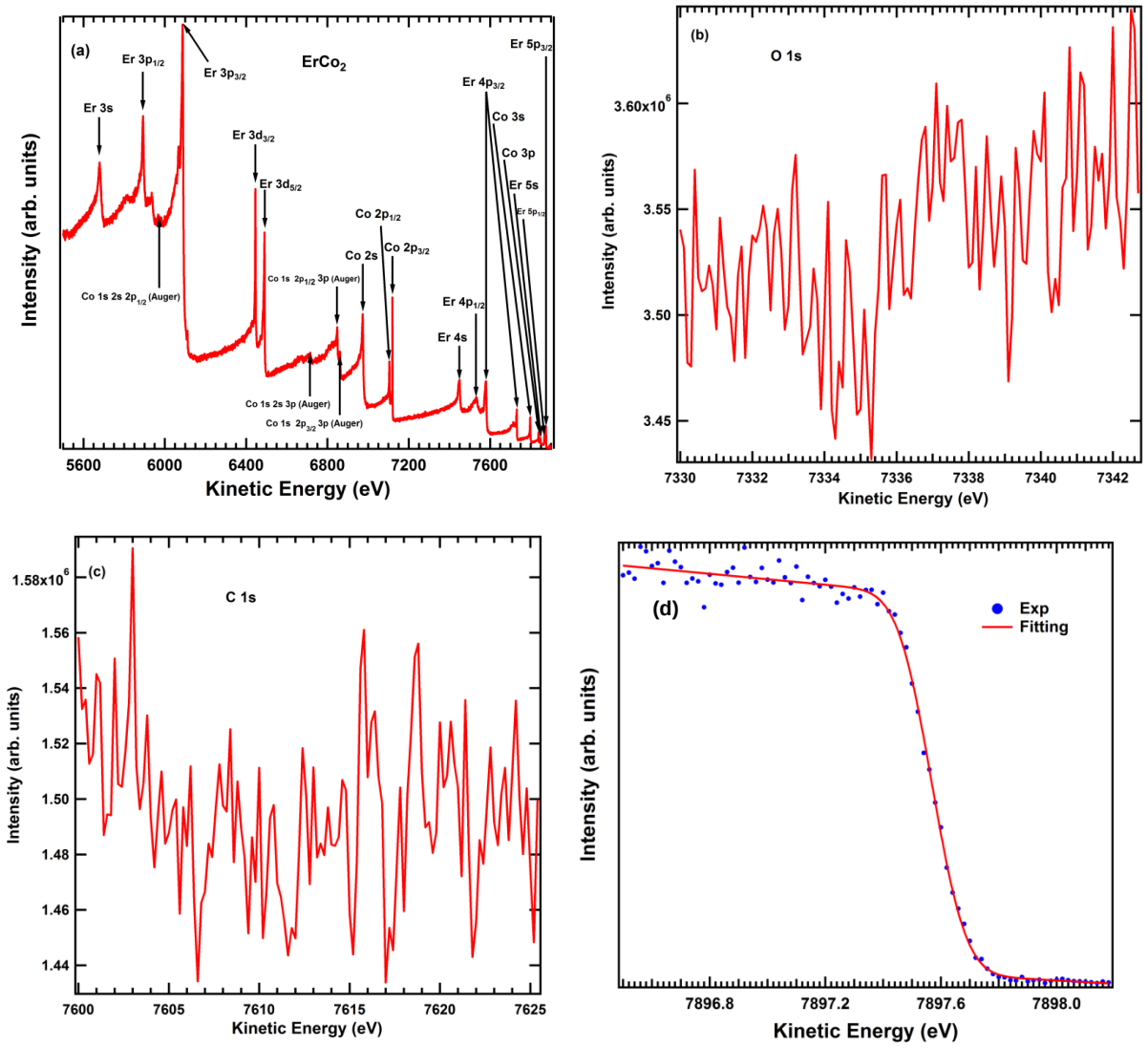

Fig. 4.3. (a) ESCA of single crystal $ErCo_2$. (b) O 1s, (c) C 1s and (d) Au at p-pol, T: 25 K, FWHM: 220 meV, E_F is 7897.57 eV, pass energy (E_P): 200 eV and hν=7.9 keV at [100] direction of $ErCo_2$.

The excited (cubic) and ground (rhombohedral) state electronic structures of $ErCo_2$ have been performed using coherent potential approximation (CPA) [4.36] and self-interaction correction-local spin density approximation (SIC-LSDA) [4.37] methods, respectively, in the framework of density function theory (DFT) [4.38] using Akai KKR (Korringa-Kohn-Rosroker) program at magic number 0.32 and Brillouin zone quality 10, these were found to be appropriate to provide results with good convergence. The valence band basis consists of *s*, *p*, *d* and *f* orbitals. The lattice parameters of this sample and which used in these calculations are $a = 7.133$ Å for the cubic structure at 45 K and are $a = 5.0552$ Å and $c = 12.3427$ Å for the rhombohedral structure at 25 K. Also, band structure calculation performed at lattice parameters extrapolated to 0 K in order to obtain more stable energy state. It is well known that LSDA band structure treatment leads to poor and insufficiently results to describe the 4*f* states due to the strongly correlated nature of 4*f* electrons [4.39]. So in order to estimate Er 4*f* photoemission spectrum, the ionic calculations of Er 4*f* including the full multiplet theory [4.40] and the local crystal electric field splitting (CEF) have been performed using XTLS 9.0 program [4.41]. The atomic parameters (**Table 4.1**), namely F for Coulomb interactions and ζ parameter for spin orbit interaction have been obtained using Cowan's code [4.42] based on Hartree-Fock method, with a reduction of about 80% for $F^2(4f\ 4f)$ from the values obtained using the Cowan's code, for $F^4(4f\ 4f)$ and $F^6(4f\ 4f)$ interactions estimated based on Carnall *etal* [4.43] to fit the Er 4*f* photoemission spectra. The electrostatic interactions in terms of products of Slater integrals F_k and angular coefficient f^k is written as [4.43, 4.44]:

$$E_e = \sum_{k=0}^{6} f^k F_k \qquad (k \text{ even}) \tag{4.1}$$

where, $$F^k = D_k F_k \tag{4.2}$$

For f electrons the coefficient D_k is given as [4.44]:

$$D_2=225,\ D_4=1089,\ \text{and}\ D_6=7361.64$$

For the trivalent Er^{3+}, the ratios $\frac{F_4}{F_2}$ and $\frac{F_6}{F_2}$ calculated from a fit of lanthanide aquo-ion data are [4.43]:

$$\frac{F_4}{F_2} = 0.152 \qquad \frac{F_6}{F_2} = 0.0167$$

By using $F^2(4f4f)$ from Cowan code after reduction and substitution in **equation (4.2)**, we can determine $F^4(4f4f)$ and $F^6(4f4f)$ based on Carnall *etal* [4.43] as shown in **Table 4.1**.

Table 4.1. Er 4*f* atomic parameters using Cowan code and based on Carnall *etal.*

	Cowan code		Based on Carnall *etal.*	
Atomic parameter	Ground state (eV)	Excited state (eV)	Ground state (eV)	Excited state (eV)
$\zeta\, 4f$	0.3023	0.3212		
$F^2(4f4f)$	16.0937	16.9651		
$F^4(4f4f)$	10.0959	10.6879	9.4682	9.9829
$F^6(4f4f)$	7.2628	7.70161	7.0321	7.4145

4.3. Results and discussion

4.3.1. $ErCo_2$ Band Structures

4.3.1.1. Magic Number

A number of attempts have been performed for band structure calculations of $ErCo_2$ in order to obtain more stable results and the best results agree well with the experimental ones, these attempts are summarized in **Appendix A** (**Table A.1**). The main factor in this scenario is the magic number; the magic number shows the degree of which SIC is correct. Where with increasing the magic number, there is no changing in $ErCo_2$ DOS expect Er 4f state. The center of gravity (C. G= $\frac{\int xf(x)dx}{\int f(x)dx}$) in DOS of Er 4*f* state shifts to lower energy as a shown in **Fig. 4.4**. The PDOSs at different magic number for Er and Co atoms in the cubic structure of $ErCo_2$ are given in **Appendix A (Fig. A.1)**, where PDOSs of Er and Co atoms have no essential difference with increasing the magic number except PDOS of Er 4*f* state shifts to a lower energy.

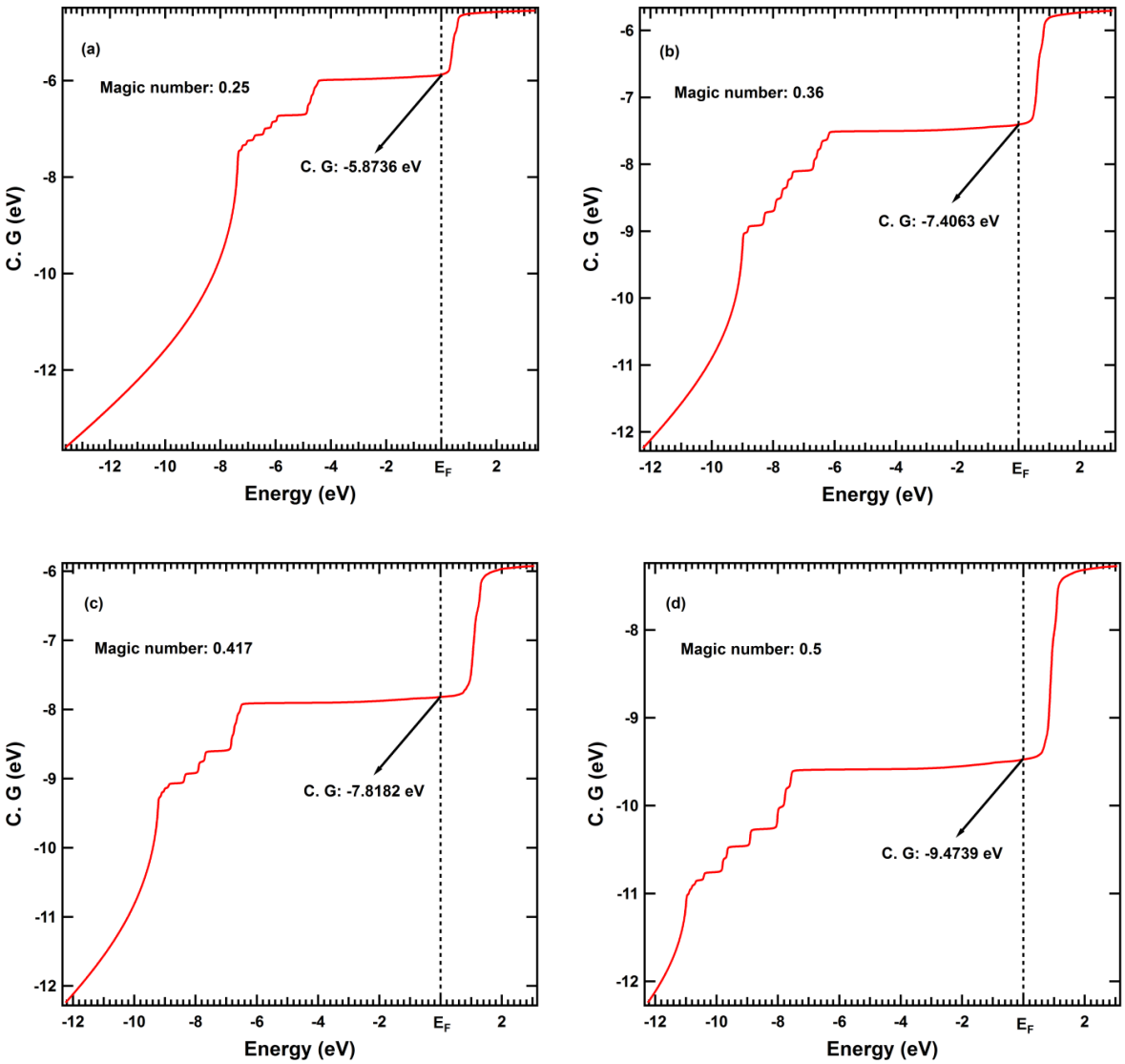

Fig. 4.4. Center of gravity of Er 4*f* state at different magic numbers.

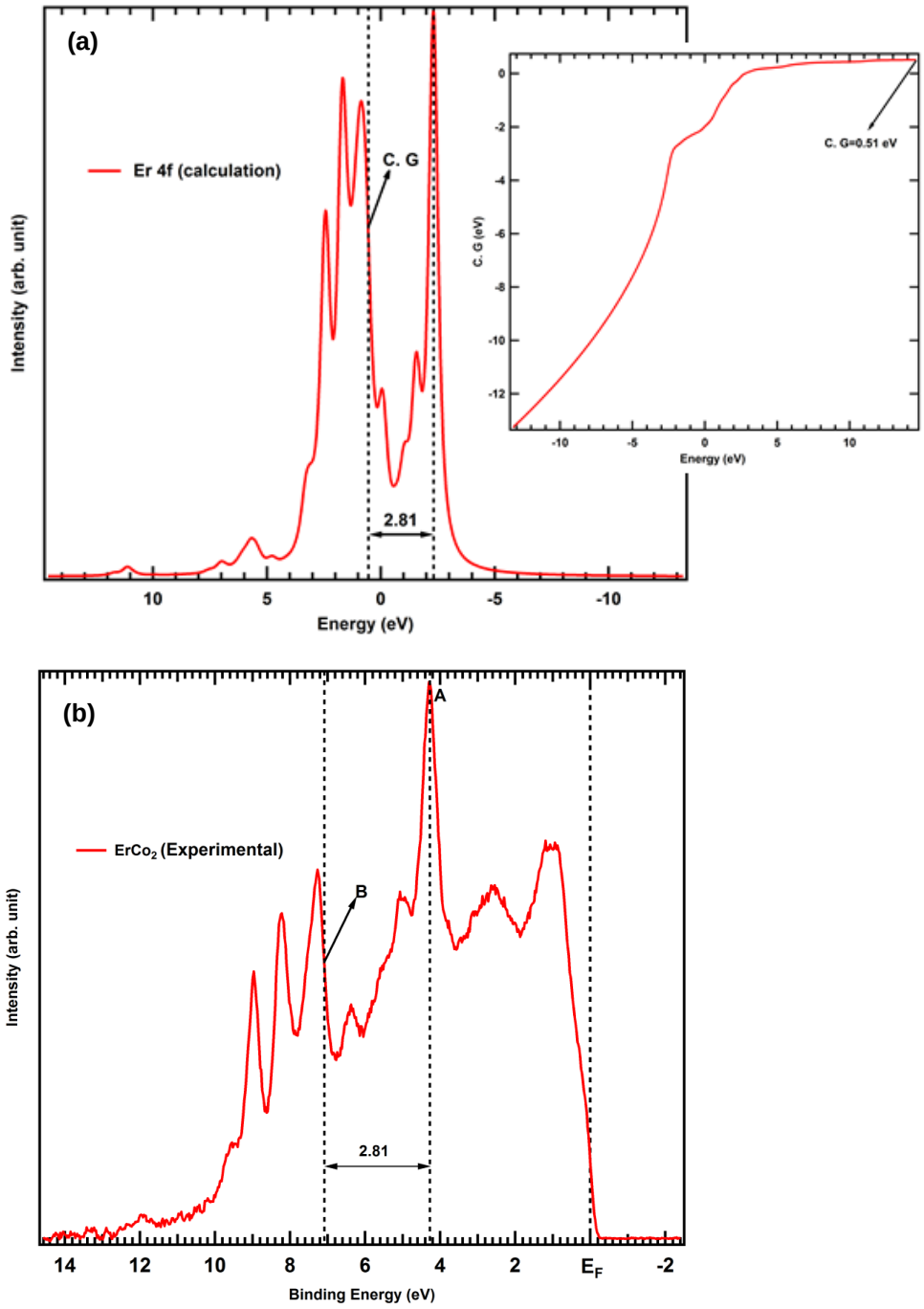

Fig. 4.5. (a) Calculated Er 4*f* photoemmision spectrum using ionic calculations, the inset is center of gravity of Er 4*f* ~0.51 eV. (b) Experiment valence band HAXPES spectrum in the cubic $ErCo_2$, where the shirely type back ground has been subtracted from the raw data.

In order to decide the best magic number, the Er 4*f* photoemission spectrum estimated using ionic calculations by XTLS program **(Fig. 4.5a)**. From the comparison between the experimental and calculated Er 4*f* photoemission spectra (**Fig. 4.5**), the center of gravity of the experimental Er 4*f* photoemission spectrum is about 7.11 eV at B in **Fig. 4.5b** which correspond to 0.32 magic number as a shown in **Fig. 4.6a**.

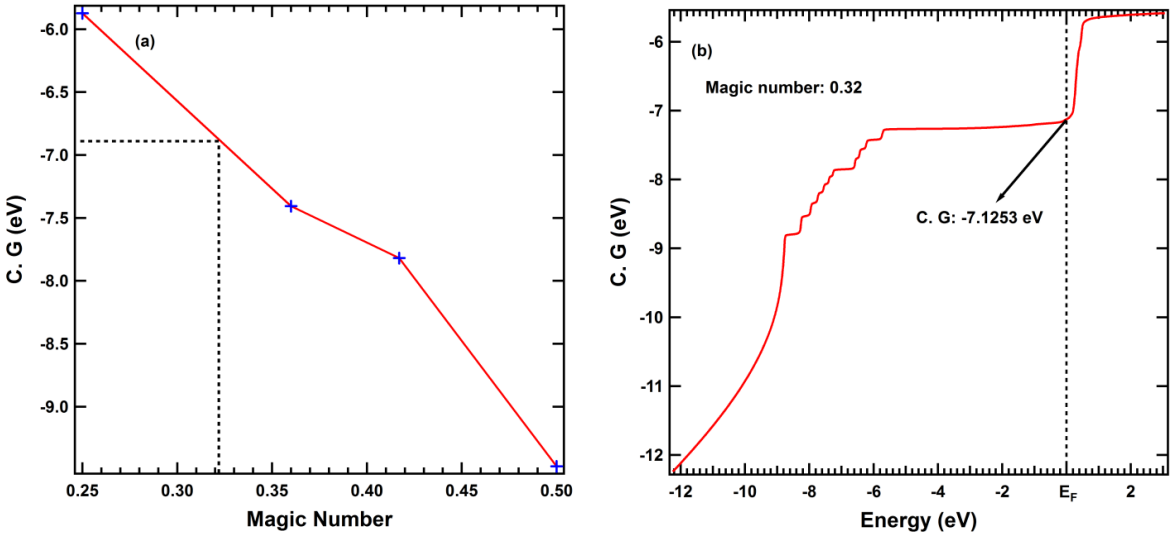

Fig. 4.6. (a) C. G of Er 4*f* state vs magic number. (b) Center of gravity of Er 4*f* state at magic number=0.32.

Fig. 4.6a represents C. G of Er 4*f* state versus magic number, 7.11 eV (experiment C.G) correspond to the magic number ≅ 0.32, so the best magic number can describe well the experimental data is ≅ 0.32. **Fig. 4.6b** illustrates C. G of Er 4*f* state at magic number 0.32, at E_F the C.G is about 7.12 eV which is near from the experimental value (7.11 eV).

4.3.1.2. $ErCo_2$ Magnetic Moment

Band structure calculations have performed in both structures of $ErCo_2$. **Table 4.2** illustrates the computed total energy and Er and Co magnetic moments in the cubic and rhombohedral structures of $ErCo_2$. The calculations have performed at lattice parameters at 45 K for the cubic structure, 25 K for rhombohedral structure and lattice parameters extrapolated to 0 K, there is no essential difference in the results of band structure in both cases. Below T_C, The calculations revealed that Er and Co magnetic moments align antiparallel to each other and there is antiparallel coupling between the spin moments of the Er and Co atoms. The total Er magnetic moment in the rhombohedral structure is higher than that in the cubic structure because PDOSs of Er 5*d*, 6*p* and 6*s* bands are spin-polarized in rhombohedral structure and non-spin polarized in cubic structure. In the ordered magnetic state, the magnetic moment of $ErCo_2$ is mostly dominated by Er sublattice, where Er magnetic moment is ≅ 8.6957 μ_B which is much larger than that of the two Co atoms, Co magnetic moment $M_{Co} \cong -1\ \mu_B$.

Table 4.2. Total energy and magnetic moments (in μ_B) of Er and Co atoms in $ErCo_2$ compound at magic number 0.32.

	M_s	**M_o**	**Total**	**M_s**	**M_o**	**Total**
	Cubic ($Fd\bar{3}m$) structure					
	T: 45K			Extrapolated to 0K		
Er (8a)	2.69	5.83	8.52	2.69	5.83	8.52
Co (16d)						
Total Energy (Ry/fu)	-31720.0980			-31720.0981		
	Rhombohedral ($R\bar{3}m$) structure					
	T: 25K			Extrapolated to 0K		
Er (6c)	2.88	5.81	8.70	2.88	5.81	8.70
Co (9e)	-0.88	-0.083	-0.96	-0.89	-0.08	-0.97
Co (3b)	-0.92	-0.13	-1.05	-0.93	-0.13	-1.06
Total Energy (Ry/fu)	- 31720.0954			- 31720.0952		

At the ambient temperature ($T>T_C$) the compound has a cubic ($Fd\bar{3}m$) structure with atomic sites: Er (8a) (0.125, 0.125, 0.125) and Co (16d) (0.5, 0.5, 0.5). At the low temperature ($T<T_C$) the compound has a rhombohedral ($R\bar{3}m$) structure with atomic sites: Er (6c) (0, 0, z), Co (9e) (0.5, 0, 0) and Co (3b) (0, 0, 0.5) [4.8].

The computed $ErCo_2$ magnetic moment is $\cong 6.6802\ \mu_B$. These results are consistent with the neutron diffraction studies and the previous band structure calculations [4.12, 4.45]. Co 3d moments are essentially due to the spin contribution, where Co spin moment (M_s) is higher than Co orbital moment (M_o). In the rhombohedral structure, Co magnetic moments at 9e sites are lower by $\cong 0.0851\ \mu_B$ than those at Co 3b sites. Unfortunately, the calculations revealed that the total energy of the cubic structure is smaller than that of the rhombohedral structure and this behavior disagree with reality. Whereas the cubic structure is the excited state structure of $ErCo_2$ while the rhombohedral structure is its ground state structure. This disagreement between calculation and reality may refer to the electron correlation effect.

4.3.1.3. $ErCo_2$ Density of State

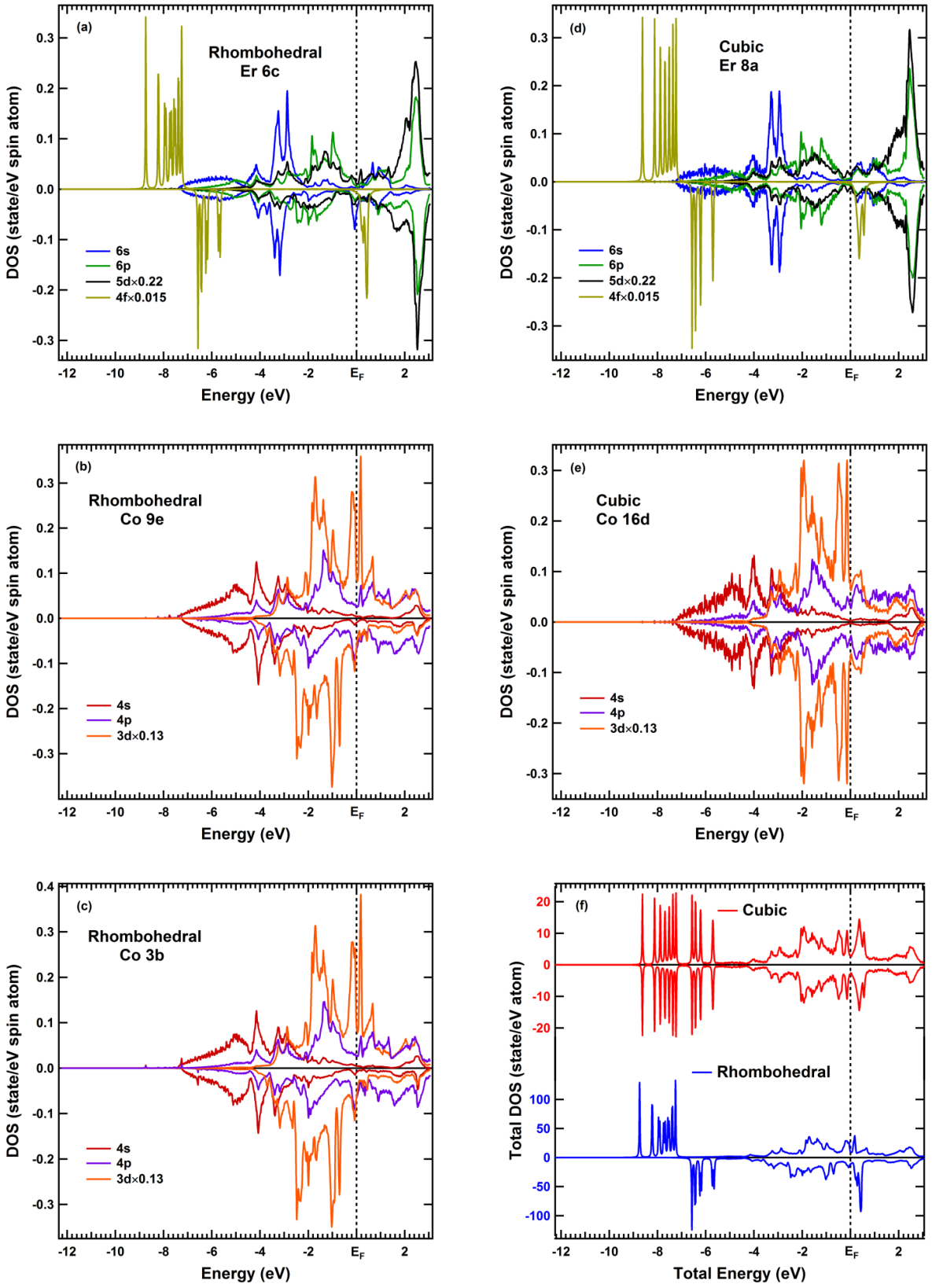

Fig. 4.7. Partial and total DOS of (a) Er 6c, (b) Co 9e, (c) Co 3b, (d) Er 8a, (e) Co 16d and (f) total DOS, in rhombohedral and cubic structures of $ErCo_2$ compound.

PDOSs and total DOS for Er and Co atoms in both structures of $ErCo_2$ are given in **Fig. 4.7**. PDOSs of Er and Co atoms have been performed for majority and minority spins, DOSs are scaled by multiplying them by 0.22, 0.015 and 0.13 for Er 5*d*, Er 4*f* and Co 3*d* bands respectively for direct comparison with other DOSs. **Fig. 4.7a** shows (*s, p, d* and *f*) PDOSs of Er atoms in the rhombohedral structure (ferrimagnetic state). The highest DOS are seen in 4*f* then 5*d* states, the center of gravity of Er 4*f* is ≅ 7.12 eV. Near E_F 4*f*, 5*d* and 6*p* bands have a very small contribution to the DOS. For Er 6*s*, E_F is located close to a peak in DOS which is high in spin down sub-band, and the corresponding DOS in the spin up sub-band is minimum. **Fig. 4.7b** and **Fig. 4.7c** present (*s*, *p* and *d*) PDOSs of Co 9e and Co 3b atoms in the rhombohedral structure respectively. Although Co atoms are located in two different sites, the PDOSs of both Co 9e and Co 3b have no significant differences. Co 3*d* revealed the highest DOS and E_F is located near a sharp peak in DOS which is high in spin up sub-band and the corresponding DOS in the spin down sub-band is rather low, this is the reason why the IEM occurs in $ErCo_2$ compounds. The 4*p* and 4*s* bands revealed a small DOS near E_F. **Fig. 4.7d** and **Fig. 4.7e** illustrate the PDOSs of Er and Co atoms in the cubic structure (paramagnetic state) respectively. In the cubic structure the majority and minority spins PDOSs are almost similar except for the Er 4*f* states. The PDOSs of Er 4*f* states in both structures of $ErCo_2$ are almost similar due to the localized natural of Er 4*f* which are unaffected by the phase transition due to the large random local magnetic moment, but in the other states there are no random local magnetic moments so the difference between PDOS in up and down spin sub band is nearly zero.

In paramagnetic calculations, near E_F, Er 6*s* band has only a small contribution to DOS, while Co 3*d* state has a high DOS in both up and down spin sub-band and the sharp peak near E_F leading to instability of Co sublattice. **Fig. 4.7f** illustrates total DOS in both structure of $ErCo_2$, where in the cubic structure the total DOS in both up and down spin sub-band is nearly identical, while in the rhombohedral structure it is different. The main contribution to the total DOS near E_F originates from Co 3*d* states contribution.

The total DOS around E_F in ferrimagnetic and paramagnetic phase of $ErCo_2$ have some agreements and disagreements with the previous band structure calculations. For example, in the ordered magnetically state the present DOS over E_F (unoccupied state) is nearly agree with DOS in ref 4.8 and 4.46 and disagree with that in ref. 4.21and 4.47 at the up spin sub-band, while in the down spin sub-band the current DOS after E_F is inconsistent with the previous studies [4.8, 4.21, 4.46, 4.47]. Just below E_F (occupied state), the present DOS in up

spin sub-band is little agree with that in ref 4.8, 4.46 and ref. 4.21 and disagree with DOS in ref. 4.47, but in the down spin state the current DOS is consistent with that in ref 4.8, 4.21 and 4.46 and inconsistent with DOS in ref. 4.47 (the peak located at E_F). in the paramagnetic state the present DOS of Co bands is nearly agree with that in ref. 47 except at 0.48 eV the peak in the down spin state is different than the corresponding peak in the up spin state. But in the present calculations the up and down spin state are similar in the paramagnetic state. PDOS and total DOS of each electronic stated separately in both structures of $ErCo_2$ are given in appendix A (**Fig. A.2**, **Fig. A.3** and **Fig. A.4**).

4.3.2. Photoionization Cross Section

The angular dependence for the differential photoionization cross section in the case of linearly-polarized light is written as [4.48]:

$$\frac{d\sigma}{d\Omega}(\theta,\varphi)=\frac{\sigma}{4\pi}\left[1+\left(\beta+\Delta\beta_{lp}\right)P_2(cos\theta)+(\gamma cos^2\theta+\delta)sin\theta cos\varphi+\eta P_2(cos\theta)cos2\varphi\right.$$
$$\left.+\mu cos2\varphi+\xi(1+cos2\varphi)P_4(cos\theta)\right] \quad (4.3)$$

where the dipole, non-dipole, photoelectron parameters, θ and φ are defined in chapter 1. **Table 4.3** reveals the dipole, non-dipole, and photoelectron parameters for the electronic structures of Er and Co atoms at photoelectron energy 7.9 keV, have been evaluated from data in ref. [4.48].

Table 4.3. Photoionization cross section parameters for the electronic structures of Er and Co atoms at 7.9 keV.

Shell	$\Delta\beta_{lp}$	η	μ	ξ	σ	β	γ	δ
Co $3d_{3/2}$	-6.250×10^{-2}	-2.210×10^{-2}	9.804×10^{-2}	-7.624×10^{-2}	2.610×10^{-3}	3.231×10^{-1}	9.049×10^{-1}	4.146×10^{-1}
Co $3d_{5/2}$	6.810×10^{-2}	-1.161×10^{-2}	8.918×10^{-2}	-7.700×10^{-2}	3.730×10^{-3}	3.366×10^{-1}	9.175×10^{-1}	4.171×10^{-1}
Co $4s_{1/2}$	-1.767×10^{-2}	1.627×10^{-2}	2.175×10^{-2}	-3.741×10^{-2}	1.870×10^{-2}	1.982	1.261	-2.600×10^{-6}
Ga $4p_{1/2}$	-3.100×10^{-2}	1.270×10^{-2}	5.806×10^{-2}	-6.941×10^{-2}	4.960×10^{-3}	9.134×10^{-1}	1.2938	1.299×10^{-1}
Er $4f_{5/2}$	-6.980×10^{-2}	-1.488×10^{-2}	1.081×10^{-1}	-9.200×10^{-2}	3.933×10^{-2}	5.778×10^{-1}	1.255	3.801×10^{-1}
Er $4f_{7/2}$	-6.360×10^{-2}	-9.649×10^{-3}	1.015×10^{-1}	-9.180×10^{-2}	4.835×10^{-2}	5.799×10^{-1}	1.236	3.918×10^{-1}
Er $6s_{1/2}$	-2.472×10^{-2}	7.900×10^{-3}	1.120×10^{-2}	-1.922×10^{-2}	1.516×10^{-2}	1.970	-1.104×10^{-1}	-1.660×10^{-3}
(Lu,Hf)$5d_{3/2}$	-1.727×10^{-2}	4.969×10^{-3}	4.441×10^{-2}	-6.199×10^{-2}	4.895×10^{-2}	1.282	1.349	1.356×10^{-1}
(Tl, Pb)$6p_{1/2}$	-8.677×10^{-3}	-1.046×10^{-3}	7.257×10^{-3}	-6.222×10^{-3}	2.483×10^{-2}	1.6744	3.313×10^{-1}	7.530×10^{-3}

Photoionization cross sections of Er and Co structures for vertical (s-pol) and horizontal (p-pol) polarized light at photoelectron energy ≅7.9keV (HAXPES) have been evaluated using **equation (4.3)** as a given in **Table 4.4**. Cross section of 4*p*, 5*d* and 6*p* structures have been evaluated using angular distribution parameters of Ga, (Lu and Hf) and (Pb and Tl) respectively. In the HAXPES with a linearly polarized excitation, p-pol

configuration is rather sensitive to the *s* and *ip* (i>4) electronic states, while s-pol configuration is highly sensitive to the *d* and *f* electronic states as illustrated in **Table 4.4** and in partial DOS of $ErCo_2$ after broadening and applying cross section (see appendix A, **Fig. A.5**). **Table 4.4** reveals that in p-pol configuration *s* and *ip* (i>4) electronic states have higher cross section than *d* and *f* electronic states, while in s-pol configuration, the cross section of *d* and *f* electronic states are higher. Therefore, the extraction of the contributions of *s* and *ip* states in addition to the *d* and *f* states in the bulk valence band of solids becomes available using linear polarization HAXPES [4.25, 4.26] and photoionization cross-section plays a crucial role in the analysis of HAXPES data.

$ErCo_2$ valence band photoemission spectrum has been estimated after broadening the calculated PDOSs with a Gaussian (edelt = 0.02) and applying the corresponding photoionization cross sections (see appendix A, **Fig. A.5** and **A.6**), except Er 4*f* partial density of state is replaced by atomic multiplets. The effect of edelt on photoemission spectrum is illustrated in appendix A (**Fig. A.5**). Photoemission spectrum for each electronic state =DOS per electron number × cross section per 1 electron.

Table 4.4. Photoionization cross section per one electron of Er and Co electronic structures for vertical (s-pol) and horizontal (p-pol) polarizations.

Structure	s-pol	p-pol
6*s*	1.26×10^{-5}	1.37×10^{-3}
6*p*	1.56×10^{-4}	1.89×10^{-3}
5*d*	2.60×10^{-4}	1.23×10^{-3}
4*f*	2.38×10^{-4}	3.75×10^{-4}
4*s*	2.84×10^{-6}	1.33×10^{-3}
4*p*	8.98×10^{-5}	2.10×10^{-4}
3*d*	2.79×10^{-5}	3.76×10^{-5}

The incident photon energy $\cong 7.9$ keV. For s-pol $\theta = 90^0$ and $\varphi = 120^o$. For p-pol $\theta = 30^o$ and $\varphi = 180^o$.

4.3.3. Temperature-dependent $ErCo_2$ valence band HAXPES spectra

Fig. 4.8a illustrates the temperature dependent valence band HAXPES spectra of single crystal [100] direction of $ErCo_2$ measured above (45 K) and below (25 K) T_C. $ErCo_2$ valence band spectrum reveals the multiplet structure of Er 4*f* levels [4.49-4.51], three peaks (a,

b, and c) ranging from binding energies about 10 to 7 eV represent Er $4f_{5/2}$, and other two peaks (d and e) ranging from about 6 to 3.6 eV represent Er $4f_{7/2}$. Also, $ErCo_2$ valence band spectrum illustrates structures f and g at binding energies about 2.64 and 1.07 eV respectively.

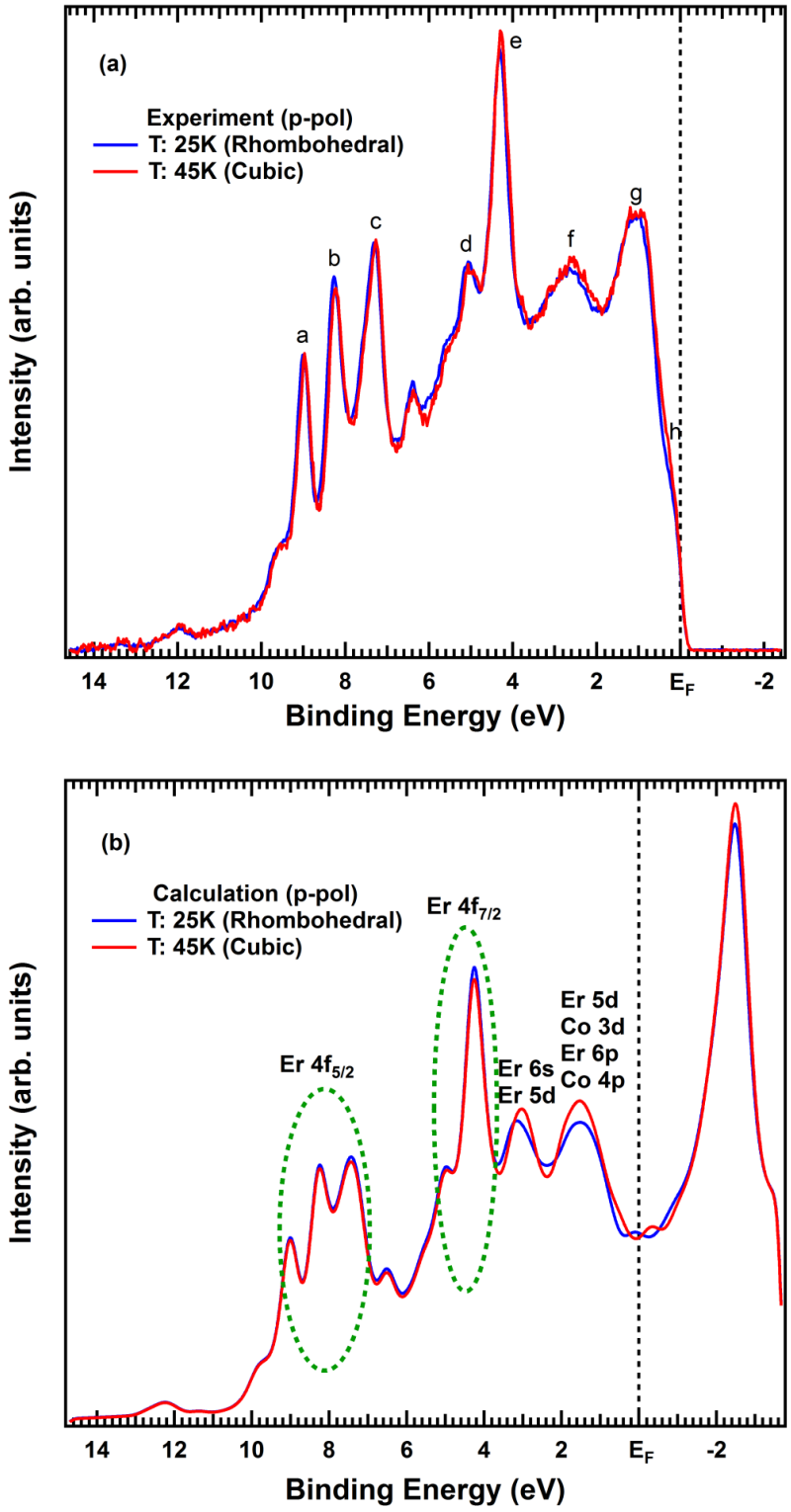

Fig. 4.8. (a) Temperature-dependent $ErCo_2$ valence band HAXPES spectra, where the Shirely-type background has been subtracted from the raw spectra, the spectra are normalized by $ErCo_2$ spectra weight. (b) Calculated temperature-dependent $ErCo_2$ valence band HAXPES spectra.

The calculated $ErCo_2$ valence band photoemission spectrum in **Fig. 4.8b** shows that the structure f represents Er 6s state and it located at binding energy about 3.02 eV which is different by 0.38 eV than the corresponding position in the experimental spectrum in **Fig. 4.8a**. While the structure near E_F is due to the contribution of Co 3*d*, Er 5*d*, Co 4*p* and Er 6*p* states and it is at binding energy about 1.52 eV, which is different by 0.45 eV than the corresponding location in the experimental spectrum in **Fig. 4.8a**. There are difference in the intensity between the experimental and calculated spectra near E_F and the peak position of structures f and g located more near from E_F in the experimental spectrum than the calculated ones. However it can be clearly observed that the peaks position of the experimental spectra are coincide very well with that of the theoretical spectra. These disagreements suggest that understanding of electronic states of $ErCo_2$ is not yet enough using the present band structure calculation. Further theoretical studies taking electron correlation is needed.

A comparison between the measured temperature dependent of $ErCo_2$ valence band HAXPE spectra and the computed ones is presented in **Fig. 4.8**. In the experimental spectra (**Fig. 4.8a**), the highest peak (e) is slightly stronger at high temperatures than low temperatures; this behavior disagrees with the corresponding peak position in the computed spectra (**Fig. 4.8b**) due to the highest contribution of DOS for Co 4s band at about 4 eV. Also, the structures at f, g, and h are slightly stronger at high temperatures than at low temperatures, and these agree with the corresponding structures in the calculated spectra. Although the calculated temperatures dependent near E_F are little larger than the experimental ones, the computed spectra reproduces well most features of the experimental HAXPES spectra.

4.3.4. Polarization-dependent $ErCo_2$ Valence Band HAXPES Spectra

A comparison between the measured polarization dependent of $ErCo_2$ valence band HAXPE spectra in the cubic symmetry along the [100] direction at T ≅ 45 K and the computed ones is displayed in **Fig. 4.9**. In **Fig. 4.9a** the highest peak (e) and Er $4f_{5/2}$ structures (a, b, and c) are stronger in the vertical polarization (s-pol) than the horizontal polarization (p-pol), structure at h is slightly stronger in s-pol, while structures at d, f, and g are stronger in p-pol, all these features agree well with the corresponding positions in the computed spectra (**Fig. 4.9b**). Here, both the measured and calculated spectra verify that s-pol suppresses the s-electronic state as shown in Er 6s states (structure f), which is one of the unique properties of linear polarized HAXPES. From this comparison, the computed polarization dependent of

$ErCo_2$ valence band photoemission spectra reproduce well the experimental polarization dependent of $ErCo_2$ valence band HAXPES spectra.

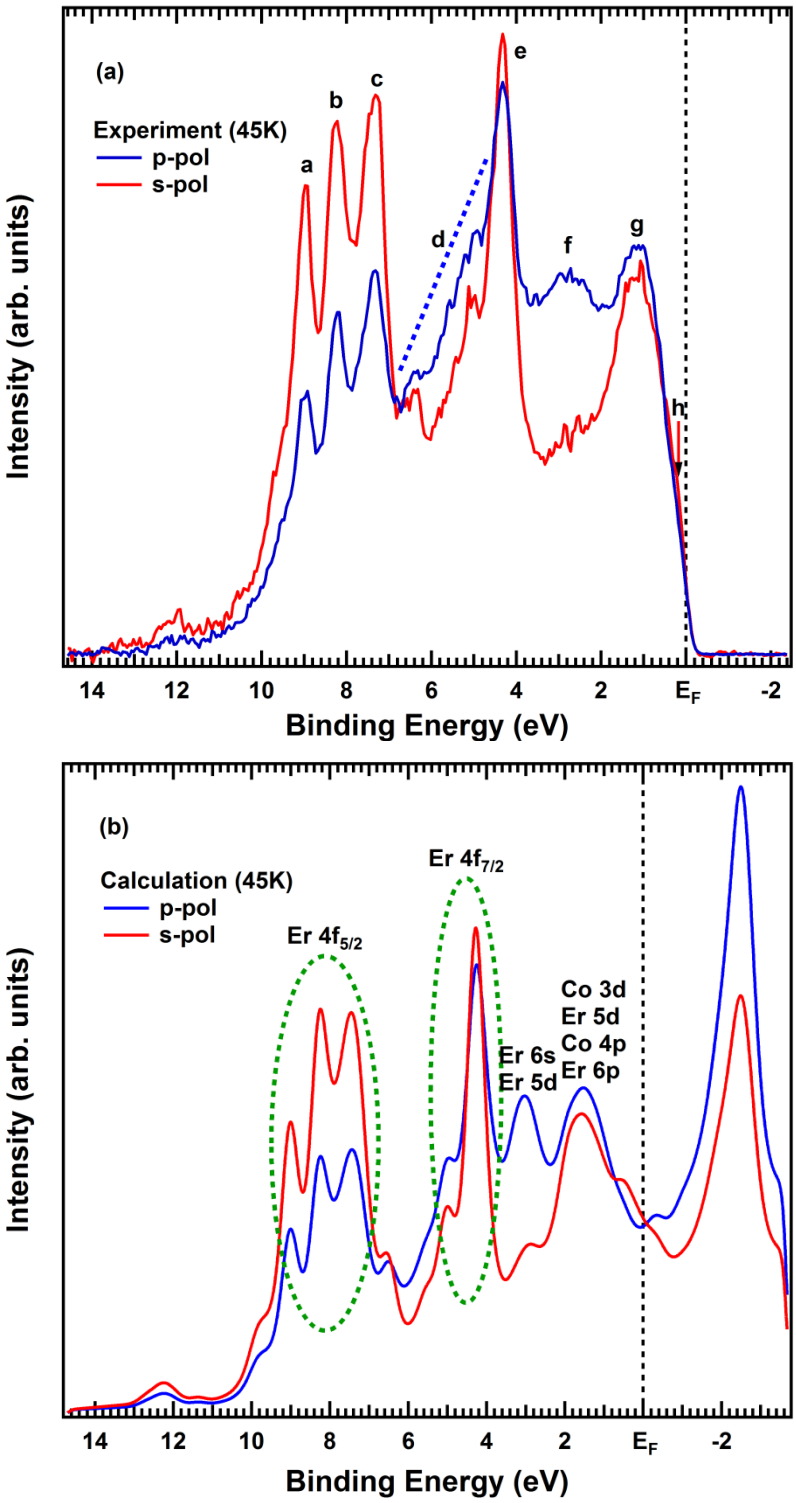

Fig. 4.9. (a) Polarization-dependent $ErCo_2$ valence band HAXPES spectra along [100] direction of cubic $ErCo_2$, measured at 45 K, where the Shirely-type background has been subtracted from the raw spectra. The spectra are normalized by $ErCo_2$ spectra weight. (b) Calculated polarization-dependent $ErCo_2$ valence band HAXPES spectra (calculated in paramagnetic phase).

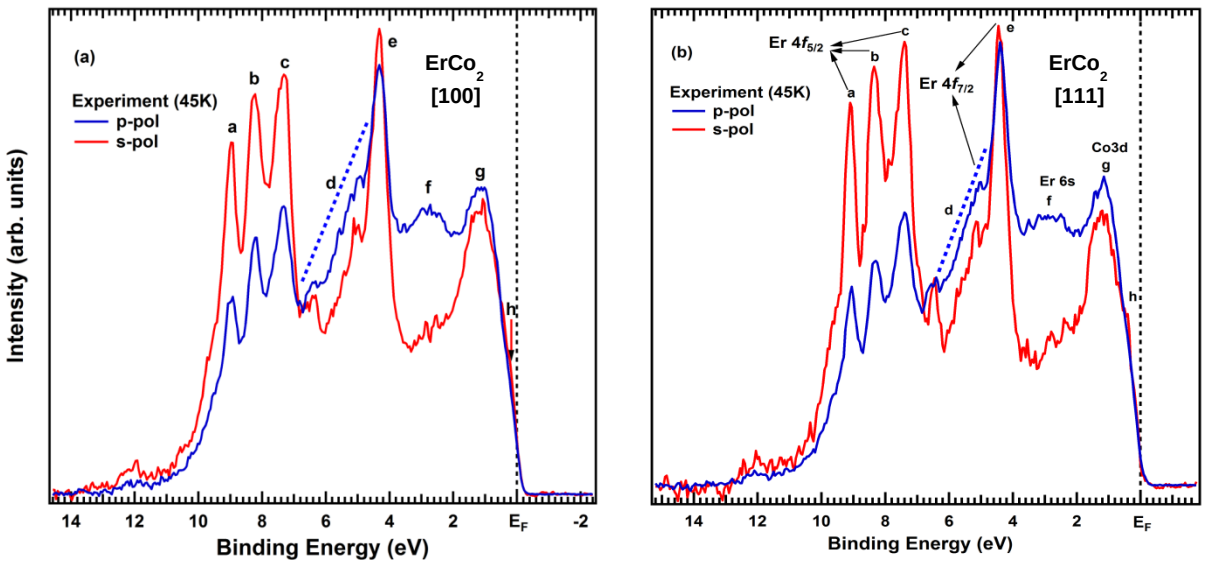

Fig. 4.10. Polarization-dependent $ErCo_2$ valence band HAXPES spectra, where the Shirely-type background has been subtracted from the raw spectra, the spectra are normalized by $ErCo_2$ spectra weight. (a) Along [100] direction. (b) Along [111] direction.

Fig. 4.10 shows the experimental polarization dependent $ErCo_2$ valence band HAXPES spectra at two different orientations [100] and [111]. In both orientations, clear polarization dependence has been observed. The highest peak (e) and Er $4f_{5/2}$ structures (a, b, and c) are stronger in s polarization than p polarization. The structure h is slightly stronger in s polarization, while structures d, f and g are stronger in p-pol. The structure (f) which represent Er 6s states confirm that s polarization suppresses s-electronic state. The overall spectral shape of polarization dependent might be seems similar between the two orientations, although the difference in the size of polarization between the two orientations. Where the polarization at the structure e is stronger in [100] direction than that at [111] direction, while polarization at the structures a, b, c and g are slightly stronger in [111] direction.

4.4. Conclusions

Band structure calculations were presented in both cubic and rhombohedral $ErCo_2$ structures. The calculations verified the ferrimagnetic coupling between Er 4*f* and Co 3*d* in ferrimagnetic phase. In the rhombohedral structure, DOS and moments of Co 9e and Co 3b have no essential differences. $ErCo_2$ band structure calculations revealed a sharp peak lies just below E_F due to the high contribution of conduction electrons Co 3*d* which is the reason in occurrence IEM in $ErCo_2$ compound. In paramagnetic phase, PDOSs of up and down spin are almost similar except Er 4*f* band. Due to the localized nature of Er 4*f* state, DOSs of Er 4*f* states in both structures have no significant differences. Moreover, temperature dependent

$ErCo_2$ valence band HAXPES have been successfully observed and the electronic structure investigated above and below T_C. Also, polarization dependent $ErCo_2$ valence band HAXPES in the cubic symmetry have been successfully observed along two different sample orientations. Furthermore, calculations of the band structures beside cross section described well most features of the experimental HAXPES data, although the discrepancy between the experimental and calculated spectra in the intensity and the peaks positions near E_F. These differences suggest that the understanding of $ErCo_2$ electronic states using the present band structure calculation is not yet enough. Further theoretical studies taking in account electron correlation is needed.

4.5. References

[4.1] E. P. Wohlfarth and P. Rhodes, Collective electron metamagnetism, Phil. Magn., Vol. 7, p. 1817 (1962). DOI: 10.1080/14786436208213848.

[4.2] N. C. Koon and J. J. Rhyne, Ground state spin dynamics of $ErCo_2$, Phys. Rev. B, Vol. 23, p. 207 (1981). DOI: 10.1103/PhysRevB.23.207.

[4.3] E. Gratz and A. S. Markosyan, Physical properties of RCo_2 Laves phase, J. Phys. Condens. Matter, Vol. 13, p. R385 (2001). DOI: 10.1088/0953-8984/13/23/202.

[4.4] N. H. Duc, D. T. Kim Anh and P. E. Brommer, Metamagnetism, giant magnetoresistance and magnetocaloric effects in RCo_2-based compounds in the vicinity of the Curie temperature. Physica B, Vol. 319, p. 1 (2002).

DOI: 10.1016/S0921-4526(02)01099-2.

[4.5] H. Yamada and T. Goto, Itinerant electron metamagnetism and giant magnetocaloric effect. Phys. Rev. B, Vol. 68, p. 184417 (2003). DOI: 10.1103/PhysRevB.68.184417.

[4.6] Z. W. Ouyang, F. W. Wang, Q. Hang, W. F. Liu, G.Y. Liu, J. W. Lynn, J. K. Liang and G. H. Rao, Temperature dependent neutron powder diffraction study of the Laves phase compound $TbCo_2$, J. Alloys Compd., Vol. 390, p. 21 (2005).

DOI: 10.1016/j.jallcom.2004.08.028.

[4.7] E. Burzo, P. Vlaic, D. P. Kozlenko, S. E. Kichanov, N. T. Dang, E. V. Lukin and B. N. Savenko, Magnetic properties of $TbCo_2$ compound at high pressures, J. Alloys Compd., Vol. 551, p. 702 (2013). DOI: 10.1016/j.jallcom.2012.10.178.

[4.8] D. P. Kozlenko, E. Burzo, P. Vlaic, S. E. Kichanov, A. V. Rutkauskas and B. N. Savenko, Sequential cobalt magnetization collapse in $ErCo_2$: beyond the limits of itinerant electron metamagnetism, Sci. Rep. nature, Vol. 5, p. 8620 (2015). DOI: 10.1038/srep08620.

[4.9] D. Bloch, D. M. Edwards, M. Shimizu and J. Voiron, First order transitions in ACo_2 compounds. J. Phys.: Metal. Phys. F, Vol. 5, p. 1217 (1975).

[4.10] A. V. Andreev, A. V. Deryagin, S. M. Zadvorkin, V. N. Moskalev and E. V. Sintsyn, Influence of the 3d-metal on the magnetic properties of quasibinary rare-earth intermetalics $Er(Fe_{1-x}Co_x)_2$, Phys. Met. Metallogr., Vol. 59, p. 57 (1985).

[4.11] A. V. Andreev, In: Handbook of Magnetic Materials, ed. K. H. J. Buschow (Elsevier, Amsterdam, 1995) Vol. 8, p. 59.

[4.12] E. Burzo, A. Chelkovski and H. R. Kirchmayr, Compounds of rare-earth elements and 3d elements, Landolt Börnstein Handbook,Vol. 19d2, Springer Verlag, 1990.

[4.13] T. Goto , T. Sakakibara, K. Murata, H. Komatsu and K. Fukamichi, Itinerant electron metamagnetism in YCo_2 and $LuCo_2$, J. Magn. Magn. Mater, Vol. 90-91, p. 700 (1990).

DOI: 10.1016/S0304-8853(10)80256-2.

[4.14] J. Campbell, Indirect exchange for rare earths in metals, J. Phys. F: Met. Phys., Vol. 2, p. L47 (1972). DOI: 10.1088/0305-4608/2/3/004.

[4.15] E. Burzo, L. Chioncel, R. Tetean and O. Isnard, On the R 5d band polarization in rare-earth–transition metal compounds, J. Phys.: Condens. Matter, Vol. 23, p. 026001 (2011).

DOI: 10.1088/0953-8984/23/2/026001.

[4.16] M. A. Laguna-Macro, J. Chaboy , C. Piquer, H. Maruyama, N. Ishimatsu, N. Kawamura, M. Takagaki and M. Suzuki, Revealing Fe magnetism in lanthanide-iron intermetallic compounds by tuning the rare-earth $L_{2,3}$-edge x-ray absorption edges, Phys. Rev. B, Vol. 72, p. 052412 (2005). DOI: 10.1103/PhysRevB.72.052412.

[4.17] H. Yamada, Electronic structure and magnetic properties of the cubic laves phase transition metal compounds, Physica B, Vol. 149, p. 390 (1988).

DOI: 10.1016/0378-4363(88)90270-7.

[4.18] S. Watanabe, N. Ishimatsu, H. Maruyama, H. Kobayashi, M. Itou, N. Kawamura and Y. Sakurai, Instability of Co spin moment in $ErCo_2$ probed by magnetic Compton scattering under high pressure, J. Phys. Soc. Jpn., Vol. 80, p. 093705 (2001).

DOI: 10.1143/JPSJ.80.093705.

[4.19] H. Yamada and M. Shimizu, Metamagnetic transition of YCo_2, J. Phys. F: Met. Phys. Vol. 15, p. L175 (1985).

[4.20] H. Yamada, J. Inoue and M. Shimizu, Electronic structure and magnetic properties of the cubic Laves phase compounds ACo_2 (A=Sc, Ti, Zr, Lu and Hf) and $ScNi_2$, J. Phys F: Met Phys., Vol. 15, p. 169 (1985).

[4.21] O. Syschenko, T. Fujita, V. Sechovský, M. Diviš and H. Fujii, Magnetism in $ErCo_2$ under high pressure, Phys. Rev. B, Vol. 63, p. 054433 (2001).

DOI: 10.1103/PhysRevB.63.054433.

[4.22] R. Hauser, E. Bauer and E. Gratz, Pressure-dependent electrical resistivity of RCo_2 compounds (R=rare-earth), Phys. Rev. B, Vol. 57, p. 2904 (1998).

DOI: 10.1103/PhysRevB.57.2904.

[4.23] K. Kobayashi, M. Yabashi, Y. Takata, T. Tokushima, S. Shin, K. Tamasaku, D. Miwa, T. Ishikawa, H. Nohira, T. Hattori, Y. Sugita, O. Nakatsuka, A. Sakai and S. Zaima, High resolution-high energy X-ray photoelectron spectroscopy using third-generation synchrotron radiation source, and its application to Si-high k insulator systems, Appl. Phys. Lett. Vol. 83, p. 1005 (2003). DOI: 10.1063/1.1595714.

[4.24] M. Kimura, H. Fujiwara, A. Sekiyama, J. Yamaguchi, K. Kishimoto, H. Sugiyama, G. Funabashi, S. Imada, S. Iguchi, Y. Tokura, A. Higashiya, M. Yabashi, K. Tamasaku, T. Ishikawa, T. Ito, S. Kimura and S. Suga, Polaronic behavior of photoelectron spectra of Fe_3O_4 revealed by both hard X-ray and extremely low energy photons, J. Phys. Soc. Jpn., Vol. 79, p. 064710 (2010). DOI: 10.1143/JPSJ.79.064710.

[4.25] A. Sekiyama, A. Higashiya and S. Imada, Polarization-dependent hard X-ray photoemission spectroscopy of solids, J. Electron Spectrosc. Relat. Phenom., Vol. 190, p. 201 (2013). DOI: 10.1016/j.elspec.2013.08.008.

[4.26] A. Sekiyama, High-energy photoemission spectroscopy for investigating bulk electronic structures of strongly correlated systems, J. Electron Spectrosc. Relat. Phenom., Vol. 208, p. 100 (2016). DOI: 10.1016/j.elspec.2016.02.001.

[4.27] H. Fujiwara, S. Naimen, A. Higashiya, Y. Kanai, H. Yomosa, K. Yamagami, T. Kiss, T. Kadono, S. Imada, A. Yamasaki, K. Takase, S. Otsuka, T. Shimizu, S. Shingubara, S. Suga, M. Yabashi, K. Tamasaku, T. Ishikawa and A. Sekiyama, Polarized hard X-ray photoemission system with micro-positioning technique for probing ground-state symmetry of strongly correlated materials, J. Synchrotron Rad., Vol. 23, p. 735 (2016) .

DOI: 10.1107/S1600577516003003.

[4.28] J. J. Yeh and I. Lindau, Atomic subshell photoionization cross sections and asymmetry parameters: $1 \leq Z \leq 10$, At. Data Nucl. Data Tables, Vol. 32, p. 1 (1985).

DOI: 10.1016/0092-640X(85)90016-6.

[4.29] M. B. Trzhaskovskaya, V. I. Nefedov and V. G. Yarzhemsky, Photoelectron angular distribution parameters for elements Z = 55 to Z = 100 in the photoelectron energy rang 100-5000 eV, At. Data Nucl. Data Tables, Vol. 82, p. 257 (2002). DOI: 10.1006/adnd.2002.0886.

[4.30] J. Czochralski, Z. Phys. Chem. 92 (1918) 219.

[4.31] E. Talik and M. Oboz, Czochralski Method for Crystal Growth of Reactive Intermetallics, Acta Phys. Pol. A, Vol. 124, p. 340 (2013). DOI: 10.12693/APhysPolA.124.340.

[4.32] A. Menovsky and J. J. M. Franse, Crystal growth of some rare earth and uranium intermetallics from the melt, J. Cryst. Growth, Vol. 65, p. 286 (1983).

DOI: 10.1016/0022-0248(83)90062-3.

[4.33] A. Sekiyama, J. Yamaguchi, A. Higashiya, M. Obara, H. Sugiyama, M. Y. Kimura, S. Suga, S. Imada, I. A. Nekrasov, M. Yabashi, K. Tamasaku and T. Ishikawa, The prominent 5d-orbital contribution to the conduction electrons in gold, New J. Phys., Vol. 12, p. 043045 (2010). DOI: 10.1088/1367-2630/12/4/043045.

[4.34] M. Yabashi, K. Tamasaku and T. Ishikawa, Characterization of the transverse coherence of hard synchrotron radiation by intensity interferometry, Phys. Rev. Lett. Vol. 87, p. 140801 (2001). DOI: 10.1103/PhysRevLett.87.140801.

[4.35] K. Okitsu, Y. Ueji. K. Sato and Y. Amemiya, X-ray double phase retarders to compensate for off-axis aberration, J. Synchrotron Rad., Vol. 8, p. 33 (2001).

https://journals.iucr.org/s/issues/2001/01/00/ht2010/ht2010.pdf.

[4.36] G. M. Stocks, W. M. Temmerman and B. L. Gyorffy, Complete Solution of the Korringa-Kohn-Rostoker Coherent-Potential Approximation Equations: Cu-Ni Alloys, Phys. Rev. Letter, Vol. 41, p. 339 (1978).

[37] J. P. Perdew and A. Zunger, Self-interaction correction to density-functional approximations for many-electron systems, Phys. Rev. B, Vol. 23, p. 5048 (1981).

DOI: 10.1103/PhysRevB.23.5048.

[4.38] a) P. Hohenberg and W. Kohn, Inhomogeneous electron gas, Phys. Rev. B, Vol. 136, p. B864 (1964). DOI: 10.1103/PhysRev.136.B864; b) W. Kohn and L. J. Sham, Self-consistent including exchange and correlation effects, Vol. 140, p. A1133 (1965). DOI: 10.1103/PhysRev.140.A1133.

[4.39] A. G. Petukhov, W. R. L. Lambrecht and B. Segall, Electronic structure of rare-earth pnictides, Phys. Rev. B, Vol. 53, p. 4324 (1996). DOI: 10.1103/PhysRevB.53.4324.

[4.40] B. T. Thole, G. van der Laan, J. C. Fuggle, G. A. Sawatzky, R. C. Karnatak and J.-M. Esteva, 3d X-ray-absorption lines and the $3d^9\ 4f^{n+1}$ multiplets of the lanthanides, Phys. Rev. B, Vol. 32, p. 5107 (1985).

[4.41] A. Tanaka andT. Jo, Resonant 3d, 3p and 3s photoemission in transition metal oxides predicted at 2p threshold, J. Phys. Soc. Jpn., Vol. 63, p. 1788 (1994).

DOI: 10.1143/JPSJ.63.2788.

[4.42] R. D. Cowan, The theory of atomic structure and spectra (University of California Press, Berkeley, (1981).

[4.43] W. T. Carnall, P. R. Fields and K. Rajnak, Electronic energy levels in the trivalent lanthanide aquo ions. I. Pr^{3+}, Nd^{3+}, Pm^{3+}, Sm^{3+}, Dy^{3+}, Ho^{3+}, Er^{3+}, and Tm^{3+}, J. Chem. Phys., Vol. 49, p. 4424 (1968). DOI: 10.1063/1.1669893

[4.44] E. U. Condon and G. H. Shortley, The theory of atomic spectra, Published by Cambridge University Press, Ch. 6, p. 179, (1935).

[4.45] R. M. Moon, W. C. Koehler and J. Farrell, Magnetic structure of rare-earth-cobalt (RCo_2) intermetallic compounds, J. Appl. Phys., Vol. 36, p. 978 (1965).

DOI: 10.1063/1.1714286.

[4.46] X. B. Liu and Z. Altounian, Magnetogaloric effect in Co-rich $Er(Co_{1-x}Fe_x)_2$ Laves phase, J. Appl. Phys. Vol. 103, p. 07B304 (2008). DOI: 10.1036/1.2829758.

[47] J. Herrero-Albillos, D. Paudyal, F. Bartolomé, L.M. García, V.K. Pecharsky, K.A. Gschneidner Jr., A.T. Young, N. Jaouen, A. Rogalev, Interplay between Er and Co magnetism in $ErCo_2$, J. Appl. Phys. Vol. 103, p. 07E146 (2008).

DOI: 10.1063/1.2836714

[4.48] M. B. Trzhaskovskaya, V. K. Nikulin, V. I. Nefedov and V. G. Yarzhemsky, Non-dipole second order parameters of the photoelectron angular distribution for elements Z = 1-100 in the photoelectron energy range 1-10 keV, At. Data Nucl. Data tables, Vol. 92, p. 245 (2006). DOI: 10.1016/j.adt.2005.12.002.

[4.49] M. Campagna, G. K. Wertheim and Y. Baer, Photoemission in solids II, hand book, ed. L. Ley and M. Cardona (Springer Verlag, 1979)) Vol. 27, P. 234.

[4.50] J. K. Lang, Y. Baer and P. A. Cox, Study of the 4f and valence band density of states in rare earth metals: II. experiment and results, J. Phys. F: Metal Phys., Vol. 11, p. 121 (1981).

DOI: 10.1088/0305-4608/11/1/015.

[4.51] T. Komesu, H. K. Jeong, J. Choi, C.N. Borca, P.A. Dowben, Electronic structure of ErAs (100), Phy. Rev B, Vol. 67, p. 035104 (2003). DOI: 10.1103/PhysRevB.67.035104.

Chapter 5

Rare-earth Fourth Order Multipole Moment in Cubic $ErCo_2$ Probed by Linear Dichroism in Core-Level Photoemission

Chapter 5

Rare-earth Fourth Order Multipole Moment in Cubic $ErCo_2$ Probed by Linear Dichroism in Core-Level Photoemission

Abstract

We have developed a method to quantify experimentally the fourth order multipole of rare-earth 4*f* orbital. Linear dichroism (LD) in Er $3d_{5/2}$ core-level photoemission spectra (XPS) of cubic $ErCo_2$ has been measured by means of bulk sensitive hard X-ray photoemission. Theoretical calculations have reproduced the observed LD and it has been shown that the observed result is consistent with the so-far suggested Γ_8^3 ground state. Theoretical calculations further showed a linear relation between the LD size and the size of the Er^{3+} ion's fourth order multipole moment, which is proportional to the expectation value $\langle O_4^0 + 5O_4^4 \rangle$ where ${O_n}^m$ are Stevens' operators. These analyses have indicated that LD in 3*d* XPS can be used to quantify the fourth order multipole moment of the rare-earth atom in the cubic crystal electric field. Moreover, temperature and polarization dependent Co 2p core level XPS of cubic $ErCo_2$ have been successfully performed .LD temperature dependent in Er $3d_{5/2}$ core-level XPS of cubic $ErCo_2$ has been observed. Also, the polarization dependent Er $3d_{5/2}$ core-level XPS has been investigated in three different orientations [100], [111] and [110] of cubic $ErCo_2$.

5.1. Introduction

$ErCo_2$ belongs to the family of Laves phase RCo_2 (*R*: rare earth element) compounds, which has been subject to extensive experimental and theoretical studies for more than five decades [5.1-5.4]. RCo_2 show very interesting magnetic phenomena which have been discussed on the basis of: (a) the combination of itinerant Co 3*d* bands and localized *R* 4*f* electrons, (b) the magnetic interaction between Co 3*d* and *R* 4*f* moments, which is ferromagnetic for light rare earths and antiferromagnetic for Gd and heavy rare earths, and (c) the crystal electric field effects (CEF) on *R* 4*f* and Co 3*d* states.

$ErCo_2$ is a ferrimagnet below T_C = 32 K. It has spontaneous moment 7 μ_B per formula unit (at 2 K) and [111] axis as the easy-magnetization direction. $ErCo_2$, together with $HoCo_2$ and $DyCo_2$, exhibits first order magnetic transition, whereas second order magnetic transitions

are found in cases of other rare-earth elements between *R*=Pr and Tm. The *R* dependence of the magnetic ordering process has been explained by Bloch *et al*.[5.5] based on the model where *R* moment interacts with Co moment of itinerant 3*d* electrons, which shows itinerant electron metamagnetism (IEM) [5.6] in the case of YCo_2.

Large magnetocrystalline anisotropy and also magnetostriction of RCo_2 have attracted much attention [5.7-5.11]. Except for *R*=Gd without orbital moment, contribution to anisotropy from *R* under CEF is larger than that from Co [5.9]. This is also supported by the fact that RAl_2, in which Co is replaced by nonmagnetic Al, tend to have the same easy magnetization direction as RCo_2 [5.8, 5.12]. For *R*=Er, 4*f* state under the CEF has been studied for both paramagnetic cubic phase [5.13] and ferrimagnetic rhombohedral phase [5.10, 5.11, 5.13]. In the paramagnetic cubic phase, the CEF Hamiltonian acting on *R* 4*f* electrons can be written as [5.14]:

$$H_{CF} = \left[\frac{16\sqrt{3}}{\sqrt{7}}\, A_4^0\langle r^4\rangle \sum_i Z_4^{cube}(\theta_i,\phi_i) + 32\sqrt{2}\, A_6^0\langle r^6\rangle \sum_i Z_6^{cube}(\theta_i,\phi_i)\right] \qquad (5.1)$$

where Z_4^{cube} and Z_6^{cube} are dimensionless fourth and sixth order multipoles (hexadecapole and tetrahexacontapole), in Racah normalization [5.15] written as:

$$Z_4^{cube}(\theta,\phi) = \frac{5\sqrt{7}}{4\sqrt{3}}\left\{\frac{x^4+y^4+z^4}{r^4} - \frac{3}{5}\right\} \qquad (5.2)$$

$$Z_6^{cube}(\theta,\phi) = -\frac{7}{\sqrt{2}}\left\{\frac{x^6+y^6+z^6}{r^6} + \frac{15}{4}\frac{x^2y^4+x^2z^4+y^2x^4+y^2z^4+z^2x^4+z^2y^4}{r^6} - \frac{15}{14}\right\} \qquad (5.3)$$

This retains the cubic symmetry. H_{CF} can be viewed that "fourth and sixth order multipole moments" Z_4^{cube} and Z_6^{cube} interact with the environment of the crystal. CEF parameters $A_4^0\langle r^4\rangle$ and $A_6^0\langle r^6\rangle$ do not depend much on *R* element within the same series of compounds. In RCo_2 series [5.3], $A_4^0\langle r^4\rangle$ is positive and $A_6^0\langle r^6\rangle$ is negative.

H_{CF} is often rewritten using the Stevens' operator equivalents as [5.14, 5.16]:

$$H_{CF} = Wx\left(\frac{O_4^0+5O_4^4}{F(4)}\right) + W(1-|x|)\left(\frac{O_6^0-21O_6^4}{F(6)}\right) \qquad (5.4)$$

here, O_n^m's are Stevens' operators and $F(n)$'s are constants; $F(4)$=60 and $F(6)$=13860 for Er^{3+}. Wx and $W(1-|x|)$ are proportional to $A_4^0\langle r^4\rangle$ and $A_6^0\langle r^6\rangle$ respectively, but the

proportionality coefficients strongly depend upon R element. Therefore, W and x values depend strongly on R; even their signs change [5.11, 5.3]. $(O_4^0 + 5O_4^4)/F(4)$ and $(O_6^0 - 21O_6^4)/F(6)$ are proportional to the fourth and sixth order multipole moments $\langle Z_4^{cube} \rangle$ and $\langle Z_6^{cube} \rangle$ respectively; $\langle (O_4^0 + 5O_4^4)/F(4) \rangle = 3.93 \times 10^3 \times \langle Z_4^{cube} \rangle$ and $\langle (O_6^0 - 21O_6^4)/F(6) \rangle = 1.58 \times 10^3 \times \langle Z_6^{cube} \rangle$ for Er^{3+} $4f^{11}$. Later in this chapter, we will show values of $\langle (O_4^0 + 5O_4^4)/F(4) \rangle$ and $\langle (O_6^0 - 21O_6^4)/F(6) \rangle$ as measures of fourth and sixth order multipole moments of *4f* electrons since they seem to be more familiar in the literature than $\langle Z_4^{cube} \rangle$ and $\langle Z_6^{cube} \rangle$.

Theoretical prediction of the values of CEF parameters is not straightforward since it is unclear which sites act as effective ligands for *f* sites. CEF parameters of RCo_2 [5.1, 5.2, 5.11, 5.13] has been investigated by analyses of such experimental results as inelastic neutron scattering spectra, anisotropy in the magnetic susceptibility of single crystals, and specific heat measurement. Direct measurement of multipole moments will enable quantitative test of interpretations based on various models including CEF. For transition metal systems, estimation of multipole moments by means of X-ray resonant Raman scattering has been demonstrated [5.17]. To our knowledge, there have been no reports about quantitative estimation of multipole moments of rare earth elements.

We have recently been investigating 4*f* ground state symmetry in heavy-fermion compounds [5.18, 5.19] by measuring 3*d* core-level photoemission spectra (3*d* XPS) by means of bulk-sensitive hard X-ray photoemission spectroscopy (HAXPES). Especially, polarization dependence (linear dichroism; LD) of the spectrum has been found to be useful in the discussion of the ground state symmetry.

In this chapter, we will report experimental result of LD in Er 3*d* XPS for cubic $ErCo_2$ and will demonstrate that comparison with theoretical calculation makes it possible to estimate the fourth order multipole moment $\langle Z_4^{cube} \rangle$ of the 4*f* electrons, which is proportional to $\langle O_4^0 + 5O_4^4 \rangle$. The idea of the experiment is to *create a fourth order multipole in the 3d core level* (denoted $\langle Z_4^{cube}(\text{core}) \rangle$) in the final state of 3*d*-XPS. The *sign of* $\langle Z_4^{cube}(\text{core}) \rangle$ *is controlled* by changing the polarization of the X-ray and the orientation of the sample. Then this $\langle Z_4^{cube}(\text{core}) \rangle$ acts as a *probe* to detect $\langle Z_4^{cube} \rangle$ of the 4*f* electrons.

5.2. Experimental and Computing Method

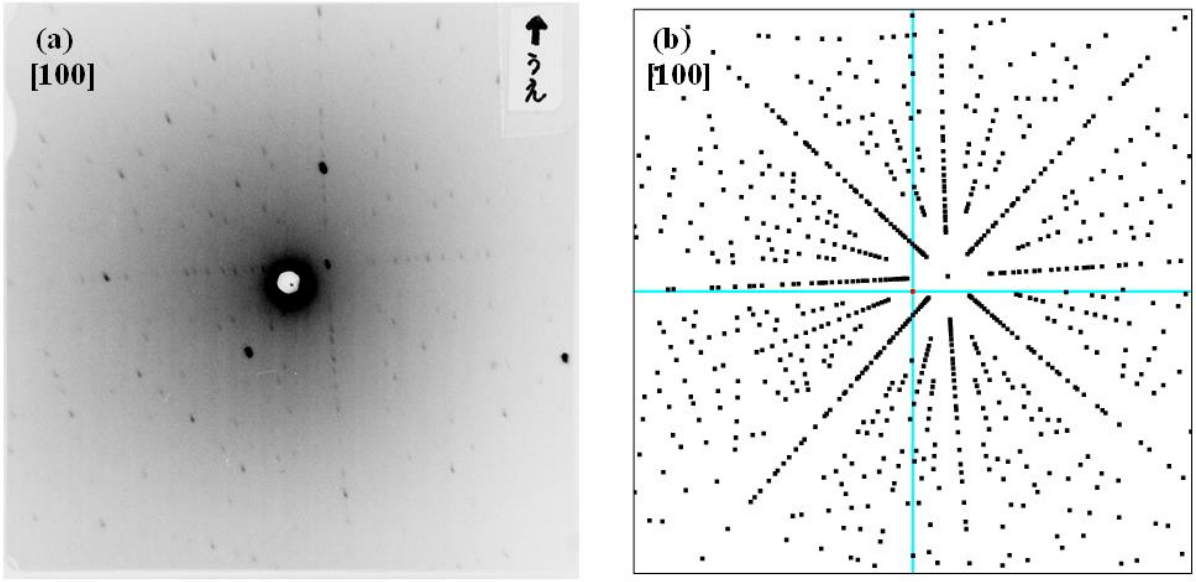

Fig. 5.1. (a) Experimental back-reflection Laue image of [100] direction of $ErCo_2$, (b) Simulted Laue image, ([H K L]~[001]), (and [hkl]~[110]), rotation angle alonge X=-1.5° and alonge Y=3.5°.

A single crystal of $ErCo_2$ was grown by a modified Czochralski method [5.20] in a tri-arc furnace on copper water-cooled bottom from 7 g mixture of the pure elements (99.9% Er, 99.99% Co). The pulling of crystal was performed under argon protecting atmosphere, using a tungsten rod as a seed, at pulling speed 10 mm/h. In order to avoid appearance of phase $ErCo_3$, the initial composition was taken as $ErCo_{1.96}$. The resulting single crystal was cylinder-shaped with a height of 20 mm and a diameter of 4 mm. Back-scattered Laue patterns confirmed the single-crystalline state of the sample as a shown in **Fig. 5.1.** The crystal was annealed at 1000°C for 1 week in quartz tube under argon atmosphere.

The polarization dependent measurements of Er 3*d* XPS by means of HAXPES with linearly polarized X-ray have been performed at BL19LXU of SPring-8 [5.21] using an MBS A1-HE hemi-spherical photoelectron spectrometer. The incident X-ray was set to ≅ 7.9 keV using Si (111) double crystal monochromator and was further monochromatized using Si (620) channel-cut crystal. Two single-crystalline (100) diamonds were used as a phase retarder placed downstream of the channel cut crystal to switch the linear polarization of the excitation light from the horizontal to the vertical direction. The thickness of each diamond plate was 0.25 mm, and the transmittance of the X-ray beam after the double diamond phase retarder was 48%. Degree of the linear polarization P_L was measured by detecting the X-ray horizontally and vertically scattered by a capton film. P_L of the polarization switched X-ray

after the phase retarder was estimated as ≅ -0.90. The excitation light was focused onto the sample by using an ellipsoidal Kirkpatrik-Baez mirror. The detection direction of photoelectrons was set in the horizontal plane with an angle to the incident photons of 60°, as shown in **Fig. 5.2**. Therefore, the experimental configuration at the horizontally (vertically) polarized light excitation corresponds to the p polarization (s polarization). To detect LD accurately in the Er 3*d* core level photoemission spectra, the photon flux was controlled so that photoelectron count rates are comparable between the s polarization and p polarization configurations.

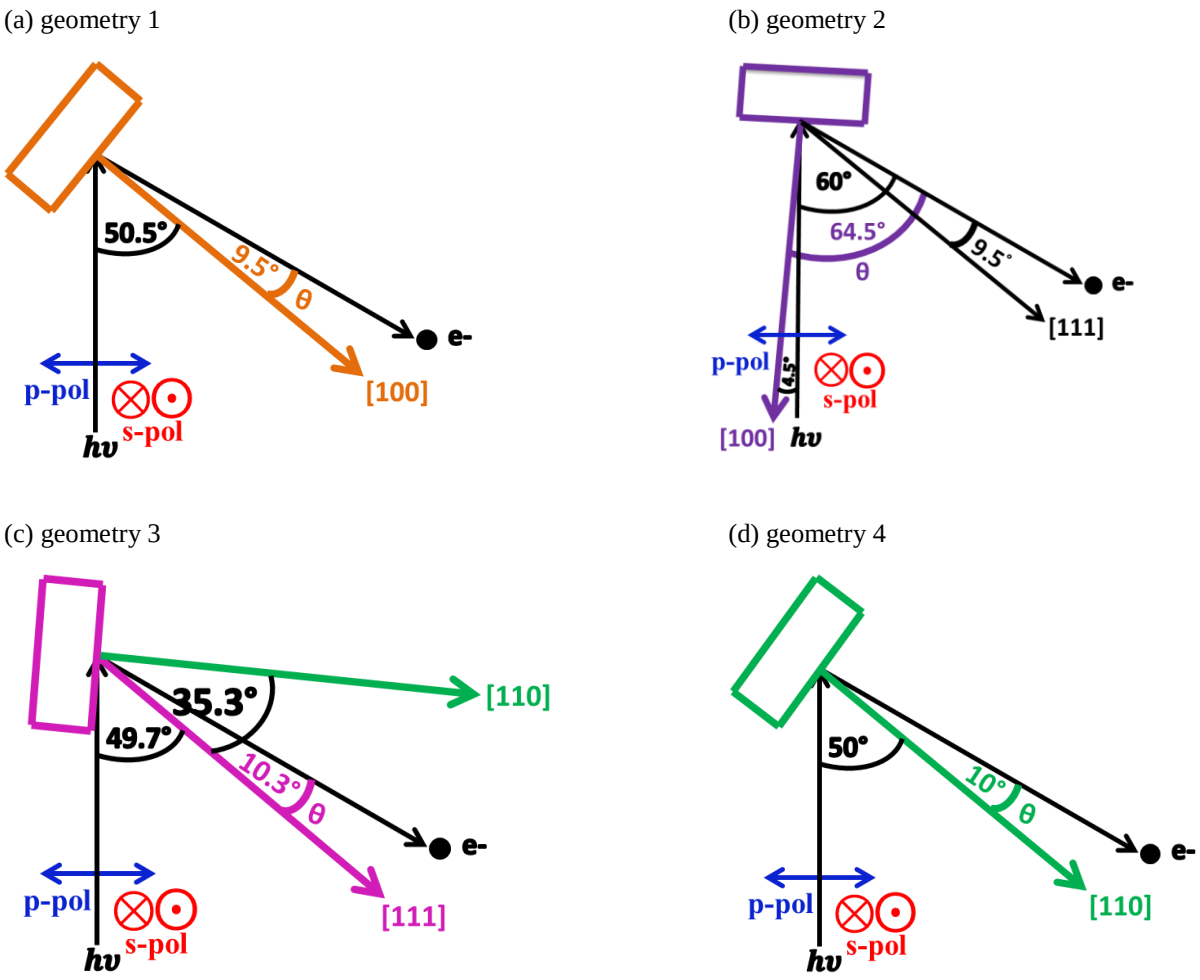

Fig. 5.2. Experimental geometry for HAXPES measurements. Rectangles represent the sample. The angle (θ) between photoelectron detection direction and crystal axis (a) [100] is 9.5°, (b) [100] is 64.5°, (c) [111] is 10.3° and (d) [110] is 10°. The sample's $(01\bar{1})$ plane is put on the plane spanned by the incident direction of X-ray ("hv") and photoelectron detection direction ("e⁻"). In geometry 1, $\langle Z_4^{cube}(\text{core})\rangle < 0$ for p polarization and $\langle Z_4^{cube}(\text{core})\rangle > 0$ for s polarization. In geometry 2, $\langle Z_4^{cube}(\text{core})\rangle > 0$ for p polarization and $\langle Z_4^{cube}(\text{core})\rangle < 0$ for s polarization.

Clean sample surface was obtained by fracturing the sample *in situ* under ultra-high vacuum (UHV) of about 1×10^{-7} Pa. The quality of the sample surface was checked on the

basis of the absence of any core level spectral weight caused by impurities as illustrated in ESCA (electron spectroscopy for chemical analysis) of the sample (**Fig. 5.3**).

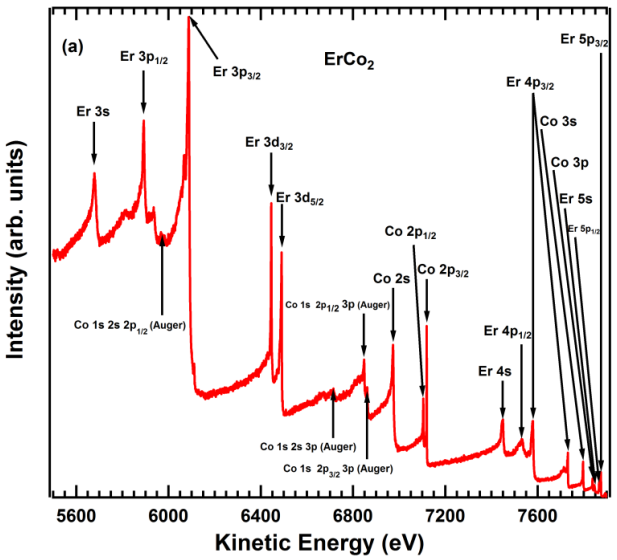

Fig. 5.3. ESCA of single crystal $ErCo_2$.

The experimental geometry was controlled using a two-axis manipulator [5.22]. In the first geometry (geometry 1), the $(01\bar{1})$ plane was set horizontally and the angle (θ) between photoelectron detection direction and crystal axis direction [100] was 9.5° (**Fig. 5.2a**). In the second geometry (geometry 2), the sample was rotated around the vertical axis until θ became 64.5° (**Fig. 5.2b**), so that the angle between [111] direction and the photoelectron detection direction was about 9.5°. In geometry 1, the sign of the fourth order moment of the 3*d* core level ($\langle Z_4^{cube}$ (core)$\rangle$) in the final state of 3*d*-XPS can be shown [5.23] to be $\langle Z_4^{cube}(\text{core})\rangle < 0$ in p polarization and $\langle Z_4^{cube}(\text{core})\rangle > 0$ in s polarization. In geometry 2, $\langle Z_4^{cube}(\text{core})\rangle > 0$ in p polarization and $\langle Z_4^{cube}(\text{core})\rangle < 0$ in s polarization, namely the signs are the opposite of those in geometry 1. $ErCo_2$ core levels (Er 3d and Co 2p) XPS spectra have been measured at 45 K along [100] direction of $ErCo_2$ at 200 eV pass energy using p polarization at the angle (θ) 9.5° (**Fig. 5.2a**) under energy resolution (FWHM) ≅ 220 meV. Also, temperature dependent Co 2p core level spectra have been performed at the same previous conditions above (45 K) and below (25 K) T_C of $ErCo_2$. Er $3d_{5/2}$ core-level spectra have been recorded at 200 eV and 500 eV pass energy for the angle (θ) 9.5° and 64.5° respectively under FWHM ≅ 240 meV and 510 meV, respectively as a shown in **Fig. 5.4a** and **b** respectively. Polarization dependent Co 2p and Er $3d_{5/2}$ core-levels spectra have been performed at 200 eV pass energy under FWHM ≅ 375.5 meV, along [111] direction at (θ) 10.3° (geometry 3 in **Fig. 5.2c**) for Co 2p and [111] direction at (θ) 10.3° (geometry 3 in **Fig. 5.2c**) and [110] directions at (θ) 10°

(geometry 4 in **Fig. 5.2d**) for Er $3d_{5/2}$. The sample temperature during polarization dependent measurements was ≅ 45K, at which $ErCo_2$ is in the paramagnetic cubic phase. Furthermore, temperature dependence of the polarization dependent Er $3d_{5/2}$ core-level spectra have been observed at 45 K and 90 K along [100] direction of $ErCo_2$ at 200 eV pass energy for the angle (θ) 9.5° (**Fig. 5.2a**) under FWHM ≅ 377 meV.

In order to clarify not only the origin of LD in the Er $3d_{5/2}$ XPS but also the relation between multipole moments and the LD, the ionic calculations including the full multiplet theory [5.24] for Er^{3+} ion under cubic CEF splitting have been performed using XTLS 9.0 program [5.25]. Using this code, we have calculated not only the 3*d* XPS spectra but also the energy levels and multipole moments of the ground state and the excited states. Atomic parameters, namely F and G parameters for Coulomb interaction and ζ parameters for spin-orbit interaction, have been assumed consulting the result of Cowan's code calculation [5.26] based on Hartree-Fock method as a shown in **Table 5.1**. For the initial state, F^2 ($4f4f$) was reduced to 80 % of the Cowan-code value and the ratios F^4/F^2 and F^6/F^2 were taken from ref. 27). For the final state of 3*d* XPS, the reduction factor was set 95% for F^n ($4f\,4f$), 85% for F^n ($3d4f$) and 80% for G^n ($3d4f$). For $\zeta(4f)$ and $\zeta(3d)$ Cowan's code results were used without reduction.

Table 5.1. Er^{3+} atomic parameters using Cowan's code.

Atomic parameter	Ground state	Excited state
$\zeta(4f)$	0.302325	0.357158
ζ(3d)		16.77171
F^4 ($4f4f$)	16.09375	17.55628
F^6 ($4f4f$)	10.09593	11.06983
F^2 ($3d4f$)	7.26282	7.979624
F^4 ($3d4f$)		11.58594
G^1 ($3d4f$)		5.506997
G^3 ($3d4f$)		8.543455
G^5 ($3d4f$)		5.015306
		3.466533

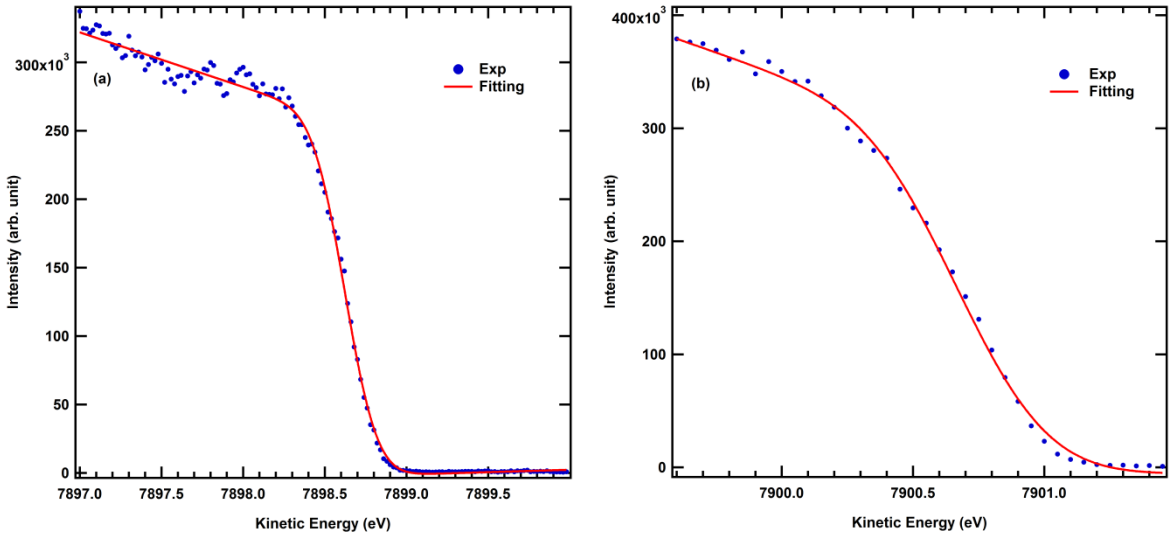

Fig. 5.4. Au at p polarization, T: 45K at [100] direction of $ErCo_2$,(a) E_P: 200 eV, E_F: 7898.626 eV, FWHM: 240 meV and (b) E_P: 500 eV, E_F: 7900.68 eV, FWHM: 510 meV.

5.3. Results and Discussion

5.3.1. $ErCo_2$ Core Level HAXPES Spectra

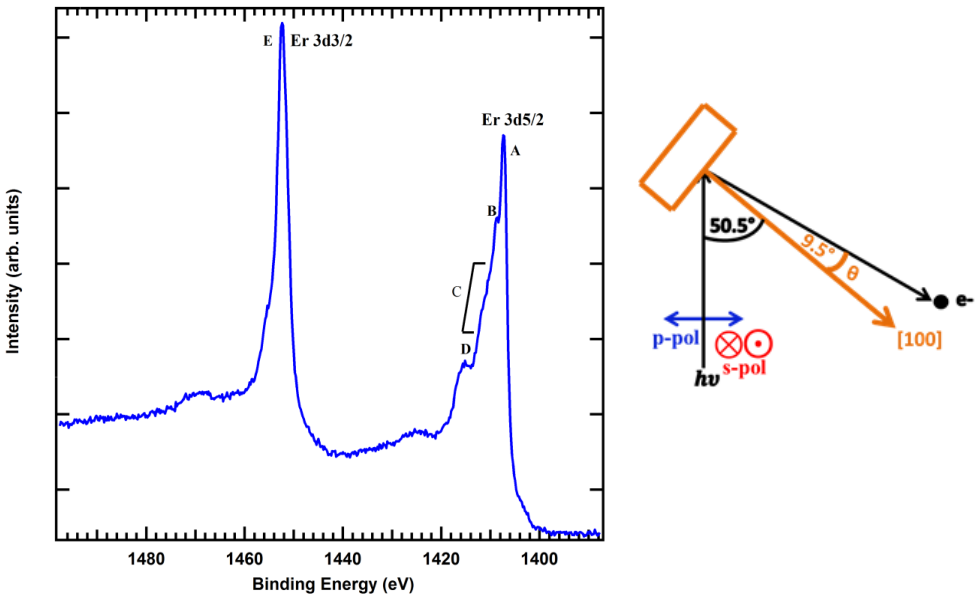

Fig. 5.5. Er 3d core level XPS spctrum along [100] direction of $ErCo_2$ at θ=9.5° meseaured at 45K using p polarization.

Fig. 5.5. shows Er 3d core level XPS spctrum along [100] direction of $ErCo_2$ at θ=9.5° meseaured at 45 K using p polariztion. Er 3d HAXPES spectrum reveals different structures as: the highest peak (E) at binding energy ~1452.4 eV represents Er $3d_{3/2}$, the second highest peak (A) at a binding energy ~1407.5 eV denotes Er $3d_{5/2}$ and other structures (B at 1408.8

eV, C between 1409.7 and 1412.4 eV, and D at 1415.2 eV). Different measurments and analyses have been performed on Er $3d_{5/2}$ XPS will be presented in this chapter.

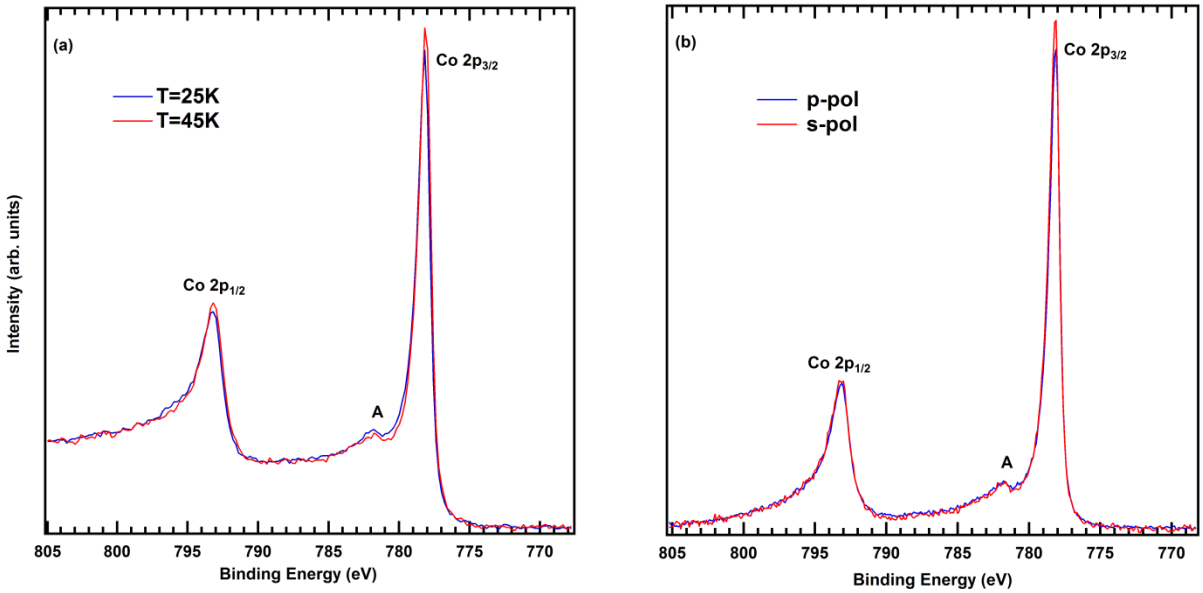

Fig. 5.6. Co 2p core level XPS spectra (a) Temperature dependent along [100] direction of $ErCo_2$ at θ=9.5°, meseaured in the disordered (45 K) and ordered (25 K) magnetic state of $ErCo_2$ using p polarization. (b) Polarization dependent along [111] direction of $ErCo_2$ measured at 45 K, the Shirley-type backgrounds have been subtracted from the raw spectra and the spectra are normalized by Co 2p spectral weight.

Fig. 5.6. illustrates temperature and polarization dependent Co 2p core level XPS spectra of $ErCo_2$ along [100] direction at θ=9.5° (geometry 1, **Fig. 5.2a**) and [111] direction (geometry 3, **Fig. 5.2c**) respectively. Co 2p core level XPS spectrum reveals different structures such as: the highest peak at binding energy ~778.17 eV signifies Co $2p_{3/2}$, the second highest peak at a binding energy ~793.17 eV represents Co $2p_{1/2}$ and structure A at binding energy ~780 eV. For the temperature dependence (**Fig. 5.6a**), the highest and second highest peaks at high temperatures are stronger than at low temperatures, while the structure A is slightly stronger at low temperature. For the polarization dependence (**Fig. 5.6b**), the highest peak is stronger in s polarization than in p polarization, while the second highest peak may be slightly stronger in s-polarization and nearly there is no polarization observed at structure A.

5.3.2. Linear Dichroism in Er $3d_{5/2}$ Core-Level HAXPES

In the case of Er^{3+} ($4f^{11}$) ions in cubic symmetry, the sixteen fold degenerate $J = \frac{15}{2}$ state splits into two doublets (Γ_6 and Γ_7) and three quartets (Γ_8^1, Γ_8^2 and Γ_8^3) as follows [5.16]

$$|\Gamma_6\rangle = 0.5818|\pm 15/2\rangle + 0.3307|\pm 7/2\rangle + 0.7182|\mp 1/2\rangle + 0.1910|\mp 9/2\rangle \quad (5.5)$$

$$|\Gamma_7\rangle = 0.6332|\pm 13/2\rangle + 0.5819|\pm 5/2\rangle - 0.4507|\mp 3/2\rangle - 0.2393|\mp 11/2\rangle \quad (5.6)$$

$$|\Gamma_8^N\rangle = \begin{cases} a_1|\pm 15/2\rangle + a_2|\pm 7/2\rangle + a_3|\mp 1/2\rangle + a_4|\mp 9/2\rangle \\ b_1|\pm 13/2\rangle + b_2|\pm 5/2\rangle + b_3|\mp 3/2\rangle + b_4|\mp 11/2\rangle \end{cases} \quad (N = 1, 2, 3) \quad (5.7)$$

where the coefficients a_n and b_n ($n = 1, 2, 3, 4$) and CEF splitting energies depend not only on N but also on x. It is natural to expect the observation of LD in cubic Er core-level photoemission, since the $4f$ charge distributions deviate from spherical symmetry due to splitting by a crystalline electric field [5.28].

The experimental and simulated polarization dependent Er $3d_{5/2}$ XPS and their LDs in $ErCo_2$ at two different orientations shown in **Fig. 5.2a** and **b** are shown in **Fig. 5.7a** and **b**, respectively. The Shirley-type backgrounds have been subtracted from the raw spectra (see appendix B (**Fig. B.5**)). The spectra are normalized by Er $3d_{5/2}$ spectral weight and then LD, the difference in spectra between p polarization and s polarization, was calculated. Experimental Er $3d_{5/2}$ XPS (**Fig. 5.7a**) reveals a peak (A) at a binding energy ~1407.5 eV and other structures (B at 1408.8 eV, C between 1409.7 and 1412.4 eV, and D at 1415.2 eV) in the energy range 1408-1420 eV. The overall spectral shape of LD might seem similar between geometry 1 (**Fig. 5.7a**) and geometry 2 (**Fig. 5.7b**), namely, LD is positive (negative) in the smaller (larger) binding energy region. However, size and shape of LD are different between the two geometries. For example, the size of LD at structure A is larger in **Fig. 5.7b** than in **Fig. 5.7a**, and LD at structure B is nearly zero in **Fig. 5.7a** but is clearly positive in **Fig. 5.7b**.

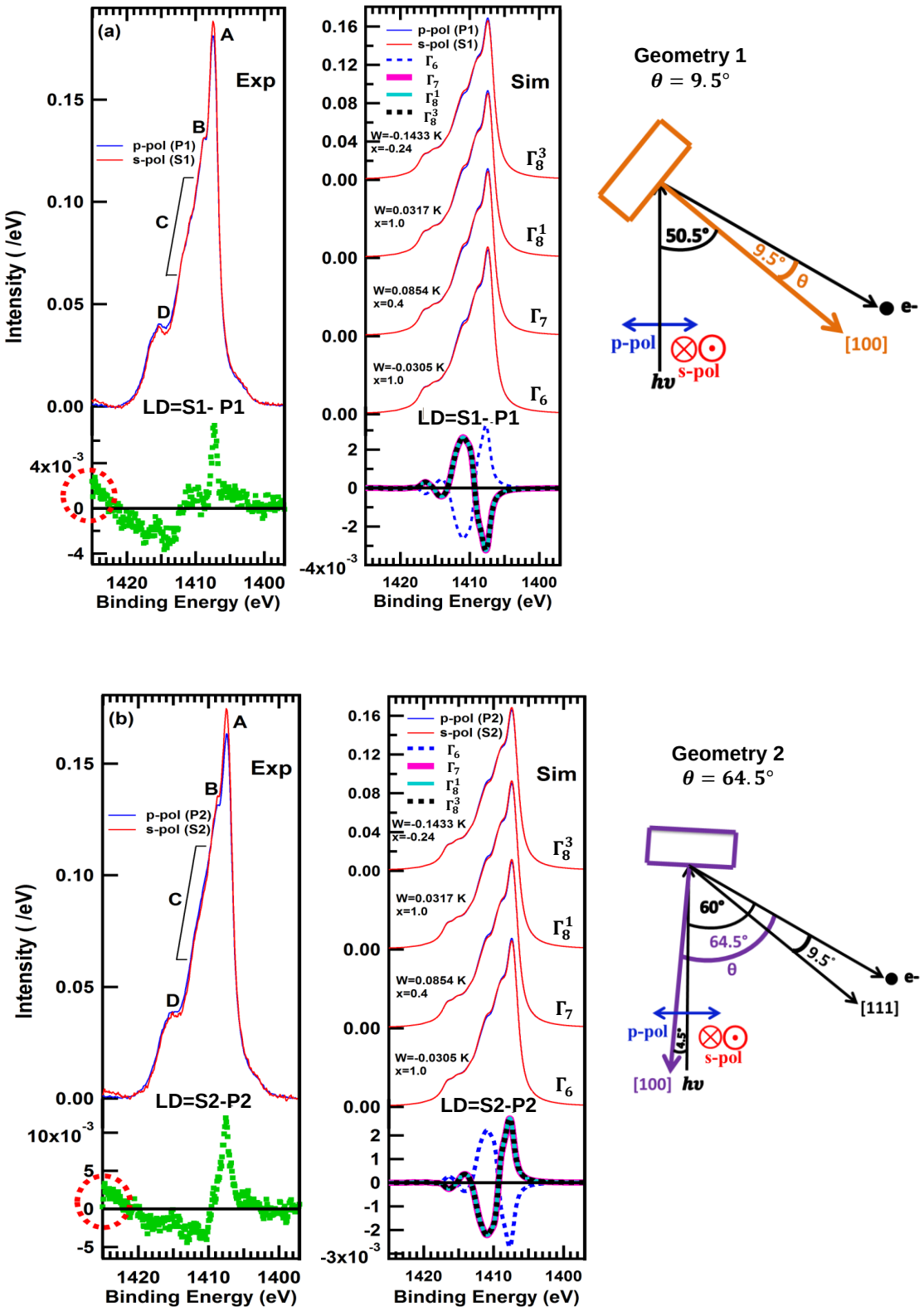

Fig. 5.7. Experimental (Exp) and simulated (Sim) polarization-dependent Er $3d_{5/2}$ XPS spectra of $ErCo_2$ and their LDs at (a) θ=9.5° and (b) θ=64.5°. Simulated polarization-dependent Er $3d_{5/2}$ core level photoemission spectra and their LDs are at the same geometrical configuration of the experiments assuming the crystal-field parameters W and x in cubic symmetry.

When we compare the experiment and the simulation in **Fig. 5.7**., the overall lineshape of $3d_{5/2}$ XPS might seem similar between experiment and simulation. However, the polarization dependence, and therefore the LD lineshape, is quite incontrast between experiment and simulation. In simulations, LD is reversed between the two angles of θ=9.5° and θ=64.5° for all the CEF parameter sets displayed here. This situation does not change even if we change the parameters values as shown in **Fig. 5.7**. The same thing happens also for different temperatures. Actually in simulation, p polarization spectrum of geometry 1 (denoted 'P1') and s polarization spectrum of geometry 2 (S2) coincide with each other. We interpret that spectra P1 and S2 are equivalent because $\langle Z_4^{cube}(\text{core})\rangle < 0$ stands in both P1 and S2, as stated above in the explanation of the experimental geometries. In the same manner, the simulated S1 and P2 spectra coincide with each other, and they are equivalent because $\langle Z_4^{cube}(\text{core})\rangle > 0$ stands in these spectra.

The reason for the disagreement between the experiment and simulation is considered to be the difference, between s and p polarizations, in the shape of background coming from Plasmon energy-loss satellite and other energy-loss components. A straightforward way to remove such difference from each spectrum in **Fig. 5.7** would be to find a realistic model reproducing the polarization-dependent background that would replace the commonly employed "Shirley background" model. However, such an appropriate polarization-dependent model has not been established yet. Therefore, we will here assume that such difference between s and p polarization can be removed by averaging the two "equivalent" spectra taken in different polarizations. Namely, we assume that intrinsic spectra for the $\langle Z_4^{cube}(\text{core})\rangle > 0$ and $\langle Z_4^{cube}(\text{core})\rangle < 0$ conditions can be obtained by calculating (S1+P2)/2 and (P1+S2)/2, respectively, as shown in **Fig. 5.8a**.

In **Fig. 5.8** clear polarization dependence has been observed. The highest peak A and the shoulder B are stronger in (P1+S2)/2 spectrum than in (S1+P2)/2 spectrum; the structure C is stronger in (S1+P2)/2 while the structure D may be slightly stronger in (P1+S2)/2. The difference in these spectra ((S1+P2)/2-(P1+S2)/2) represents the intrinsic LD in Er $3d_{5/2}$ XPS (see the lower panel of **Fig. 5.8a**. The finite LD spectrum at the higher binding energy at θ=9.5° and θ=64.5° (red dash circle at the lower panel in **Fig. 5.7**) is not essential because it disappeared in the present LD as illustrated in **Fig. 5.8a**.

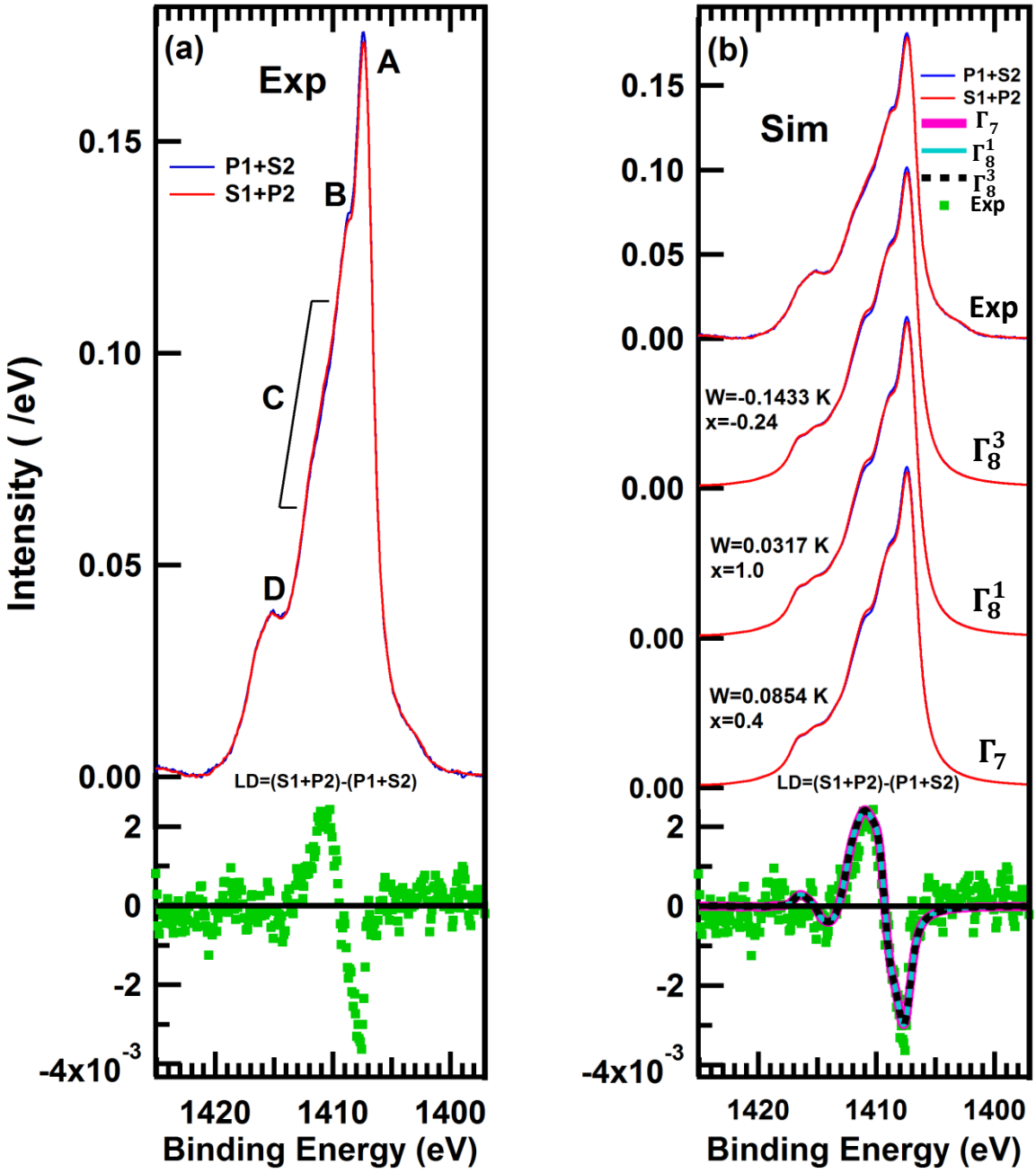

Fig. 5.8. (a) Polarization-dependent Er $3d_{5/2}$ XPS spectra in [100] direction of $ErCo_2$ and its LD. The spectra are normalized by Er $3d_{5/2}$ spectra weight. (b) Simulated polarization-dependent Er $3d_{5/2}$ XPS and their LDs in [100] direction of $ErCo_2$ assuming the crystal-field-split ground state in cubic symmetry. LDs at the lower panel. In the figure "/2" is droped because of the lack of space; for example, S1+P2 stands for (S1+P2)/2. Difference in the total energy resolution between geometries 1 and 2, namely FWHM of 240 meV and 510 meV, respectively, was reconciled by broadening the data for geometry 1 by convoluting with a Gaussian of 450 meV FWHM before adding the spectra of geometries 1 and 2.

LD ((S1+P2)-(P1+S2)) in Er $3d_{5/2}$ XPS spectra can be reproduced, in both shape and size, by the Er^{3+} $4f$ electronic state under such sets of CEF parameters as $(x = -0.24, W = -0.1433\ \text{K})$, $(x = -0.45, W = -0.071\ \text{K})$, $(x = 1.0, W = 0.0317\ \text{K})$ and $(x = 0.4,$

$W = 0.0854$ K) and temperature of 45 K, where three of them are shown as examples in **Fig. 5.8b.** The ground states for the first two parameter sets are both Γ_8^3 and those for the last two parameter sets are Γ_8^1 and Γ_7, respectively [5.16]. Also, this LD can reproduced at the same ground states and other crystal field parameters as a shown in appendix B (**Fig. B.1**) which reveals how LD size depend on the CEF parameters. The inelastic neutron scattering study [5.11] and the specific heat study [5.13] both concluded that the Γ_8^3 state is the ground state in the paramagnetic cubic state of $ErCo_2$. This conclusion is supported by the present study since the observed LD in Er 3d XPS is consistent with the Γ_8^3 ground state.

5.3.3. Multipole Moment

Next, we would like to ask ourselves a question: "What is the essential information that LD of Er 3*d* XPS gives us?" As a first step to answer this question, we calculated the fourth order multipole moment for the above mentioned four parameter sets at 45 K and it is found that they equally yield $\langle (O_4^0 + 5O_4^4)/F(4) \rangle = -36$.

We have also found that the shape of LD is the same independently of CEF parameters and temperature; only the size of LD is changed. Therefore, the "LD size" can safely be defined as the difference between the two extrema in the LD. Here we define the LD size as LD (1407.7eV)-LD (1411.0eV). The experimental LD size is equally -5.8x10^{-3} /eV, and LD size for the above mentioned four parameter sets at 45 K is equally -5.4x10^{-3} /eV according to **Fig. 5.8b**. Therefore, if we make a plot of LD size as a function of the fourth order multipole moment $\langle (O_4^0 + 5O_4^4)/F(4) \rangle$, the points representing the four parameter sets ($x = -0.24$, $W = -0.1433$ K), ($x = -0.45$, $W = -0.071$ K), ($x = 1.0$, $W = 0.0317$ K) and ($x = 0.4$, $W = 0.0854$ K) fall on the same position at 45 K as shown by the left lower red point in **Fig. 5.9a**. On the other hand, $\langle (O_6^0 - 21O_6^4)/F(6) \rangle$ values for these parameters are found to be different with each other as shown by the four lower red dots in **Fig. 5.9b**. The red triangles in **Fig. 5.9a** and **b**, correspond to the parameter set ($x = 1.0$, $W = -0.0305$ K) under 45 K. Its ground state is Γ_6 and the LD spectrum is reversed in sign compared with the four parameter sets shown above, as can be seen in **Fig. 5.9**. In addition, calculations for 0 K have been performed for the so far mentioned five parameter sets and they are shown as five blue dots in each of **Fig. 5.9 a** and **b**.

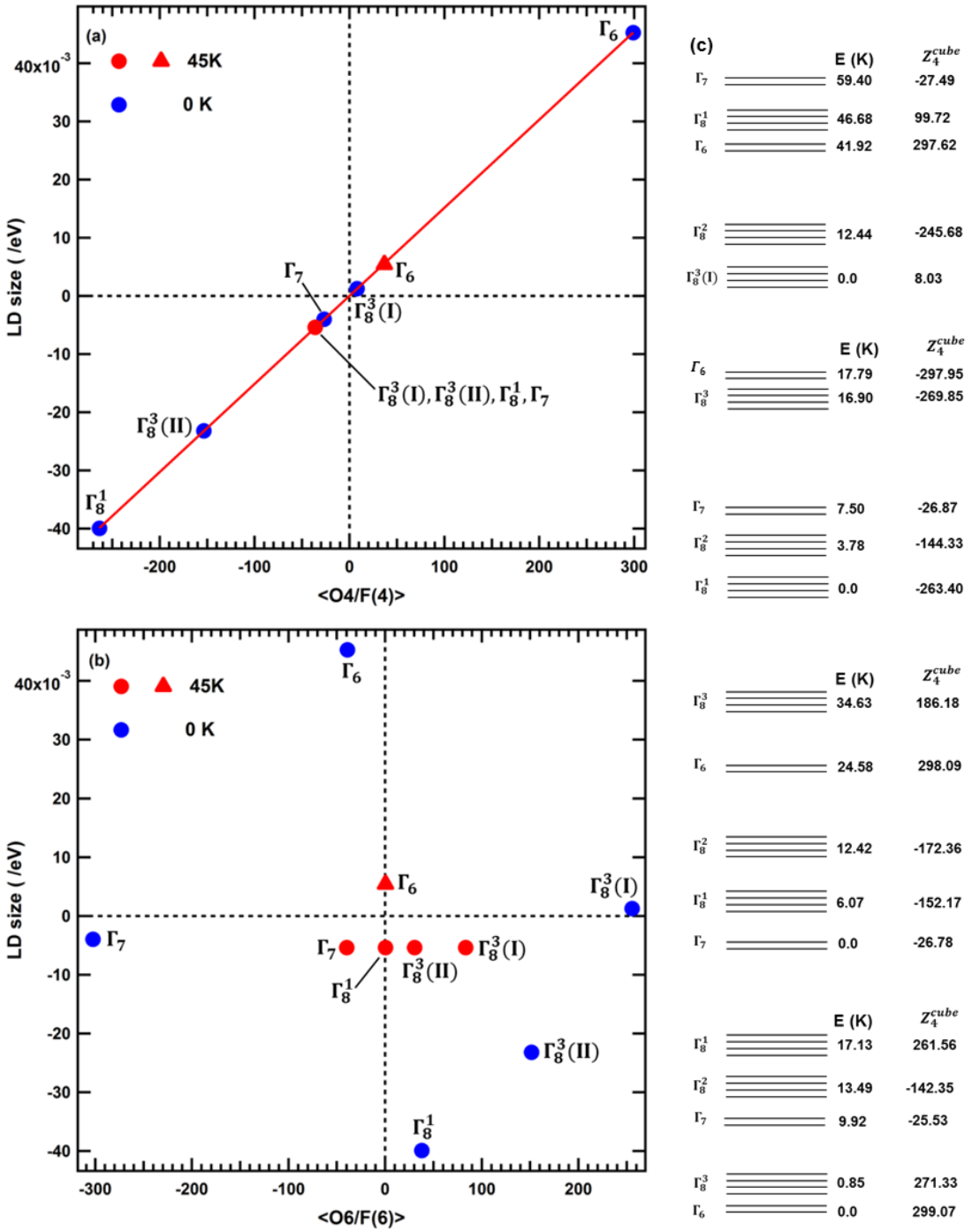

Fig. 5.9. LD size in Er $3d_{5/2}$ XPS vs (a) fourth order multipole moment, (b) sixth order multipole moment, of f^{11} electron system in the cubic Er^{3+} ion within $J = 15/2$. Parameter sets are represented as Γ_8^3 (I): $(x = -0.24, W = -0.1433\ \text{K})$, Γ_8^3 (II): $(x = -0.45, W = -0.071\ \text{K})$, Γ_8^1 $(x = 1.0, W = 0.0317\ \text{K})$, $\Gamma_7 (x = 0.4, W = 0.0854\ \text{K})$ and $\Gamma_6 (x = 1.0, W = -0.0305\ \text{K})$. $\langle O_4/F(4)\rangle$ represents $\langle (O_4^0 + 5O_4^4)/F(4)\rangle$ and $\langle O_6/F(6)\rangle$ represents $\langle (O_6^0 - 21O_6^4)/F(6)\rangle$. (c) Energy level and fourth order moment schemes of Er under different CEF.

Fig. 5.9a clearly indicates that *LD size of Er 3d XPS is proportional to the fourth order multipole moment of Er 4f electrons*, where the coefficient $\langle (O_4^0 + 5O_4^4)/F(4)\rangle$/(LD size) is $6.6\text{x}10^3$, which is obtained from the red line in **Fig. 5.9a**. Therefore, we conclude that we can experimentally obtain the fourth order multipole moment value of rare earth $4f$ orbital under

cubic symmetry by measuring LD of *R* 3*d* XPS. The present experiment indicates $\langle(O_4^0 + 5O_4^4)/F(4)\rangle$ of Er 4*f* electrons in $ErCo_2$ is -36 at 45 K. Since we are not free from the finite escape depth of photoelectrons, thus obtain value is the fourth order multipole moment value averaged over the probed sample region, namely from surface down to ~10 nm deep in the case of HAXPES with hν=8keV. We consider that the bulk value of $\langle(O_4^0 + 5O_4^4)/F(4)\rangle = -56$, obtained based on the parameters ($x = -0.24$ and $W = -0.34$ K, yielding Γ_8^3 ground state) given by the specific heat measurement [5.13], is fairly consistent with the presently obtained value of -36 because 4*f* state in the surface-most part of the sample would be different from the bulk.

Fig.5.9b indicates that there is no relation between LD of Er 3*d* XPS and the sixth order multipole moment. The reason why the fourth order multipole can be probed by 3*d* XPS but sixth order one cannot is that the *d* state (l=2), which is excited in 3*d* XPS, can acquire fourth order mulipole moment but cannot acquire sixth order multipole moment. This is because of the well-known rule that all *n*th order multipole moment vanishes if $n>2\,l$, where l is the orbital quantum number of the single electrons, as is shown for example in section 4a of ref. 5.14. **Fig.5.9c** shows schematic representation of energy levels and fourth order multipole of f^{11} electron system in the cubic Er^{3+} ion within $J = 15/2$. Where this figure elucidates that the changing in energy levels and fourth order multipole depend on the sign and value of CEF parameters x and w.

5.3.4. Temperature Dependent Linear Dichroism and Multipole Moment in Er $3d_{5/2}$ Core-Level Photoemission

Temperature dependence of XPS spectra and LD originates from a partial occupation of excited state *i* split by Δ_i from the ground state at high temperatures T with a fraction of [5.29]:

$$\frac{\exp[-\Delta_i/(k_B T)]}{[1 + \sum_i \exp[-\Delta_i/(k_B T)]]} \tag{5.8}$$

which lead to the isotropic spectra at sufficiently high temperature. When all states are equally occupation the polarization should vanish entirely. **Fig. 5.10a** shows the simulated LD [(S1+P2)-(P1+S2)] temperature dependent in Er^{3+} $3d_{5/2}$ XPS in [100] direction of $ErCo_2$ at CEF parameters ($x = -0.24, W = -0.1433$ K, yielding Γ_8^3 ground state). Confirming that at

sufficient high temperature (from 30 K), LD reduces gradually and has isotropic spectra without flip of its sign. Namely, the shape of LD is the same independently of temperature; only the size of LD is changed as a shown in **Fig. 5.10b**. However, the behavior of LDs at low temperatures is non-isotropic as a shown in **Fig. 5.10a** and **b**, where firstly at a very low temperature (0 K) the sign of LD is positive, but with increasing the temperature gradually to 5 K the sign of LD flips (negative), then LD starts to increase with increasing the temperature to 20 K due to the contribution of first excited state. With continuing increasing the temperature, LD starts to reduce at sufficient high temperature (30 K) due to the population of the next excited states without changing its sign and shape.

This behavior of LD temperature dependent at CEF parameters ($x = -0.24, W = -0.1433$ K, yielding Γ_8^3 ground state) can be explained according to the behavior of the corresponding fourth order multipole moment temperature dependent of Er 4*f* at the same conditions as illustrated in **Fig. 5.10c**. In **Fig. 5.10c**, at very low temperatures (0 K) the sign of fourth order multipole moment is positive then become negative with increasing temperature (to 5 K), then start increase with increasing temperature (to 20 K), then start decreasing with continuous increasing temperature (from 30 K) as has done in **Fig. 5.10a** and **b**. It is normal that the fourth order moment of *R* 4*f* electrons can reflect the behavior of LD of *R* 3*d* XPS at different temperatures under cubic CEF where, as previously mentioned, LD size of *R* 3*d* XPS is proportional to the fourth order multipole moment of *R* 4*f* electrons as a shown in **Fig. 5.10d**. **Fig. 5.10d** clearly indicates that the simulated LD size of Er 3*d* XPS is proportional to the fourth order multipole moment of Er 4*f* electrons at CEF parameters ($x = -0.24, W = -0.1433$ K, yielding Γ_8^3 ground state), where the coefficient $< (O_4^0 + 5O_4^4)/\mathrm{F}(4) >$/(LD size) is 6.6×10^3, which is obtained from the fitting line in **Fig. 5.10d**.

Fig. 5.10e reveals that along all temperature ranges, the sixth order multipole moment has a positive sign and decreases gradually with increasing temperature at CEF parameters ($x = -0.24, W = -0.1433$ K, yielding Γ_8^3 ground state). **Fig. 5.10f** reveals that there is no relation between LD of Er 3*d* XPS and the sixth order multipole moment as explained before in **Fig 5.9b**.

Fig. 5.11a illustrates the simulated LD [(S1+P2)-(P1+S2)] temperature dependent in Er^{3+} $3d_{5/2}$ XPS in [100] direction of $ErCo_2$ at CEF parameters ($x = 1.0, W = 0.0317\ K$, yielding Γ_8^1 ground state). In this case, along all temperature ranges LD reduces gradually with

increasing temperature and has isotropic spectra without changing its sign (negative). This means that the shape of LD is also temperature independent and only the size of LD depends on the temperature, as a shown in **Fig. 5.11b**. This behavior of LD is found at CEF Parameters (x: $\pm 1, \pm 0.8, \pm 0.6$), see Appendix B (**Fig. B. 3**).

As mentioned before, this behavior of LD temperature dependent at CEF parameters ($x = 1.0, W = 0.0317\,K$, yielding Γ_8^1 ground state) can be explained according to the behavior of the fourth order multipole moment temperature dependent of Er 4f at the same conditions, as a shown in **Fig. 5.11c**. In **Fig. 5.11c,** the fourth order multipole moment is negative and decreases gradually with increasing temperature along all temperature ranges. Also, **Fig. 5.11d** obviously reveals that the simulated LD size of Er 3d XPS is proportional to the fourth order multipole moment of Er 4f electrons at CEF parameters ($x = 1.0, W = 0.0317\,K$, yielding Γ_8^1 ground state), where the coefficient $\langle(O_4^0 + 5O_4^4)/\mathrm{F}(4)\rangle$/(LD size) is 6.6×10^3, which is obtained from the fitting line in **Fig. 5.11d**.

At CEF parameters ($x = 1.0, W = 0.0317\,K$, yielding Γ_8^1 ground state) the sixth order multipole moment decreases gradually with increasing temperature along all temperature ranges (**Fig. 5.11e**). LD size of Er 3d XPS is proportional to it (**Fig 5.11f**), although the sign (positive) of the sixth order moment is reverse to the sign of LD (negative).

Fig. 5.12a shows the simulated LD [(S1+P2)-(P1+S2)] temperature dependent in Er^{3+} $3d_{5/2}$ XPS in [100] direction of $ErCo_2$ at CEF parameters ($x = 0.4, W = 0.0854\,K$, yielding Γ_7 ground state). This confirms that LD reduces gradually with increasing temperature and has isotropic spectra without flipping its negative sign at high temperatures (from 20 K) due to the contribution of the next excited states. Here, the shape of LD is also independent of temperature and only the size of LD can be changed as a shown in **Fig. 5.12b**. However, the behavior of LDs at more low temperatures (from 0 K to 10 K) is inversed where LD increases with increasing temperature due to the contribution of first excited state. This behavior of LD was found at CEF Parameters (x: $\pm 0.4, +0.2$), see Appendix B (**Fig. B.3**).

Fig. 5.12c reveals that at CEF parameters ($x = 0.4, W = 0.0854\,K$, yielding Γ_7 ground state)**,** the fourth order moment increases with increasing temperature at low temperatures (from 0 K to 10 K), while at more high temperatures (from 20 K) it starts to decrease with continuous increasing temperature without flipping its negative sign, this explains the behavior of LD in **Fig. 5.12a** and **b**. Also, **Fig. 5.12d** clearly demonstrates that

the simulated LD size of Er 3*d* XPS as proportional to the fourth order multipole moment of Er 4*f* electrons at CEF parameters ($x = 0.4, W = 0.0854\ K$, yielding Γ_7 ground state), where the coefficient $< (O_4^0 + 5O_4^4)/F(4) >$/(LD size) is 6.6×10^3, which is obtained from the fitting line in **Fig. 5.12d**.

At CEF parameters ($x = 0.4, W = 0.0854\ K$, yielding Γ_7 ground state), **Fig. 5.12e** elucidates that along all temperature ranges, the sixth order multipole moment has a negative sign and decreases gradually with increasing temperature. While **Fig. 5.12f** shows that LD size of Er 3*d* XPS is proportional to the sixth order moment only at high temperatures. From this discussion, it clearly indicates that under cubic CEF the fourth order multipole moment of Er 4*f* electrons have the same behavior along all Er 4*f* ground states (LD size of Er 3d XPS is proportional to the fourth order multipole moment of Er 4*f* electrons), while the behavior of the sixth order multipole moment is different for each ground state.

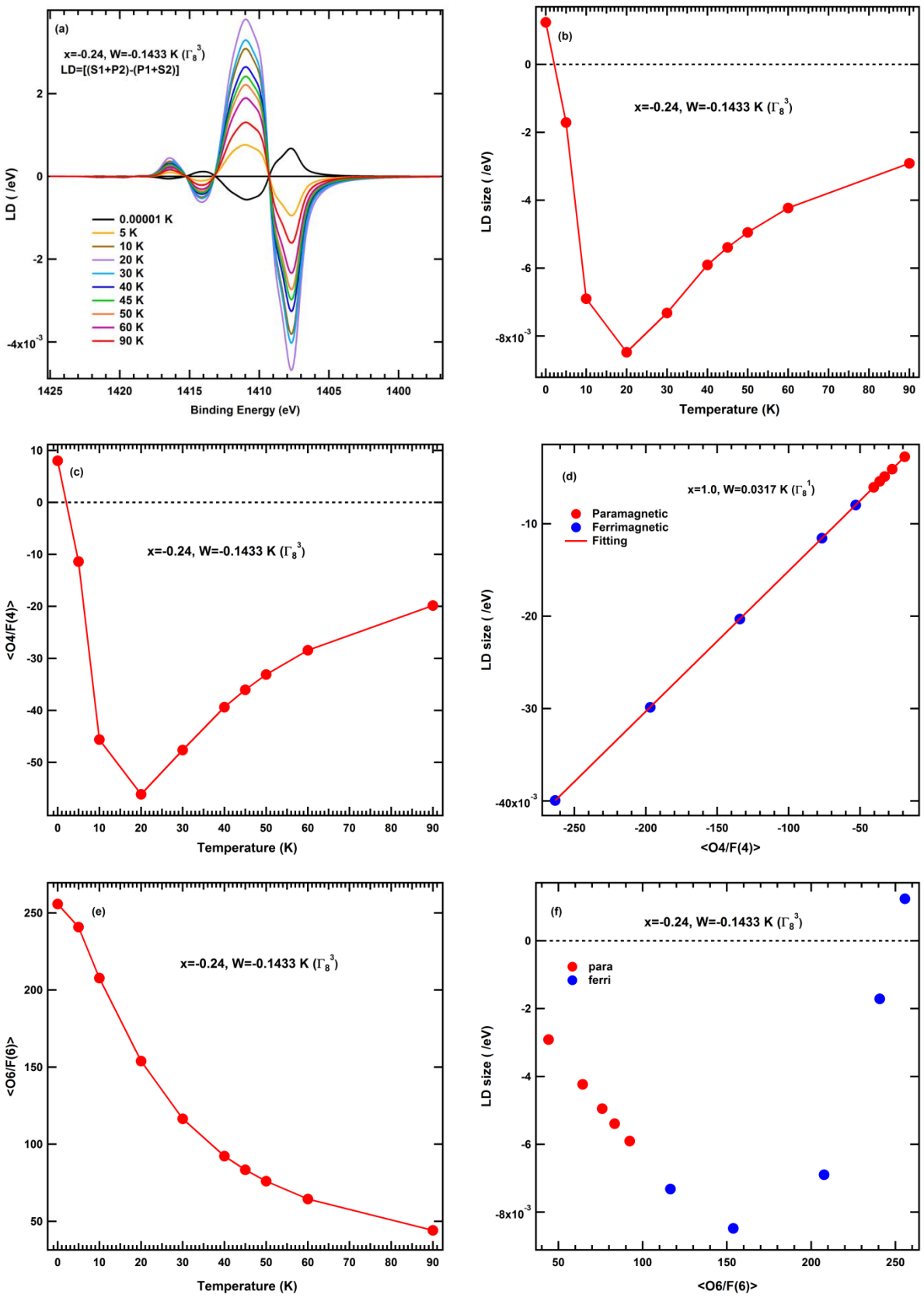

Fig. 5.10. Simulated temperature dependent in Er^{3+} $3d_{5/2}$ XPS (a) LD, (b) LD size, (c) fourth order multipole moment and (e) sixth order multipole moment. Simulated LD size in Er $3d_{5/2}$ XPS vs (d) fourth order multipole moment and (f) sixth order multipole moment, of f^{11} electron system in the cubic Er^{3+} ion within J = 15/2 for the ground state Γ_8^3 $(x = -0.24, W = -0.1433\ \mathrm{K})$. $\langle O_4/F(4)\rangle$ represents $\langle (O_4^0 + 5O_4^4)/F(4)\rangle$ and $\langle O_6/F(6)\rangle$ represents $\langle (O_6^0 - 21O_6^4)/F(6)\rangle$.

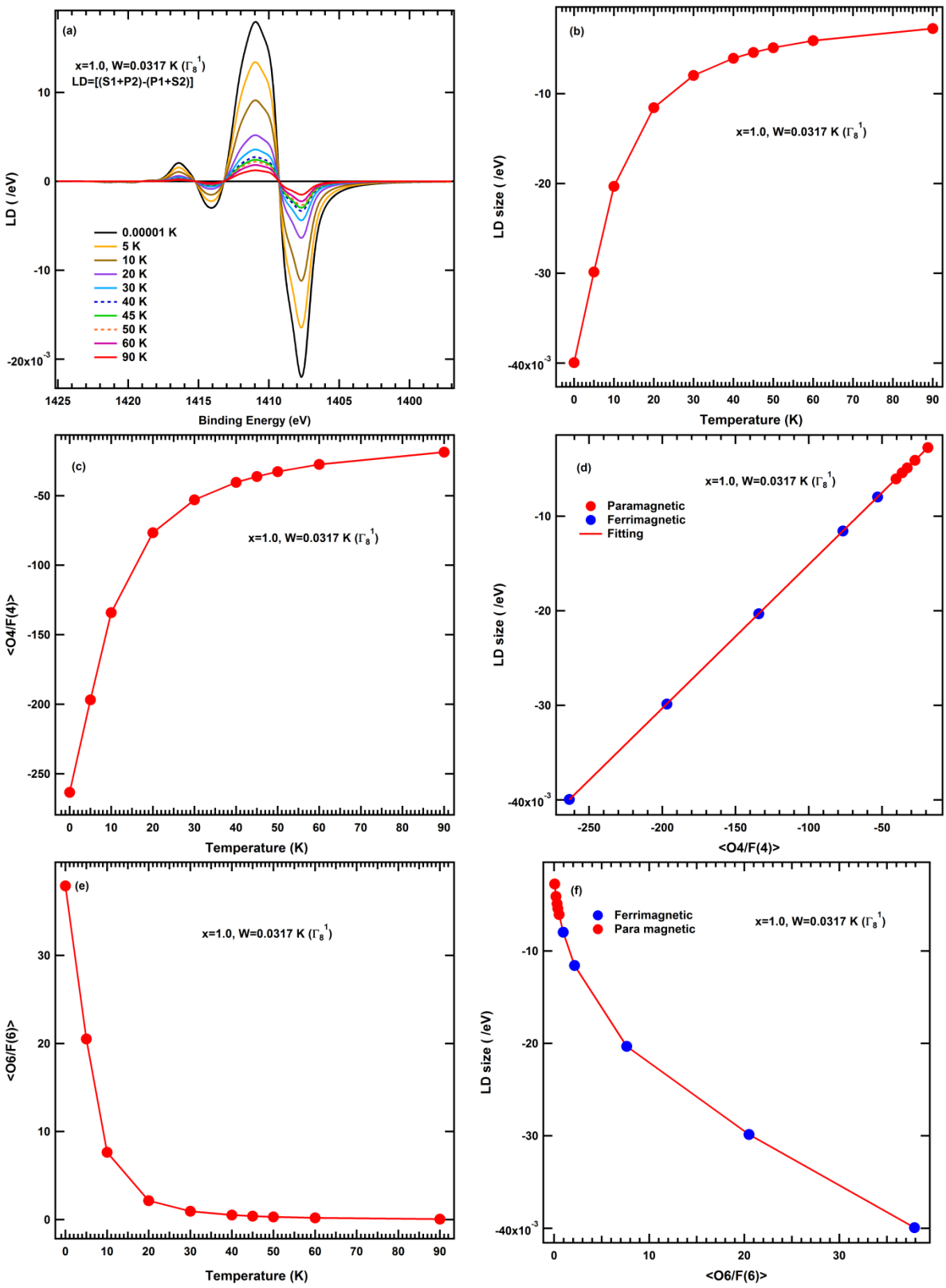

Fig. 5.11. Simulated temperature dependent in Er $3d_{5/2}$ XPS (a) LD, (b) LD size, (c) fourth order multipole moment and (e) sixth order multipole moment. Simulated LD size in Er $3d_{5/2}$ XPS vs (d) fourth order multipole moment and (f) sixth order multipole moment, of f^{11} electron system in the cubic Er^{3+} ion within J = 15/2 for the ground state Γ_8^1 $(x = 1.0, W = 0.0317\ K)$. $\langle O_4/F(4)\rangle$ represents $\langle (O_4^0 + 5O_4^4)/F(4)\rangle$ and $\langle O_6/F(6)\rangle$ represents $\langle (O_6^0 - 21O_6^4)/F(6)\rangle$.

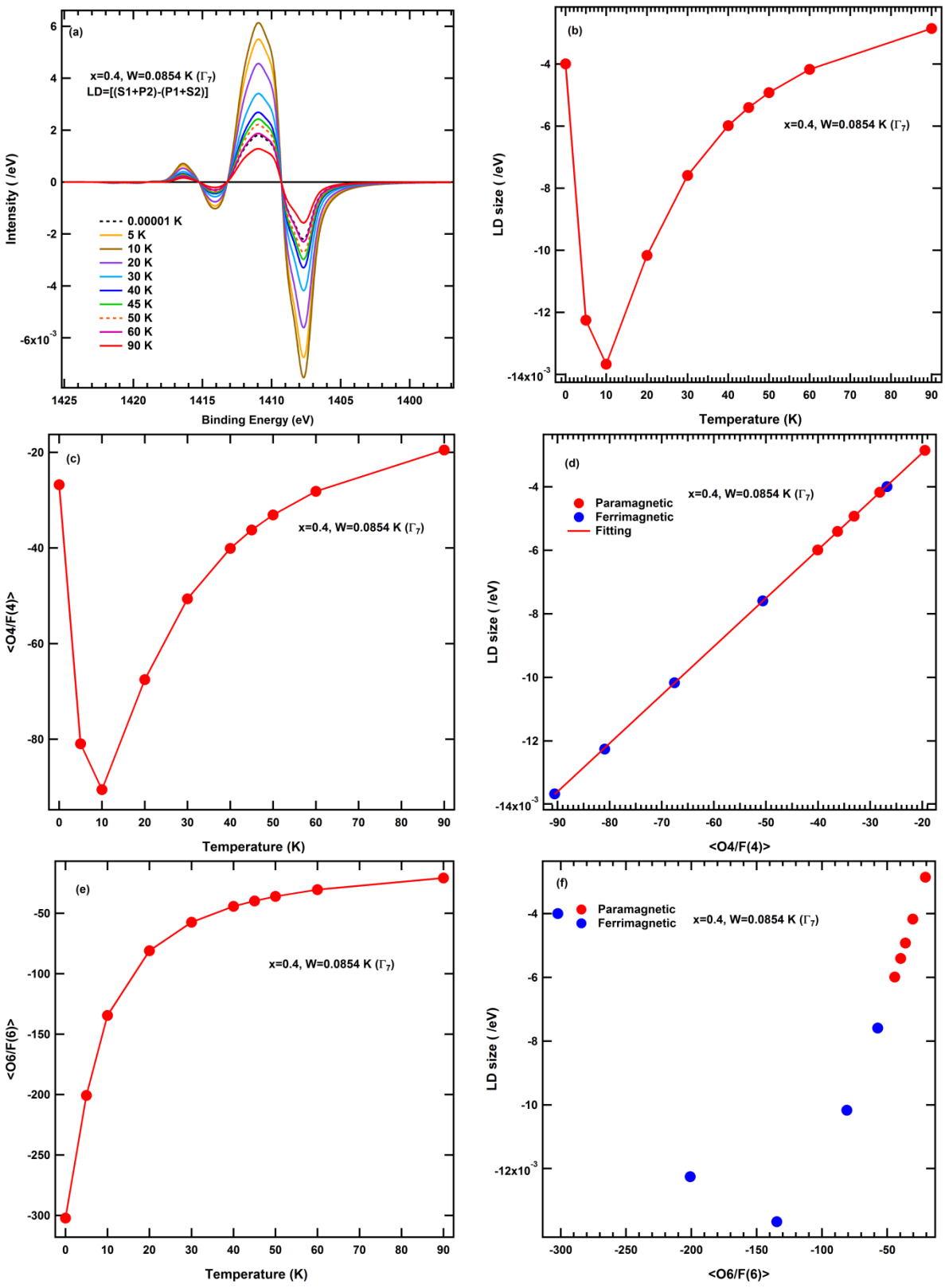

Fig. 5.12. Simulated temperature dependence in Er $3d_{5/2}$ XPS (a) LD, (b) LD size, (c) fourth order multipole moment and (e) sixth order multipole moment. Simulated LD size in Er $3d_{5/2}$ XPS vs (d) fourth order multipole moment and (f) sixth order multipole moment, of f^{11} electron system in the cubic Er^{3+} ion within J = 15/2 for the ground state $\Gamma_7(x = 0.4, W = 0.0854\ K)$. $\langle O_4/F(4)\rangle$ represents $\langle(O_4^0 + 5O_4^4)/F(4)\rangle$ and $\langle O_6/F(6)\rangle$ represents $\langle(O_6^0 - 21O_6^4)/F(6)\rangle$.

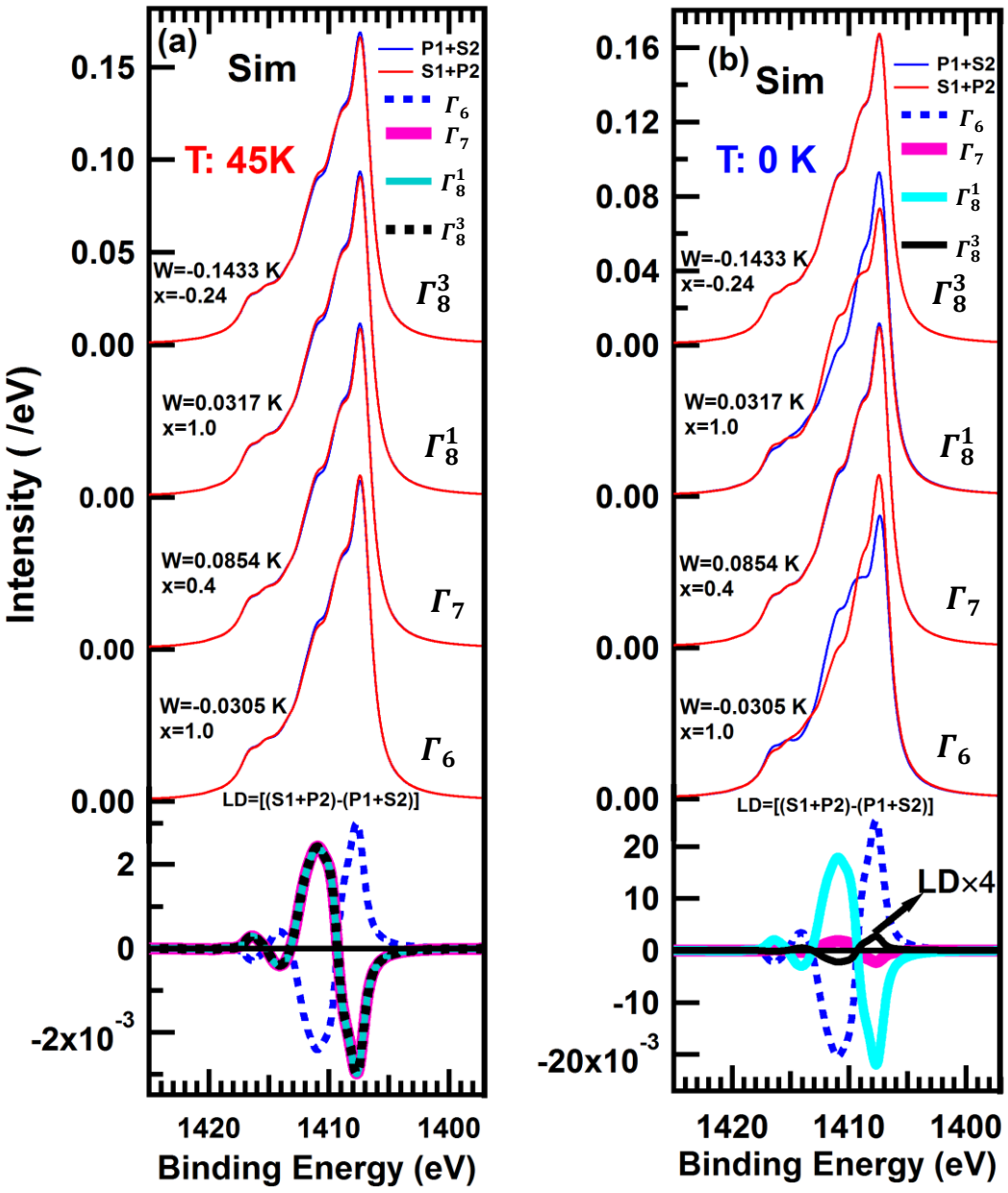

Fig. 5.13. Simulated temperature dependence of the polarization-dependent Er^{3+} $3d_{5/2}$ core level photoemission spectra and their LDs in [100] direction of $ErCo_2$ assuming the crystal-field-split ground state in cubic symmetry. LDs at the lower panel. (a) T: 45 K and (b) T: 0 K.

Fig. 5.13 shows the simulated temperature and polarization-dependent Er^{3+} $3d_{5/2}$ core level photoemission spectra in [100] direction of $ErCo_2$. The difference in the spectra between p polarization and s polarization was calculated as LD [(S1+P2)-(P1+S2)], verifying that LD size reduces at high temperatures without any change in its sign and spectral shape, for the trivalent Er^{3+} 4*f* ground states. But at low temperatures the behavior of LD is different as explained before according to the behavior of Fourth order multipole moment of Er 4*f* electrons.

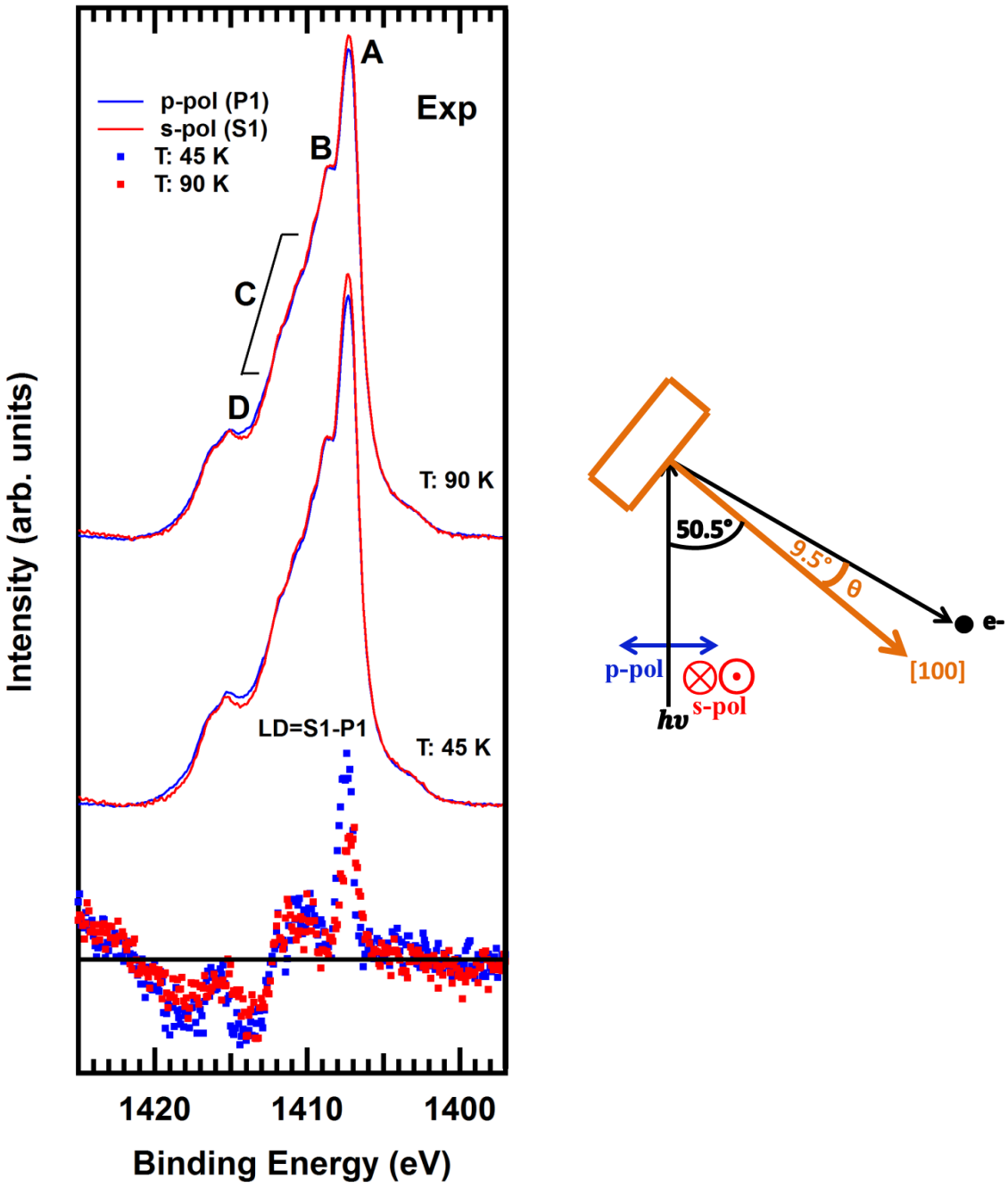

Fig. 5.14. Experimental temperature dependence of the polarization dependent Er^{3+} $3d_{5/2}$ core level HAXPES spectra in [100] direction of $ErCo_2$ at θ =9.5° (geometry 1) and their LDs.

Fig. 5.14 tells the experimantal temperature and polarization-dependent Er^{3+} $3d_{5/2}$ core level XPS spectra in [100] direction of $ErCo_2$ at $\theta = 9.5^0$. The Shirley-type backgrounds have been subtracted from the raw spectra. The spectra are normalized by Er $3d_{5/2}$ spectral weight and then LD. Experimental Er^{3+} $3d_{5/2}$ core level HAXPES spectrum (**Fig. 5.14**) demonstrates structures (A, B, C and D) as explained before in **Fig. 5.7a**. The difference in the spectra between p polarization and s polarization was calculated as LD=S1-P1, verifying that LD is reduced at high temperatures without flipping its sign or changing its spectral shape. Where

LD at 45 K is higher than that at 90 K and both have the same sign and shape (LD is positive (negative) in the smaller (larger) binding energy region). Unfortunately, we couldn't measure temperature and polarization-dependent Er^{3+} $3d_{5/2}$ core level XPS spectra in [100] direction of $ErCo_2$ at the other orientation ($\theta = 64.5^0$), so we couldn't perform the previous analysis (LD [(S1+P2)-(P1+S2)]) on this data.

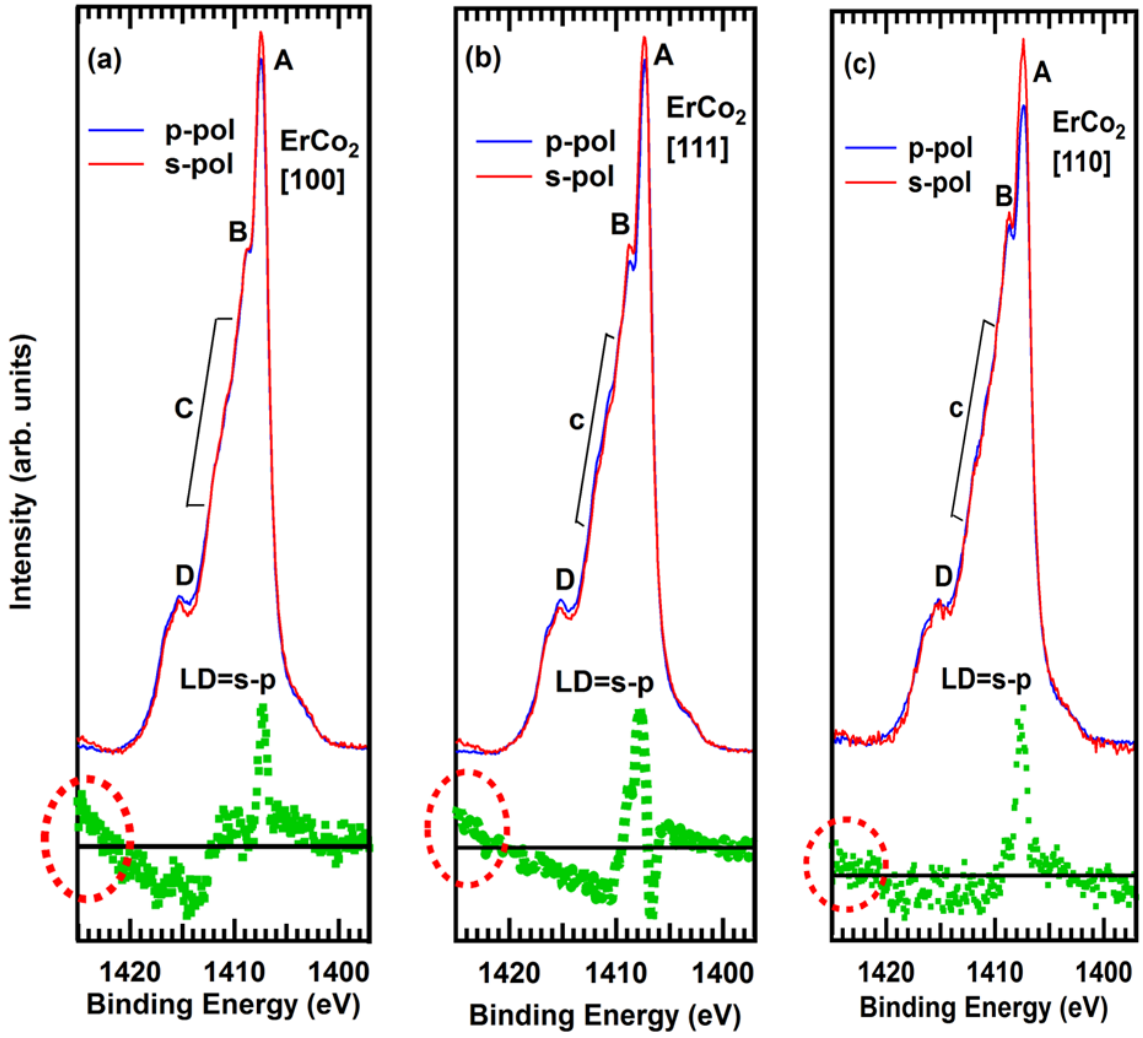

Fig. 5.15. Experimental polarization-dependent Er $3d_{5/2}$ XPS spectra of $ErCo_2$ and their LDs at different orientations (a) [100] (geometry 1); (b) [111] (geometry 3) and (c) [110] (geometry 4). where the Shirely-type background has been subtracted from the raw spectra. The spectra are normalized by Er $3d_{5/2}$ spectral weight.

The experimental polarization dependent Er $3d_{5/2}$ core level XPS spectra and their LDs in $ErCo_2$ at three different orientations [100], [111] and [110] are shown in **Fig. 5.15a, b** and **c** respectively. Er^{3+} $3d_{5/2}$ core level XPS spectrum (**Fig. 5.15**) demonstrates structures (A, B, C and D) as previously mentioned in **Fig. 5.7a**. The overall lineshape of $3d_{5/2}$ XPS seem similar at the three orientations. Although the difference in the shape and size of LD. LD (s-p) calculated by the difference in the spectra weight between p polarization and s polarization

The sign of LD seems similar between [100] and [110] directions, where LD is positive in the lower binding energy region and negative in the higher one, although the size and shape of LD are different between the two orientations. On the other hand, LD in [111] direction has a negative sign in both low and high binding energy regions, while it has a positive sign in the lower one. At the highest peak A the size of LD is larger in [110] direction than other directions, also LD at the structure B is nearly zero in [100] direction but clearly it is positive in [111] and [110] directions.

5.4. Conclusions

In conclusion, bulk sensitive measurements in Co 2p, Er 3d and Er $3d_{5/2}$ core levels of XPS of $ErCo_2$ in the paramagnetic cubic phase have been successfully performed. Temperature and polarization dependent Co 2p core level XPS of cubic $ErCo_2$ have been already observed. Intrinsic LD was extracted by cancelling out the polarization dependent background based on measurements at two different sample orientations. The observed LD has been compared with the calculated LD obtained by full multiplet theory under cubic CEF. It has been confirmed that the Γ_8^3 ground state is consistent with the present experiment. Furthermore, theoretical calculations showed that there is a linear relationship between the size of LD and the size of the fourth order multipole moment of Er^{3+} ion in the cubic CEF. Using the experimental LD size we have estimated that the value of the fourth order multipole moment at 45 K as: $\langle (O_4^0 + 5O_4^4)/F(4) \rangle = -36$. This value is consistent with the CEF parameter estimated based on the specific heat measurement. Using the simulated LD temperature dependent, the value of the fourth and sixth order multipole moment has been estimated at different temperatures for Er 4*f* ground states. This value indicated that the behavior of the fourth order moment of Er 4*f* electrons is the same while that of the sixth order moment is different for each ground state. These calculations revealed the crucial role of the fourth order moment to interpret LD temperature dependent data. Also, LD temperature dependence in Er $3d_{5/2}$ XPS along [100] direction of $ErCo_2$ has been successfully observed. Moreover, polarization dependent Er $3d_{5/2}$ XPS and their LDs have been successfully confirmed at three different orientations [100], [111] and [110] of the cubic $ErCo_2$.

5.5. References

[5.1] H. Kirchmayr and C. Poldy, in Handbook on the Physics and Chemistry of Rare Earths, ed. K. A. Gschneidner, Jr. , and L. Eyring (North-Holland, Amsterdam, 1979) Vol. 2, p. 151.

[5.2] K. H. J. Buschow, in Ferromagnetic Materials, ed. E. P. Wohlfarth (North-Holland, Amsterdam, 1980) Vol. 1, p. 297.

[5.3] J. J. M. Franse and R. J. Radwanski, in Handbook of Magnetic Materials, ed. K. H. J. Buschow (Elsevier, Amsterdam, 1993) Vol. 7, p. 307 .

[5.4] E. Gratz and A. S. Markosyan, Physical properties of RCo_2 Laves phase, J. Phys. Condens. Matter, Vol. 13, p. R385 (2001). DOI: 10.1088/0953-8984/13/23/202.

[5.5] D. Bloch, D. M. Edwards, M. Shimizu and J. Voiron, First order transitions in ACo_2 compounds. J. Phys.: Metal. Phys F, Vol. 5, p. 1217 (1975).

DOI: 10.1088/0305-4608/5/6/022.

[5.6] E. P. Wohlfarth and P. Rhodes, Phil. Magn., Vol. 7, p. 1817 (1962).

[5.7] V. V. Aleksandryan, R. Z. Levitin, A. S. Markosyan, V. V. Snegirev and A. D. Shchurova, Properties of isotropic and anisotropic magnetoelastic interactions of intermetallic RCo_2 compounds, Sov. Phys. JETP, Vol. 65, p. 502 (1987).

[5.8] A. V. Andreev, in Handbook of Magnetic Materials, ed. K. H. J. Buschow (Elsevier, Amsterdam, 1995) Vol. 8, Chap. 2, p. 59.

[5.9] A. V. Andreev, A. V. Deryagin, S. M. Zadvorkin, V. N. Moskalev and E. V. Sintsyn, Influence of the 3d-metal on the magnetic properties of quasibinary rare-earth intermetalics Er(Fe_1-xCox)2, Phys. Met. Metallogr., Vol. 59, p. 57 (1985).

[5.10] G. Petrich and R. L. Mössbauer, Phys. Lett. A, Vol. 26, p. 403 (1968).

[5.11] N. C. Koon and J. J. Rhyne, Ground state spin dynamics of $ErCo_2$, Phys. Rev. B, Vol. 23, p. 207 (1981). DOI: 10.1103/PhysRevB.23.207.

[5.12] H.-G. Purwins and A Leson, Adv. Phys., Vol. 39, p. 309 (1990).

[5.13] H. Imai, H. wada and M. Shiga, Calorimetric study on magnetism of $ErCo_2$, J. Magn. Magn. Mater, Vol. 140-144, p. 835 (1995). DOI: 10.1016/0304-8853(94)01471-X

[5.14] M. T. Hutchings: in Solid State Physics, ed. F. Seitz and D. Turnbull (Academic Press, New York, 1964) Vol. 16, Chap. 3, p. 227.

[5.15] H. Kusunose, Description of multipole *in f-electron* systems, J. Phys. Soc. Jpn., Vol. 77, p. 064710 (2008). DOI: 10.1143/JPSJ.77.064710.

[5.16] K. R. Lea, M. J. M. Leask and W. P. Wolf, The raising of angular momentum degeneracy of f-electron terms by cubic crystal fields, J. Phys. Chem. Solids, Vol. 23, p. 1381 (1962). DOI: 10.1016/0022-3697(62)90192-0.

[5.17] G. van der Laan, G. Ghiringhelli, A. Tagliaferri, N. B. Brookes and L. Braicovich, Phys. Rev. B, Vol. 69, p. 104427 (2004).

[5.18] T. Mori , S. Kitayama, Y. Kanai, S. Naimen, H. Fujiwara, A. Higashiya, K. Tamasaku, A. Tanaka , K. Terashima, S. Imada , A. Yasui, Y. Saitoh, K. Yamagami, K. Yano, T. Matsumoto, T. Kiss, M. Yabashi, T. Ishikawa, S. Suga, Y. Ōnuki, T. Ebihara and A. Sekiyama, Probing strongly correlated 4f-orbital symmetry of the ground state in Yb compounds by linear dichroism in core-level photoemission, J. Phys. Soc. Jpn., Vol. 83, p. 123702 (2014). DOI: 10.7566/JPSJ.83.123702.

[5.19] Y. Kanai, T. Mori , S. Naimen , K. Yamagami, H. Fujiwara, A. Higashiya, T. Kadono, S. Imada, T. Kiss, A. Tanaka , K. Tamasaku, M. Yabashi, T. Ishikawa, F. Iga and A. Sekiyama, Evidence for Γ_8 ground-state symmetry of cubic YbB_{12} probed by linear dichroism in core-level photoemission, J. Phys. Soc. Jpn., Vol. 84, p. 073705 (2015).

DOI: 10.7566/JPSJ.84.073705

[5.20] A. Menovsky and J. J. M. Franse, J. Cryst. Growth, Vol. 65, p**.** 286 (1983).

[5.21] M. Yabashi, K. Tamasaku and T. Ishikawa, Phys. Rev. Lett., Vol. 87, p. 140801 (2001).

[5.22] H. Fujiwara, S. Naimen, A. Higashiya, Y. Kanai, H. Yomosa, K. Yamagami, T. Kiss, T. Kadono, S. Imada, A. Yamasaki, K. Takase, S. Otsuka, T. Shimizu, S. Shingubara, S. Suga, M. Yabashi, K. Tamasaku, T. Ishikawa and A. Sekiyama, J. Synchrotron Rad., Vol. 23, p. 735 (2016) .

[5.23] Calculation of the sign of $\langle Z_4^{cube}(core)\rangle$, which will be presented elsewhere, can be performed in a similar way as in S. M. Goldberg, C. S. Fadley, S. Kono, J. Electron Spectrosc. Relat. Phenom., Vol. 21, p. 285 (1981).

[5.24] B. T. Thole, G. van der Laan, J. C. Fuggle, G. A. Sawatzky, R. C. Karnatak and J.-M. Esteva, Phys. Rev. B, Vol. 32, p. 5107 (1985).

[5.25] A. Tanaka, and T. Jo, J. Phys. Soc. Jpn., Vol. 63, p. 2788 (1994).

[5.26] R. D. Cowan, The Theory of Atomic Structure and Spectra (University of California Press, Berkeley, 1981).

[5.27] W. T. Carnall, P. R. Fields and K. Rajnak, J. Chem. Phys., Vol. 49, p. 4424 (1968).

[5.28] U. Walter, Charge distributions of crystal field states, Z. Phys. B, Vol. 62, p. 299 (1986).

[5.29] E. Holland-Moritz, D. Wohlleben and M. Loewenhaupt, Anomalous paramagnetic neutron spectra of some intermediate-valence compounds, Phys. Rev. B, Vol. 25, p. 7482 (1982). DOI: 10.1103/PhysRevB.25.7482

Chapter 6

Conclusions and Suggestions for Future Work

Chapter 6

Conclusion and Suggestions for Future Work

6.1. Conclusion

In this thesis, the electronic states (valence band and core level) of the first order ferrimagnet single crystal $ErCo_2$ studied by polarization dependent hard X-ray photoemission spectroscopy (HAXPES). Bulk sensitive measurement of temperature dependent $ErCo_2$ valence band HAXPES has been successfully performed and $ErCo_2$ electronic structure has been investigated above and below T_C. Also, the polarization dependent $ErCo_2$ valence band photoemission spectra have been fruitfully observed in the paramagnetic cubic phase using linear polarized HAXPES at two different sample orientations.

Moreover, band structure calculations have been performed in both rhombohedral and cubic structure of $ErCo_2$; and these calculations revealed many characteristics for $ErCo_2$ electronic structure in the disordered and ordered magnetic state such as: (a) verifying the antiparallel orientation between Er 4*f* and Co 3*d* magnetic moment in the ordered magnetic state, (b) demonstrating a sharp peak lies just below E_F in Co 3d band due to the high contribution of itinerant electrons Co 3d which is the reason for IEM in $ErCo_2$ compound, (c) in the paramagnetic phase, PDOSs of majority and minority spins are almost same except Er 4*f* band due to its localized natural, so DOS of Er 4*f* band in both $ErCo_2$ structures has no essential differences, (d) in the rhombohedral structure, although Co 9e and Co 3b atoms located in two different positions, the DOS and moments of two Co atoms have no crucial differences, (e) in the ordered magnetic state, the magnetic behavior of $ErCo_2$ is mostly dominated by the Er sublattice where Er magnetic moment is much higher than that of the two Co atoms, (f) the main contribution to the total DOS around Fermi level is due to the contribution of Co 3*d* subbands.

Furthermore, band structure calculations and photoionization cross section reproduced and described well most features of the experimental $ErCo_2$ valence band HAXPES data. Both the experimental and calculated $ErCo_2$ valence band photoemission spectrum confirmed that the *s* electronic state was suppressed in the case of vertical polarized light. However, the discrepancy between the experimental and calculated spectra in the intensity and the peaks positions near E_F. These differences suggest that the present band structure calculation is not

yet enough for understanding $ErCo_2$ electronic states. Further theoretical studies taking in account electron correlation is needed.

Er 3*d* and Co 2*p* core-levels photoemission spectra of cubic $ErCo_2$ have been investigated using linear polarized HAXPES. Temperature and polarization dependent Co 2*p* core level XPS of cubic $ErCo_2$ have been successfully performed. Polarization dependent Er $3d_{5/2}$ core-level photoemission spectra (XPS) and their LDs have been successfully observed by means of bulk sensitive hard X-ray photoemission at different orientations of cubic $ErCo_2$. Intrinsic LD has been extracted by cancelling out the polarization dependent background based on the measurements at two different sample orientations. The calculated LD by full multiplet theory under cubic CEF reproduced the observed LD in both shape and size at Er^{3+} 4*f* ground states ($\mathbf{\Gamma_8^3}$, $\mathbf{\Gamma_8^1}$ and $\mathbf{\Gamma_7}$).

Theoretical calculations elucidated that the multipole moment of Er^{3+} 4*f* electrons in the cubic crystal electric field can be estimated using LD in Er 3*d* XPS. These calculations revealed that there is a linear relationship between the size of LD and the size of fourth order moment, while there is no relation between LD and sixth order multipole moment. Using the experimental LD size we have estimated that the value of the fourth order multipole moment at 45 K is $\langle(\boldsymbol{O_4^0 + 5O_4^4})/\boldsymbol{F(4)}\rangle = \mathbf{-36}$. This value is consistent with the CEF parameter estimated based on the specific heat measurement.

LD temperature dependent in Er 3*d* XPS was estimated for all Er^{3+} ground states by means of the full multiplet theory under cubic CEF, the results confirmed that at sufficient high temperature LD reduces gradually and has isotropic spectra without flip of its sign. However, it was observed that sometimes LD has non-isotropic spectra (difference in shape, sign or size) at low temperatures; this behavior of LD along high and low temperature ranges can be interpreted by the fourth order multipole moment. The ionic calculations including the full multiplet theory for Er^{3+} ion under cubic CEF splitting elucidated the crucial role of the fourth order multipole moment to interpret the behavior of LD temperature dependent at all temperatures range.

6.2. Future Work

The study presented in this thesis is expected to be valuable for both the academic research and the applications in the field of photoemission spectroscopy owing to the developed method to quantify experimentally the fourth order multipole of rare-earth 4*f*

orbital. This interesting finding motivated the author in the future plan to proceed towards extending the present study along the series of RCo_2 and R-T compounds crystalized in the cubic , tetragonal and hexagonal structures. But the estimation of the fourth order multipole in tetragonal and hexagonal structure is a little difficult, because in the tetragonal structure there are two component of fourth order multipole moment (O^0_4 and O^4_4). So we have to measure two LDs and found which one correspond to each component of fourth order multipole moment. Then, we will found the relation between them.

Furthermore, we will try demonstrating the relation between sixth order multipole moments of *f* electron system and LD in R-T compounds. But HAXPES core level measurement is not straightforward to estimate sixth order multipole moments. There are three techniques will be performed using synchrotron radiation depending on polarization and crystal axis might be include on information about sixth order multipole moments such as:

(1) Extract pure 4*f* spectrum from valence band PES [performed at Spring8].

(2) Resonant PES [performed at Spring8].

(3) Resonant inelastic X-ray scattering (RIXS) [performed at SLS, NSRRC (Taiwan) and SYNCH. in Stanford (USA)].

Also, we will try to spread our results in international journals and conferences.

Appendices

Appendix (A)

The Main Factors in Band Structure Calculations

A.1. Magic number

Band structure calculations have been performed at different magic numbers 0.25, 0.32, 0.36, 0.417, and 0.5 for the cubic structure of $ErCo_2$ in ferrimagnetic phase (lattice constant at 45 K). Also, band structure calculations have been done at magic number 0.32 for the cubic structure of $ErCo_2$ in paramagnetic phase (lattice constant at 45 K) and rhombohedral structure (lattice constant at 25 K) of $ErCo_2$ in ferrimagnetic phase. These process summarized in **Table A.1**. **Fig. A.1** reveals that the PDOSs of Er and Co atoms have no essential difference with increasing the magic number except PDOS of Er 4*f* state shifts to a lower energy.

Table A.1 Magnetic moments (in $\boldsymbol{\mu_B}$) of Er and Co atoms in $ErCo_2$ compound at different magic numbers (continued to the next page).

			Er			Co			
State	**bzqlty**	**ewidth**	**Field (Ry)**	**M_S**	**M_O**	**Field (Ry)**	**M_S**	**M_O**	**Comment**
Magic Number: 0.25									
1	4	0.9	0.025	3.35200	6.23105	0.0	-1.01290	-0.09374	Convergence
2	4	0.9	0.0			0.0			No convergence Using state 1 data
3	10	1.0	0.0	3.12768	5.50474	0.0	-0.84016	-0.08512	Convergence Using state 1 data
Magic number: 0.32 (Cubic (Ferrimagnetic))									
1	4	0.9	0.025	3.40170	5.56940	0.0	-1.03216	-0.10123	Convergence
2	10	0.9	0.0	2.88724	5.80497	0.0	-0.88192	-0.09263	Convergence Using state 1 data
Magic number: 0.32 (Cubic (Paramagnetic))									
1	7	0.9	0.0	2.69462	5.82573	0.0	0.0	0.0	Convergence Using state 2 data at (cubic (ferrimagnetic))

Table A.1. (continued from the previous page) Magnetic moments (in $\boldsymbol{\mu_B}$) of Er and Co atoms in $ErCo_2$ compound at different magic numbers.

			Er			Co				
State	**bzqlty**	**ewidth**	**Field (Ry)**	**M_S**	**M_O**	**Field (Ry)**		**M_S**	**M_O**	**Comment**
Magic number: 0.32 (Rhombohedral (Ferrimagnetic from cubic)										
1	7	0.9	0.0	2.88255	5.81323	Co 9e	0.0	-0.88131	-0.08387	Convergence Using state 2 data at (cubic (ferrimagnetic))
						Co 3b	0.0	-0.92289	-0.12742	
Magic number: 0.32 (Rhombohedral (Ferrimagnetic)) from nothing										
1	4	0.9	0.03	3.48374	4.59813	Co 9e	0.0	-1.11799	-0.09571	Convergence Er orbital moment is small
						Co 3b	0.0	-1.13167	-0.14260	
2	4	0.9	0.025	3.38439	4.59456	Co 9e	0.0	-1.08667	-0.09373	Convergence Er orbital moment is small
						Co 3b	0.0	-1.09624	-0.14112	
3	7	0.9	0.05			Co 9e	0.0			No Convergence
						Co 3b	0.0			
4	4	1.0	0.025	3.40550	5.15382	Co 9e	0.0	-1.04938	-0.08001	Convergence Er orbital moment is little smaller
						Co 3b	0.0	-1.05783	-0.11786	
5	4	0.85	0.025	3.41235	4.82611	Co 9e	0.0	-1.06051	-0.08943	Convergence Er orbital moment is small
						Co 3b	0.0	-1.06717	-0.13360	
6	4	0.9	0.02			Co 9e	0.0			No Convergence
						Co 3b	0.0			
7	4	1.0	0.05	3.62649	5.31233	Co 9e	0.0	-1.18694	-0.10287	Convergence
						Co 3b	0.0	-1.21468	-0.15895	
8	4	1.0	0.03	3.32281	5.32977	Co 9e	0.0	-1.14248	-0.10814	Convergence Using state 7 data
						Co 3b	0.0	-1.17340	-0.16689	
9	4	1.0	0.0			Co 9e	0.0			No convergence Using state 8 data
						Co 3b	0.0			
10	4	1.0	0.0			Co 9e	0.0			No convergence Using state 7 data
						Co 3b	0.0			
11	4	0.9	0.0			Co 9e	0.0			No convergence Using state 8 data
						Co 3b	0.0			
12	10	0.85	0.0	2.97091	5.71803	Co 9e	0.0	-0.88180	-0.08167	Convergence Using state 8 data
						Co 3b	0.0	-0.91905	-0.12234	
Magic number: 0.36										
1	4	1.0	0.03			0.0				No convergence
2	4	0.9	0.03			0.0				No convergence
3	4	0.9	0.05	3.54052	6.23406	0.0		-1.17354	-0.10998	Convergence
4	10	0.9	0.0	2.96306	5.74078	0.0		-0.90278	-0.08717	Convergence Using state 3 data
Magic number: 0.417										
1	4	0.9	0.05	3.38023	6.12511	0.0		-1.19135	-0.10819	Convergence
2	10	0.9	0.0	3.09589	5.75693	0.0		-0.88361	-0.08069	Convergence Using state 1 data
Magic number: 0.5										
1	4	0.9	0.025	3.57678	5.95473	0.0		-1.17343	-0.10482	Convergence
2	10	0.9	0.0	3.20744	5.80499	0.0		-0.89481	-0.08380	Convergence Using state 1 data

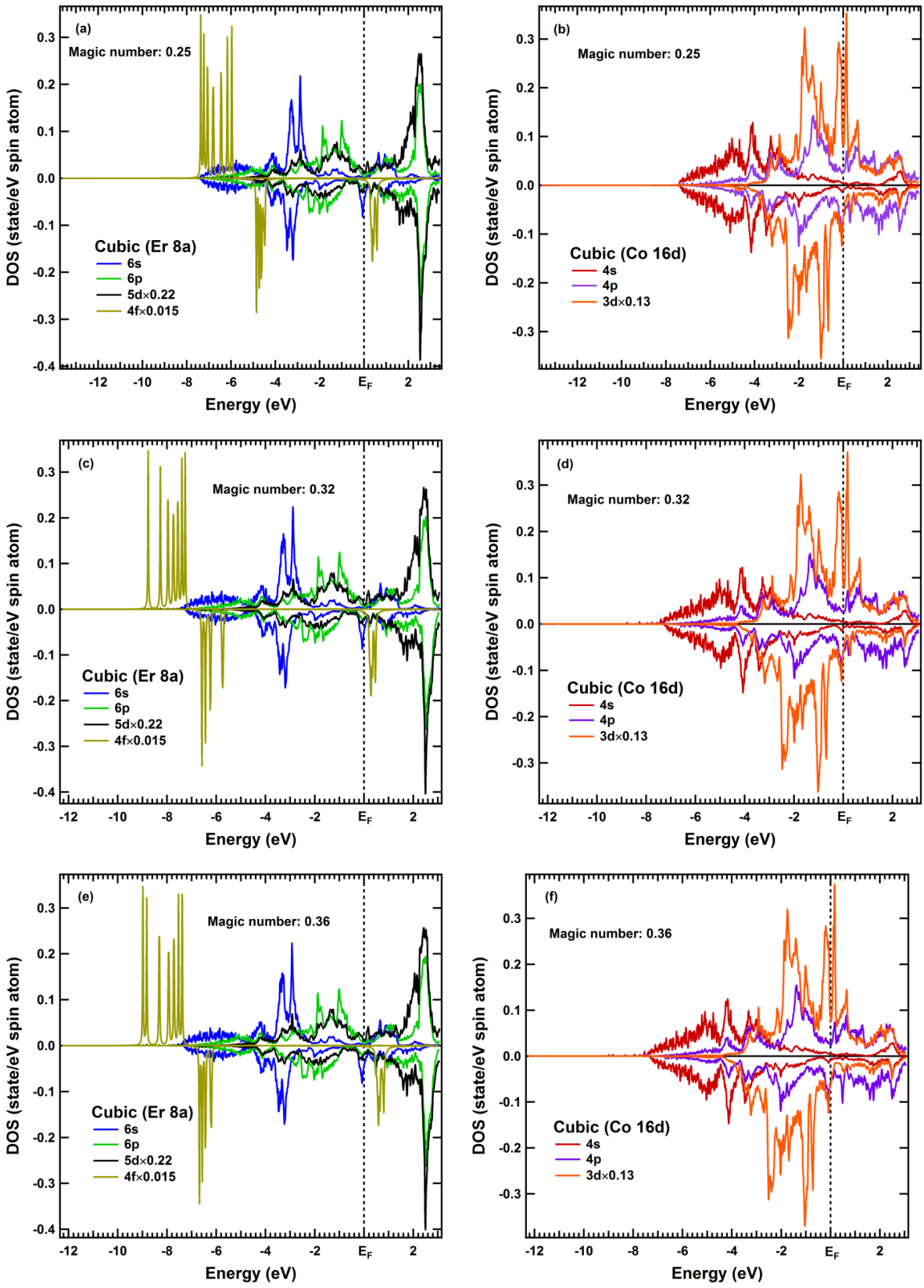

Fig. A.1. Partial DOS for the cubic structure of $ErCo_2$ in ferrimagnetic phase at different magic numbers (continued to the next page).

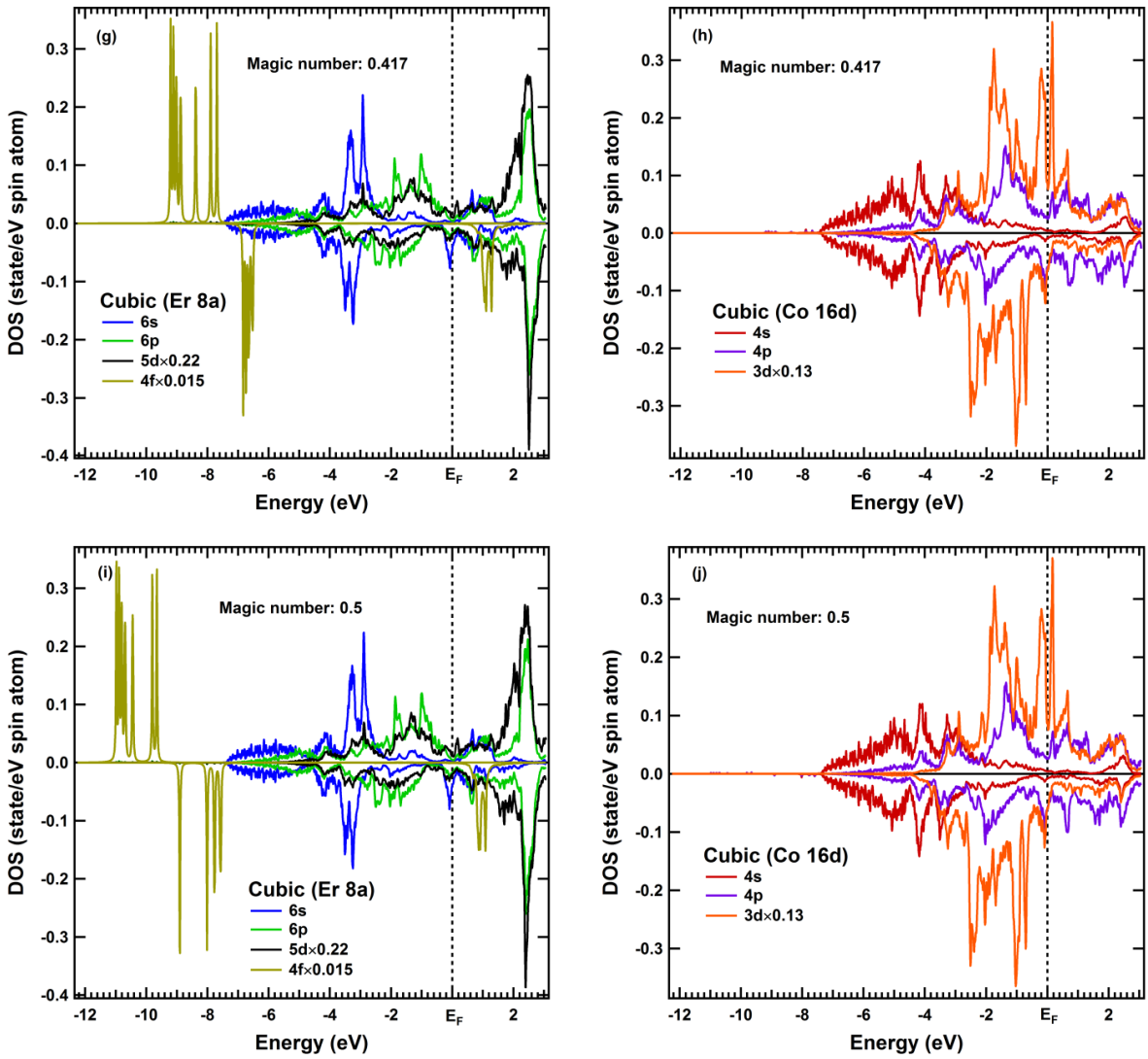

Fig. A.1. (continued from the previous page) Partial DOS for the cubic structure of $ErCo_2$ in ferrimagnetic phase at different magic numbers.

A.2. PDOS and Total DOS at Magic Number 0.32 in Both Structure of $ErCo_2$

A.2.1. Cubic Structure (Paramagnetic)

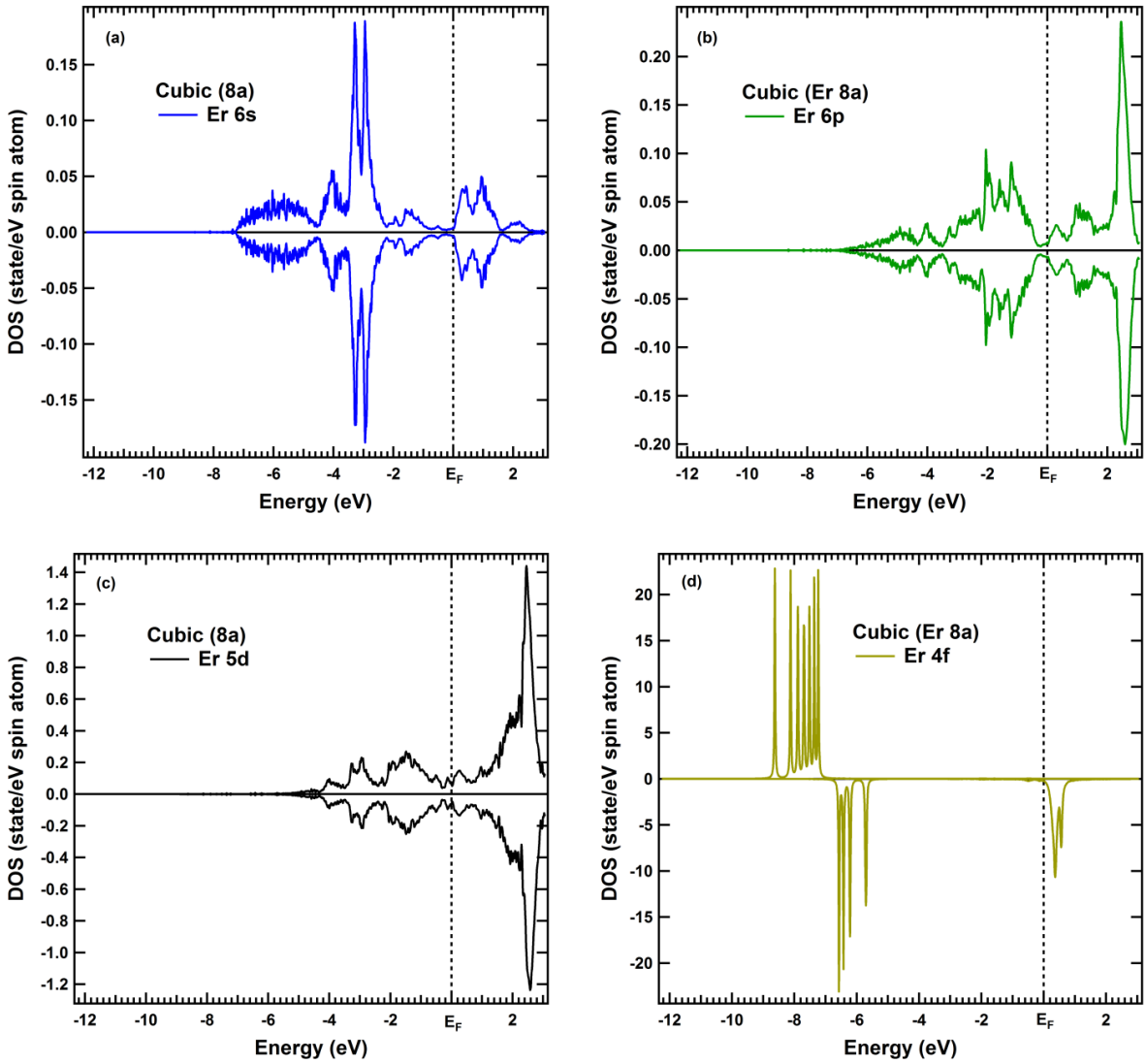

Fig. A.2. Partial and total DOS in the cubic structure (paramagnetic) of $ErCo_2$ compound (a) Er 6*s*; (b) Er 6*p*; (c) Er 5*d*; (d) Er 4*f* ; (e) Co 4*s*; (f) Co 4*p*; (g) Co 3*d*, (h) total DOS and (i) total DOS integration (number of electron at E_F=64.009) (continued to the next page).

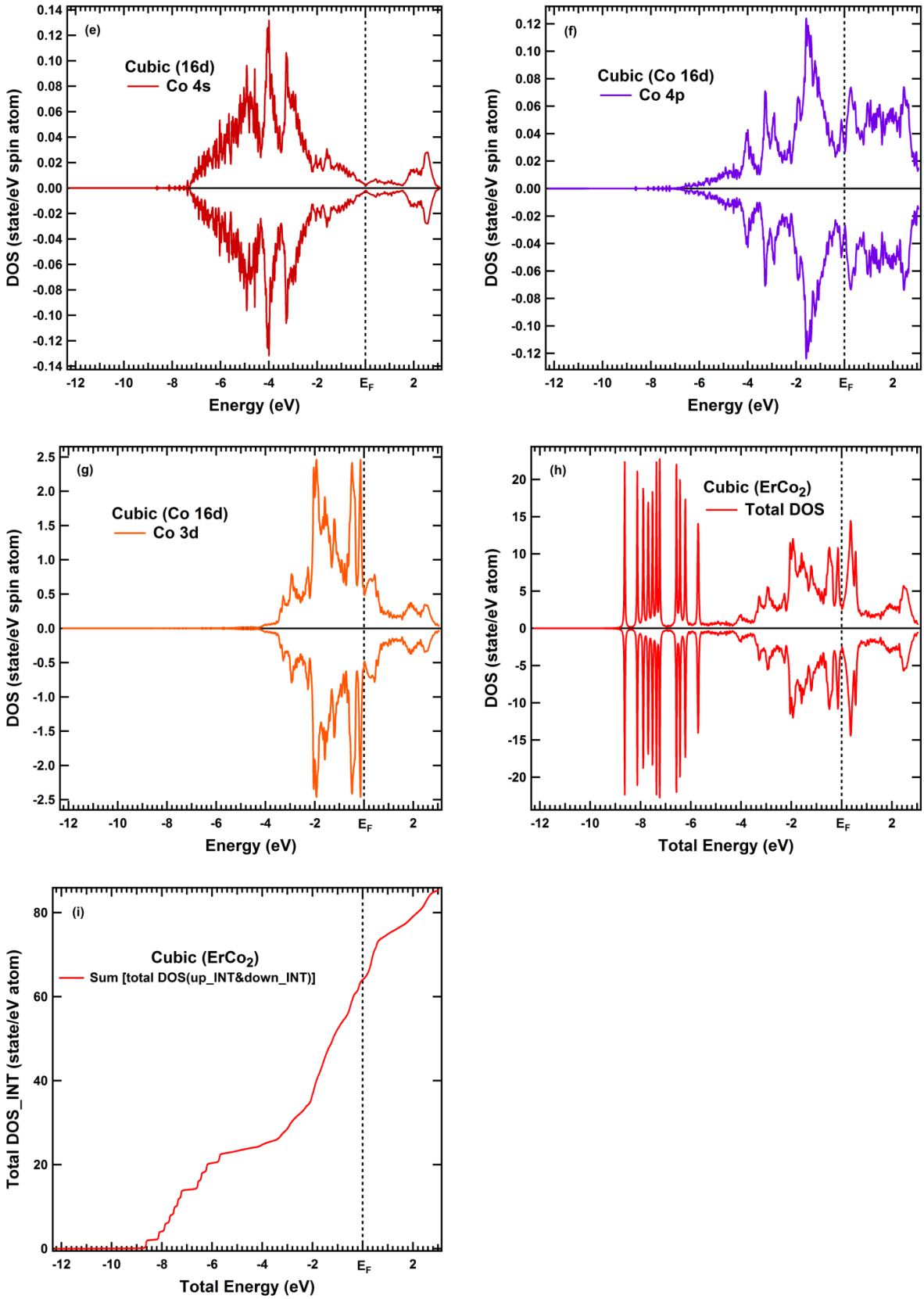

Fig. A.2. (continued from the previous page) Partial and total DOS in the cubic structure (paramagnetic) of $ErCo_2$ compound (a) Er 6s; (b) Er 6*p*; (c) Er 5*d*; (d) Er 4*f* ; (e) Co 4s; (f) Co 4*p*; (g) Co 3*d*; (h) total DOS and (i) total DOS integration (number of electron at E_F=64.009).

The properties of partial and total DOS in the cubic structure (paramagnetic) of $ErCo_2$ are shown in **Fig. A.2** and explained in **Chapter 4**. The electronic structure of Er and Co atoms are:

$$Er^{68}=[Xe]\ 4f^{12}\ 6s^2 \qquad\qquad Co^{27}=[Ar]\ 3d^7\ 4s^2$$

Band structure calculations in paramagnetic phase have been performed using two Er atoms and four Co atoms, so the total number of electrons will be:

For Er=2(12+2)=28 electrons, for Co=4(7+2)=36 electrons and the total number of electrons=28+36=64.

Fig. A.2i shows the sum of the integration of the total DOS in up and down spin sub band in in the cubic structure of $ErCo_2$. Number of electrons at $E_F \cong 64.009$ which agree with the real total number of electron (64).

A.2.2. Rhombohedral structure (Ferrimagnetic from nothing)

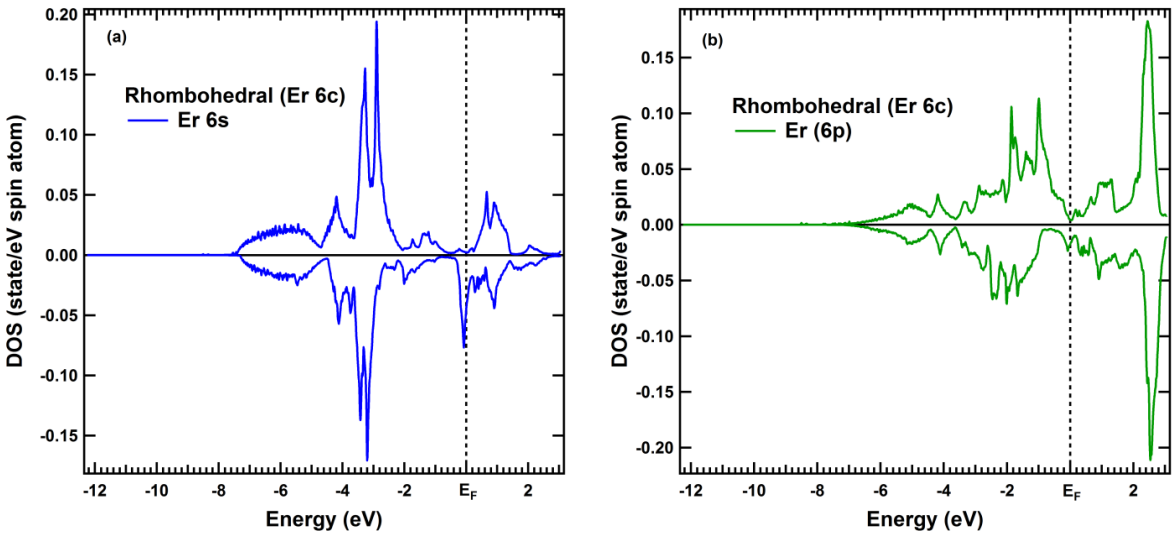

Fig. A.3. Partial and total DOS in rhombohedral structure of $ErCo_2$ compound (a) Er 6*s*; (b) Er 6*p*; (c) Er 5*d*; (d) Er 4*f*; (e) Co (9e) 4*s*; (f) Co (9e) 4*p*; (g) Co (9e) 3*d*; (h) Co (3b) 4*s*; (i) Co (3b) 4*p*; (j) Co (3b) 3*d*; (k) total DOS, and (l) total DOS integration (number of electron at E_F=191.96) (continued to the next page).

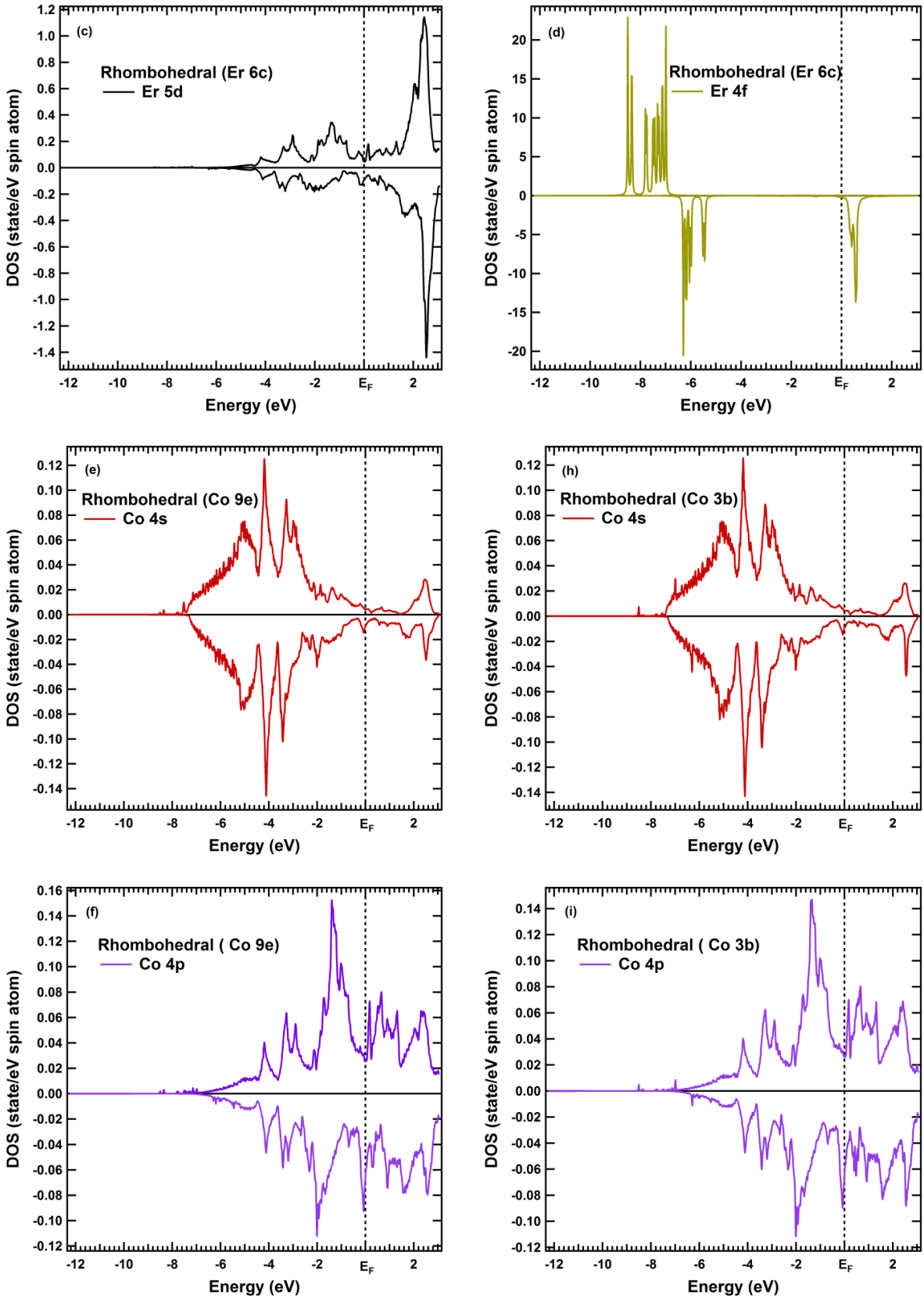

Fig. A.3. (continued from the previous page) Partial and total DOS in rhombohedral structure of $ErCo_2$ compound (a) Er 6*s*; (b) Er 6*p*; (c) Er 5*d*; (d) Er 4*f*; (e) Co (9e) 4*s*; (f) Co (9e) 4*p*; (g) Co (9e) 3*d*; (h) Co (3b) 4*s*; (i) Co (3b) 4*p*; (j) Co (3b) 3*d*; (k) total DOS, and (l) total DOS integration (number of electron at E_F=191.96) (continued to the next page).

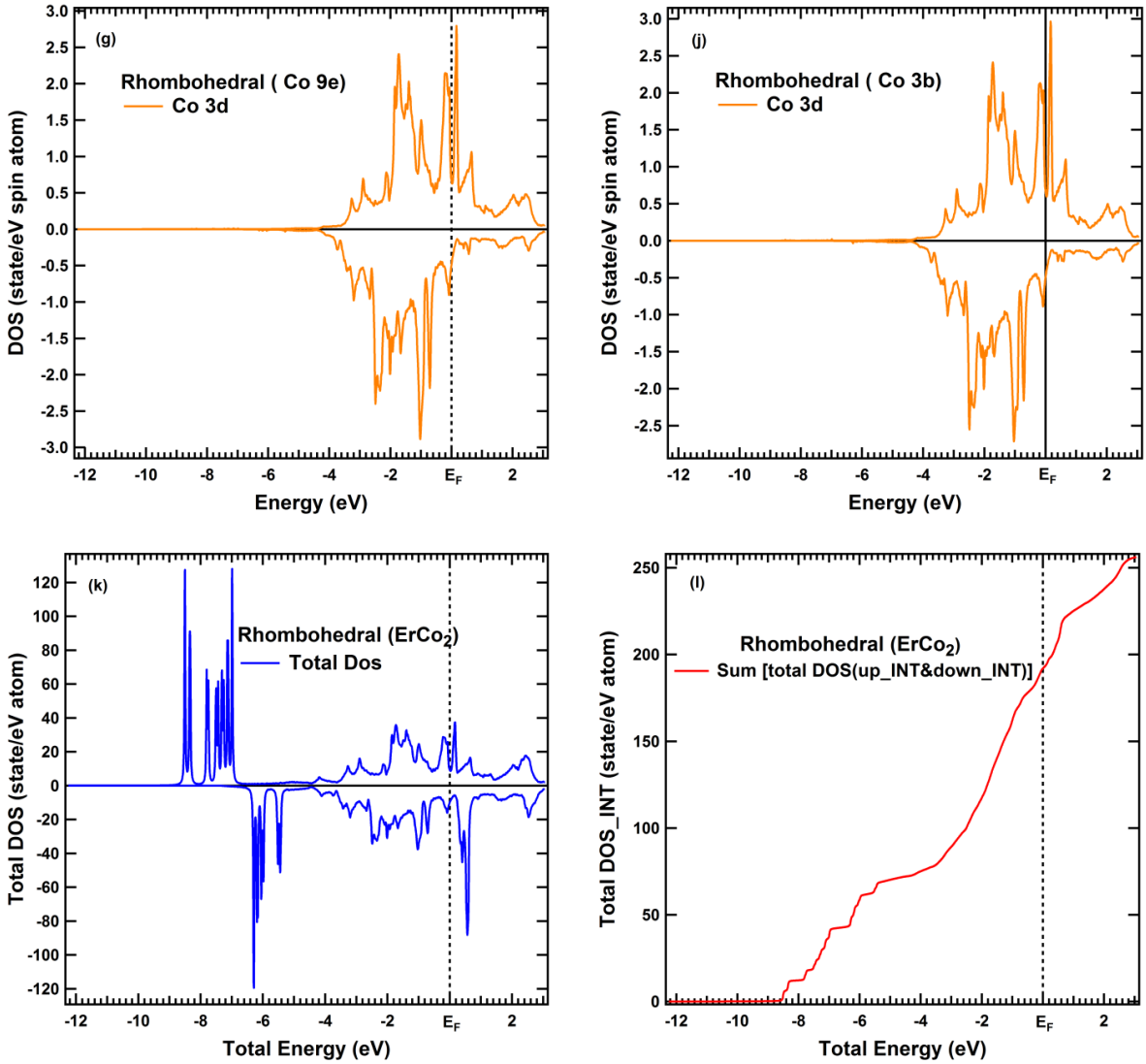

Fig. A.3. (continued from the previous page) Partial and total DOS in rhombohedral structure of $ErCo_2$ compound (a) Er 4*f* ; (b) Er 5*d*; (c) Er 6*p*; (d) Er 6*s*; (e) Co (9e) 3*d*; (f) Co (9e) 4*p*; (g) Co (9e) 4*s*; (h) Co (3b) 3*d*; (i) Co (3b) 4*p*; (j) Co (3b) 4*s*; (k) total DOS, and (l) total DOS integration (number of electron at E_F=191.96).

A.2.3. Rhombohedral structure (Ferrimagnetic phase using paramagnetic data)

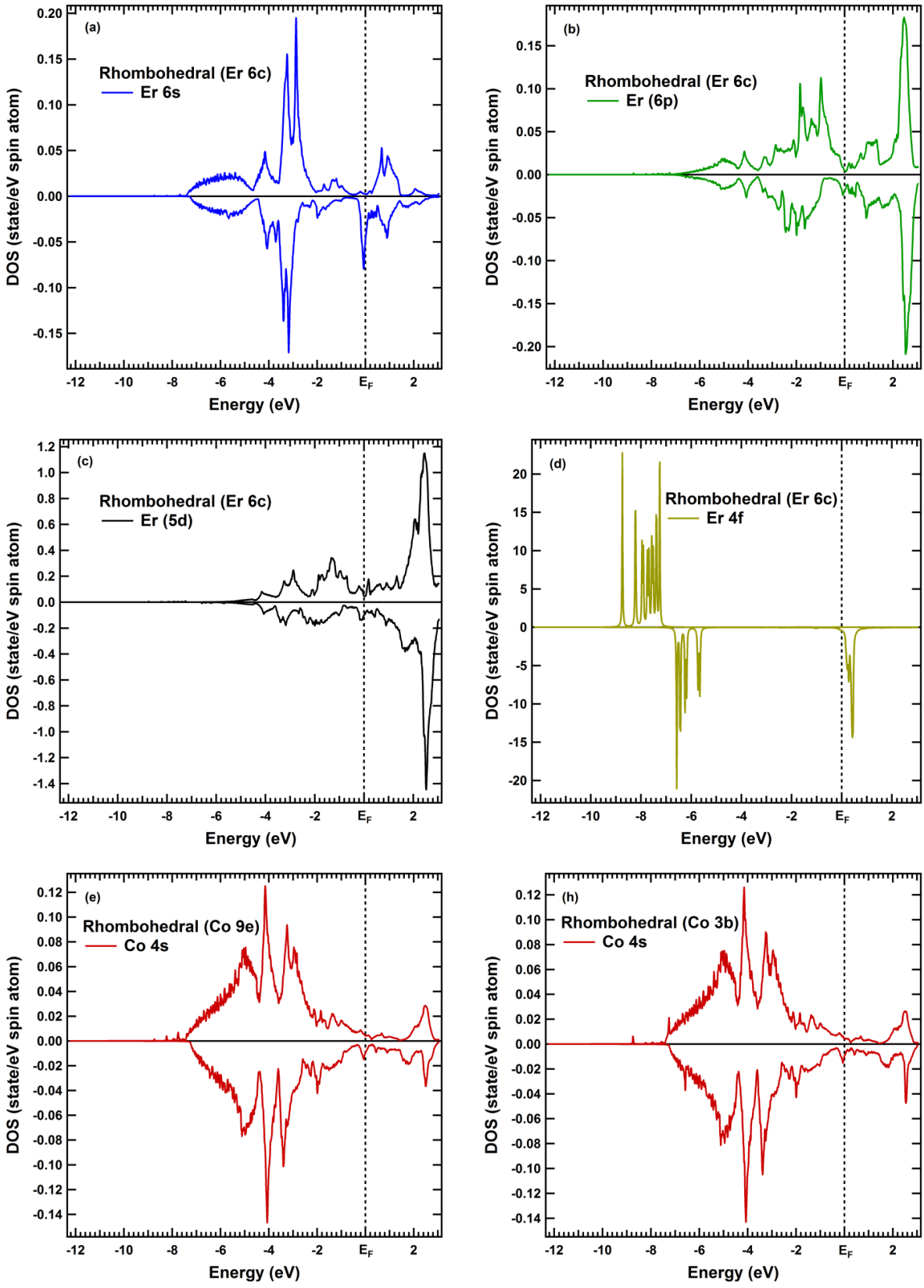

Fig. A.4. Partial and total DOS in rhombohedral structure of $ErCo_2$ compound (a) Er 6*s*; (b) Er 6*p*; (c) Er 5*d*; (d) Er 4*f* ; (e) Co (9e) 4*s*; (f) Co (9e) 4*p*; (g) Co (9e) 3*d*; (h) Co (3b) 4*s*; (i) Co (3b) 4*p*; (j) Co (3b) 3*d* ; (k) total DOS, and (l) total DOS integration (number of electron at E_F=191.96) (continued to the next page).

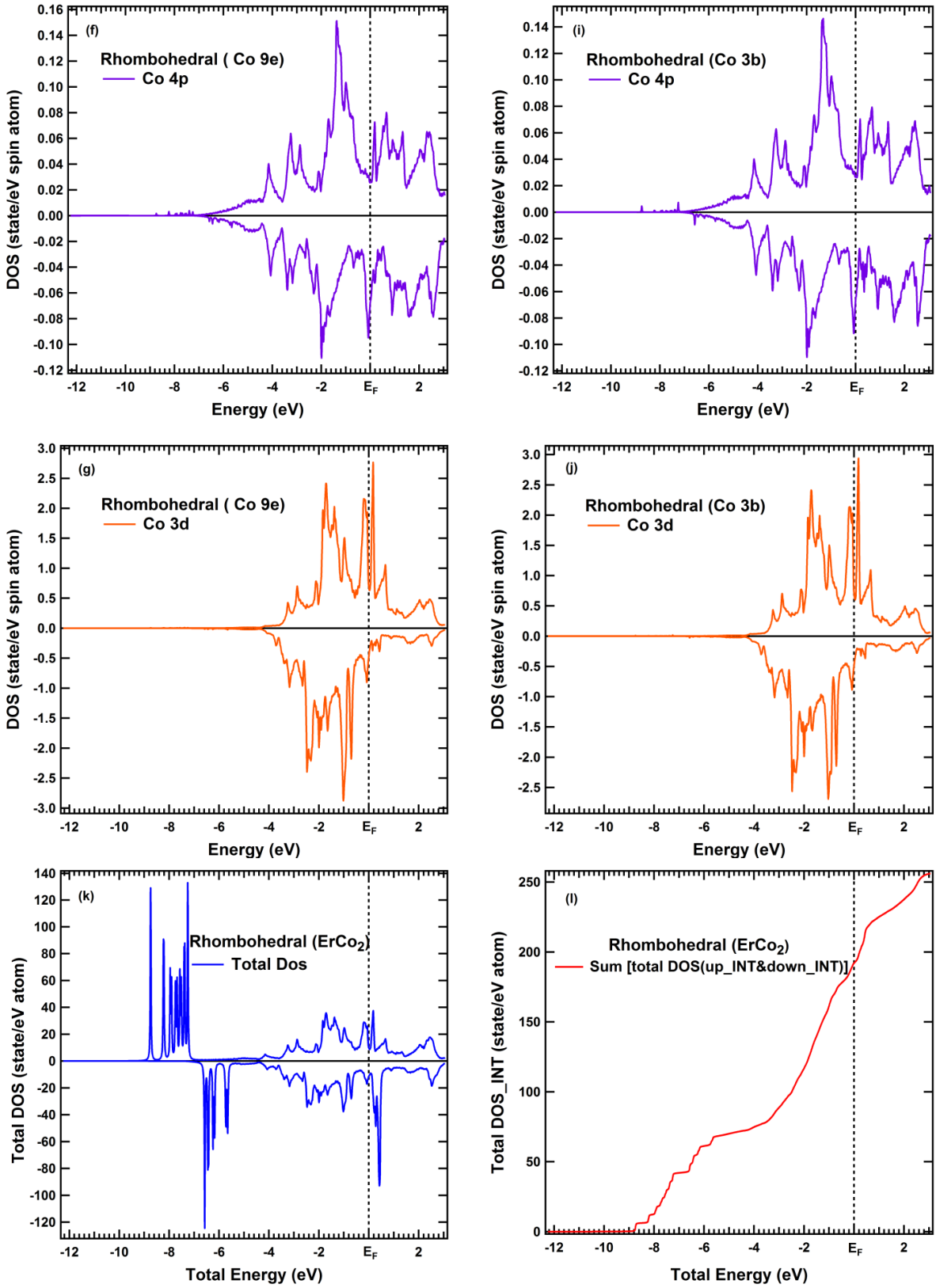

Fig. A.4. (continued from the previous page) Partial and total DOS in rhombohedral structure of $ErCo_2$ compound (a) Er 6*s*; (b) Er 6*p*; (c) Er 5*d*; (d) Er 4*f* ; (e) Co (9e) 4*s*; (f) Co (9e) 4*p*; (g) Co (9e) 3*d*; (h) Co (3b) 4*s*; (i) Co (3b) 4*p*; (j) Co (3b) 3*d*; (k) total DOS, and (l) total DOS integration (number of electron at E_F=191.96).

The properties of Partial and total DOS in the rhombohedral structure (ferrimagnetic) of $ErCo_2$ (**Fig. A.3** and **A.4**) explained in chapter 4. Band structure calculations in the rhombohedral structure from nothing (**Fig. A.3**) or using cubic data (**Fig. A.4**) have no essential difference. Band structure calculations in feriimagnetic phase have been performed using 6 Er atoms and 12 Co atoms, so the total number of electron will be:

For Er=6(12+2)=84 electron, for Co=12(7+2)=108 electron and the total number of electron=28+36=192.

Fig. A.3l and **Fig. A.4l** reveals the sum of the integration of the total DOS in up and down spin sub band in in the rhombohedral structure of $ErCo_2$. Number of electrons at $E_F \cong 191.96$ and this agree with the real total number of electron (192).

A.3. Effect of edelt

Fig. A.5. shows PDOSs per electron number × cross section per 1 electron, in the cubic structure of $ErCo_2$ compound for s and p polarization after broadening by Gaussian (edelt = 0.02) at 7.9 keV. These calculations confirmed that in p-pol *s* (Co 4*s*) electronic state has higher cross section than *d* (Co3*d*) electronic state, while in s-pol the cross section of *d* (Er 5*d* and Co 3*d*) electronic states are higher than *s* and *p* (Er 6*s*, Er 6*p*, Co4*s* and Co4*p*) electronic states. Therefore, the extraction of the contributions of *s* and *ip* states as well as the *d* and *f* states in the bulk valence band of solids becomes available using linear polarization HAXPES and photoionization cross-section plays a vital role in the analysis of HAXPES data.

Fig. A.6 illustrates calculated $ErCo_2$ valence band photoemission spectrum in the paramagnetic phase for p-polarization configuration at different edelt, where with increasing edelt gradually the DOS broadening increase.

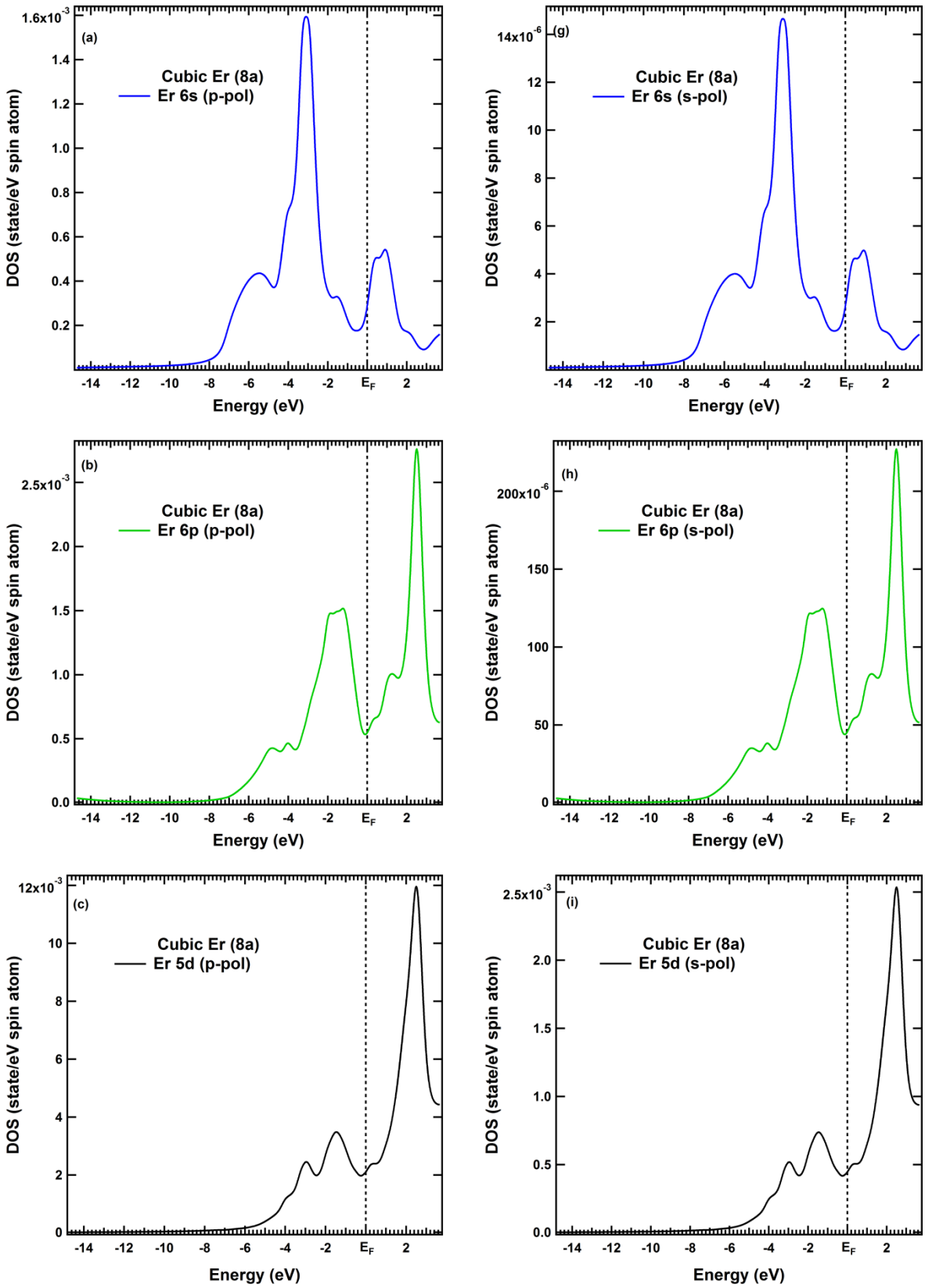

Fig. A.5. Partial DOS per electron number × cross section per 1 electron, in the cubic structure of $ErCo_2$ compound for s and p polarization after broadening by edelt: 0.02 at 7.9 keV, (a) Er 6*s*; (b) Er 6*p*; (c) Er 5*d*; (d) 4*s*; (e) Co 4*p* and (f) Co 3*d*, for s-polarization. (g) Er 6*s*; (h) Er 6*p*; (i) Er 5*d*; (j) 4*s*; (k) Co 4*p* and (l) Co 3*d*, for p-polarization (continued to the next page).

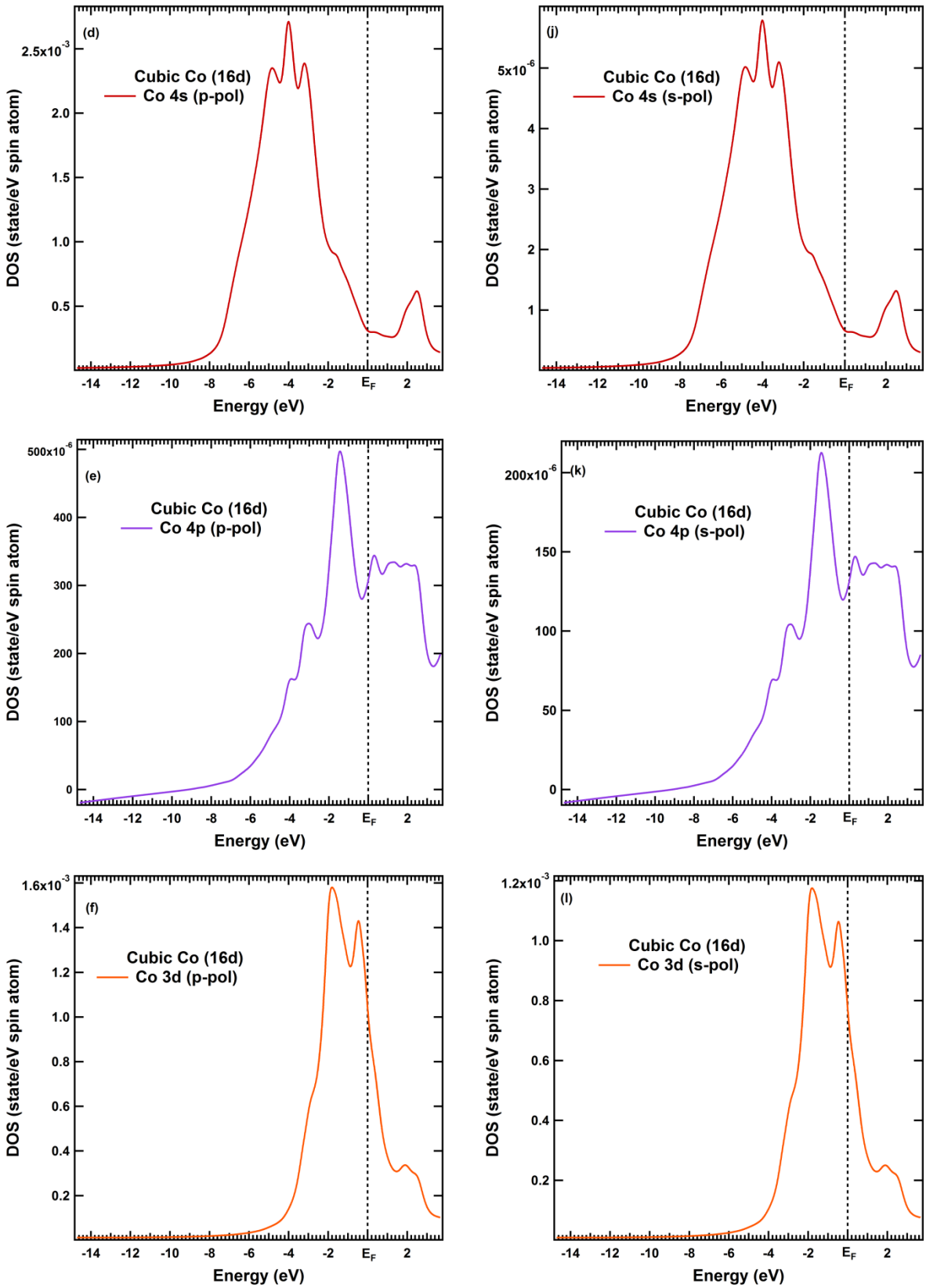

Fig. A.5. (continued from the previous page) Partial DOS per electron number × cross section per 1 electron, in the cubic structure of $ErCo_2$ compound for s and p polarization after broadening by edelt: 0.02 at 7.9 keV, (a) Er 6*s*; (b) Er 6*p*; (c) Er 5*d*; (d) 4*s*; (e) Co 4*p* and (f) Co 3*d*, for s-polarization. (g) Er 6*s*; (h) Er 6*p*; (i) Er 5*d*; (j) 4*s*; (k) Co 4*p* and (l) Co 3*d*, for p-polarization.

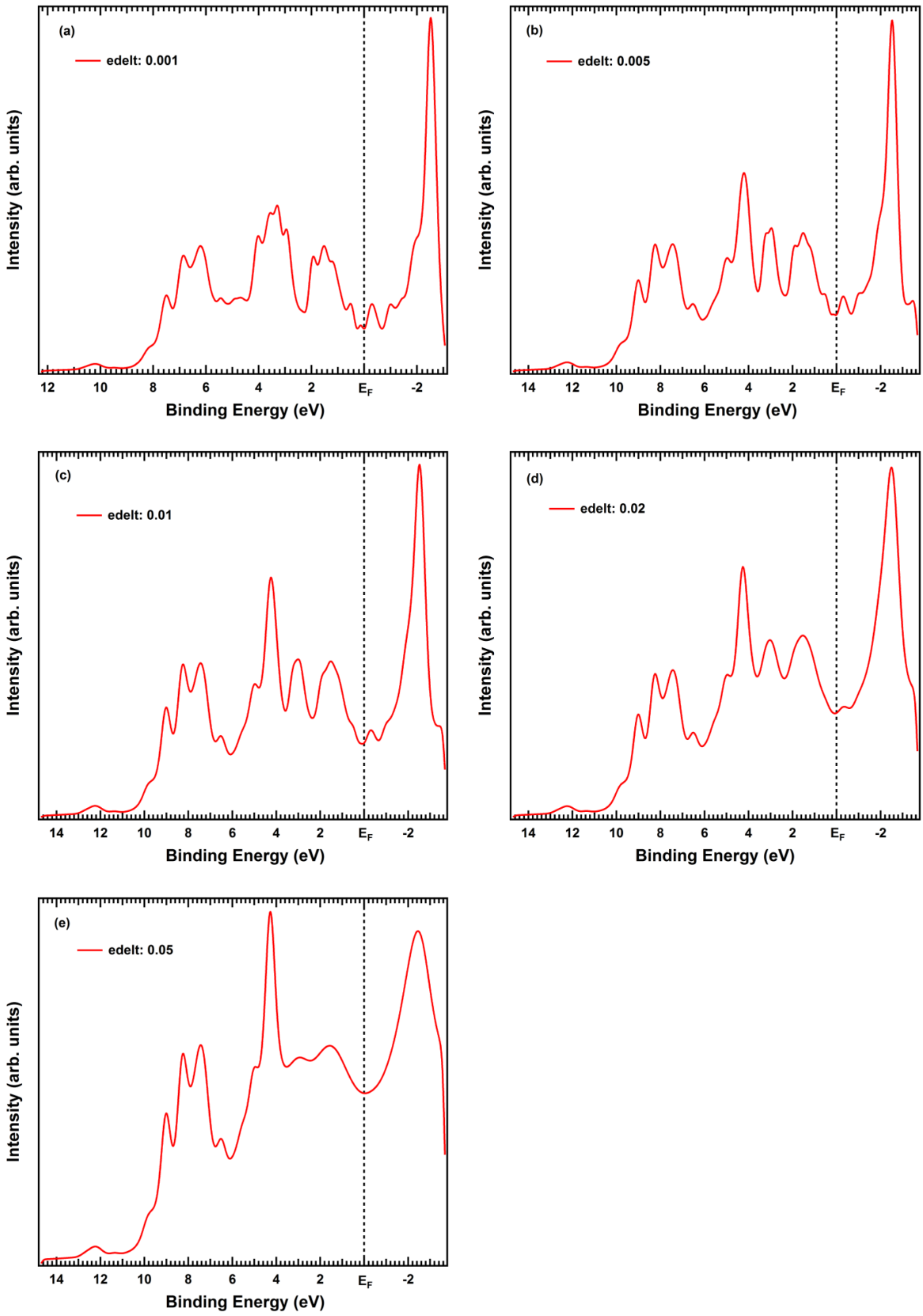

Fig. A.6. Calculated $ErCo_2$ valence band photoemission spectrum in the cubic structure (paramagnetic phase) for p-polarization configuration at different edelt.

Appendix B

B.1. LD CEF Parameters Dependence in Er^{3+} $3d_{5/2}$ XPS

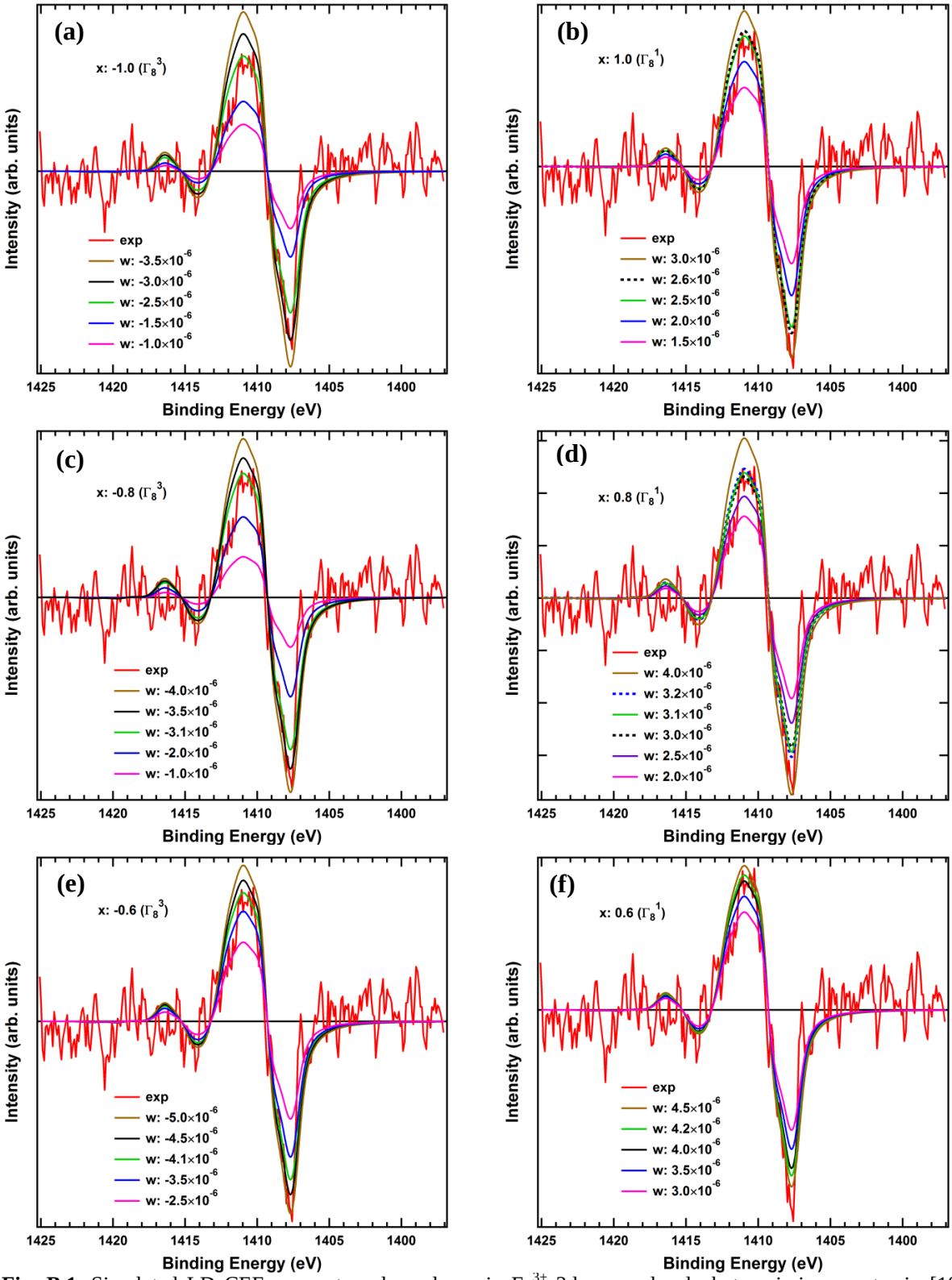

Fig. B.1. Simulated LD CEF parameters dependence in Er^{3+} $3d_{5/2}$ core level photoemission spectra in [100] direction of $ErCo_2$ at $\theta = 9.5^0$ assuming the crystal-field-split ground state in cubic symmetry (continued to the next page).

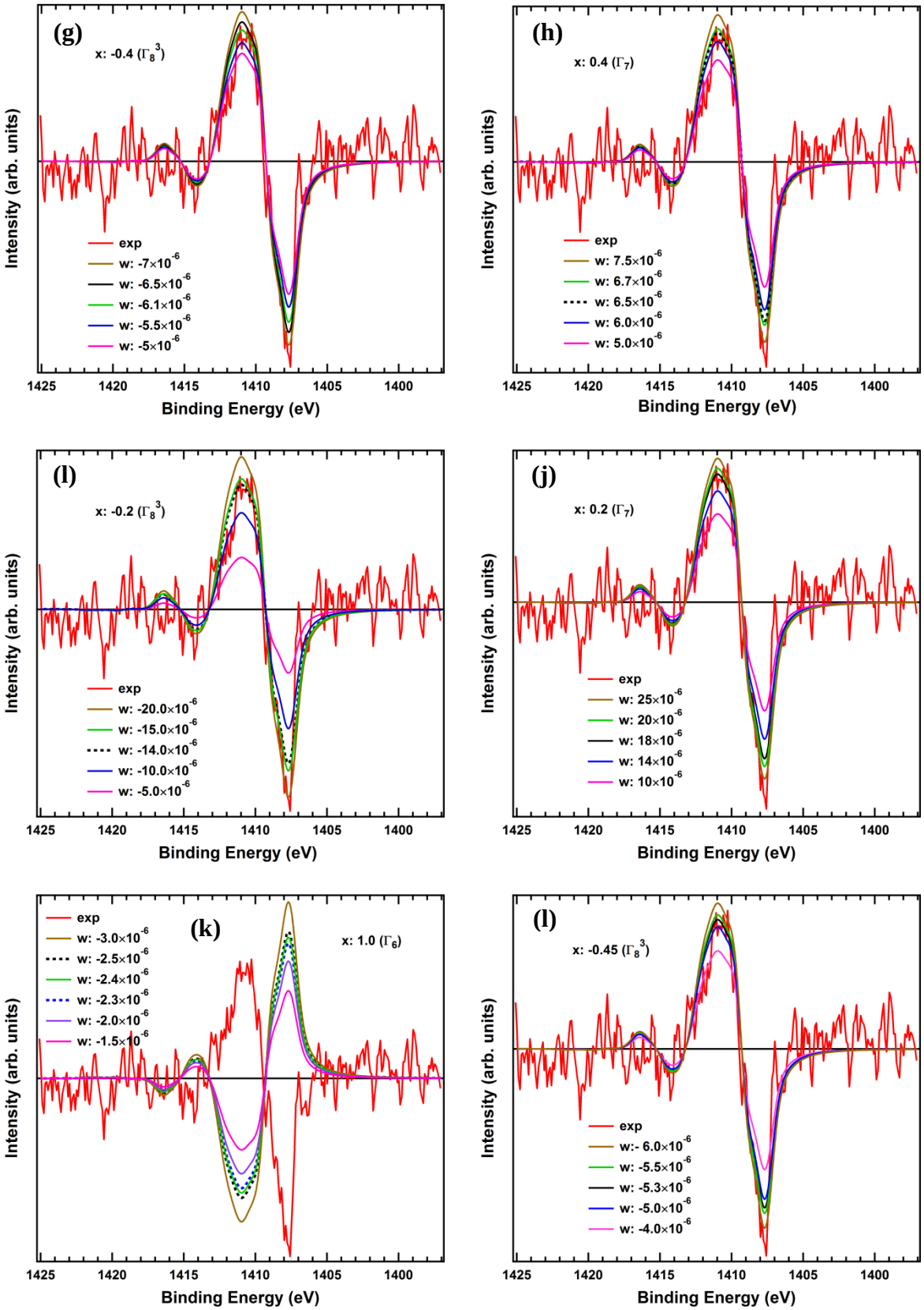

Fig. B.1. (continued from the previous page) Simulated LD CEF parameters dependence in Er^{3+} $3d_{5/2}$ core level photoemission spectra in [100] direction of $ErCo_2$ at $\theta = 9.5^0$ assuming the crystal-field-split ground state in cubic symmetry.

Fig. B.1. Shows simulated LD CEF parameters dependence in Er^{3+} $3d_{5/2}$ core level photoemission spectra in [100] direction of $ErCo_2$ at $\theta = 9.5^0$ assuming the crystal-field-split ground state in cubic symmetry for Er 4*f* ground states and it reveals how LD changes with changing CEF parameters. Also, this figure illustrates the CEF parameters which agree with the experimental LD for all the ground state which displayed here.

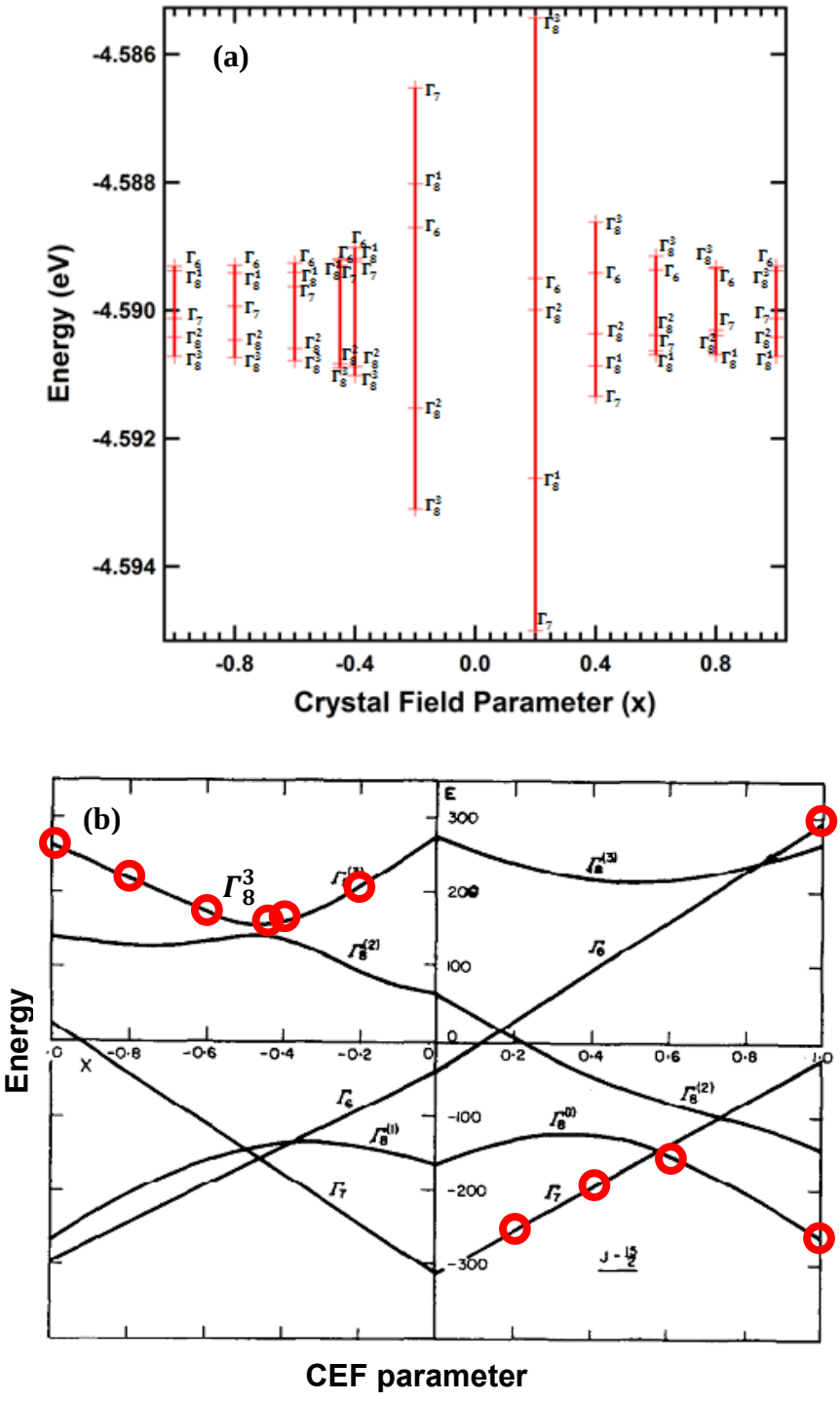

Fig. B.2. ground state symmetry in the trivalent Er^{3+} (J=15/2), (a) energy level diagram and (b) at different CEF parameters.

Fig. B.2a. reveals energy level diagram of trivalent Er^{3+} ground state symmetry in the case of J=15/2 at different CEF parameters which agree with experiment. Where the changing in energy level depend on the sign and value of CEF parameters x and W. **Fig. B.2b** is for $W = +1$, therefore in the case of negative W the sign of energy will be reversed. Also, in **Fig. B.2b** open red circle indicate CEF parameters which agree with experiment.

B.2. Simulated LD Temperature Dependence

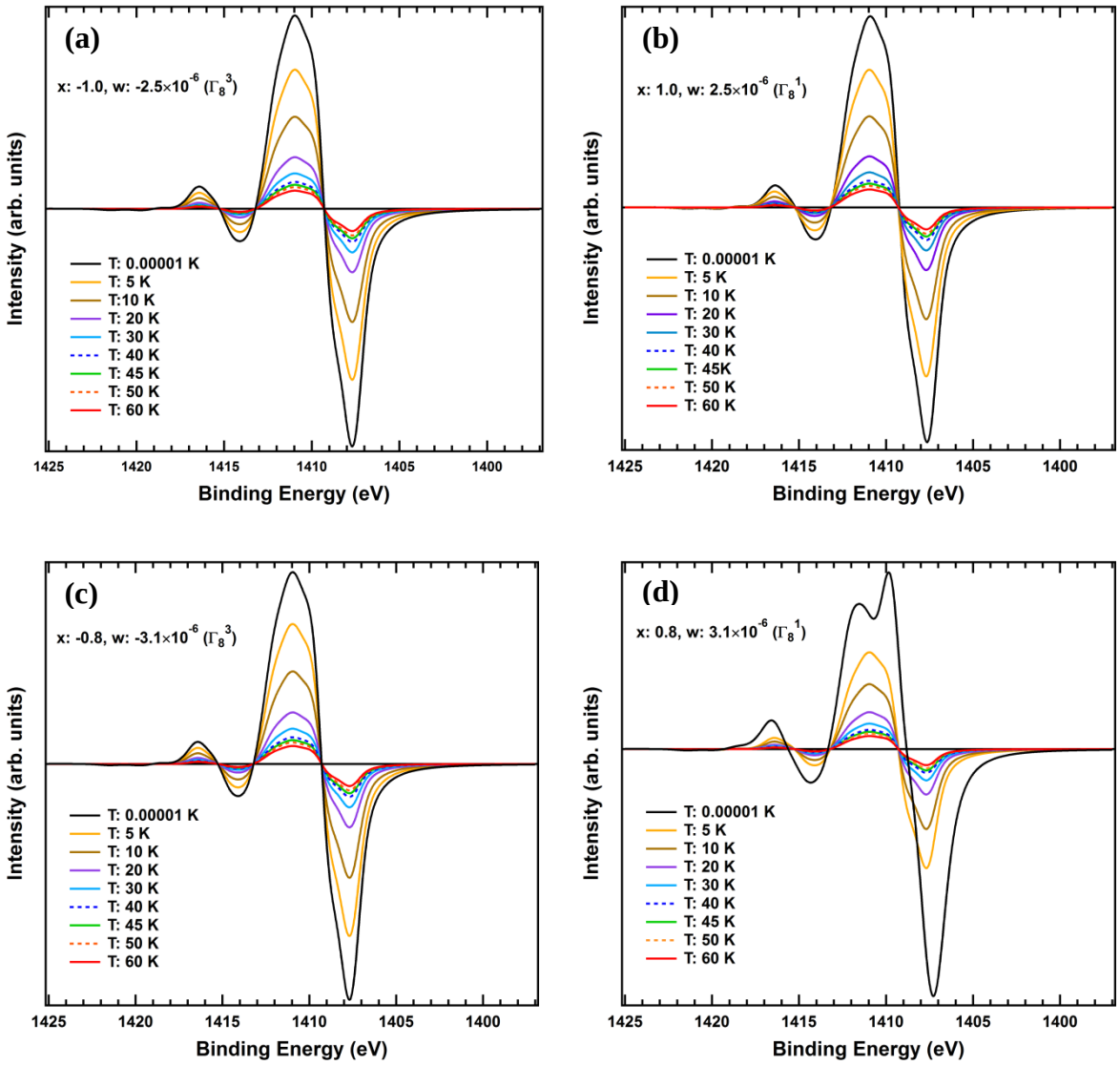

Fig. B.3. Simulated LD temperature dependence at different CEF parameters in Er^{3+} $3d_{5/2}$ core level photoemission spectra in [100] direction of $ErCo_2$ at $\theta = 9.5^0$ assuming the crystal-field-split ground state in cubic symmetry (continued to the next page).

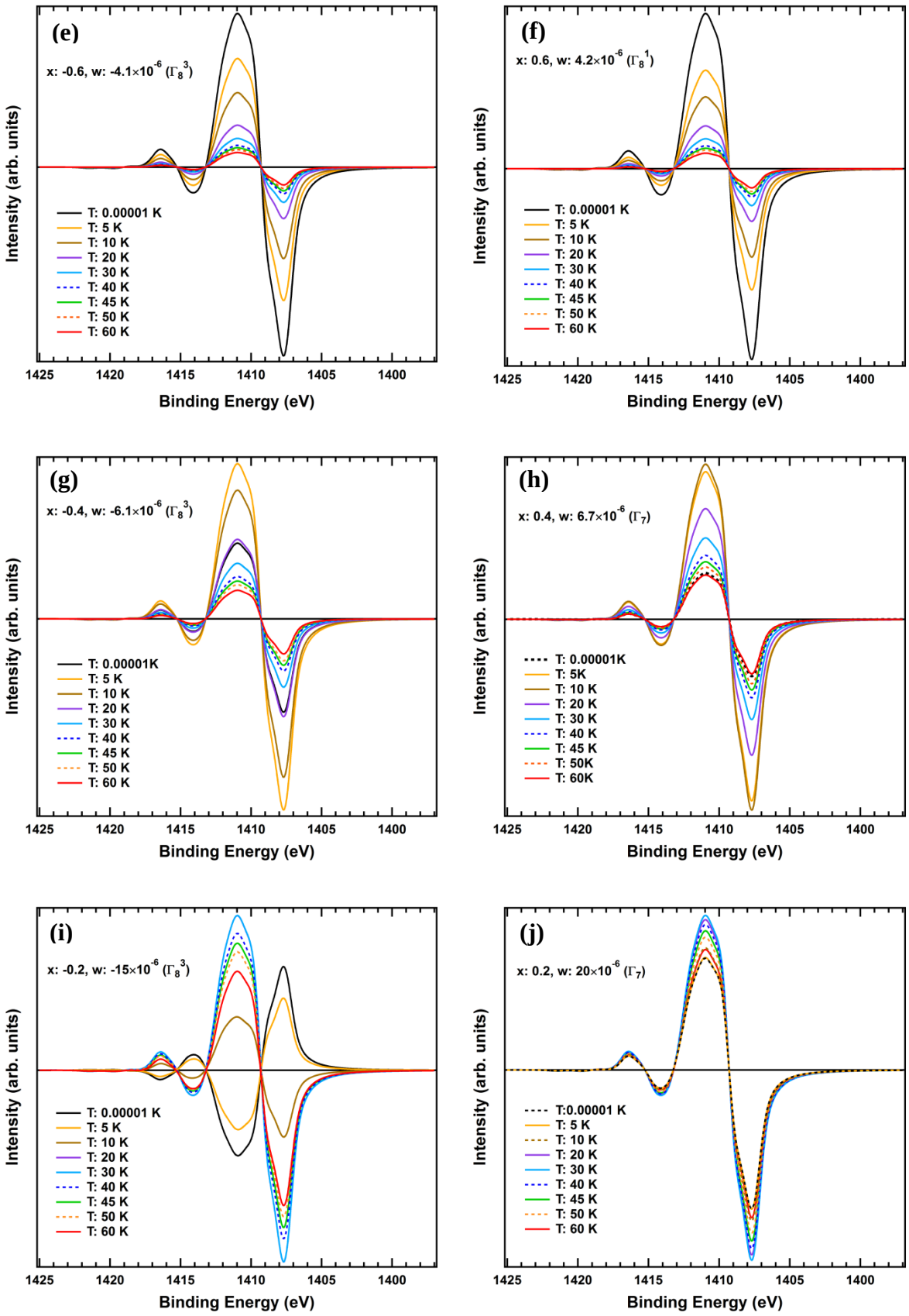

Fig. B.3. (continued from the previous page) Simulated LD temperature dependence at different CEF parameters in Er^{3+} $3d_{5/2}$ core level photoemission spectra in [100] direction of $ErCo_2$ at $\theta = 9.5^0$ assuming the crystal-field-split ground state in cubic symmetry (continued to the next page).

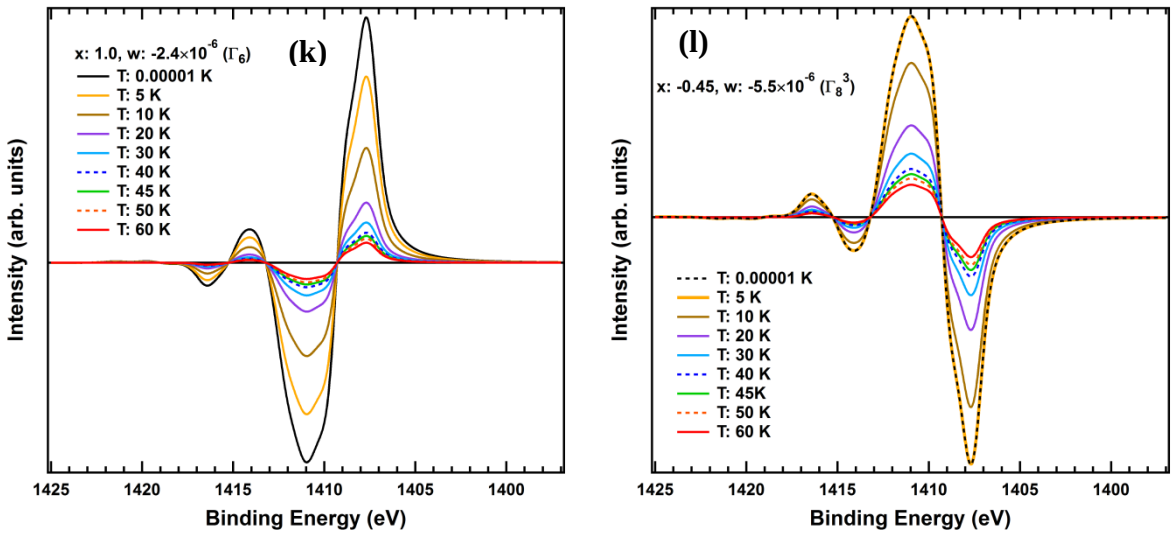

Fig. B.3. (continued from the previous page) Simulated LD temperature dependence at different CEF parameters in Er^{3+} $3d_{5/2}$ core level photoemission spectra in [100] direction of $ErCo_2$ at $\theta = 9.5^0$ assuming the crystal-field-split ground state in cubic symmetry.

Fig. B.3. illustrates the simulated LD temperature dependent at different CEF parameters in Er^{3+} $3d_{5/2}$ core level photoemission spectra in [100] direction of $ErCo_2$ at $\theta = 9.5^0$, confirming that LD at sufficient high temperatures reduced with increasing temperature without changing in it is sign and shape for the trivalent Er^{3+} $4f$ ground state symmetry. At low temperatures, the behavior of LD is non-isotropic in Γ_7 and Γ_8^3 ground state at CEF parameters ((x: 0.4, W: 6.7× 10^{-6} eV) and (x: 0.2, W: 20 × 10^{-6} eV) for Γ_7 and ((x: -0.4, W: -6.1× 10^{-6} eV) and (x: -0.2, W: -15 × 10^{-6} eV)) for Γ_8^3 as illustrated in **Fig. B.3h, j**, **g** and **i** respectively. Where the behavior of LD temperature dependent at **Fig. B.3h, j and g** is first LD increase with increasing temperature due to the contribution of first excited state then LD start decrease with increasing temperature due to the population of the next excited states. While in **Fig. B.3i**, first the sign of LD is positive, then with increasing temperature gradually the sign of LD flip (negative), the LD start increase with increasing temperature due to the contribution of first excited state then LD start reduce at sufficient high temperature due to the population of the next excited states.

B.3. Experimental Data Analysis

B.3.1. Extracting of pure s-pol Measured Spectrum

The switching of polarization using the diamond phase retarder is not perfect, and the s-pol measured spectrum included a p-polarized light component. Therefore, in order to obtain pure s-pol measured spectrum, it is necessary to subtract the p-polarized light component, given by the following relation:

$$I_s = I_{so} - \frac{A}{B} I_{po} \tag{B.1}$$

where, I_s: is pure s-pol measured spectrum (after subtracting p-polarized light component).

I_{so}: is original s-pol measured spectrum (before subtracting p-polarized light component).

A= p-pol light intensity during s-pol measurement × number of scans.

B= p-pol light intensity during p-pol measurement × number of scans.

I_{po}: is p-pol measured spectrum.

An example is shown below:

Table B.1. Number of scans of p-pol count in s and p-pol component in Er $3d_{5/2}$ core level XPS in [100] direction of $ErCo_2$ at 45 K and θ=9.5°.

No. of scans	p-pol light intensity during s-pol measurement	p-pol light intensity during p-pol measurement
25	804	7377
25	789	7481
25	855	7730
25	857	7118

A=25×(804+789+855+857)=82625

B= 25×(7377+7481+7730+7118)=742650

$$I_s = I_{so} - 0.11\, I_{po}$$

B.3.2. Shirley Background

The Shirley background correction method is one of the most frequently used mathematical methods for correcting the measured photoemission (XPS or UV) spectrum in solids. The Shirley method, considers the background at any point is due to inelastic scattered electrons, is assumed to arise only from the scattering of electrons of higher kinetic energy, the Shirley method removes the extrinsic energy loss contributions [B.1].

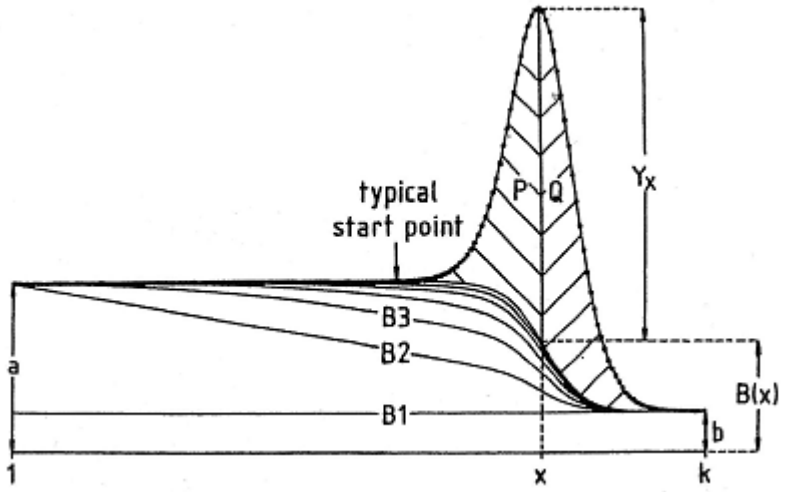

Fig. B.4. Inelastic background determination [B.2].

From **Fig. B.4**, the background $B(x)$ at point x in the spectrum which contains k equally spaced points of separation h, written as [B.2]:

$$B(x) = \frac{(a-b)Q}{(P+Q)} + b \qquad (B.2)$$

where, a is the average start point, b is the average end point, $(P+Q)$ is the total background subtracted (BS) peak area and Q is the BS peak area from point x to point k. Using the trapezoidal rule, Q expressed as [B.2]:

$$Q = h[\sum_{i=x}^{k} y_i - 0.5(y_x + y_k) \qquad (B.3)$$

where the term $0.5(y_x + y_k)$ is the correction introduced by the trapezoidal rule to the simple sum of points over the range x to k. Initial, the BS areas are calculated by choosing a linear constant background of magnitude b (correspond to line B1 in **Fig. B.4**). By substituting in

equation (B.2) obtains the background B2 which is then used to calculate new BS areas resulting in the background B3. This process repeated until $(P + Q)$ remains essentially unchanged on the successive iterations. In order to minimize the number of required iterations the start point is chosen close to the peak [B.2].

The Shirley background is calculated iteratively by:

$$S_{S,i}(E) = k \int_{E}^{+\infty} dE \, (j(E) - S_{S,i-1}(E)) \qquad (B.4)$$

S refers to Shirely, j(E) is the measured spectrum at energy E, k is constant, and the initial approximation $S_{S,o}$ is a constant background. **Fig. B.5.** shows example on the subtracted Shirley back ground process from Er $3d_{5/2}$ core level XPS in [100] direction of $ErCo_2$ measured using linear polarized light (s-pol) at 45 K and θ=9.5°.

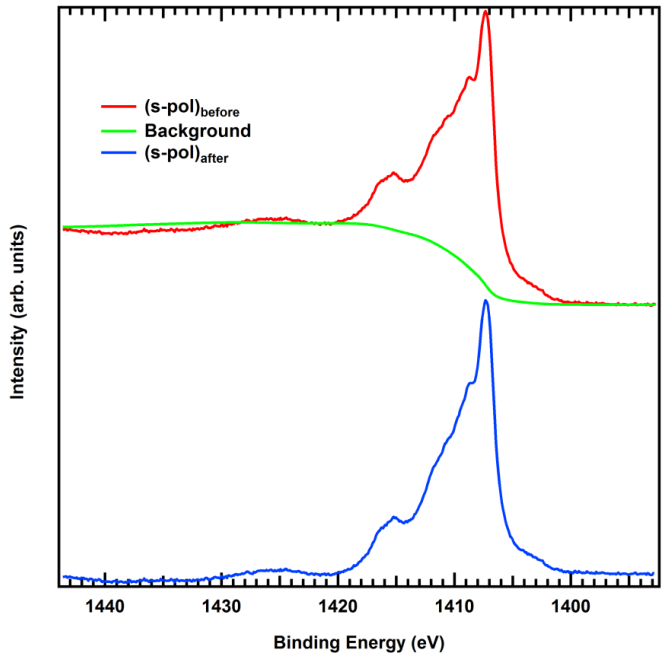

Fig. B.5. subtracted Shirley back ground process from Er $3d_{5/2}$ core level XPS in [100] direction of $ErCo_2$ measured using linear polarized light (s-pol) at 45 K and θ=9.5°.

B. 4. Reference

[B.1] D. A. Shirley, High-Resolution X-Ray Photoemission Spectrum of the Valence Bands of Gold, Phys. Rev. B, Vol. 5, p. 4709 (1972).

[B.2] A. Proctor and P. M. A. Sherwood, Data analysis techniques in X-ray photoelectron spectroscopy, Anal. Chem., Vol. 54 (1), p. *13 (1982)*, DOI: 10.1021/ac00238a008.

List of Publications

List of Publications

1. Publications in International Journals

1.1. Chapter 4

"Electronic Structure of the Laves Phase Compound $ErCo_2$ Studied by Polarization Dependent Hard X-Ray Photoemission Spectroscopy"

Amina A. Abozeed, Toshiharu Kadono, Akira Sekiyama, Hidenori Fujiwara, Atsushi Higashiya, Atsushi Yamasaki, Yuina Kanai, Kohei Yamagami, Kenji Tamasaku, Makina Yabashi, Tetsuya Ishikawa, Alexander V. Andreev, Hirofumi Wada, and Shin Imada.

J. Alloys Compd., to be submitted.

1.2. Chapter 5

"Rare-Earth Fourth-Order Multipole Moment in Cubic $ErCo_2$ Probed by Linear Dichroism in Core-Level Photoemission"

Amina A. Abozeed, Toshiharu Kadono, Akira Sekiyama , Hidenori Fujiwara, Atsushi Higashiya, Atsushi Yamasaki, Yuina Kanai, Kohei Yamagami, Kenji Tamasaku, Makina Yabashi, Tetsuya Ishikawa, Alexander V. Andreev, Hirofumi Wada, and Shin Imada.

J. Phys. Soc. Jpn (letter)., accepted.

2. Publications in Conferences

2.1. "Polarization Dependent Hard X-ray Photoemission of Single Crystal Laves Phase Ferrimagnet $ErCo_2$", **Amina Abozeed** , T. Kadono, A. Sekiyama , H. Fujiwara, A. Higashiya, A.Yamasaki, M. Murata, S. Taniguchi, M. Iwano, C. Morimoto, Y. Kanai, K. Yamagami, K. Tamasaku, M. Yabashi, T. Ishikawa, A. V. Andreev, H. Wada, and S. Imada, *Physical society of japan conference (JPS), Tohoku University- Japan, March,* ***2016.***

2.2. "The electronic structure of the Laves phase compound $ErCo_2$ studied by hard X-ray photoemission spectroscopy", **Amina Abozeed** , T. Kadono, A. Sekiyama , H. Fujiwara, A. Higashiya, A.Yamasaki, M. Murata, S. Taniguchi, M. Iwano, C. Morimoto, Y. Kanai, K.

Yamagami, K. Tamasaku, M. Yabashi, T. Ishikawa, A. V. Andreev, H. Wada, and S. Imada, *Japanese Society for Synchrotron Radiation Research (JSSR), Art Center of Kobe-Japan, January, **2017**.*

2.3. " Hard X-Ray Photoemission and Comparison with Band Structure Calculations of $ErCo_2$", **Amina Abozeed** , T. Kadono, A. Sekiyama , H. Fujiwara, A. Higashiya, A.Yamasaki, M. Murata, S. Taniguchi, M. Iwano, C. Morimoto, Y. Kanai, K. Yamagami, K. Tamasaku, M. Yabashi, T. Ishikawa, A. V. Andreev, H. Wada and S. Imada, *Physical society of japan (JPS) conference, Osaka University-Japan, March, **2017**.*

2.4. " The assessment of Quadrupole moment of R element in $R_2Fe_{14}B$ (R=Pr, Nd, Dy) by 3d-XAS Liner Dichroism", S. Taniguchi, H. Kada, S. Kato, **A. Abozeed**, C. Morimoto, T. Kadono, T. Isaji, K. Terashima, M. Yano, A. Manabe, A. Tanaka, J. Wang, L. Liang, L. T. Zhang, S. Hirano, T. Muro, T. Kinoshita and S. Imada, *Physical society of japan conference (JPS), Tohoku University- Japan, March, **2016**.*

2.5. " Hard X-ray photoelectron spectroscopy of Mn_3Ge, MnGa thin-films, M. Murata, T. Kadono, **A. Abozeed**, S. Iwano, S. Taniguthi, C. Morimoto, Y. Kanai, S. Fujioka, K. Yamagami, A. Sekiyama, H. Fujiwara, A. Higashiya, A. Yamasaki, K. Tamasaku, M. Yabashi, T. Ishikawa, T. Sakon, T. Kanomata, M. Doi, S. Imada, *Physical society of japan conference (JPS), Tohoku University- Japan, March, **2016**.*

Acknowledgement

Acknowledgement

I thank Allah, Almighty, for all gifts He gave me.

I would like to express the deepest appreciation to the head of our research group, Professor Dr. Shin Imada, who has the attitude and the substance of a genius: he continuously and in a convincing manner transferred to me the spirit of adventure in research and the excitement in teaching. I wish to thank Professor Imada for suggesting the project of the thesis and for his helpful guiding, insight, interest, patience, valuable supervision, and wisdom on both the academic and personal levels. Without his guidance and ongoing help this thesis would not have been possible.

I wish to take this opportunity to thank Professor Akira Sekiyama and his group members. Also, I would like to acknowledge Professor Alexander V. Andreev and Professor Hirofumi Wada for supporting us by the studied samples and their valuable explanation of some results.

Also I would like to thank Assistant Professor Dr. Toshiharu Kadono, M. Murata, S. Taniguchi, M. Iwano, C. Morimoto and K. Sakamoto for their help and efforts for experimental support. I owe my deepest gratitude to any member of our research group who gave me a helping hand or kind treatment. I thank the great country Japan represented in Ritsumeikan University for giving me this chance to get my PhD degree from Japan.

No words can express my deepest gratitude to my dear parents, my lovely husband, my son Mohamed, and my daughter Mariam on their care, kindness, understanding, tolerance, and assistance. Finally, I dedicate this work to my country, Egypt.

March 2018

Amina Abozeed

PhD candidate, Graduate School of Science and Engineering, Ritsumeikan University, Japan
Assistant Lecturer, Faculty of Science, Assiut University, Egypt